



CONFEDERATION OF EUROPEAN AEROSPACE SOCIETIES

AAAF AIAE AIDAA DGLR FTF NVvL RAeS SVFW

Proceedings of CEAS Forum on Aeroacoustics of Rotors and Propellers

9-11 June 1999, Rome, Italy

DISTRIBUTION STATEMENT A
Approved for Public Release
Distribution Unlimited

20000619 031

Organized by

~~AIDAA~~

Associazione Italiana Di Aeronautica e Astronautica

DTIC QUALITY INSPECTED 4

AD NUMBER		DATE	DTIC ACCESSION NOTICE
1. REPORT IDENTIFYING INFORMATION		REQUEST	
A. ORIGINATING AGENCY UNIVERSITA DEGLI STUDI ROMA TRE, ITALY		1. Put your n on reverse	
B. REPORT TITLE AND/OR NUMBER CEAS FORUM ON AEROACOUSTICS OF ROTORS & PROPELLERS		2. Complete	
C. MONITOR REPORT NUMBER R+D 8734-AN-02		3. Attach for mailed to	
D. PREPARED UNDER CONTRACT NUMBER N68171-99-H-5840		4. Use unde informat	
2. DISTRIBUTION STATEMENT		5. Do not on for 6 to 1	
APPROVED FOR PUBLIC RELEASE		DTIC:	
DISTRIBUTION UNLIMITED		1. Assign /	
PROCEEDINGS		2. Return	

20000619 031

IONS ARE OBSOLETE

Scientific Committee

L. Morino, University of Rome III, Rome, Italy
H. Brouwer, NLR, Marknesse, The Netherlands
R. Munt, DERA, Farnborough, United Kingdom
J. Prieur, ONERA, Chatillon, France
W.R. Splettstoesser, DLR, Braunschweig, Germany

The Forum is

- *sponsored by* CEAS
- *organized by* AIDAA
- *supported by:*

ERO (European Research Office)
EOARD (European Office of Aerospace Research and Development)
ONREUR (Office of Naval Research Europe)
CIRA (Italian Center for Aerospace Research)
University of Rome III; Department of Mechanical and Industrial Engineering

Announcement and Call for Papers

CEAS Forum on Aeroacoustics of Rotors and Propellers

9-11 June 1999, Rome, Italy

Confederation of European Aerospace Societies

The Confederation of European Aerospace Societies (CEAS) comprises the following national societies:

- Association Aéronautique et Astronautique de France (AAAF)
- Asociación de Ingenieros Aeronáutico de España (AIAE)
- Associazione Italiana di Aeronautica e Astronautica (AIDAA)
- Deutsche Gesellschaft für Luft- und Raumfahrt Lilienthal-Oberth (DGLR)
- Flygtekniska Foeringen (FTF)
- Nedrelanse Vereniging voor Luchtvaarttechniek (NVvL)
- Royal Aeronautical Society (RAeS)
- Schweizerische Vereinigung für Flugwissenschaften (SVFW)

Scientific Committee

Luigi Morino	University of Rome III, Chairman
Roel Houwink	NLR
Rodger Munt	DERA
Jean Prieur	Onera
Wolf R. Splettstoesser	DLR
Sandro Ianniello	CIRA, Secretariat

Scope of Forum

The CEAS Forum on Aeroacoustics of Rotors and Propellers is intended to give a comprehensive survey of the state of the art in the field and to provide an opportunity to scientists and engineers from industry, research establishments and universities to present new results based on their recent studies, to exchange opinions and experiences, and to discuss directions of future research.

The program's technical content will include theoretical, numerical, and experimental contributions that describe original research results and/or innovative design concepts. In addition, papers that provide in-depth reviews and timely surveys of appropriate subjects will be considered.

Papers that cover all aspects of exterior aeroacoustics of rotors and propellers (including tilt rotors) are solicited. Also of interest are papers dealing with those aspects of aerodynamics and blade dynamics that are particularly relevant in the understanding of aeroacoustic phenomena, such as BVI (Blade Vortex Interaction). Indeed, of particular interest are those papers regarding comprehensive analyses of the BVI interplay of aeroacoustics with aerodynamics and blade dynamics. Although CEAS comprises aerospace societies, the Forum will not be limited to aeronautical applications (e.g., helicopter rotors, airplane propellers, tiltrotors). Hence, papers on related fields (e.g., windturbines, fans, ship propellers) are also encouraged.

Submission of Abstracts and Manuscripts

The language of the Forum will be English. Abstracts of about 500 words should be submitted (by mail, e-mail, or fax), by **15 March 1999** to:

Prof. Luigi Morino
University of Rome III
Dipartimento di Ingegneria Meccanica e Industriale
via della Vasca Navale, 79
00149 Rome, Italy
Tel: +39 06 55173260
Fax: +39 06 5593732
e-mail: farp99@thames.dimi.uniroma3.it
WWW : <http://gange.dimi.uniroma3.it/~farp99>

Please include **names, title, affiliation, addresses, phone and fax numbers, and e-mail addresses of all the authors**. Unless otherwise requested by the authors, only the first author will be notified (by **1 April 1999**) of the acceptance.

The Forum will be organized into formal presentations, with Proceedings of all the papers presented. The "no paper, no podium" rule will apply to the Forum (an author cannot give his/her presentation if a written paper has not been prepared and made available at the Forum). A camera-ready to be included in the Proceedings should be sent by **15 May 1999**, to the above address.

Key dates

Receipt of Abstracts: **15 March, 1999**
Notification of Authors: **1 April, 1999**
Receipt of Manuscripts: **15 May, 1999**

Registration fee

The registration fee for the Forum is **250,000 Italian lire** (approximately 130 Euros). This includes coffee breaks and proceedings.

CEAS Forum on Aeroacoustics of Rotors and Propellers

9-11 June 1999, Rome, Italy

List of attendees

name	address	affiliation
S. Ahmed	Syed.Ahmed@dlr.de	DLR, Braunschweig, Germany
P. Bassanini	<u>Bassanin@mat.uniroma1.it</u>	Università "La Sapienza", Rome, Italy
G. Bernardini	nanni@gange.dimi.uniroma3.it	Università di Pisa, Pisa, Italy
H. Brouwer	brouwer@nlr.nl	NLR, Marknesse, The Netherlands
P. Bulgarelli	upbulga@rios6.insean.it	INSEAN, Rome, Italy
A. Cafiero	giordano@alenia.finmeccanica.it	Alenia Aerospazio, Napoli, Italy
F.X. Caradonna	caradonna@merlin.arc.nasa.gov	Ames Research Center, Moffet Field, CA, USA
A. Corbelli	corbelli@nilo.dimi.uniroma3.it	Università "La Sapienza", Rome, Italy
M. Costanzo	m.costanzo@mail.insean.it	INSEAN, Rome, Italy
E. De Bernardis	e.debernardis@insean.it	INSEAN, Rome, Italy
R. Drobietz	drobietz@lu.ilr.rwth-aachen.de	ILR RWTH, Aachen, Germany
M. Elefante	ceimm@insean.it	CEIMM, Rome, Italy
P.G. Esposito	giorgio@rios2.insean.it	INSEAN, Rome, Italy
A. Frediani	a.frediani@adm.unipi.it	Università di Pisa, Pisa, Italy
M. Gennaretti	m.gennaretti@uniroma3.it	Università "Roma Tre", Rome, Italy
G. Guj	guj@uniroma3.it	Università "Roma Tre", Rome, Italy
H. Heller	<u>hanno.heller@dlr.de</u>	DLR, Braunschweig, Germany
S. Ianniello	s.ianniello@cira.it	CIRA, Capua, Italy
U. Iemma	u.iemma@uniroma3.it	Università "Roma Tre", Rome, Italy

J.L. Johnson	jjohnson@mail.arc.nasa.gov	Aerospace Computing Inc, Los Altos, CA, USA
V. Kloeppel	valentin.kloeppel@eurocopter.de	Eurocopter, Germany
D. Knoerzer	Dietrich.Knoerzer@dg12.cec.be	European Commission Dg XII, Bruxelles, Belgium
V. F. Kopiev	vkopiev@mx.iki.rssi.ru	TsAGI, Moscow, Russia
V. M. Kuznetsov	vkopiev@mx.iki.rssi.ru	TsAGI, Moscow, Russia
E. Messina	messina@cs.unibo.it	Università di Bologna, Bologna, Italy
M. Messina	bit0293@iperbole.bologna.it	Università "La Sapienza", Rome, Italy
E. Maury	eric.maury@avions.aerospatiale.fr	Bnp Aerospatiale, Toulouse, France
L. Morino	l.morino@uniroma3.it	Università "Roma Tre", Rome, Italy
F. Nitzsche	Fred. Nitzsche@nrc.ca	National Research Council Canada, Ottawa, ON, Canada
P. Ouzts		European Research Office
A. Pagano	a.pagano@cira.it	CIRA, Capua, Italy
H.V.L. Patrick	patrickh@db.erau.edu	Embry Riddle Aeronautical Univ., Daytona Beach, FL, USA
N. Peake	N.Peake@damtp.cam.ac.uk	Cambridge University, Cambridge, UK
J. Prieur	<u>prieur@onera.fr</u>	ONERA, Chatillon, France
P. Renzoni	<u>p.renzoni@cira.it</u>	CIRA, Capua, Italy
S. Sampath	ssampath@army.ehis.navy.mil	European Research Office
L.N. Sankar	lsankar@ae.gatech.edu	George Institute of Technology , Atlanta GA, USA
D. Theofiloyiannakos	dtheof@cres.gr	Center for Renewable Energy Sources, Pikerni, Greece
S.G. Voutsinas	christin@fluid.mech.ntua.gr	National Technical University of Athens, Athens, Greece

CEAS Forum on Aeroacoustics of Rotors and Propellers

Informal Proceedings

The Forum was held on June 9–11, 1999 at the University of Rome III, viale Guglielmo Marconi nr. 499, Rome, Italy. It has been a single-session event and a total of 28 papers were presented by speakers coming from ten different countries (Belgium, Canada, France, Germany, Greece, Italy, The Netherlands, Russia, UK, USA; see Programme included in the formal Proceedings).

Of particular interest were:

1. the keynote lecture held by Dr. Dietrich Knoerzer of the Division General XII of the European Commission: "On Technology Acquisition in Aeronautics through the Research Framework Programme,"
2. a Special Session on Activity of EU Research Establishments (H. Heller, DLR; C. Tung and F.X. Caradonna, NASA Ames; J. Prieur, ONERA; S. Ianniello, CIRA; F. Nitzsche, NRC Canada; D. Theofiloyiannakos and S.G. Voutsinas, Center for Renewable Energy Sources, Greece), and
3. a Special Session on Projects Sponsored by EU (V. Kloeppel, HELIFLOW; P. Renzoni, EROS; A. Pagano, ROSAA; H. Brouwer, X-NOISE; E. Maury, APIAN; A. Paonessa and A. Cafiero, SNAAP).

A total of 40 people attended the Forum (see list of attendees).

The Forum was very well received; the Scientific Committee was complimented on the technical content of the papers as well as on the organization.

Table of Contents

Foreword	ii
Program of the Forum	iii
S.R. Ahmed, J.P. Yin <i>Interactional Aerodynamics and Aeroacoustics of Helicopter. Main-Rotor/Tail-Rotor and Main-Rotor/Fuselage</i>	1
F.X. Caradonna <i>The BVI Prediction Problem and the Role of CFD</i>	26
M. Costanzo, M.Elefante <i>Noise Levels Measurements at the INSEAN Circulating Water Channel with a Twin Screw Ship Model</i>	52
R. Drobietz, G. Neuwerth, D. Jacob <i>Noise Reduction Potential of Swept Propeller Blades</i>	65
J.L. Johnson, L.A. Young <i>Tilt Rotor Aeroacoustic Model Project</i>	78
V.F. Kopiev, A.A. Maslov <i>The Mechanism of Noise Intensification and Suppression for a Propeller in a Short Duct</i>	99
V.M. Kuznetsov, L.S. Krymova, S.Yu. Makashov <i>Research of Propfan Acoustics Characteristics</i>	108
F. Nitzsche, A. Solaiman, F.F. Afagh <i>"Smart" Blade Effects on the Aeroelastic Characteristics of Helicopter Rotors</i>	119
A. Paonessa, A.Cafiero <i>Study of noise and Aerodynamics of Advanced Propellers (SNAAP Project)</i>	132
H.V.L. Patrick, G. Tchotchoua <i>A Subsonic Propeller Acoustic Scaling Law</i>	142
L.N. Sankar, N. Hariharan, C. Tung <i>First Principles Based Methods for the Prediction of Loading over Fixed and Rotary Wing Geometries</i>	150
D. Theofiloyiannakos, S.G. Voutsinas <i>Noise from Wind Turbines</i>	160
S.G. Voutsinas, D.G. Triantos <i>Aeroacoustics of Full Helicopter Configurations using Vortex Particle Flow Approximation</i>	175

Foreword

These Proceedings contains most of the contributed papers presented at the CEAS Forum on Aeroacoustics of Rotors and Propellers, held at the University of Rome III, Rome, Italy, on June 9-11, 1999. The two Special Sessions held on Thursday, June 10, consists of invited papers for which a written paper was not required at the time of the Forum; a special issue of *Aerotecnica Missili e Spazio*, the Journal of AIDAA, will be dedicated to this Forum and will contain all the papers not included in these Proceedings.

I wish to express my gratitude to Dr. Dietrich Knoerzer of the European Commission DG XII, for the endorsement of the Forum and for his contribution to the organization of the two Special Sessions. I also wish to thank CEAS for sponsoring the Forum and AIDAA for the support in its organization; in particular I wish to thank my collaborators, Dott. Ing. Giovanni Bernardini, Andrea Corbelli and Vincenzo Marchese, for the time that they generously dedicated to the organization of the Forum. Finally, the financial contributions of ERO (European Research Office), EOARD (European Office of Aerospace Research and Development), ONREUR (Office of Naval Research Europe), CIRA (Italian Center for Aerospace Research) and the University of Rome III, Department of Mechanical and Industrial Engineering - that made this Forum possible - are gratefully acknowledged.

Luigi Morino

CEAS
Forum on Aeroacoustics of Rotors and Propellers
9-11 June 1999, Rome, Italy

Program of the Forum

Wednesday, June 9

	Chairman: J. Prieur
10.00-10.20	Welcome F. Gori - <i>Dean, Faculty of Engineering, University of Rome III</i>
10.20-11.00	The BVI Prediction Problem and the Role of CFD (Keynote) F.X. Caradonna - <i>Ames Research Center, Moffett Field, CA, USA</i>
11.00-11.20	Coffee Break
11.20-12.00	Interactional Aerodynamics and Aeroacoustics of Helicopter Main-Rotor/Tail-Rotor and Main-Rotor/Fuselage (Keynote) S.R. Ahmed, J.P. Yin - <i>DLR, Braunschweig, Germany</i>
12.00-12.40	The Investigations of Acoustic Characteristic of Propans (Keynote) V.M. Kuznetsov, L.S. Krymova, S.Yu. Makashov <i>State Scientific Research Center TsAGI, Moscow, Russia</i>

	Chairman: F.X. Caradonna
14.20-15.00	Asymptotic Methods in Propeller Noise Prediction (Keynote) N. Peake - <i>Cambridge University, Cambridge, UK</i>
15.00-15.30	First Principles Based Methods for the Prediction of Loading Over Fixed and Rotary Wing Geometries L.N. Sankar - <i>Georgia Institute of Technology, Atlanta, GA, USA</i> N. Hariharan - <i>CFD Reasearch Corporation, Huntsville, AL, USA</i> C. Tung - <i>NASA Ames Research Center, Moffett Field, CA, USA</i>
15.30-16.00	Coffee Break
16.00-16.30	The Mechanism of Noise Intensification and Suppression for a Propeller in a Short Duct V.F. Kopiev, A.A. Maslov <i>State Scientific Research Center TsAGI, Moscow, Russia</i>
16.30-17.00	Tilt Rotor Aeroacoustic Model Project J.L. Johnson - <i>Aerospace Computing Inc., Los Altos, CA, USA</i> L.A. Young - <i>NASA Ames Research Center, Moffett Field, CA, USA</i>

Program of the Forum

Thursday, June 10

Overview on EU Research Collaboration

	Chairman: L. Morino
9.00-9.30	Technology Acquisition in Aeronautics through the Research Framework Program (Keynote) D. Knoerzer - <i>European Commission, DG XII</i>

Special Session on Activity of Research Establishments

	Chairman: V. Kloeppel
9.30-10.10	A Concise Ten-Year Survey on DLR's Involvement in European Rotor Noise Research Activity (Keynote) H. Heller - <i>DLR, Braunschweig, Germany</i>
10.10-10.40	Rotorcraft Aero-Acoustic Research in the US C. Tung, F.X. Caradonna <i>NASA Ames Research Center, Moffett Field, CA, USA</i>
10.40-11.00	Coffee Break
11.00-11.30	Recent Helicopter Rotor Noise Studies at ONERA J. Prieur - <i>ONERA, Chatillon, France</i>
11.30-12.00	1989-1999 Ten Years of Rotors' (Numerical) Aeroacoustics at CIRA S. Ianniello - <i>CIRA, Capua, Italy</i>
12.00-12.30	The National Research Council Canada Program on Helicopter Individual Blade Control F. Nitzsche - <i>National Research Council Canada, Ottawa, ON, Canada</i>
12.30-13.00	Noise from Wind Turbines D. Theofiloyiannakos - <i>Center for Renewable Energy Sources, Pikermi, Greece</i> S.G. Voutsinas - <i>National Technical University of Athens, Athens, Greece</i>

Special Session on Projects Sponsored by European Union

	Chairman: D. Knoerzer
14.30-15.00	HELIFLOW - an Attempt to Simulate Aerodynamic/Aeroacoustic Interference. Problems in the Wind Tunnel V. Kloeppel - <i>Eurocopter Deutschland, Holland</i>
15.00-15.30	The EROS Project P. Renzoni - <i>CIRA, Capua, Italy</i>
15.30-16.00	The ROSAA Project A. Pagano - <i>CIRA, Capua, Italy</i>
16.00-16.30	Coffee Break
16.30-17.00	The X-Noise Project H. Brouwer - <i>NLR, Marknesse, The Netherlands</i>
17.00-17.30	The APIAN Project E. Maury - <i>BNP Aerospatiale, Toulouse, France</i>
17.30-18.00	Study of Noise and Aerodynamics of Advanced Propellers (SNAAP) A. Paonessa, A. Cafiero - <i>ALENIA Aerospazio, Napoli, Italy</i>

Program of the Forum

Friday, June 11

	Chairman: S.R. Ahmed
9.00-9.30	Aeroacoustics of Full Helicopter Configurations Using Vortex Particle Flow Approximation S.G. Voutsinas, D. Triantos <i>National Technical University of Athens, Athens, Greece</i>
9.30-10.00	Noise Levels Measurements at the INSEAN "Circulation Water Channel" with a TwinScrew Ship Model M. Costanzo - <i>INSEAN, Rome, Italy</i> - M. Elefante <i>CEIMM, Rome, Italy</i>
10.00-10.30	"Smart" Blade Effects on the Aeroelastic Characteristics of Helicopter Rotors F. Nitzsche - <i>National Research Council Canada, Ottawa, ON, Canada</i> A. Solaiman, F.F. Afagh - <i>Carleton University, Ottawa, ON, Canada</i>
10.30-11.00	Coffee Break
11.00-11.30	Noise Reduction Potential of Swept Propeller Blades R. Drobietz, G. Neuwerth, D. Jacob <i>ILR, RWTH Aachen, Germany</i>
11.30-12.00	Screws Propellers and Fans Based on the Mobius Strip M. Gilinsky - <i>Hampton University, Hampton, Virginia, USA</i>
12.00-12.30	A Subsonic Propeller Acoustic Scaling Law H.V.L. Patrick - <i>Embry-Riddle Aeronautical Univ., Daytona Beach, FL, USA</i> G. Tchotchoua - <i>The University of Florida, Gainesville, Florida, USA</i>

	Chairman: S.G. Voutsinas
14.15-14.45	A Combined Interior-Exterior Model for Propeller Acoustics U. Iemma, M. Gennaretti - <i>University of Rome III, Rome, Italy</i>
14.45-15.15	Towards a Global Model for CAAA (Computational Aeroacoustics/ Aeroelasticity/ Aerodynamics) of Rotors and Propellers L. Morino, M. Gennaretti, U. Iemma - <i>University of Rome III, Rome, Italy</i> G. Bernardini - <i>University of Pisa, Pisa, Italy</i> A. Corbelli - <i>University of Rome "La Sapienza", Rome, Italy</i>

16.00-17.30	Visit to the Etruscan Museum of "Valle Giulia"
-------------	---

INTERACTIONAL AERODYNAMICS AND AEROACOUSTICS OF HELICOPTER MAIN-ROTOR/TAIL-ROTOR AND MAIN-ROTOR/FUSELAGE

S.R. Ahmed, J.P. Yin
*German Aerospace Center (DLR)
Institute of Design Aerodynamics
Braunschweig, Germany.*

April 29, 1999

ABSTRACT

This paper address two problems of the helicopter flowfield: the aerodynamic and aeroacoustic interaction between a) the main- and the tail rotor and, b) between the main rotor and the fuselage. The first interaction is analysed with a numerical approach; the main rotor/fuselage interaction study, restricted to aerodynamics, is based on wind tunnel experiments.

The rotor interactions studied are for a) a two-blade main- and tail rotor in hover, and b) a four-blade main- and a two-blade tail rotor in climb flight. Parameters varied for the hover configuration are the lateral spacing between the main- and tail rotor and the sense of tail rotor rotation.

The unsteady pressure on the main- and tail rotor blade surface is calculated with a 3-D unsteady free wake panel method and used as input to a Ffowcs Williams Hawkins-equation based code to evaluate the aeroacoustics.

Main rotor effects a significant change in the noise directivity pattern and noise level of the tail rotor. Tail rotor contribution to the total noise dominates during the climb flight.

Main rotor/fuselage aerodynamic interaction is analysed from pressure, and flow visualisation data of wind tunnel tests. Test parameters are rotor thrust and advance ratio.

Rotor downwash and fuselage flow vary with flight condition and govern the flow aerodynamics. The global flowfield is strongly dependent on the rotor thrust and advance ratio.

INTRODUCTION

Aerodynamic and aeroacoustic interaction between helicopter main rotor (MR), tail rotor (TR) and the fuselage are an important area of current research, motivated by the need to increase the cruise speed, improve the handling qualities, reduce the vibrations and pilot workload and lessen the noise impact on the environment.

The helicopter MR operates in close vicinity of the TR and the fuselage and major aerodynamic interactions occur between these components which govern also the noise generation and radiation in the flow field.

The fuselage displaces spatially the oncoming flow causing the the rotor blades to experience varying incidence over the azimuth. The fuselage distorts the MR wake and blade tip-vortex trajectory, changing thereby the blade/vortex interactions (BVI); the fuselage itself is immersed in the MR downwash. The MR and TR wakes interact and merge to form a complex vorticity dominated wake flow region. The TR is exposed to the wakes coming off the fuselage rear-end and the MR hub. The intensity of these interactions varies with the flight conditions. All these phenomena are unsteady and generate fluctuating vehicle loads, vibrations and noise.

Helicopter noise, due to its characteristic impulsive and tonal content, is a source of community annoyance. The main sources of helicopter noise are its MR, TR, engine, and the drivetrain components. The MR and the TR operate in free atmosphere and radiate noise unobstructed into the environment. With rising concern for environmental issues, helicopter noise has gained importance on par with performance, safety and reliability. For military helicopters, noise is a source of early detection.

The contents of this paper address two problems of helicopter flowfield, namely the MR/TR interaction and the interaction between the MR and the fuselage. The first interaction phenomena is analysed with a numerical approach; the MR/fuselage interaction study is based on wind tunnel experiments.

MR/TR INTERACTION ANALYSIS

The main research effort in the past was concentrated on the MR aerodynamics and aeroacoustics, where extensive work, both theoretical and experimental helped to deepen the understanding of the aerodynamic and noise generating mechanisms. Even though the TR has been recognised early [1] as a significant source of helicopter noise, research effort towards TR aerodynamics and noise has been less extensive [2, 3, 4, 5, 6 and 7].

The complex flow in which the TR operates poses an extreme challenge both for experimental and theoretical study. The complex flow around the TR is the product of the interacting flows generated by the main rotor wake, fuselage, rotor hub, engine exhaust and empennage in addition to its own wake.

Research on TR noise has produced some contradictory results which are as yet unexplained. Leverton's work in the seventies [1], with the Lynx helicopter and simple theoretical model studies identified the interaction of blade tip vortices of the MR with the TR as the main source of TR noise. Based on this, a significant reduction in TR noise could be achieved by reversing the sense of rotation of the TR [2]. In contrast the detailed experimental investigations of Schultz et al [7], on a model scale MR/TR set-up in the DNW-wind tunnel show that the noise generated by the TR under the interaction of MR was less than the noise of the TR alone. Results of Schultz et al have been substantiated by the experimental results of Fitzgerald et al [8] and Martin et al [9]. It appears that either findings are restrictive to particular configurations investigated.

Theoretical analysis of MR/TR interaction in earlier work is based on the aerodynamic interaction between the MR tip vortices and the TR blades. George et al [10] made a comparative study of different TR noise mechanisms. They conclude that the MR tip vortex/TR interaction generates the excess noise compared to that of TR in isolation. Also Tadghigi [11], using a similar approach comes to same conclusions.

The work most relevant to the present paper is the analysis of Quackenbusch et al [12]. The flow field in the inlet plane of the TR disc was calculated without simulating the TR or its wake and then using this data to compute the TR acoustics. They note the importance of simulating the full-span wake of the MR to correctly capture the TR acoustics.

Interaction of MR/TR is also the subject of the work of Baron et al [13] where the aerodynamics are investigated using a lifting surface representation for the blade and a Lagrangian vortex lattice free wake. Aerodynamic interaction between multiple rotor configurations was investigated by Bagai et al [14] where a full-span wake with a roll-up concept is used to simulate the tip vortices.

The MR/TR interaction results presented here are from an ongoing effort at DLR to simulate the aerodynamics and aeroacoustics of a helicopter MR/TR configuration in subsonic flow. A generic two-blade MR/TR configuration in hover and a four-blade MR with a two-blade TR configuration in climb mode is studied without the fuselage. The results are meant to demonstrate the ability of the code to capture the physics of the interaction.

The approach employs a 3-D free wake panel method [15], to compute the unsteady pressure distribution on the MR and TR blade surface. This serves as input to a Ffowcs Williams, Hawkins (FWH)-equation based acoustic code to evaluate the aeroacoustics. The panel method used accounts for blade thickness, twist and arbitrary planform as well as lead/lag, flapping and pitching motions of the blades. The simultaneous rotation of both rotors captures the mutual interaction between the MR and TR. The wakes of both rotors evolve in a Lagrangian fashion as full-span vortex lattice free wakes as the computation proceeds in the time domain. For the hover configuration, the effect of tail rotor sense of rotation and the lateral distance between the rotor axis on the aerodynamics and aeroacoustics is investigated.

1. Numerical Model of Rotor Aerodynamics

A 3-D free wake panel method developed by the authors [16,17] to treat the flow around single rotors in arbitrary motion was extended to treat two simultaneously turning rotors. The boundary condition of flow tangency on the M- or TR surface is satisfied at every time instant with consideration of the interaction between the MR/TR blades and their free wakes.

The lifting rotor blade is modeled with the following elements (Fig. 1):

- a) a source/sink distribution over the blade surface simulating blades of *finite* thickness,
- b) a *prescribed* doublet distribution over the blade mean surface to simulate the blade lift and,
- c) a short zero-thickness elongation of the blade trailing edge (*Kutta panel*). This fixes the strength of the blade circulation.

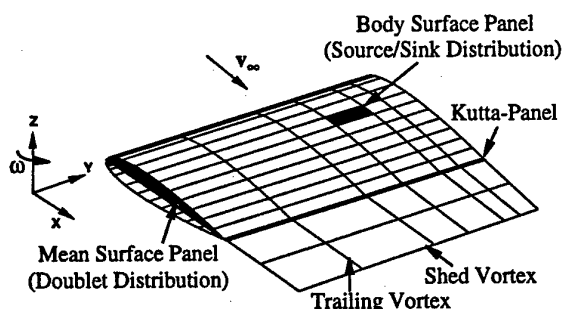


Fig. 1 Numerical Model of a Blade and Wake Segment

The numerical procedure consists of partitioning the blade and mean surface into small planar surface elements (panels), which carry a source/sink or doublet distribution of unknown strength.

Imposing the flow tangency condition at a collocation point on each blade- and Kutta panel leads to a system of *linear* algebraic equations whose solution gives the strength of the collocation

point singularities (source/sink or doublet) after each computation (time) step. With this the induced velocities on the blade surface and wake elements are evaluated. After each computation step, vortex panels are released from the blade trailing edge and move in space (over the duration of the time step) with velocities induced by the entirety of blade- and wake vortex panels plus the velocity components due to blade motion. A full-span free wake is generated in this manner behind the blades as the computation proceeds. The pressure on the blade surface is calculated using the *unsteady* Bernoulli equation. A more detailed description of the numerical scheme is available in [15].

The non-linearity of the problem stems from the *a priori* unknown spatial location of the wakes. An additional complexity in the case of MR/TR operation arises due to the relative motion between the M- and TR blades, whose consideration is essential to correctly capture the interaction effects.

1.1 Blade Motion Definition in Inertial Frame of Reference

All blade motions are referred to a ground-fixed inertial frame of reference (i-frame), denoted by the superscript 'i', Fig.2. The motion in i-frame can be transferred to a blade-fixed reference frame (b-frame; denoted by a superscript 'b') by five transformation matrices T , which account for the pitching-, lead/lag-, flapping-, and rotational motion of the rotor blade besides the rotor shaft tilt:

$$\mathbf{X}^{(i)}(t) = \begin{bmatrix} X_1^{(i)} \\ X_2^{(i)} \\ X_3^{(i)} \end{bmatrix} = \begin{bmatrix} U_x t \\ U_y t \\ U_z t \end{bmatrix} + T_{\alpha_t} T_{\Psi} T_{\beta} T_{\xi} T_{\alpha} \begin{bmatrix} X_1^{(b)} \\ X_2^{(b)} \\ X_3^{(b)} \end{bmatrix} + T_{\alpha_t} T_{\Psi} T_{\beta} \begin{bmatrix} 0 \\ e \\ 0 \end{bmatrix} \quad \dots (1)$$

$\mathbf{X}^{(i)}(t)$ is the position vector of a point on the MR blade in the i-reference frame and $\mathbf{X}^{(b)}(t)$ the corresponding vector in the b-reference frame at time t . The vector \mathbf{X} has the components X_1, X_2 and X_3 , and the translational velocity vector \mathbf{U} (in the i-frame), the components U_x, U_y , and U_z . The subscripts α, β, ξ and ψ are the blade pitching-, flapping-, lead/lag- and azimuth angles, whereas α_t denotes the tilt of the rotor shaft from the i-frame normal. The flap offset is denoted by e .

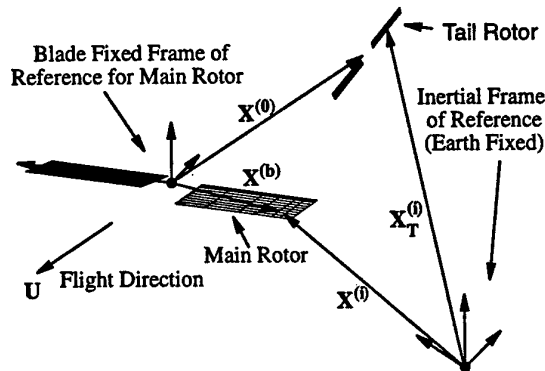


Fig. 2 Blade Fixed- and Inertial Frame of Reference

The position vector for a point on the TR blade in the i-frame, $\mathbf{X}_T^{(i)}(t)$ is related to the position vector of the same point in the TR b-frame of reference, $\mathbf{X}_T^{(b)}(t)$, by the following six transformation matrices (see Fig.2):

$$\mathbf{X}_T^{(i)}(t) = \begin{bmatrix} X_{T1}^{(i)} \\ X_{T2}^{(i)} \\ X_{T3}^{(i)} \end{bmatrix} = \begin{bmatrix} U_{xt} \\ U_{yt} \\ U_{zt} \end{bmatrix} + T_{\alpha_t} T_{90} T_{\Psi_T} T_{\beta_T} T_{\xi_T} T_{\alpha_T} \mathbf{X}_T^{(b)} \quad \dots (2)$$

$$+ T_{\alpha_t} T_{90} T_{\Psi_T} T_{\beta_T} \begin{bmatrix} 0 \\ e_T \\ 0 \end{bmatrix} + T_{\alpha_t} \mathbf{X}^{(0)}$$

with

$$T_{90} = \begin{bmatrix} \cos 90^\circ & 0 & \sin 90^\circ \\ 0 & 1 & 0 \\ -\sin 90^\circ & 0 & \cos 90^\circ \end{bmatrix}, \quad \mathbf{X}^{(0)} = \begin{bmatrix} X_1^{(0)} \\ X_2^{(0)} \\ X_3^{(0)} \end{bmatrix}, \quad \mathbf{X}_T^{(b)} = \begin{bmatrix} X_{T1}^{(b)} \\ X_{T2}^{(b)} \\ X_{T3}^{(b)} \end{bmatrix} \quad \dots (3)$$

The subscript T denotes the matrices for the tail rotor. $\mathbf{X}^{(0)}$ represents the lateral distance vector between the axis of the M- and TR. T_{90} is the transformation needed to account for the TR plane being normal to the MR disc

1.2 Numerical Implementation

The discretization of the blade- and wake- surface through a finite number of planar panels leads to a system of *linear* algebraic equations

$$\sum_{j=1}^{m_s} A_{ij} X_j + \sum_{j=1}^{n+m_k} B_{ij} Y_j = R_j - \sum_{j=1}^p C_{ij} Z_j \quad \dots (4),$$

with the index $i = 1, 2, 3, \dots (m_s + m_k)$. Hereby is m_s the total number of panels on the M- and TR, n the total number of panels on the MR/TR-blade mean surface, and m_k the total number of M- and TR Kutta panels. The number of panels on the blade surface and the number of Kutta panels (and with it the number of collocation points) remains constant. The number of wake panels p , however, increases as the computation progresses. The above system of equations is solved iteratively for each time step. A_{ij} , B_{ij} and C_{ij} are the mutual „influence coefficients“ of the (surface and wake) panels. Since the relative position of the MR/TR blades and their wakes changes after each

time step, these influence coefficients need to be updated after *each* computation step.

2. The Computation of Aeroacoustics

The unsteady blade pressures calculated by the aerodynamic code serve as input to the computation of the aeroacoustics. The code employed is based on formulation 1a of Farassat et al [18,19] with thickness and loading terms only. The thickness noise can be calculated from blade profile and blade motion description. For the incompressible flow studied here, quadrupole noise contribution is assumed to be small. The calculations are performed in the time domain and the obtained pressure time history Fourier-analysed to arrive at the acoustic spectrum.

For potential flow the acoustic pressure at a location \mathbf{x} and time t can be expressed as:

$$4\pi P'_T(\mathbf{x}, t) = \int_{f=0} \left[\rho_0 C_0^2 \frac{\dot{M}_n}{C_0 r (1 - M_r)^2} \right]_{\text{ret}} dS + \int_{f=0} \left[\rho_0 C_0^2 M_n \frac{r \dot{M}_i \hat{r}_i + c_0 M_r - c_0 M^2}{C_0 r^2 (1 - M_r)^3} \right]_{\text{ret}} dS \quad \dots (5)$$

$$4\pi P'_L(\mathbf{x}, t) = \int_{f=0} \left[\dot{P} \frac{\hat{n}_i \hat{r}_i}{C_0 r (1 - M_r)^2} \right]_{\text{ret}} dS + \int_{f=0} \left[P \frac{\hat{n}_i \hat{r}_i}{C_0 r (1 - M_r)^2} + \frac{\hat{n}_i \hat{r}_i - \hat{n}_i M_i}{r^2 (1 - M_r)^2} + \frac{\hat{n}_i \hat{r}_i (r \dot{M}_i \hat{r}_i + C_0 M_r - C_0 M^2)}{C_0 r^2 (1 - M_r)^3} \right]_{\text{ret}} dS \quad \dots (6)$$

Here P'_T and P'_L denote the acoustic pressure due to thickness and loading noise respectively. The integration is carried over the elemental area of the surface panels and summed up for the entire MR/TR blade surface $f=0$. The subscript ,ret' indicates that the integrand is evaluated at the retarded time. ρ_0 and C_0 are density and speed of sound in the undisturbed medium. M is the local Mach number and r the distance between a point on the blade surface and the observer location. Subscripts n and r represent directions normal to and in the direction of the observer. P is the unsteady pressure calculated from the aerodynamic code. The dots on some quantities signify the time derivative with respect to source time. The roof sign (\cdot , \wedge) on n and r denotes the unit vectors in those directions.

For the computation, the blade surface is divided into a number of flat panels. This discretization may not be identical to that used for the aerodynamics calculations. Next the retarded time for a specific observer time and collocation point is calculated iteratively. The azimuth angle at the retarded time and the corresponding pressure at the collocation point is evaluated subse-

quently. The acoustic pressure is then given by the equations 5 and 6. The acoustic pressure at a time instant t is the sum of the contributions of all surface panels.

MR/TR-INTERACTION RESULTS

3. Aerodynamics

3.1 Two-blade M- and TR in Hover

As a first example, a generic two-blade MR and TR configuration in *hover* was studied. The TR is a quarter scale version of the MR which in turn is identical to the Caradonna and Tung rotor with a symmetric blade profile [20]. The TR turns at twice the MR rpm and has the same collective pitch as the MR. The TR axis lies in the plane of the MR disc. Parameters varied are the lateral distance between the M - and TR and the sense of rotation of the TR. The computations performed were for a MR azimuth step size of 5 degrees and both rotors were impulsively started at the same time with the TR rotating clockwise (,adv. side down', ASD-mode), Fig. 3

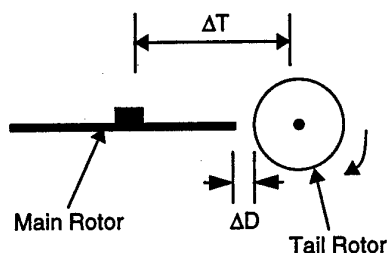


Fig. 3 Relative Positions of Main- and Tail Rotor

3.2 Wake Development

The progressive evolution of the M- and TR wakes is shown in Fig. 4, where the wakes after one, two and three revolutions of the MR are depicted. The lateral distance between the axis of the rotors is $1.33 R_M$, with R_M as the MR radius.

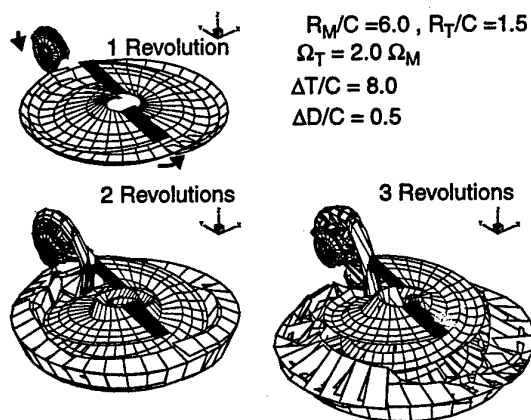


Fig. 4 Development of the Wake of Two-blade Main- and Tail Rotor in hover

The strong induction of the MR wake pulls and distorts the TR wake; after three MR revolutions the lower part of the TR wake is fully drawn into the MR wake. The induction effect of TR wake on the MR wake is weak. The MR blade cuts across the TR wake. The TR blades pass very close to the MR wake but do not cut it. The wake edges roll up as seen in the sequence of the wake plots.

3.3 MR/TR Section-Lift Time History

Variation of section lift at various radial stations (r/R) of the M- and TR blades over MR revolutions is shown in Figs. 5 and 6. Also plotted are the corresponding results for the isolated M- and TR.

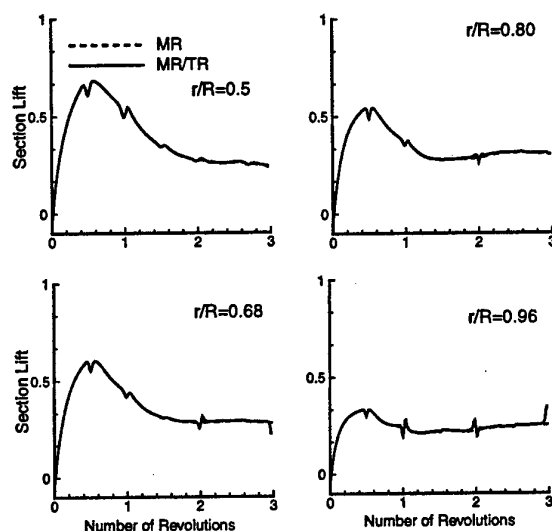


Fig. 5 Time History of Main Rotor Section Lift

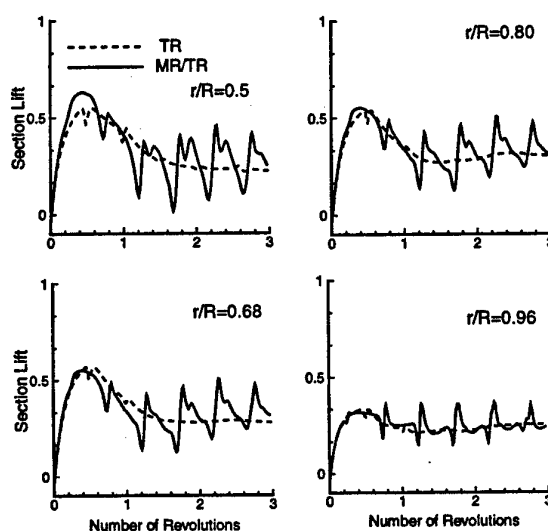


Fig. 6 Time History of Tail Rotor Section Lift

The section lift increases steeply at the start and settles down to an approximately constant value later. This is due to the 'starting vortex' generated by the impulsive start of the rotors. As the computation progresses, these vortices move downwards (or sideways for the TR) and the more realistic blade/wake interaction phenomena sets in.

Effect of TR wake on the MR section lift appears to be weak as seen from the one per rev. peaks in the plots of Fig. 5.

The amplitude of the peaks increases towards the blade tip. Obviously these impulsive variations in section lift are a source of vibrations and noise.

In contrast, the section lift history for the TR exhibits large amplitude impulsive variations in all radial sections, Fig.6.

Note the two per rev. peaks in the plots, which are a consequence of the TR turning at twice the main rotor rpm. The comparison with the results of the TR in isolation exhibit the strong interaction effects experienced by the TR which adversely influence the flight stability, vibrations and noise generation.

3.4 Effect of Lateral Distance Between MR and TR Axis

The lateral distance between the axis of the M- and TR ($=\Delta T$), was varied in the range of 8, 9 and 12 times the MR blade chord C , keeping other parameters of the configuration constant. Fig. 7 shows the effect of this variation on the M- and TR wakes after three MR revolutions.

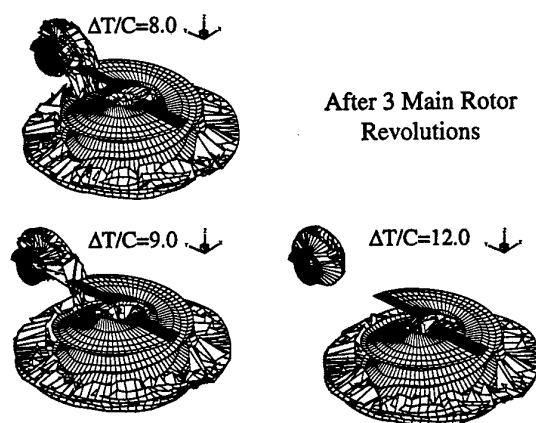


Fig. 7 Effect of ΔT on Wake Development

As evident, for the smaller values of $\Delta T/C$, the induction effects of MR wake on the TR wake are present, but disappear for the larger value of 12.

It is instructive to examine the section lift variation over the blade azimuth to locate the position of the blade/ wake interaction. In Figs. 8 and 9, a polar plot of the section lift variation over the azimuth angle for the T- and the MR are shown. Results are plotted for various r/R -stations for the last revolution.

The TR blade experiences strong Blade/Vortex Interaction (BVI) as it approaches the MR disc from below and not, as expected, when it is in the plane of the rotor disc, Fig.8.

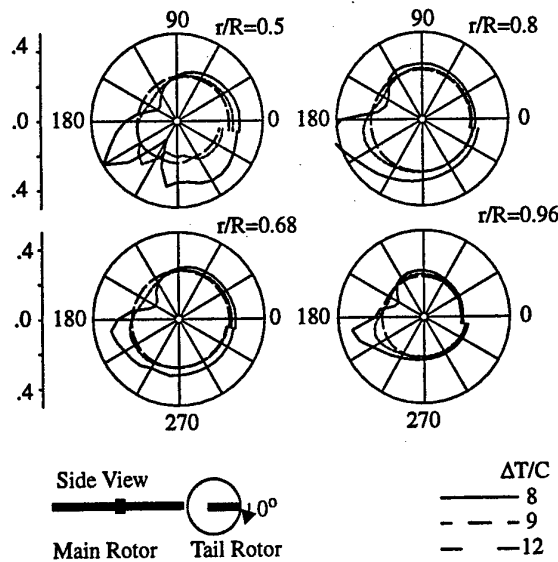


Fig. 8 Polar Directivity of Tail Rotor Section Lift

This result is of consequence for the directivity of the radiated noise. As seen, the lateral distance also influences the location of the BVI, initiating it earlier for larger values of $\Delta T/C$. However, the intensity of the interaction diminishes with increasing value of the lateral distance. Whereas the interaction effects are felt over the entire span of the TR blade, these effects are confined to the tip region of the MR, Fig.9.

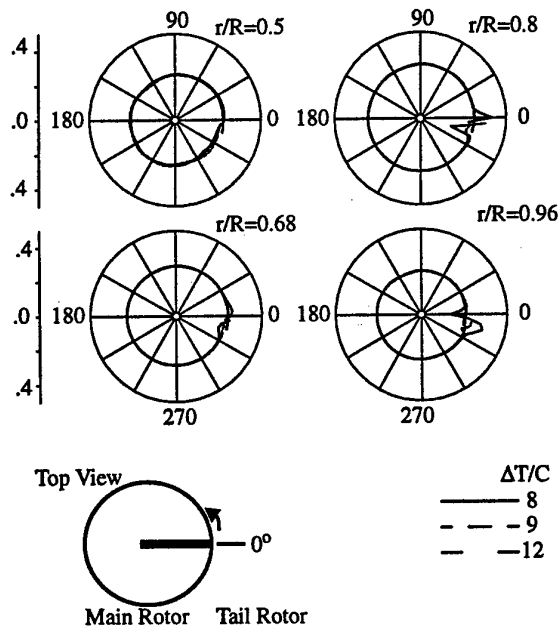


Fig. 9 Polar Directivity of Main Rotor Section Lift

Also here, the interaction starts somewhat earlier than the time the MR blade enters the plane of TR and, as mentioned earlier, the amplitude of the abrupt change in section lift is small. The effect of a variation in $\Delta T/C$ for the MR is similar to that observed earlier for the TR.

4. Aeroacoustics

4.1 Two-blade M- and TR in Hover

4.1.1 MR/TR Interaction Effects

To investigate the directivity of the generated noise, the overall sound pressure level (OASPL) in a horizontal plane 5m wide and 8m long ($=2.5 \times 4$ MR diameters) located 2.5m ($=1.25$ MR diameters) below the MR disc was evaluated, Figs.10, and 11.

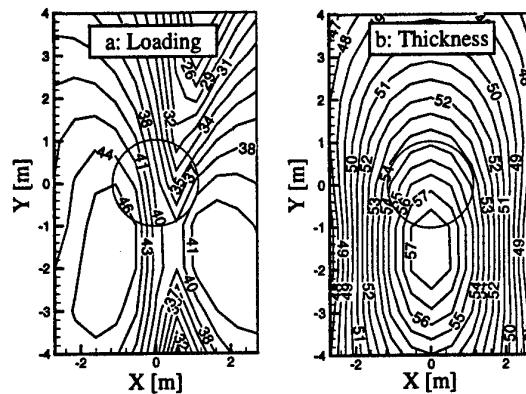


Fig. 10 OASPL Contours for the Isolated Tail Rotor.
a) Loading and b) Thickness Noise

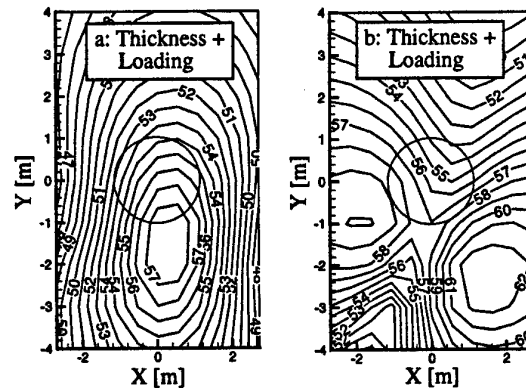


Fig. 11 OASPL Contours for the Total Noise.
a) Isolated TR and b) MR/TR

In Fig.10, the OASPL contours in the horizontal plane for the *isolated* TR are shown separately, with plot a) for the loading- and plot b) for the thickness noise contribution. The location of the MR disc is indicated by the circle.

The reason for choosing the OASPL noise metric was to correctly assess the low frequency content of the spectrum generated by the low TR/MR rpm ratio selected for the computations. The loading noise contours show two high noise regions ('hot spots') on either side of the plane of rotation. The hot spot on the outflow side of TR plane has a higher OASPL level than the inflow side, **Fig.10 a**. The thickness noise propagates symmetrically on either side of the (vertical) TR plane and shows a higher level hot spot than the loading noise, **Fig.10 b**.

The effect of MR/TR interaction on the noise is seen in **Fig.11**, where the the OASPL contours of TR total (thickness+loading) noise are plotted for a) the TR in isolation and b) under interaction with the MR.

The single hot spot visible for the TR in isolation in **Fig.11a** is replaced by two hot spots under the action of the MR, **Fig.11b**. Also the OASPL of both hot spots is higher than that for the isolated TR.

MR noise directivity is shown in **Fig.12a** for the isolated rotor and in **Fig.12b** for the rotor under MR/TR interaction. Also here, the strong distortion of the noise radiation pattern due to the interaction and increase in the sound pressure level are visible

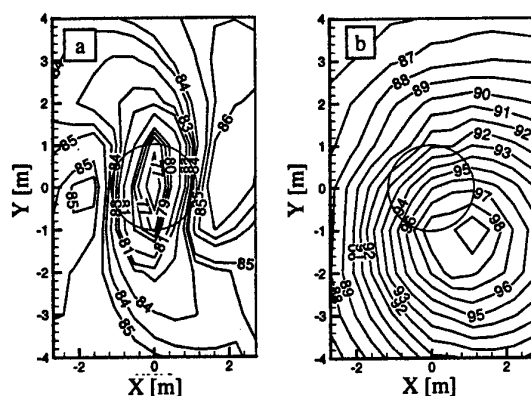


Fig. 12 OASPL Contours for the Main Rotor.
a) Isolated MR and b) MR/TR

4.1.2 Effect of TR Sense of Rotation

To examine the effect of TR sense of rotation, the aeroacoustics with the TR rotating in the advancing side down (ASD) and in the advancing side up (ASU) mode were computed keeping rest of the parameters unchanged.

A comparison of the section lift variation over azimuth for the TR turning in the ASD and ASU modes is presented in **Fig.13**. The two modes show a difference in the shape and phase of the section lift variation, but not a consistent change in the pressure peak amplitude.

OASPL contours for the TR in the the MR/TR combination for ASD and ASU turning modes are depicted in **Fig. 14**. Both turning modes show a hot spot on either side of the TR plane. The change from ASD to ASU mode effects a shift of the hot spot on the left from upstream to a downstream location and vice versa for the spot on the right, **Fig.14**

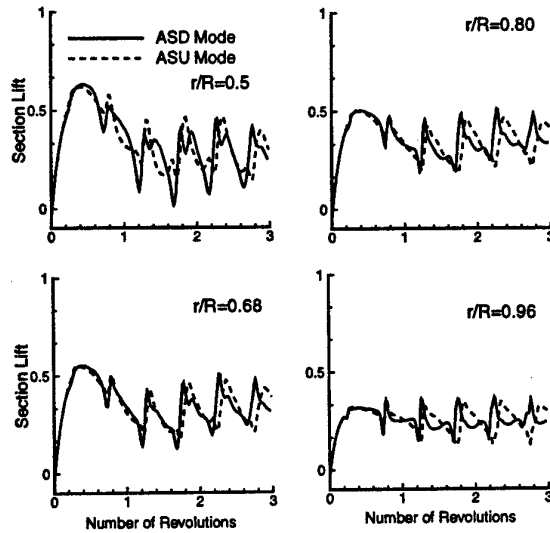


Fig. 13 Effect of TR Turning mode on TR Section Lift

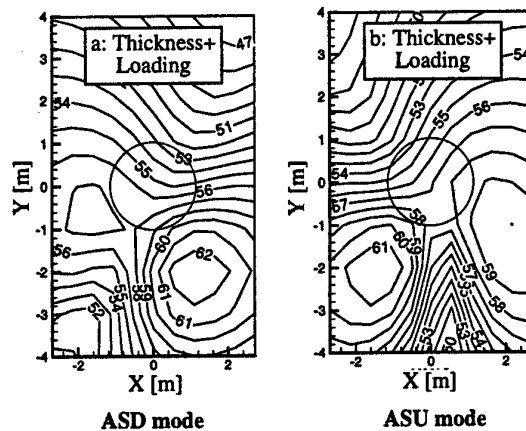


Fig. 14 Effect of TR Turning Mode on TR Total Noise. (OASPL Contours)

The effect of the turning mode on the MR noise radiation is seen in Fig.15. As expected from earlier discussion, the effect of TR on the MR is, for the configuration studied, small. Accordingly, for both turning modes, the results for the MR noise radiation differ only slightly.

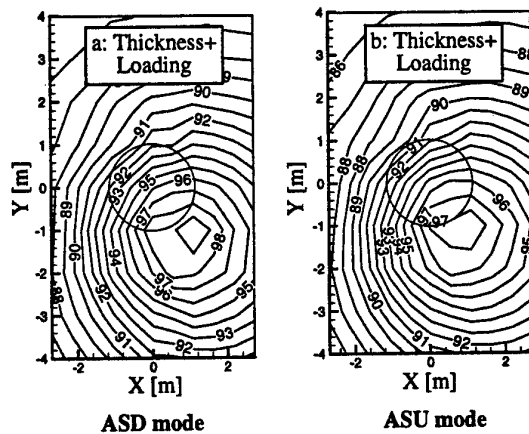


Fig. 15 Effect of TR Turning Mode on MR Total Noise. (OASPL Contours)

4.2 Four-Blade MR/ 2-Blade TR in 12° Climb

As a final example of the computational study, a four-blade MR and a two-blade TR configuration in a 12° climb flight condition was investigated. The TR is turning in the ASD mode. This configuration, which corresponds to the BO105 helicopter, has been extensively tested as a quarter scale model in the DNW tunnel [7]. Unfortunately the precise flapping movement data for the TR blades could not be acquired during these tests. In our calculations, only an approximate simulation of this flapping motion is performed. The predicted acoustics, due to this reason, cannot be compared with the wind tunnel results.

Fig.16 depicts the development of the MR/TR-wakes in the climb mode. The perspective chosen is such as to illustrate the interaction of the wakes clearly. The MR blades are seen to come clear of their wakes and no blade/wake interaction is visible. The lower part of the TR wake interacts and merges with the MR wake.

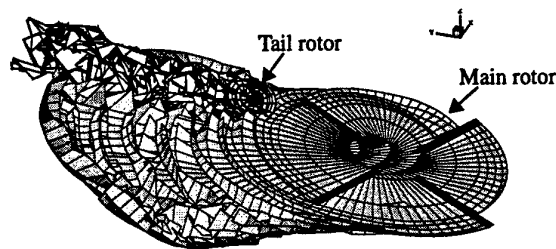


Fig. 16 Development of MR and TR Wakes During Climb

In Fig.17a,b,c the *PNLT* contours for the TR, the MR and the combined result for the M- and TR are presented. The results for the T- and MR are with both rotors in operation. It is seen that the TR noise contribution is relatively large and dominates the total noise radiation during the climb. This result is in qualitative agreement with the experimental results of Schultz et al [7].

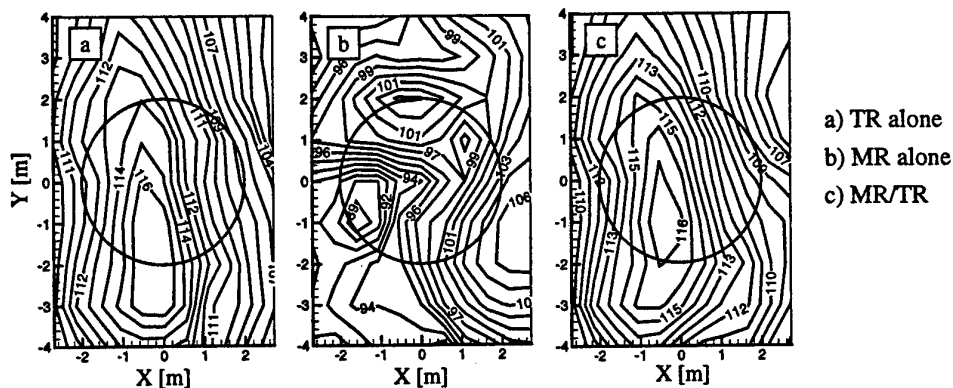


Fig. 17 PNLT Contours for the MR/TR Configuration

MAIN ROTOR/ FUSELAGE INTERACTION

5. The Wind Tunnel Model and Test Set-up

5.1 The Rotor/ Fuselage Model

The rotor/ fuselage used in the wind tunnel tests is a 1:6.5 scale powered model of the BO105 helicopter with a 4-blade rotor of 1.5 m diameter. The rotor tip speed is identical to the full scale version and blade mass distribution, torsional-, flap- and lag stiffness match well with the full scale blades. A detailed description of the model is available in [21].

5.2 Test Set-up in the Wind Tunnel

The tests were performed in the DLR 3.25 x 2.8m subsonic wind tunnel at Braunschweig. Rotor blade tip speed was maintained at 220 m/s and advance ratio changed by varying the tunnel wind speed. Rotor thrust was changed by collective blade pitch and trimming for zero moments obtained by adjustments of the cyclic pitch. Only the main rotor and fuselage were modeled. An approximate representation of the tail boom is effected by the model support sting.

A photograph of the test set-up in the wind tunnel is reproduced in Fig. 18 a, b.

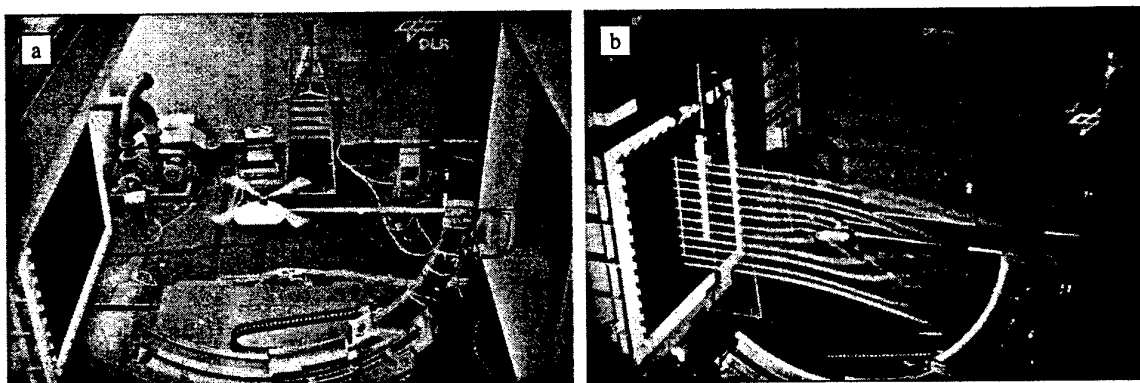


Fig. 18 a) Helicopter model test set-up in DLR 3.25 x 2.8 m subsonic wind tunnel,
b) Set-up with Smoke Rake

5.3 Test Spectrum

Detailed (time-averaged) surface pressure measurements on the fuselage surface were made during the tests, [21].

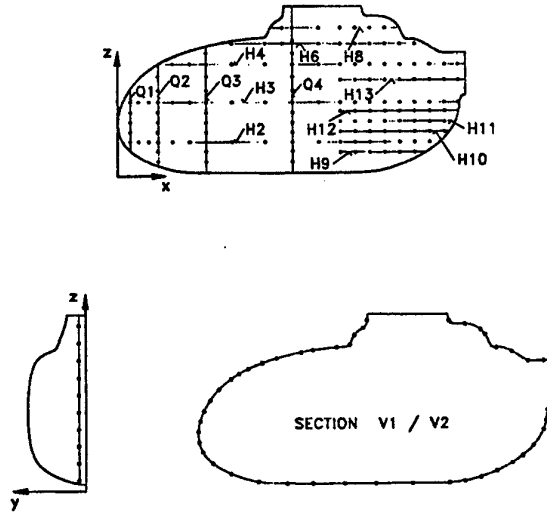


Fig. 19 Pressure Tap Locations on Fuselage Surface

Fig. 19 gives an overview of the pressure tap locations in the various horizontal and vertical sections of the fuselage. In all 450 pressure taps were placed at locations of interest. Unsteady pressure at a few locations was measured for a qualitative assessment of possible noise sensitive areas. Rotor thrust, advance ratio, and fuselage incidence were varied during the tests. Baseline configuration was the isolated fuselage without rotor blades.

5.4 Non-dimensional Test Parameters

The pressure distribution is non-dimensionalized with the rotor tip speed dynamic pressure and a multiplicative factor of 100:

$$C_p^* = 100 (p - p_\infty) / \left(\frac{\rho}{2} \Omega^2 R^2 \right) \quad \dots (7)$$

with ρ as air density, p , p_∞ the surface and free stream pressures, Ω the rotor rotational speed and R the rotor radius. The thrust coefficient C_T and advance ratio μ , which were the parameters varied during the tests are defined as:

$$C_T = T / (\rho \pi \Omega^2 R^4) \quad \dots (8)$$

and

$$\mu = V_\infty / (\Omega R) \quad \dots (9)$$

with T as the rotor thrust and V_∞ the tunnel free stream velocity.

5.5 Time-averaged Pressures on the Fuselage Surface

For the sake of clarity, the pressure data has been plotted over equidistant abscissa intervals;

these do not correspond to the actual abscissa coordinates of the pressure taps.

The effect of increasing the rotor thrust on the pressure along the fuselage plane of symmetry is shown in Fig. 20.

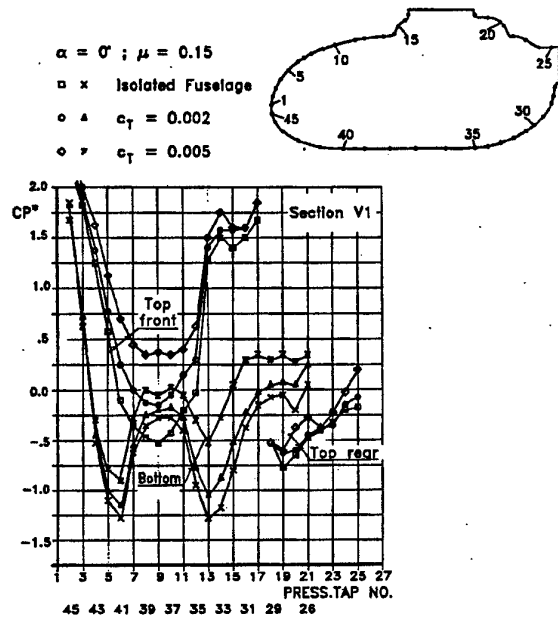


Fig. 20 Influence of Rotor Thrust on Fuselage Surface Pressure Distribution in Section V1

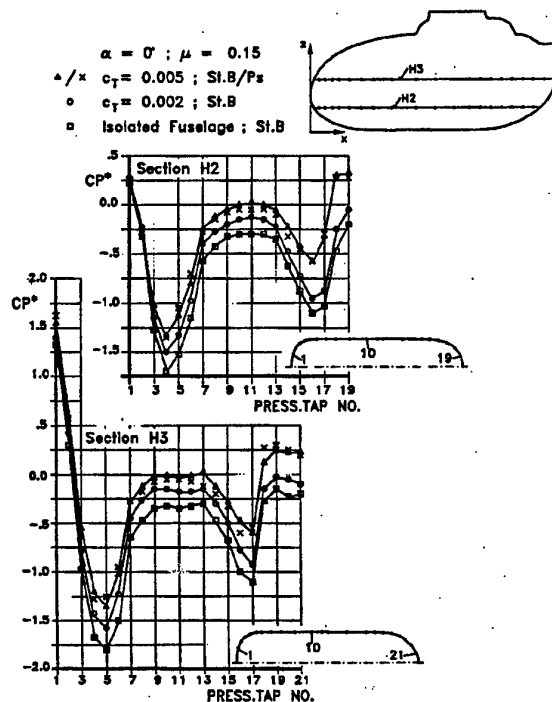


Fig. 21 Influence of Rotor Thrust on Fuselage Surface Pressure Distribution in Sections H2 and H3

The rotor downwash decelerates the oncoming flow and also impinges on the fuselage upper surface. Both of these events raise the static pressure above that which is present on the fuselage without the rotor. The pressure rise on the upper side is stronger than on the lower side, but the entire underside is affected by the skewed main rotor wake for the forward flight situation shown.

Also the pressure distribution on the fuselage sides is affected in a similar manner, as seen in Fig. 21.

A comparison of the pressures on the starboard and port side of the fuselage (St.B and Ps in Fig. 21) exhibits only slight asymmetry indicating insignificant side force or turning moments due to this rotor-induced asymmetry. However asymmetry of pressure is noticeable on the upper fuselage surface, in Section H6, as seen in Fig. 22. This pressure asymmetry is of interest for the location of power plant intake.

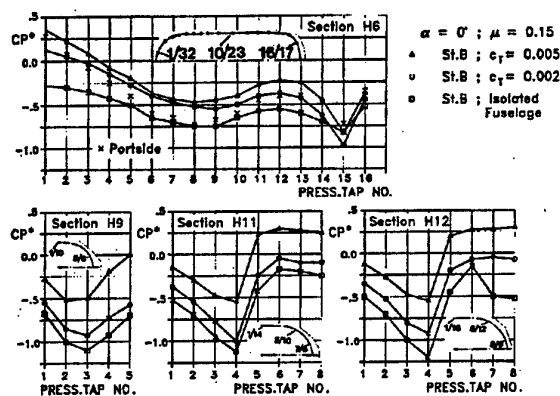


Fig. 22 Influence of Rotor Thrust on Fuselage Surface Pressure Distribution in Sections H6, H9, H11 and H12

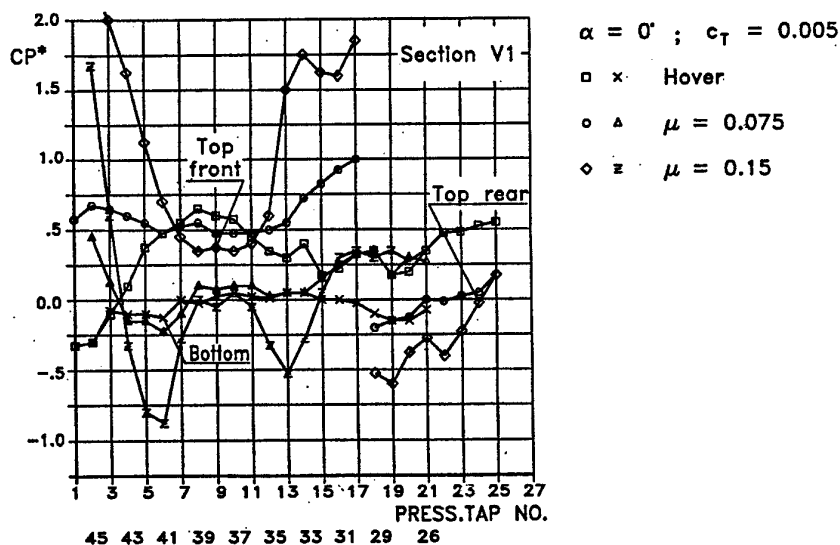


Fig. 23 Influence of Advance Ratio on Fuselage Surface Pressure Distribution in Section V1

The rear-end pressure distribution in sections H9, H11 and H12 show also a pressure recovery with increase in rotor thrust, over that for the isolated fuselage. This has a beneficial effect on the drag of the helicopter.

The influence of advance ratio is investigated in Fig. 23. With increasing advance ratio, the flow becomes more and more similar to that of the isolated fuselage, (see Fig. 18). It is evident from this result that for the high speed flight, the flow characteristics of the fuselage become important..

5.6 Unsteady Pressures on Fuselage

To assess the magnitude of unsteady pressures generated and their variation with rotor thrust and advance ratio, 14 Kulite sensors were installed flush with the fuselage surface at locations indicated in Fig. 24 (inset). The data acquisition frequency of these sensors was 6.3 kHz and with a rotor rpm of 2800, an azimuth resolution of about 2.67 degrees could be attained.

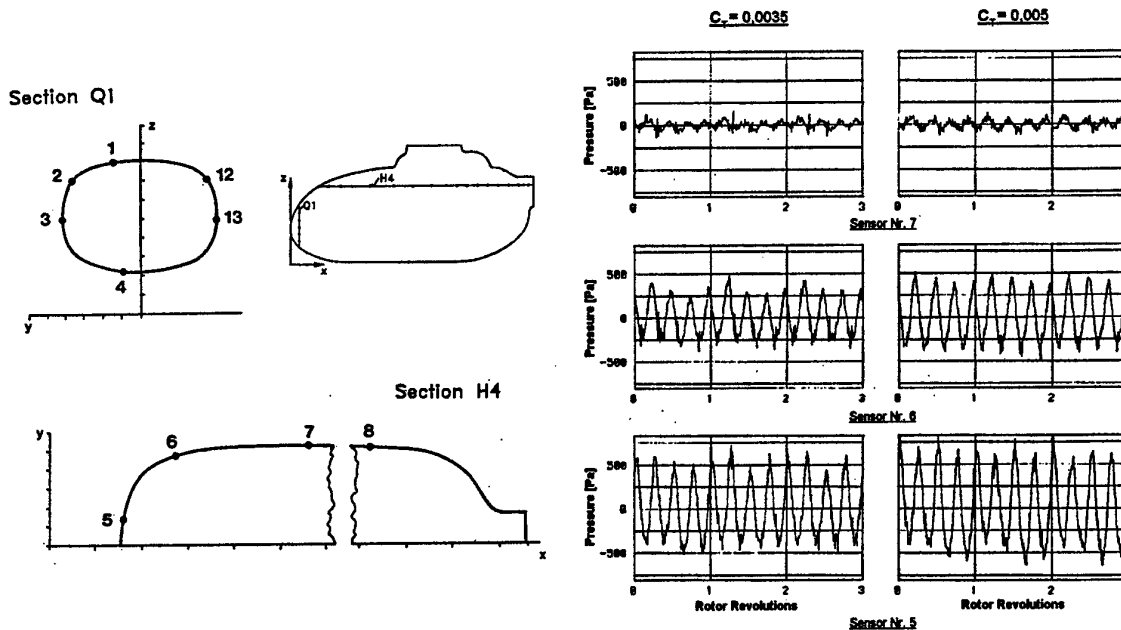


Fig. 24 Unsteady Pressures on Fuselage Surface. Influence of Rotor Thrust

Signatures of the unsteady pressure for the sensors 5, 6 and 7 are shown in Fig. 24 for two values of rotor thrust, $C_T = 0.0035$ and 0.005 plotted over the rotor revolutions. The traces for the sensors 5 and 6 show the passage of the four blades as four peaks per revolution. The blade tip vortices pass close to the location of these sensors and a strong pressure pulse is recorded. The signal at sensor 7 is weak and not so distinctive since the blade tip passes this sensor at a larger lateral distance.

The nose area of the fuselage is a high intensity fluctuating pressure region which radiates noise to the exterior as well as into the fuselage interior. As this area is also the location of the pilot and provides the forward vision, noise and vibration absorption measures are difficult to implement here. The increase in thrust increases the amplitude of the pressure pulse indicating increased interior and exterior noise contribution from the fuselage during e.g. take-off.

A change in forward speed from the hover flight condition generates the unsteady pressure traces recorded for the sensors 4, 5 and 6 in Fig. 25. Sensor 4, located at the bottom of the fuselage experiences pressure fluctuations which decay in amplitude as the advance ratio increases. The pressure fluctuations are not related to the blade passage but rather the result of flow separations at the fuselage bottom. This region of separated flow during hover disappears progressively with increase in advance ratio and the sensor records only weak pressure fluctuations.

As discussed above both the sensors 5 and 6 record clearly the passage of the four blades; the pressure amplitude at first decreases from that of the hover condition to rise again with a further increase in the advance ratio. This is plausible since with increasing advance ratio, the trajectory of the tip vortices comes closer to the location of the sensors 5 and 6.

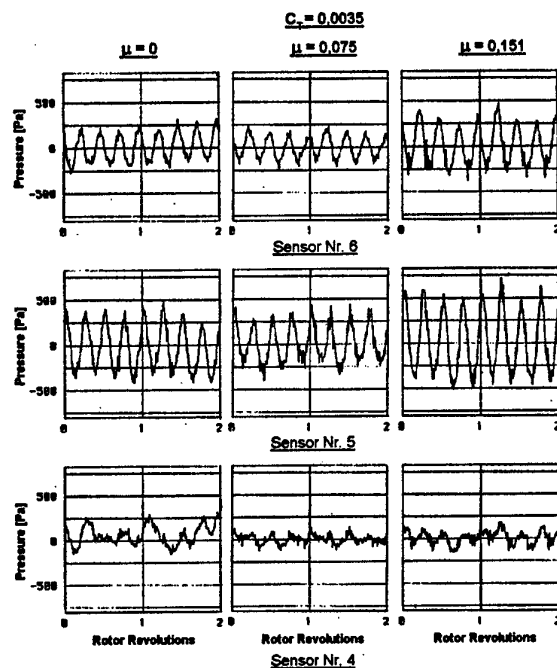


Fig. 25 Unsteady Pressures on Fuselage Surface. Influence of Advance Ratio

5.7 Visualisation of the Global Flow Field

Visualisation of the flow around the rotor/fuselage model was done by introducing smoke filaments in the plane of symmetry. A smoke rake was fixed vertically on the nozzle exit as seen in Fig. 18 b.

The photographs of Fig. 26 demonstrate the effect of rotor thrust on the global flow characteristics in the plane of symmetry. At zero thrust (Fig. 26 a), the flow remains fairly parallel to the fuselage axis. The flow going over the rotor disc at the upstream edge appears to be due to the negative twist at the blade tip.

Tail boom and empennage area is immersed in the low energy fuselage wake flow. With increasing thrust (Figs. 26 b,c), the flow pattern in the front and fuselage rear changes drastically. Fig. 26 b represents qualitatively the climb and Fig 26 c transition from hover to climb flight. The adverse flow conditions around the tail rotor and empennage, generated by the rotor/fuselage in-

teraction are demonstrated by these results.

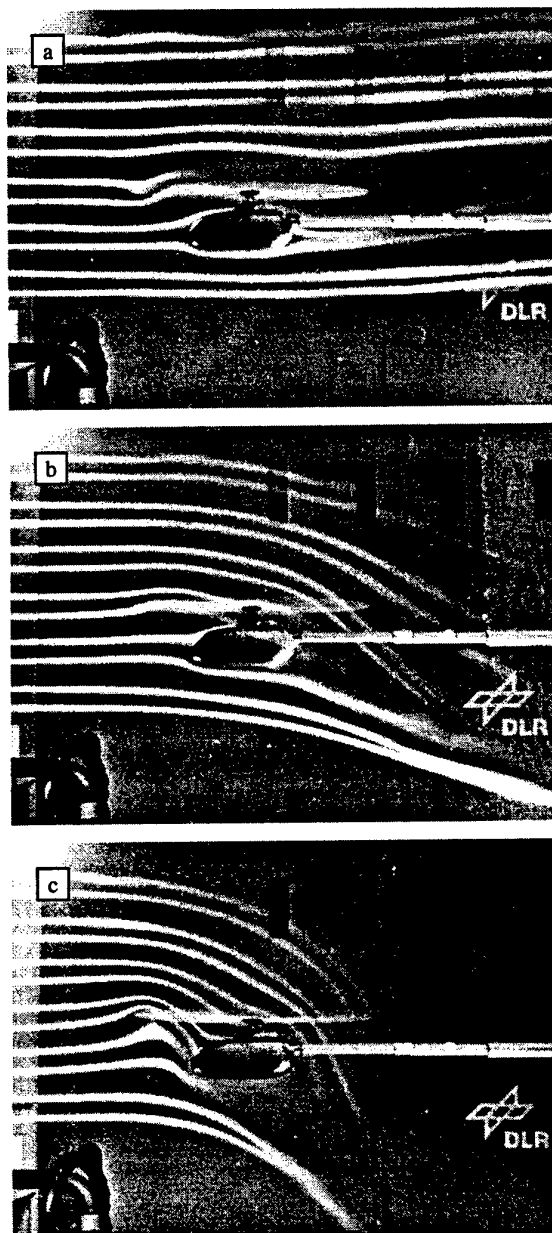


Fig. 26 Influence of Rotor Thrust on Global Flow. Smoke Filaments lie in Fuselage Plane of Symmetrie
a) $c_T = 0.000$, b) $c_T = 0.002$, c) $c_T = 0.005$
a, b, c) $\mu = 0.05$

The effect of advance ratio, shown in the picture series of Fig. 27, is just the opposite to that seen in Fig. 26. With rotor thrust held constant, increasing the advance ratio makes the flow progressively similar to that of the isolated fuselage and the rotor wake wholly engulfs the tail boom, the tail rotor and the empennage location. A consequence of this is that during high speed flight,

the characteristics of the isolated fuselage flow become more important for the performance of the helicopter and the tail rotor and the empennage flow is strongly perturbed by the unsteady main rotor wake.

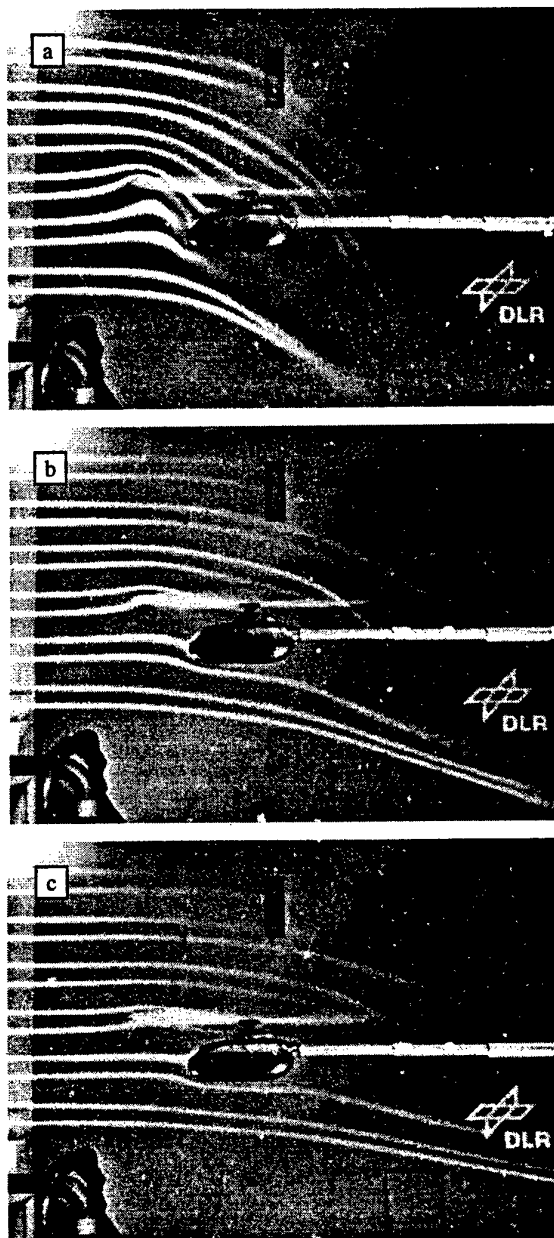


Fig. 27 Influence of Advance Ratio on Global Flow. Smoke Filaments lie in Fuselage Plane of Symmetrie
a) $\mu = 0.025$, b) $\mu = 0.075$, c) $\mu = 0.100$
a, b, c) $c_T = 0.005$

SUMMARY AND CONCLUSIONS

6. Main Rotor / Tail Rotor Interaction

Aerodynamics and aeroacoustics of helicopter MR/TR interaction was studied with a numerical model. A two-blade MR/TR-configuration in *hover* and a four-blade MR/ two-blade TR-configuration in *climb* flight condition were investigated.

The main conclusions drawn are:

HOVER Flight

1. The TR wake is strongly deformed and drawn into the MR wake. MR wake approaches the TR but remains almost unaffected by the interaction.
2. The MR effects a strong change in the directivity pattern and level of the generated noise, over the conditions for the TR in isolation.
3. The sense of TR rotation influences the TR noise radiation pattern and intensity. The ASU rotation mode exhibits larger regions of high noise than the ASD mode for the configuration studied
4. A generalisation of the above result obtained for the MR/TR noise level and sense of tail rotor rotation was not possible and appears to be configuration specific
5. With increasing lateral distance between the MR/TR axis, the adverse interaction effects diminish.

CLIMB Flight

6. As in hover, the TR wake is strongly distorted by the MR interaction whereas the MR wake remains almost unperturbed by the TR interaction.
7. The TR contribution to the total noise dominates during the climb which is consistent with the wind tunnel findings.

7. Main Rotor / Fuselage Interaction

The basis of main rotor/ fuselage interaction was the *time averaged* pressure distribution over the fuselage surface obtained in wind tunnel tests with a Mach-scaled model of the BO105 helicopter and flow visualisation with smoke filaments.

Some of the conclusions arrived at are:

8. The pressure over the entire fuselage surface is affected by the rotor downwash, variation of rotor thrust and the advance ratio
9. The low pressure areas at the bottom and rear of the fuselage experience a pressure recovery with increasing rotor thrust and advance ratio
10. Only the fuselage upper surface pressure exhibits an asymmetry which may influence the power plant intake location
11. The upper region of fuselage front is exposed to rotor induced fluctuating pressures. The amplitude of these pressures increases with rotor thrust and advance ratio
12. At high speeds, the tail rotor and empennage area is completely engulfed by the unsteady rotor and fuselage wakes. Fuselage aerodynamics become prominent feature of the global flow during high speed flight

REFERENCES

- [1] Leverton, J.W., Pollard, J.S. and Willis, C.R., "Main Rotor-Wake/ Tail Rotor Interaction", *Vertica*, Vol.1, pp. 213-224, 1977.
- [2] Leverton, J.W., "Reduction of Helicopter Noise by Use of a Quiet Tail Rotor", Paper No. 24, European Rotorcraft Forum, Sept. 1980.
- [3] Balcerak, J.C., "Parametric Study of the Noise Produced by the Interaction of Main Rotor Wake with the Tail Rotor", NASA-CR-145001, 1976.
- [4] Pegg, R.J. and Schidler, P.A., "Exploratory Wind Tunnel Investigations of the Effect of Main Rotor Wake on Tail Rotor", *Helicopter Acoustics*, NASA CP-2052, May 1987.
- [5] Edwards, B.D., Peryea, M.A. and Brieger, J.T. "1/5th Scale Model Studies of Main Rotor and Tail Rotor Interactions", *Proceedings of the AHS National Specialist's Meeting on Aerodynamics and Aeroacoustics*, Feb. 1987.
- [6] Ahmadi, A.R., "An Experimental Investigation of Blade Vortex Interaction at Normal Incidence", NASA-CR-177338, Sept. 1984.
- [7] Schultz, K.-J., Splettstoesser, W.R., "Helicopter Main Rotor/ Tail Rotor Noise Radiation Characteristics from Scaled Model Rotor Experiments in the DNW", 49th AHS Annual Forum, St. Louis, Missouri, May 19-21, 1993.
- [8] Fitzgerald, J. and Kohlepp, F., "Research Investigation of Helicopter Main Rotor/Tail Rotor Interaction Noise", NASA CR 4143, May 1988.
- [9] Martin, R.M., Burley, C.L., "Acoustic Test of a Model Rotor and Tail Rotor, Results for the Isolated Rotors and Combined Configuration", NASA TM 101550, Feb. 1989.
- [10] George, A.R. and Chou, S.T., "A Comparative Study of Tail Rotor Noise Mechanisms", 41st AHS Annual Forum, Fort Worth, Texas, May 1985.
- [11] Tadghighi, H., "An Analytical Model for Prediction of Main Rotor/ Tail Rotor Interaction Noise", AIAA Paper 89-1130, April 1989.
- [12] Quackenbush, T. R., Bliss, D.B. and Mahajan, A., "High Resolution Flow Field Prediction for Tail Rotor Aeroacoustics", 45th AHS Annual Forum, Boston, MA, May 1989.
- [13] Baron, M. and Boffadossi, M., "Unsteady Free Wake Analysis of Closely Interfering Helicopter Rotors", Paper No. 108, 19th European Rotorcraft Forum, Cernobbio, Italy, Sept. 14-16, 1993.
- [14] Bagai, A. and Leishman, G.J., "Free-Wake Analysis of Tandem, Tilt-Rotor and Coaxial Rotor Configurations", 51st AHS Annual Forum, Fort Worth, Texas, May 9-11, 1995.
- [15] Ahmed, S.R. and Vidjaja, V.T., "Unsteady Panel Method Calculation of Pressure Distribution on BO105 Model Rotor Blades", *Journal of the American Helicopter Society*, pp. 47-56, Jan. 1998.
- [16] Ahmed, S.R. and Vidjaja, V.T., "Unsteady Panel Method Calculation of Pressure Distribution on BO105 Model Rotor Blades and Validation with DNW Test Data", 50th AHS Annual Forum, Washington, DC, May 11-13, 1994.
- [17] Yin, J.P. and Ahmed, S.R., "Prediction- and its Validation- of the Acoustics of Multiblade Rotors in Forward Flight Utilising Pressure Data from a 3-D Free Wake Unsteady Panel Method", 20th European Rotorcraft Forum, Amsterdam, The Netherlands, Oct. 4-7, 1994.
- [18] Farassat, F. and Succi, G.P., "The Prediction of Helicopter Rotor Discrete Frequency

Noise", Vertica, Vol.7, No.4, 1983.

[19] Brenntner, K.S., "Prediction of Helicopter Discrete Frequency Noise", NASA TM 87721, Oct. 1986.

[20] Caradonna, F.X. and Tung, C., "Experimental and Analytical Studies of a Model Helicopter Rotor in Hover", NASA TM 81232, 1981.

[21] Ahmed, S.R. and Meyer, F.W., "A Mach-Scaled Powered Model for Rotor-Fuselage Interactional Aerodynamics and Flight Mechanics Investigations", Proceedings of the International Technical Specialist's Meeting on Rotorcraft Basic Research, Georgia Institute of Technology, Atlanta, USA, March 1991

THE BVI PREDICTION PROBLEM AND THE ROLE OF CFD

Francis X. Caradonna

Research Scientist

US Army Aeroflightdynamics Directorate, AVRDEC, AMCOM

Army/NASA Rotorcraft Division

Ames Research Center

Moffett Field, CA

Abstract

Recent BVI tests are discussed together with directly related computational studies. These show that good prediction of BVI-induced loads and acoustics is obtained only when the wake location and strength are well known. The ability to predict the wake is, then, the most basic problem in BVI aeroacoustics. This problem is considered from a CFD viewpoint. A simple scale argument shows that the global wake prediction problem requires exceedingly large grids. A review of various computational studies seems to support these grid size estimates and indicates that the global wake problem is a long-term challenge. It is suggested that new approaches to CFD should be considered, specifically, methods in which vortex cores are not resolved, but nevertheless preserved. The methods of vortex embedding and vorticity confinement are shown to be in this category. Until such methods are developed, the working aeroacoustic roles of CFD will be as local blade-flow solvers coupled to comprehensive codes.

1. Introduction

Public acceptance of helicopter operations is dependent on the acoustic properties of these aircraft – especially for those many low-speed operations that the helicopter is uniquely able to perform near population centers. At these low speeds the rotor flow environment is best characterized by its multitude of nearby shed vortices. Rotor interactions with vortices are most common in these flight conditions (especially in descent or maneuver) and the Blade/Vortex Interaction (BVI) is the predominant noise source. The ability to reliably predict BVI is one of the essential computational needs for the development of ever-quieter rotorcraft that must meet a wide range of operational demands. And while practical predictive tools are becoming available, there still remain important accuracy issues of a fundamental nature and, as we shall see, the biggest of these involves the prediction of the wake.

Wakes have been the subject of computational studies since the first rotor vortex-lattice studies in the 1960's and these methods have always relied on a variety of physical/numerical models. These models have included assumptions on the location of wake (specified wake geometries and/or shedding initiation points), on the larger-scale wake structure (for example, single or multiple vortex roll-up models) and on small-scale structure (core size and velocity distribution). A primary purpose of these models has been to enable fast computations within the context of what is known (quantitatively and/or qualitatively) about the structure of wakes. These models have been used in conjunction with vortex-lattice methods and an important goal has always been to increase analysis speed (mainly by limiting the number of wake filaments). These analyses then enable efficient comprehensive rotor codes. These comprehensive analyses have been used as bases for performing BVI computations by coupling local blade solvers and using them to provide required input for acoustic solvers. CFD methods have proven to be efficient as local interaction solvers and their coupling process is described in ref. 1. It is only because of the above developments that there are now practical rotor/wake BVI analyses available to the

engineering community. However, we shall see that there is typically a considerable scatter in the results obtained by the various analyses of this type. Such scattering of results is probably caused by both the specific vortex-matrix implementations and the behavior (generality, applicability, and accuracy) of the various, required physical wake assumptions. Such analyses must therefore be performed with skill and art. In addition, such methods will always require much testing.

The hope of new wake method development efforts is that a "first-principles" approach will obviate the current need for much of the above modeling and, therefore, for the expense and burden of testing. It is for this reason that CFD methods are also being studied not only as local blade flow solvers but also as an alternate way to predict the global wake. These efforts are still far from attaining their goal and BVI work will remain both a computational and experimental effort.

This paper aims at reviewing some selected research efforts, mainly conducted at or with the Army/NASA organizations at Ames Research Center, in order to illuminate major findings and challenges in the area of BVI acoustics prediction. The discussion will first briefly assess the current state of our current BVI acoustics predictive ability in the light of two well-instrumented rotor tests that have resulted in extensive computational studies. In these studies CFD will have been used only as a local blade solver. These computational/experimental comparisons will illustrate the great importance of improving our global wake prediction capabilities. The ensuing discussion will center on the global wake prediction problem, beginning with a rough estimate of the CFD problem magnitude and then reviewing several important wake studies. The difficulty of the problem will then lead to considering new alternate classes of solution methods in which any attempt to resolve the vortex core region is abandoned.

2. Rotor BVI Testing and Related Computational Studies

An understanding of the overall BVI problem is gained from a consideration of two philosophically different rotor experiments: one which treats the BVI in isolation and the other, which studies a complete rotor system in a realistic flight state and undergoing many BVIs. For both of these studies a range of local computational blade flow models are used to provide input to an acoustic propagation code. The two tests and their analyses differ primarily in the degree to which the interacting vortices are known.

2.1 An Isolated BVI Experiment

There are many types of rotor-vortex interactions, but the strongest is that in which an interacting blade and vortex are parallel to each other. In order to study this interaction under closely controlled conditions, a test was performed in the 80x120 foot wind-tunnel at the Ames Research Center (ref.2). In this test a stiff, non-lifting rotor was allowed to interact with a vortex generated by an upstream wing. This arrangement permitted good knowledge of the relative rotor and vortex positions and produced a simple interaction that was conducive to computation by a wide range of methods. Blade pressure instrumentation and traversing microphones acquired surface load and far-field noise data. Figures 1 and 2 show a sketch and photograph of the test. An unusual feature of the pressure data is that it clearly showed wave behavior on the blade surface. This is seen in figure 3, which shows pressure time histories for a chordwise array of pressure transducers. When the vortex impacts the leading edge (actually the vortex misses the rotor by .25 chords in this case), a wave clearly emanates (from the leading edge), travels downstream and is reflected back upstream from the trailing edge. Clearly the leading edge region is the main acoustic source. It is inferred therefore that a comparison of predicted and measured leading edge pressures should provide a good indicator of the effectiveness of a blade

load prediction for acoustic radiation purposes. Of course, the best indicators are comparisons with the far-field microphone data. With the loads and acoustic data it was possible to evaluate a wide range of aeroacoustic (that is, combined local aerodynamics and propagation methods) prediction methods. A fairly complete array of aerodynamic methods were represented in the ensuing computational study (ref.3). Aerodynamic methods included analytic (indicial), potential and Euler CFD (Computational Fluid Dynamics), and singularity or integral methods (compressible and compressibility-corrected incompressible). The vortex structure required for these computations was inferred from previous experiment and was usually assumed to be axisymmetric. With only one exception, all of these methods assumed the vortex structure to be fixed throughout the interaction. (This was done both for simplicity and because of the far greater cost, especially with CFD, of fully-interacting computations.) Although the fixed-vortex-structure assumption seems fairly drastic, uniformly good results were obtained. Figure 4 shows a comparison of filtered pressure time histories from the leading edge region and shows that all methods do well. These blade aerodynamic computations were then used as input to various noise propagation codes, most of which were implementations of the Ffowcs-Williams Hawkins (FWH) equations. Figure 5 shows a comparison of several of these methods with the acoustic data and again very good comparisons were obtained. This study did leave questions open – for instance, it is not clear that the vortex size was really representative of that on an operational rotor (actually, there does not appear to be very extensive measurements of this sort for an operational rotor). Also, the apparent success of the undisturbed-vortex model is puzzling. Nevertheless, the present results were all very good and indicate the availability of operationally effective BVI models. However, there is one critical feature of this test that is rarely available in other rotor BVI tests, that is, the fact that the vortex position with respect to the rotor is directly controlled and well known.

2.2 BVI Test of a Complete Rotor System

The above mentioned test was aimed at isolating the BVI. While this sort of test provides a basic understanding, it is also necessary to conduct tests which integrate such understanding into a working whole. Such a test was conducted at the DNW (Duits-Nederlandse Wind Tunnel) by a consortium of DLR (Deutsche Forschungsanstalt für Luft-und Raumfahrt), DNW, ONERA (Office National d'Etudes et de Recherches Aérospatiales), AFDD (Army Aeroflightdynamics Directorate), and NASA-Langley (ref. 4). The rotor tested was a dynamically and Mach scaled BO-105 rotor. This test, shown in figure 6, achieved realistic simulations of operational flight conditions and was instrumented to obtain detailed blade loading and acoustic surveys. Since this test required knowledge of the relative blade-vortex distances, measurements of blade motion/deformation and vortex visualization/measurement were performed. An important objective of this test was to employ higher-harmonic pitch control (HHC) to minimize BVI noise and vibratory loading. (Minimum vibration and BVI noise were found to require quite different HHC settings.) It is of great interest that, for the particular baseline condition studied, it was possible to reduce BVI noise by about 6 db by use of HHC. (Such improvements demonstrate the feasibility of reducing BVI noise and, hence, the importance of understanding and predicting it.) Blade trajectory/deformation measurements indicated that the effect of HHC for the low-noise case was to increase the blade-vortex separation distance and that changes both in vortex and blade trajectory were largely accountable for this improvement. All test participants performed computations of airloads (ref. 5) and BVI acoustics (ref. 6) for flight conditions that included a baseline descent case, a minimum BVI noise case (achieved with HHC) and a minimum vibratory load case (also using HHC). These computations were performed both prior to actual testing (to provide instrumentation location guidance) and after testing (in order to capitalize on

modeling improvements found to be needed from the test data). Figures 7 and 8 show a range of predicted blade loadings performed both before and after the test. All of these computations employ a simple local blade aerodynamic model, some type of vortex lattice method (for predicting the wake and inflow), a structural model, and trim iteration. It is apparent that there is a wide range of results, both for pre-test and post-test computations (which have included modifications both to the structural and aerodynamic models). A similar range of results is also predicted for the BVI acoustics (figure 9 shows retreating- and advancing-side microphone data, while figs. 10 through 13 show pre-test and post-test results for the various methods – all use a FWH approach). The main result of these comparisons is probably the wide scattering of results, rather than which of these is the best comparison, because the methods are fairly similar and the reasons for the differences are not known.

2.3 Test Conclusions

We thus have results from two types of tests, both obtaining extensive loading and acoustic data and accompanied by a large number of different independent computations. The isolated BVI test with stiff rotor and controlled vortex location has produced a wide variety of very good comparisons between data and computation. The full operational rotor test, with a complex wake structure and an elastic rotor, has produced no such agreement between computations. Of these latter computations, modification to the blade structural model, or even specification of blade motion from data, has not resulted in greatly improved comparison with measured acoustics.

One can conclude from the former test that the ability to predict blade loads and resulting acoustics does exist when the wake location is known. From the latter test it appears that we do not yet have the ability to predict the rotor wake. Wake prediction, then, is the central unsolved problem in BVI computations and the remainder of this review is concerned with this problem.

3.0 Prediction of Global Rotor Wakes

3.1 The Magnitude of the Wake Prediction Problem

A first indicator of the magnitude of the rotor wake prediction problem is obtained by considering the size of the smallest significant characteristic wake region (the vortex core) and then estimating the number of grid points required to resolve this region throughout the flow. Estimates or measurements of core structure typically show the tip-vortex core diameter (the distance between velocity peaks) to vary between 0.1 – 0.3 blade chords. For a typical rotor, an average core size then is of the order of .01 rotor diameter, D . Assuming ten points across a vortex core gives a resolution distance of .001 D , which in a cubical region of size, D , requires 10^9 grid points. This is a rough estimate obtained using several simplifying assumptions, including:

1. The smallest characteristic scale is the core size. There are smaller scales in the overall problem. These include inner turbulent scales both in the vortex core and on the blade surface. The latter are very important because they exist in adverse pressure-gradient regions and determine stall behavior. This is beyond the scope of the present work, however. Concerning the turbulent vortex core, this region does not usually operate in a strong adverse pressure gradient region; it is mainly convected and diffused. If inner scales have a global effect, it is probably through turbulent diffusion of the cores. At present, we have no knowledge of such global influence. (In other words, the best we dare hope for, with any

method, is a solution that is correct to the order of the outer core scale. We assume and hope that this is sufficient.)

2. The number of grid points required for adequate resolution. Wake and Choi performed a very careful study of required resolution (ref. 7). This work entailed two-dimensional studies of vortex convection using a 5th order solver. These computations showed the need for 14 points across a vortex in order to prevent its dissipation. Of course, this number would decrease with an even higher order method. It is also assumed that equal resolution is required in all directions. This is not true when a grid is aligned to a vortex, but such alignment is difficult to achieve in general.
3. The size of the resolution region. The size of the region that must be resolved is a function of advance ratio; it becomes deeper and larger as advance ratio decreases. The depth of a fine-resolution region might ultimately be as small (or smaller) than 0.25D, but this is speculative. Moreover, the overall grid region must be much larger than the rotor diameter.
4. No tracking of high-gradient regions and subsequent concentration of grids. Such grid concentration entails the use of unstructured grids or special overset grid structures and could greatly decrease the size of the required grid. There is much development activity in this area (refs. 8, 9). Technical obstacles to be overcome include grid stretching limitations imposed by accuracy, order limitations of current unstructured solvers and interface conditions, and the fact that the wake structure is so large and convoluted that it must occupy a large fraction of the solution region. In addition, the adaptive approaches (for the wake) tend to require use of parallel machines and efficient load-balancing algorithms have yet to be developed for these problems. The present assumption is a worst-case scenario, but is reasonable until the technology improves.

The important point of the above grid number estimate is that, even if it were incorrect by an order of magnitude, the problem is far bigger than can be solved by currently existing computational models. We can only hope that the 10^9 figure is an upper limit. However, since no rigorous numerical solution yet exists (one that demonstrates validated results that are independent of the grid), we cannot really know the precise magnitude of the problem.

A problem of this size can only be treated by large-scale direct numerical simulation or by some type of modeling.

3.2 Direct Numerical Simulations

One of the best direct numerical models of BVI was also the first. This was the study of Rai (ref. 10), which, though two-dimensional, points out the major difficulties of the problem. Although this study was aimed only at computing an isolated BVI, this was a fully interacting computation that required the convection of a vortex for some distance before its interaction with an airfoil. This work, which produced good comparisons with BVI data, employed a 5th order thin-layer, Navier-Stokes solver and a very large grid. The grid, shown in figure 14 was designed to concentrate points along the known, undisturbed path of the vortex on its way toward the airfoil. Figure 15 shows the resulting computed convection and interaction of a vortex with a high-speed airfoil. For this problem the vortex was injected into the flow well upstream of the airfoil to avoid starting transients. The vortex then convected to its meeting with the airfoil. With inadequate resolution, the vortex would have dissipated before the BVI occurred. The two-dimensional problem is convenient because the vortex path is known (grid points can easily be concentrated on this path) and relatively short (6-10 chords, by contrast, hundreds of chords are required in three dimensions). Nevertheless these 2-D grids required about 65,000 points. If this grid were extended into the third dimension using a wake-resolving grid size, and for a multi-

bladed rotor, the overall grid size could easily exceed 10^8 . This grid-size problem is the reason that no attempt at computing Eulerian convection was made in the BVI computations of ref. 3.

Three-dimensional rotor/wake computations have also been performed for many years. These have mainly been aimed at predicting rotor performance. The need for capturing the wake is equally important for both BVI and low-speed (especially hover) performance and the following discussion assumes that they are equivalent problems.

The computational work of Wake and Baeder(ref. 11) studied the hover performance of the 4-bladed UH-60 rotor using a single-block C-grid and periodic fore-and-aft boundary conditions. This was a 3rd order thin-layer, Navier-Stokes approach that used about 10^6 grid points. It was found that the wake trajectory was quite incorrect, to the point of actually colliding with the first subsequent passing blade (It is known that this does not occur for this particular rotor, ref. 12). Surprisingly, fairly good performance values were predicted, which in view of the well-known sensitivity to wake trajectory, suggest the presence of competing errors of unknown origin. Such results indicate that the effects of wake dissipation can be subtle – sometimes giving good numbers for the wrong (or even unexplained) reasons. Much more recently, Ahmad and Strawn (ref. 13) also attacked this same problem. In this case a 4th order method was used with a larger and simpler grid. An overset approach was used whereby a blade-conforming grid was embedded in an outer stretched Cartesian grid. This computation also employed periodic boundary conditions, that is, only one blade was computed. The grid size was about 8×10^6 points. It was found that the same type of trajectory errors occurred as in ref. 11.

This Ahmad & Strawn paper also included a very interesting study of a much simpler two-bladed rotor (ref. 14). The advantage of computing this particular rotor is in its geometry (low blade aspect-ratio, no twist, 2 blades), which results in a relatively large blade-vortex distance and less sensitivity to wake capturing – it is the simplest known rotor for which surface pressure data is available. The advantage of the low aspect ratio (large chord) is that the vortex core is larger and fewer grid points are required for resolution. Successively finer grids were used with the largest containing about 17×10^6 points. The finest grid (fig. 16) resulted in a solution wherein the identity of the tip vortices was retained for over 630° or wake age (fig. 17) and a reasonable comparison with the measured load distribution was obtained (fig. 18). The effect of increasing grid size was also found to increase the rotor power for a given thrust value and for the largest grid the power is overpredicted. Reference 13 is easily the best direct computational treatment of this simplest of 3-D rotor/wake problems – and it is one of the few 3-D grid size studies to date – but the problem is not quite solved yet.

It is interesting to use these last computations to infer a grid requirement for a realistic rotor. Increasing the rotor aspect ratio (this rotor had an aspect ratio of 6, which is less than half of typical values), doubles the wake resolution requirement – or increases the total grid size by a factor of 8. In addition, this computation was only performed over 180° because of the use of a periodic boundary condition. A full computation, such as would be required for BVI must be performed over the entire azimuth – or another factor of 2. With a baseline grid of 17×10^6 , this results in 2.7×10^8 points. With a larger base grid the original grid-size estimate could be closely approached.

Clearly, the direct numerical approach will only be possible with much larger computational resources than exist today. The only alternative to the use of large resources is to resort to some type of modeling.

4. Vortex Core Modeling

It is clear from the discussion of resolution that a requirement to resolve the vortex core can make direct CFD wake methods impractical. For computation of larger-scale flow features, however, CFD methods are quite practical. If CFD is to be used successfully, therefore, it will be necessary to model the vortex core regions. At its simplest level, such modeling need not imply the enforcement of physically known vortex characteristics (as is done with the vortex-lattice methods). Rather, it is only required that the solution be modified such that the vortex existence is preserved. Preservation of the vortex implies that the solution process must, at a minimum, keep the core size small (with respect to all other length scales, with the exception of surface viscous scales) and to maintain its strength (circulation). CFD methods with these minimum properties are being developed and are now discussed.

4.1 Vortex Embedding

The first use of core modeling in CFD arises from the generalization of potential methods. Recall that, since vortex core regions are small, the global rotor/wake problem is essentially inviscid and irrotational and can be treated with potential methods. Potential methods intrinsically constitute a model of the wake or vortex structure in that vortical regions (wake or vortex cores) are taken to be infinitesimal. However, none of the standard potential CFD solvers can freely convect wakes, because the discontinuity logic restricts the wake to grid planes. This limitation is removed by allowing the vortical region to have a finite (but small) size. The mass conservation equation,

$$(1) \quad \rho_t + \nabla \cdot \rho \mathbf{V} = 0, \quad \text{is solved with a velocity decomposition,}$$

$$(2) \quad \mathbf{V} = \nabla \Phi + \mathbf{Q}^v,$$

assumed to consist of irrotational and rotational components. The rotational component, \mathbf{Q}^v , is chosen to be non-zero only in a thin layer about the shed wake and functions simply to contain the wake circulation. That is, the significance of \mathbf{Q}^v is in its integral properties rather than its specific functional form. It is required that its integral (normal to the sheet and through the \mathbf{Q}^v layer) equals the local potential jump, Γ , of the sheet.

In fact, a particular functional form is chosen for \mathbf{Q}^v , the Clebsch potential,

$$(3) \quad \mathbf{Q}^v = - \Gamma \nabla \lambda, \quad \text{which}$$

expresses \mathbf{Q}^v as the product of a magnitude term (Γ) and a normal spacial distribution term ($\nabla \lambda$). Here λ is chosen to be a half-sine wave (whose zero-crossing is at the sheet and wavelength is chosen to be a multiple, typically 8, of the local grid interval). The main difficulty in evaluating the Clebsch function is that the wake markers do not align or coincide with the grid nodes. This requires that, at each grid point, the Γ and λ be treated as a weighted average from all wake markers that are within a selected region of influence. The overall process is to: (1) find

the velocity field (eq. 1) and rotor circulation distribution, (2) convect wake markers from the rotor trailing edge to their exit from the grid, (3) use eq. 3 to convert the wake markers to a Q^v distribution, and then repeat the process until the wake and loading converges. The process is summarized in figure 19.

The vortex embedding method has mainly been used for the prediction of hover performance and has had much success in these applications (ref. 15). Figure 20 shows a typical shed wake and radial load prediction computed with the embedding method. The size of the required grids is a good indicator of the value of core modeling. A grid required for the computation of a typical operational rotor blade in hover (such as for figure 20) requires about 2×10^5 grid points, which is about 3 orders of magnitude less than that required by a direct numerical simulation.

Vortex embedding has been demonstrated to be applicable to the computation of BVI (ref. 16). For this computation, the tip vortex was represented by the edge of a sheet of markers, convecting at undisturbed freestream velocity (figure 21), and produced BVI blade loads that compared reasonably well with data (compare figure 22 with figure 3). The significance of this computation is that a vorticity embedding method capable of accurately predicting wake trajectories should also predict BVI in the process. At the present time, however, forward flight BVI computations have only been performed for high-speed cases where the wake is undistorted (ref. 17).

Vorticity embedding is probably the fastest possible CFD approach to computing rotor wake convection. This is because it requires a fairly coarse grid – there is no wake dissipation – and uses a potential flow model (on average, these are an order of magnitude faster than Euler solvers). The greatest difficulty with this approach is that it is necessary to explicitly construct the vortex structure (via the Clebsch potential), which, in present implementations, requires cumbersome and costly searches. Such inconveniences can be obviated with the use of simple Cartesian grids, and this is an area of future development for the vorticity embedding approach.

4.2 Vorticity Confinement

The previous approach modeled the vortex core region by explicitly constructing an inner vortical region – whose only property of importance is the vortex strength – and imposing it on the flow. This explicit construction process eliminated the dissipation of vorticity. It is also possible to obtain wake-preserving solutions whose inner vortical region is constructed implicitly by the solution process. This will require the modification of the flow equations.

Our goal is to achieve a wake-preserving solution where inner vortical regions exist only insofar as they contain a non-dissipating circulation in small regions, but which, because of the grid, are not resolved. This lack of resolution implies that the flow in these small regions has no physical meaning other than their circulation. Under these conditions, it is permissible to modify the flow equations in these regions. Such a scheme has been described in ref. 18. A modified, incompressible, Navier-Stokes equation is used as an example.

$$(4) \quad \nabla \cdot \mathbf{V} = 0$$

$$(5) \quad \mathbf{V}_t + \mathbf{V} \nabla \cdot \mathbf{V} = - \nabla p / \rho + \nu \nabla^2 \mathbf{V} + \epsilon \mathbf{P},$$

where

$$(6) \quad \mathbf{P} = -\mathbf{n} \times \boldsymbol{\omega}, \quad \mathbf{n} = \nabla \eta / |\nabla \eta| \text{ and } \eta = |\boldsymbol{\omega}|.$$

The modification here consists of an acceleration term, \mathbf{P} , added to the momentum equations. This acceleration is in the direction of the tangential flow induced by a vortex and is proportional to vorticity, ω (it is nonzero only in the inner vortical regions). Since the nonvortical flow is unaffected by this term, the circulation of a vortex is unchanged. The effect of the velocity increase induced by this term is therefore to drive vorticity inward and to decrease the vortex size. There is a limit to the extent to which vorticity can be driven inward (an infinite velocity is not possible) and this limit is set by the numerical dissipation. That is, the confinement acceleration and the numerical dissipation reach an equilibrium, which sets the core size. This core size can be varied by choosing various values of ϵ and can approach two mesh intervals. Within this small region the solution has no physical significance other than its circulation, which is the property we seek.

The ability to preserve wakes is shown in figure 23, which shows two computations of the downstream convection of a tip vortex using a standard compressible Euler solver. The two computations differ only by whether or not a confinement term is added to the momentum equations. It is seen that the unmodified equations dissipate the tip vortex (visualized using vorticity contours) with great rapidity. The solution using the confinement modification is quite different and shows convection of the tip vortex for an indefinite distance with no dissipation. Figure 24 shows a plot of tangential velocity across the vortex in these two solutions at a distance of 2.0 chords downstream of the wing trailing edge. It is seen that the confined solution shows a much more intense core region that is confined to within a distance of about 2 grid cells.

The confinement approach has also been demonstrated on BVI problems. In reference 19 a two-dimensional, BVI is computed with an incompressible solver, both for inviscid flow and for a low Reynolds Number. It was demonstrated that this interaction (produced by a strong vortex, with a small core passing close to the blade surface) resulted in a strong surface pressure perturbation adjacent to the passing vortex. The viscous solution resulted in a greatly thickened boundary layer next to the vortex and an even stronger pressure perturbation than the inviscid case (figures 25 and 26). It was also shown that without the use of confinement the vortex would dissipate rapidly resulting in a much weaker interaction. Favorable comparisons with experimental flow visualizations were also obtained. Surface pressure comparisons with the data from ref. 2 could not be made because the data was not then available. We can only remark at this time that the BVI in ref. 2 is weaker than the demonstration computations of ref. 19, because the latter assumes a far greater circulation and smaller core size. (The pressure data of ref. 3 does not show a convecting pressure peak such as seen in ref. 19.) These computations are of interest in that they do indicate the possibility of surprising viscous behavior in the BVI.

The confinement approach is currently being developed for the computation of global wake problems. The first such problem to be so treated should be the 2-bladed rotor of ref. 14.

5.0 Concluding Remarks

Isolated BVI rotor testing has shown that a wide range of methods (including potential and Euler CFD) are able to predict the loading produced by the interaction of a rotor blade with a vortex of known strength and location – and, as a result, the acoustics are well predicted. Similarly uniform results do not occur with realistic rotor tests where a complex rotor wake must be predicted. Such results lead to the conclusion that the central problem in BVI computation is that of predicting the wake. Of course, the prediction of wakes is the oldest problem in rotor aerodynamics. Acoustic predictions often require that the rotor/vortex passage distance be predicted to within a small fraction of a chord. It has not been demonstrated that any computation

method possesses this level of accuracy. Vortex lattice methods are widely used because they are fast. Moreover, they can be readily corrected to account for known wake errors. Unfortunately we rarely, if ever, know the wake trajectories prior to performing a calculation. Furthermore, we do not understand the extent to which present wake solutions can be applied to other and different rotor configurations. Basically, wake prediction seems to be an inconsistent process and this situation will degrade our ability to design new quieter rotorcraft with confidence. We can always test new configurations (in fact, this will remain a necessity), but we will not be able to make the design compromises and tradeoff decisions that can only happen with the availability of a reliable analysis.

Over the years, great hope has been placed in the development of CFD methods as a way to perform rotor/wake computations that require little or no user intervention or empiricism. Simple estimates show that, for structured grids, the grid size requirements (and hence, the cost) are enormous, purely as a result of the disparity in size between the total computation region and the smallest flow feature to be resolved, namely, the vortex core region. Recent direct numerical simulations of rotor/wake flows seem to support these large grid estimates and indicate that great increases in computer resources are required. These resources are becoming available with the recent impressive growth in large parallel computers. Such methods are already beginning to be applied usefully to flows where vortices and separation regions are relatively large (complex fuselage flows, for instance). However, for the rotor wake and BVI problems, direct numerical simulations are not likely to become practical engineering tools for years. Unstructured, adaptive grids, can greatly reduce grid requirements, but not necessarily the cost until an effective unsteady adaptation scheme is devised.

However, CFD can be a practical tool, for BVI and other rotor/wake problems, if the essence of the wake, its strength and small size, can be preserved without actually resolving the vortical core regions. There has been little thought concerning such methods within the CFD community. Nevertheless, such approaches do exist. The central idea of these methods is to use a numerical model of the vortex core rather than to attempt to resolve it.

One such method is the vortex embedding approach, which explicitly constructs a non-dissipating wake core. This approach has been applied successfully to the prediction of hover performance – another rotor problem that is acutely dependent on the prediction of the wake. The grid required for such computations is probably 2 to 3 orders of magnitude less than that for a direct numerical simulation. The embedding approach has been demonstrated for the prediction of BVI, however the method has not yet been applied to a complete advancing rotor wake solution.

A more general approach to obtaining non-resolving wake solutions is to implicitly model the vortex core region. In the method of vorticity confinement, a vorticity-concentration term is added to the momentum equations in high-gradient vortical regions. The resulting core region does not reflect any particular physical model, but is only determined by the equilibrium between numerical dissipation and the confinement. This core can be contained to within a region of about 2 grid cells across. This approach has demonstrated the ability to compute a number of vortex flows, including simple parallel BVIs and is under active development.

It would be incorrect to rule out any of the above lines of development in future research planning, because the problem is too far from solution. It is clear however, that the vortex lattice method will remain a primary working tool for the foreseeable future. Within this framework CFD will find much use as a local coupled solver. The global wake problem, however, is clearly a long-term challenge. Development of higher order methods, massive parallelization and adaptive gridding is underway and can make important contributions to this problem. It is not unlikely that a variety of the above methods could be used. However, it is also clear that there is a need for a new approach to CFD (other than adding grid points and improving resolution). The

development of these new approaches has already begun in the current development of embedding and confinement methods. If these non-resolving methods are successful in the treatment of the general global wake problem, the door could then open to solving other flow problems whose difficulties are scale-related.

REFERENCES

1. A. Hassan, B. Charles, H. Tadghighi, and C. Burley, "A Consistent Approach for Modeling the Aerodynamics of Self-Generated Rotor Blade-Vortex Interaction," 49th Annual Forum of the American Helicopter Society, St. Louis, Missouri, May 19-21, 1993
2. Kitaplioglu, C., and Caradonna, F., "Aerodynamics and Acoustics of Blade-Vortex Interaction Using an Independently Generated Vortex," AHS Technical Specialists' Conference, San Francisco, CA January 1994
3. Caradonna, Kitaplioglu, McCluer, Baeder, Leishman, Berezin, Visintainer Bridgeman, Burley, Epstein, Lyrintzis, Koutsavdis, Rahier, Delrieux, Rule and Bliss, "A Review of Methods for the Prediction of BVI Noise," American Helicopter Society Technical Specialists' Meeting for Rotorcraft Acoustics and Aerodynamics, Williamsburg, VA, October, 1997
4. Splettstoesser, W., Kube, R., Wagner, W., Seelhorst, U., Boutier, A., and Pengel, K., "Key Results from a Higher Harmonic Control Aeroacoustic Rotor (HART)," Journal of the American Helicopter Society, Vol. 42, No. 1, January 1997
5. C. Tung, R. Kube, T. Brooks and G. Rahier, "Prediction and Measurement of Blade-Vortex Interaction," AIAA Journal of Aircraft, Vol. 35, Number 2, Pages 260-266, March-April 1998
6. J. Gallman, K. Schultz, P. Spiegel, and C. Burley, "Effect of Wake Structure on Blade-Vortex Interaction Phenomena: Acoustic Prediction and Validation," AIAA Journal of Aircraft, Vol. 35, Number 2, Pages 267-273, March-April 1998
7. B.E. Wake, and D. Choi, "Vortex Prediction and Convection Using Upwinded Navier-Stokes Solvers," American Helicopter Society Specialists' Meeting for Aeromechanics Technology and Product Design for 21st Century, Bridgeport, CT, Oct. 11-13, 1995
8. R. Strawn, and T. Barth, "A Finite-Volume Euler Solver for Computing Rotary Wing Aerodynamics on Unstructured Meshes," Journal of the American Helicopter Society, Vol. 38, No. 2, April, 1993, pp. 61-67
9. M. Dindar, A. Lemnios, M. Shephard, and K. Jansen, "Effect of Tip-Vortex Resolution on UH-60A Rotor-Blade Hover Performance Calculations," 54th Annual Forum of the American Helicopter Society, Washington, D.C., May 20-22, 1998
10. M. Rai, "Navier-Stokes Simulations of Blade-Vortex Interaction Using High-Order Accurate Upwind Schemes," AIAA 25th Aerospace Sciences Meeting, Reno, NV, Jan. 12-15, 1987

11. B. Wake, and J. Baeder, "Evaluation of a Navier-Stokes Analysis Method for Hover Performance Prediction," Journal of the American Helicopter Society, Vol. 41, No. 1, Jan. 1996, pp.1-17
12. P.F. Lorber, R.C. Stauter, and A.J. Landgrebe, "A Comprehensive Hover Test of the Airloads and Airflow of an Extensively Instrumented Model Helicopter Rotor," 45th Annual Forum of the American Helicopter Society, Boston, MA, May 1989
13. J. Ahmad, and R. Strawn, "Hovering Rotor and Wake Calculations with an Overset-Grid Navier-Stokes Solver," 55th Annual Forum of the American Helicopter Society, Montreal, Canada, May 25-27, 1999
14. F. Caradonna, and C. Tung, "Experimental and Analytical Studies of a Model Helicopter Rotor in Hover," NASA Technical Memorandum 81232, September, 1981
15. K. Ramachandran, R.C. Moffit, S.J. Owen and F.X. Caradonna, "Hover Performance Prediction Using CFD," 50th Annual Forum of the American Helicopter Society, Washington, DC, May, 1994
16. J.O. Bridgeman, and F.X. Caradonna, "A Computational Analysis of Parallel Blade-Vortex Interactions Using Vorticity Embedding," 50th Annual Forum of the American Helicopter Society, Washington, DC, May, 1994
17. A.K. Bangalore, M.A. Moulton and F.X. Caradonna, "The Development of an Overset/Hybrid Method for Rotorcraft Applications," AHS Technical Specialists' Meeting for Rotorcraft Acoustics and Aerodynamics, Williamsburg, VA, October 28-30, 1997
18. C. Wang, J. Bridgeman, J. Steinhoff, and Y. Wenren, "The Application of Computational Vorticity Confinement to Helicopter Rotor and Body Flows," 49th Annual Forum of the American Helicopter Society, St. Louis, MO, May, 1993
19. J. Steinhoff, and G. Raviprakash, "Navier-Stokes Computation of Blade-Vortex Interaction Using Vorticity Confinement," AIAA 95-0161, AIAA 33rd Aerospace Sciences Meeting, Reno, NV, January 1995

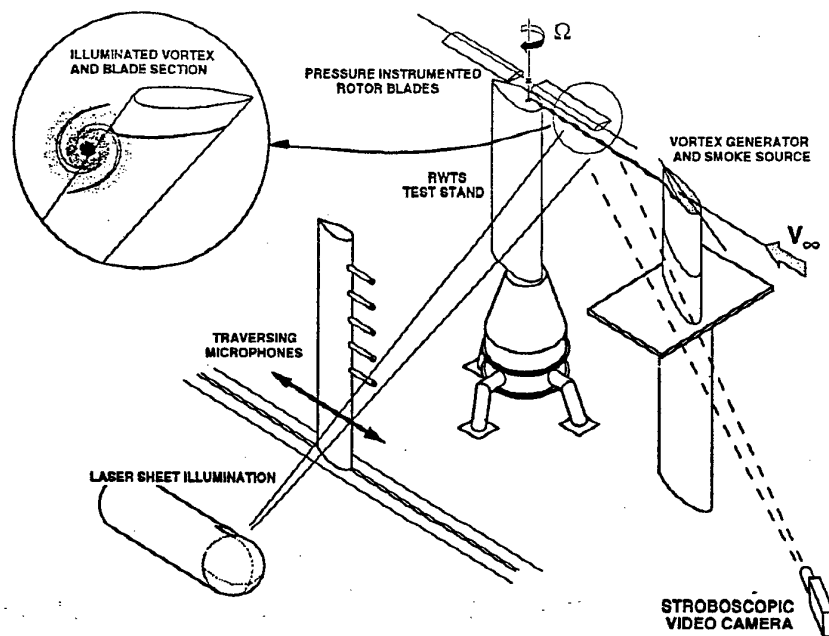


Figure 1. A sketch of an isolated BVI aeroacoustic test. [2]

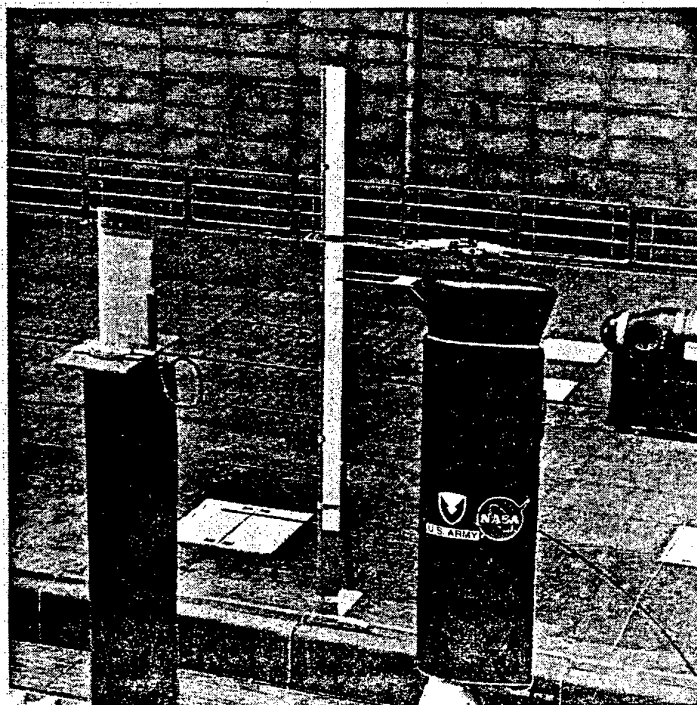


Figure 2. Photograph of the isolated BVI test in the Ames 80x120' tunnel. [2]

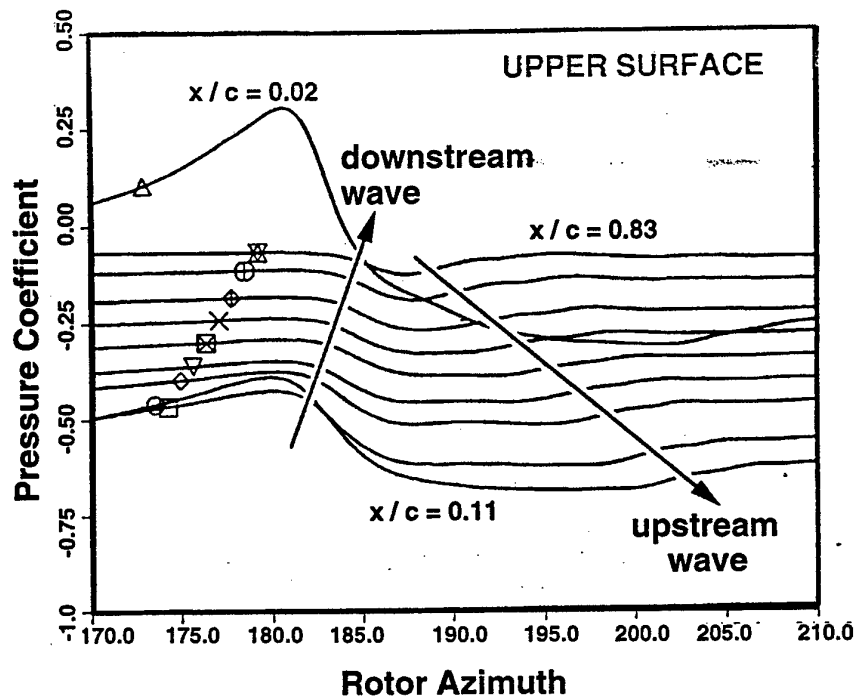


Figure 3. Pressure-time histories for a chordwise array of surface pressure transducers on a rotor blade. [16]

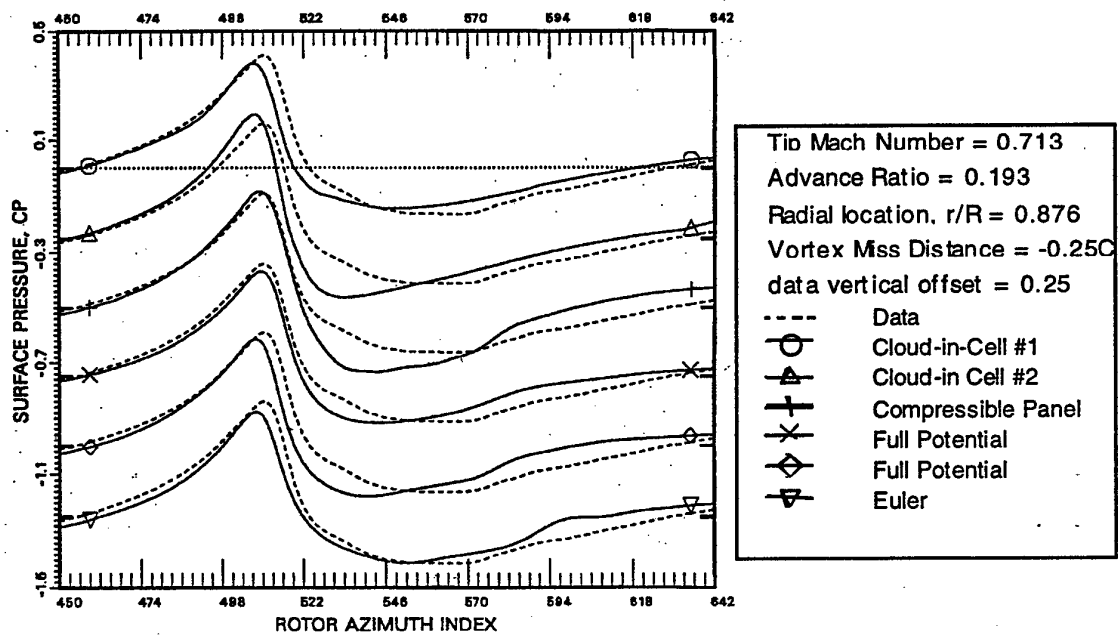


Figure 4. A comparison of several computed BVI leading-edge region pressure histories with data for an isolated BVI. [3]

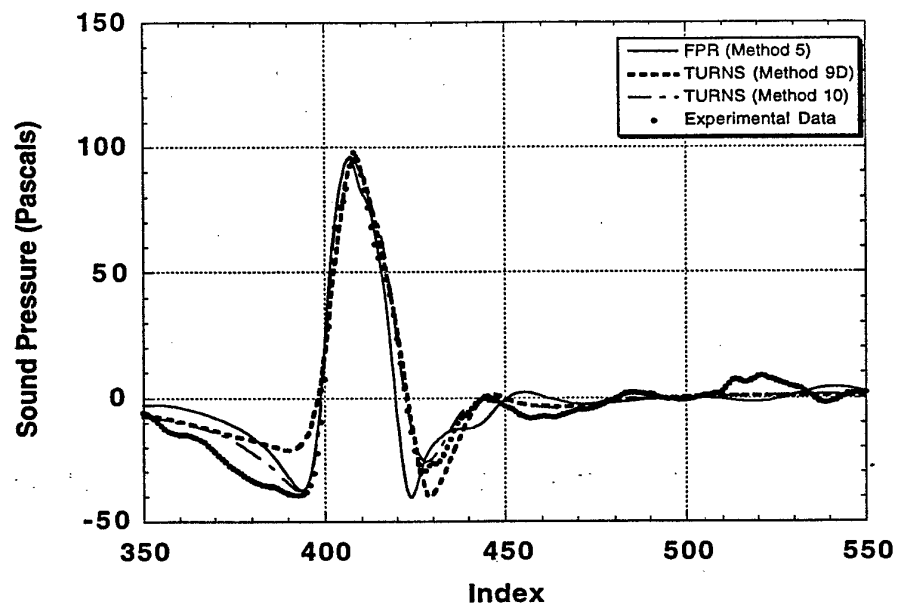


Figure 5. A comparison of predicted acoustic pressures with data for an isolated BVI.[3]

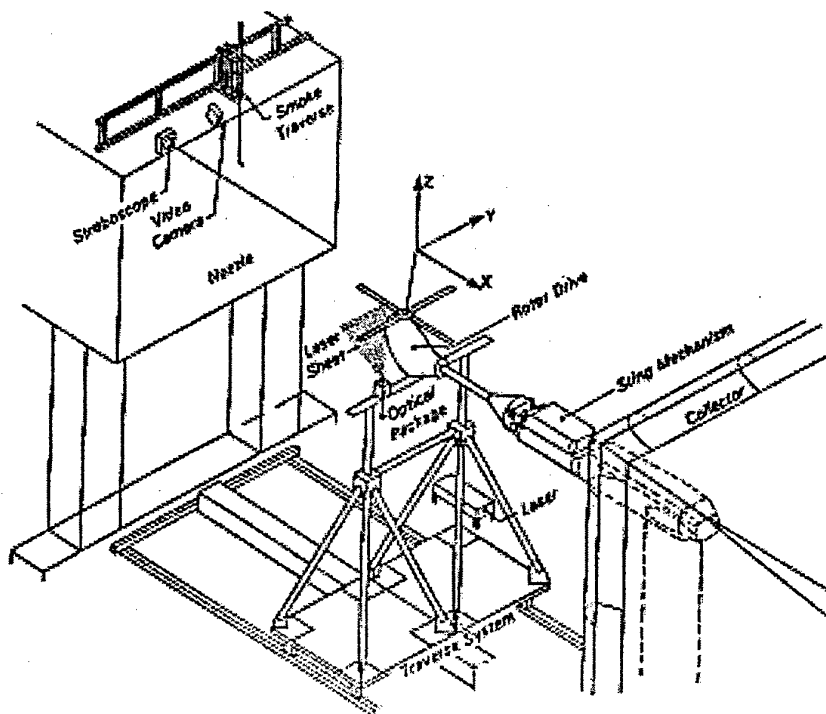


Figure 6. Test setup for a full rotor aeroacoustic test in the DNW tunnel. [4]

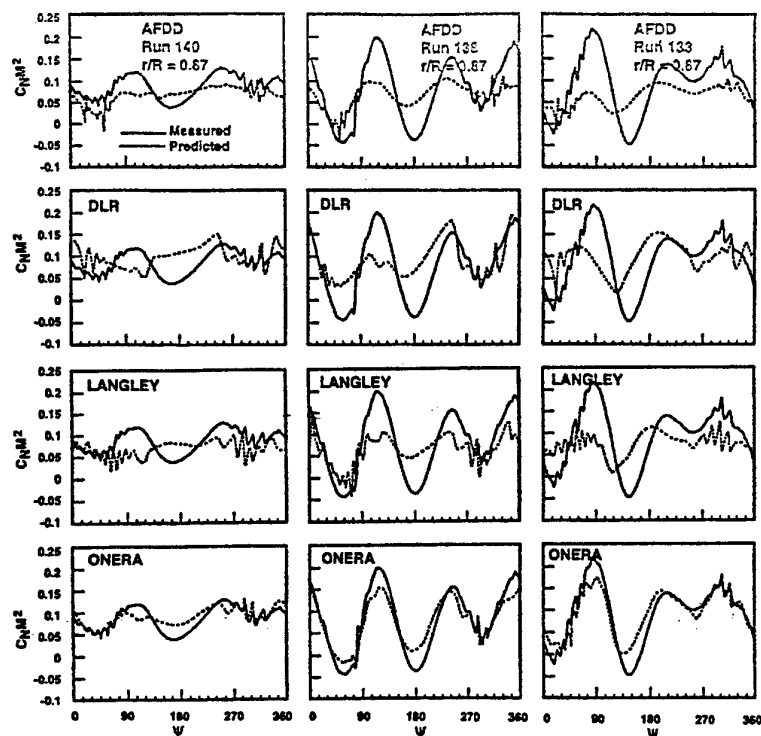


Figure 7. Pre-test BVI loading computations compared with data from the DNW tunnel.[5]

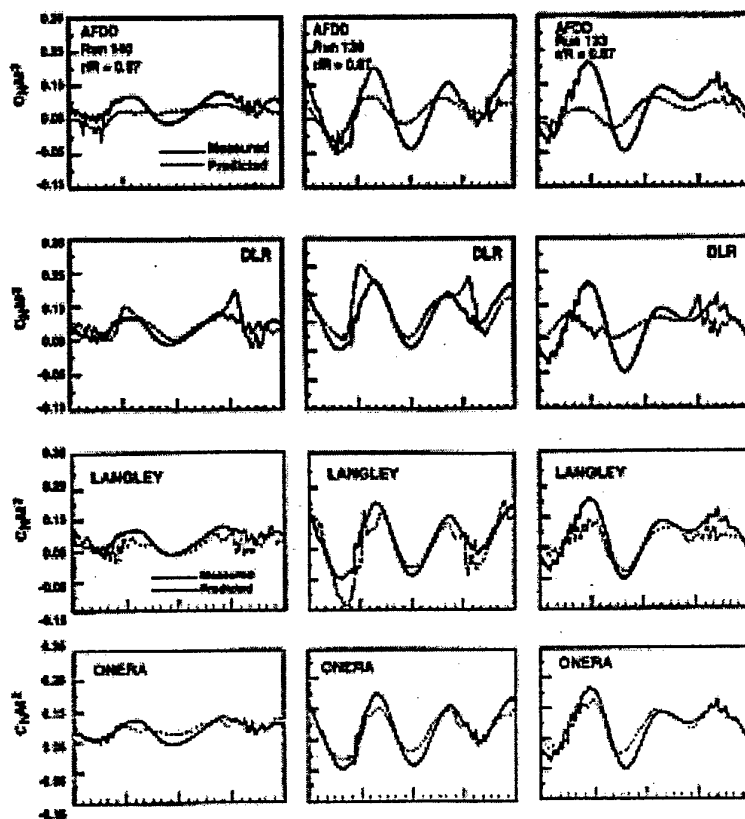


Figure 8. Post-test BVI loading computations compared with data from the DNW tunnel.[6]

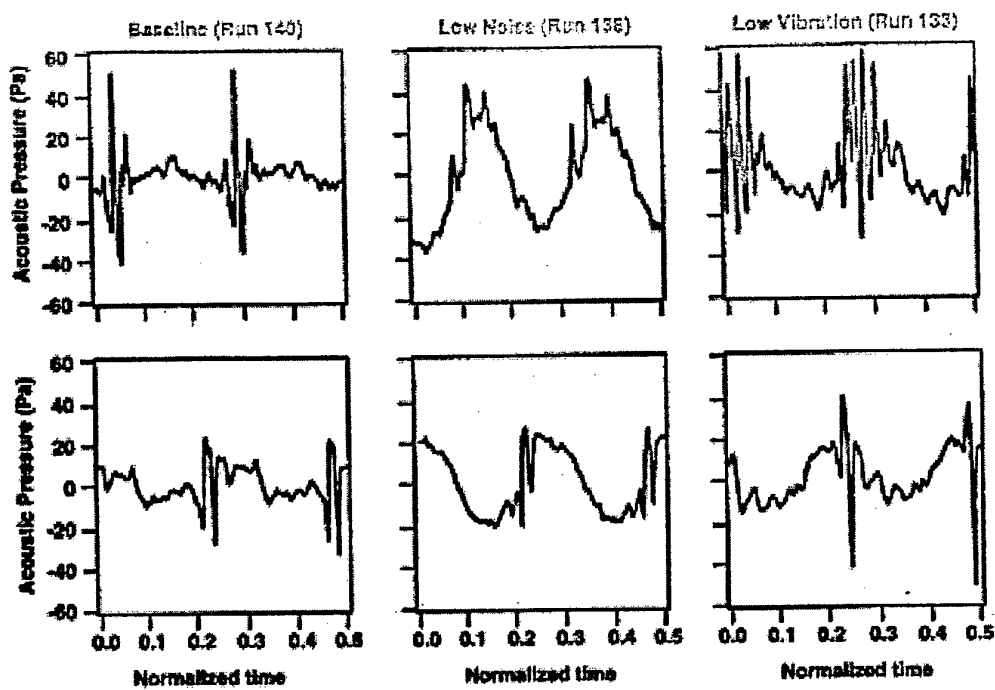


Figure 9. Acoustic pressure histories taken from advancing-side (top row) and retreating side (bottom row) microphone data. [6]

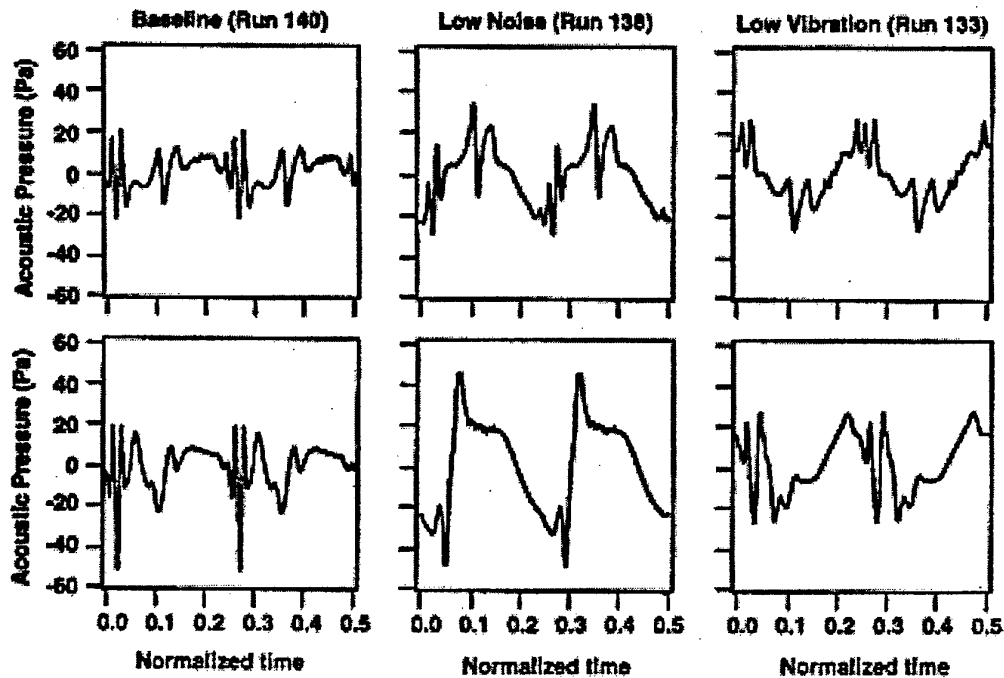


Figure 10. Advancing-side DLR pre-test and post-test acoustic predictions. [6]

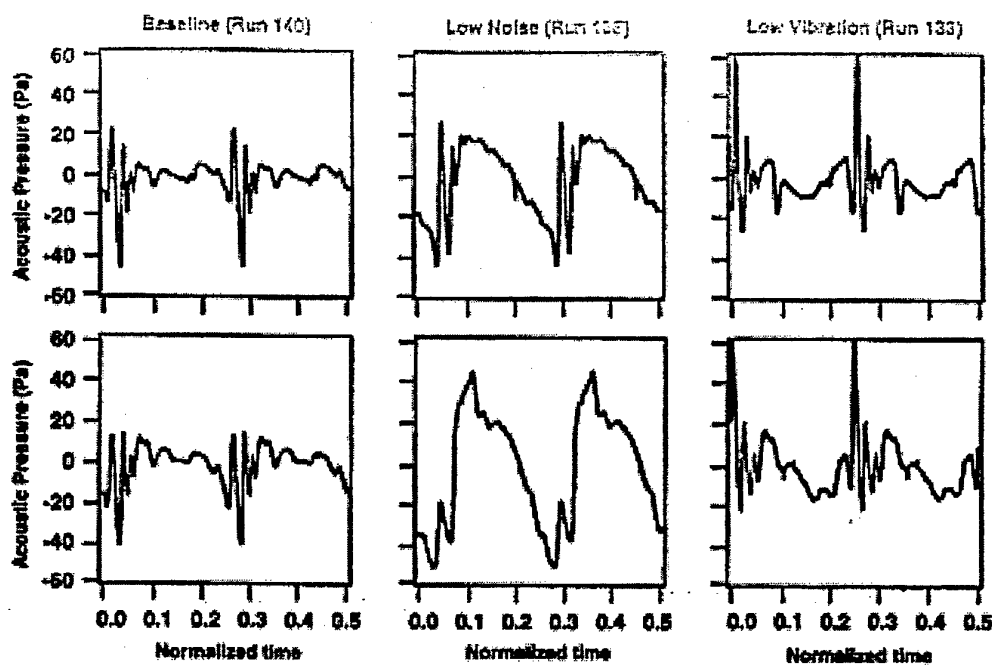


Figure 11. Advancing-side Langley pre-test and post-test acoustic predictions. [6]

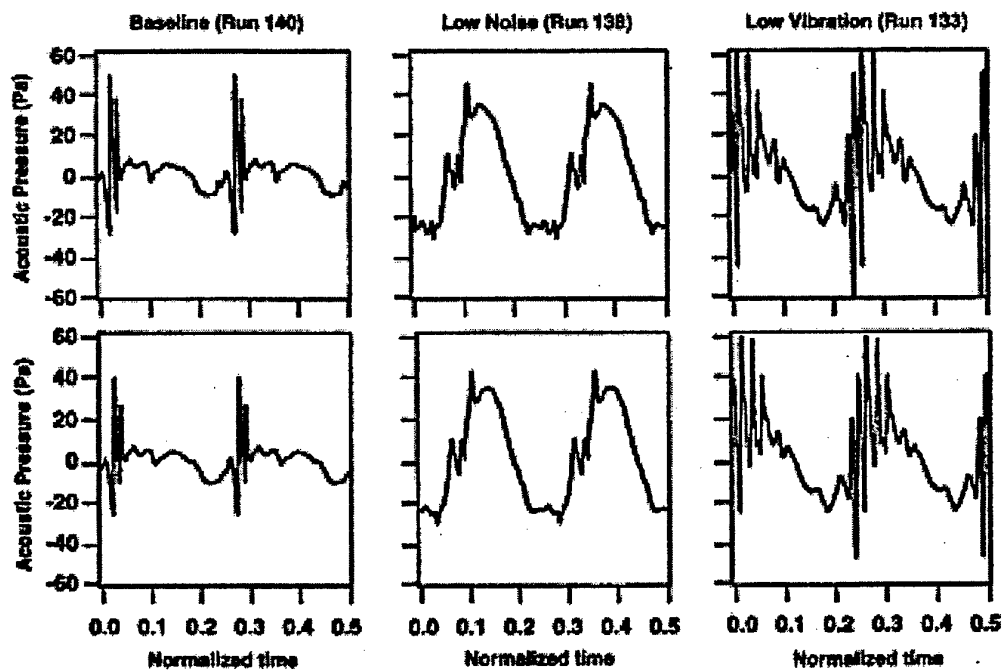


Figure 12. Advancing-side ONERA pre-test and post-test acoustic predictions. [6]

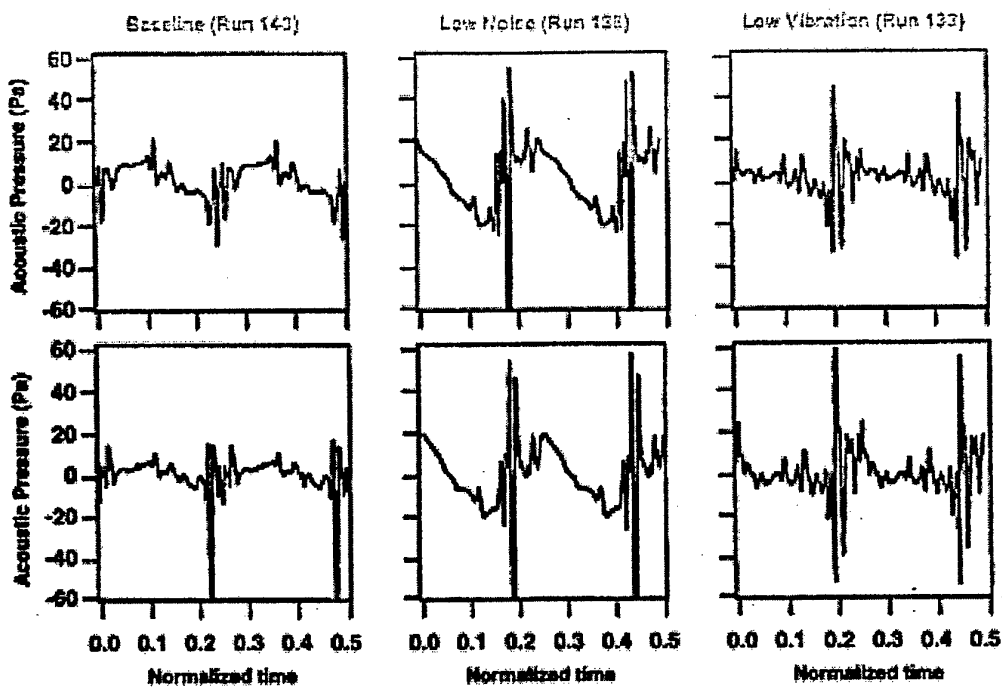


Figure 13. AFDD advancing-side pre-test and post-test acoustic predictions. [6]

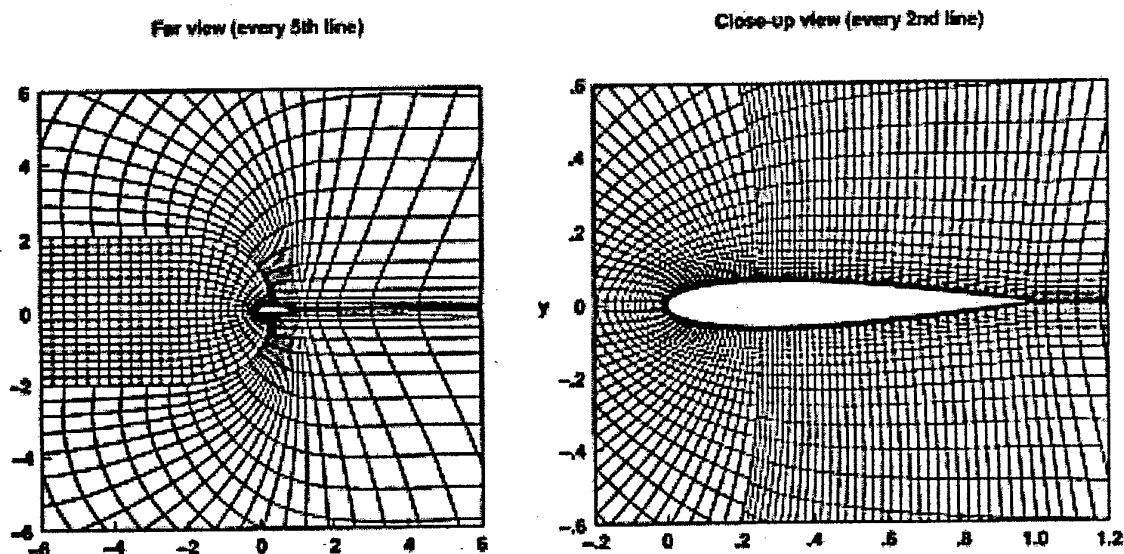


Figure 14. A grid used to perform two-dimensional computations of the BVI. [10]

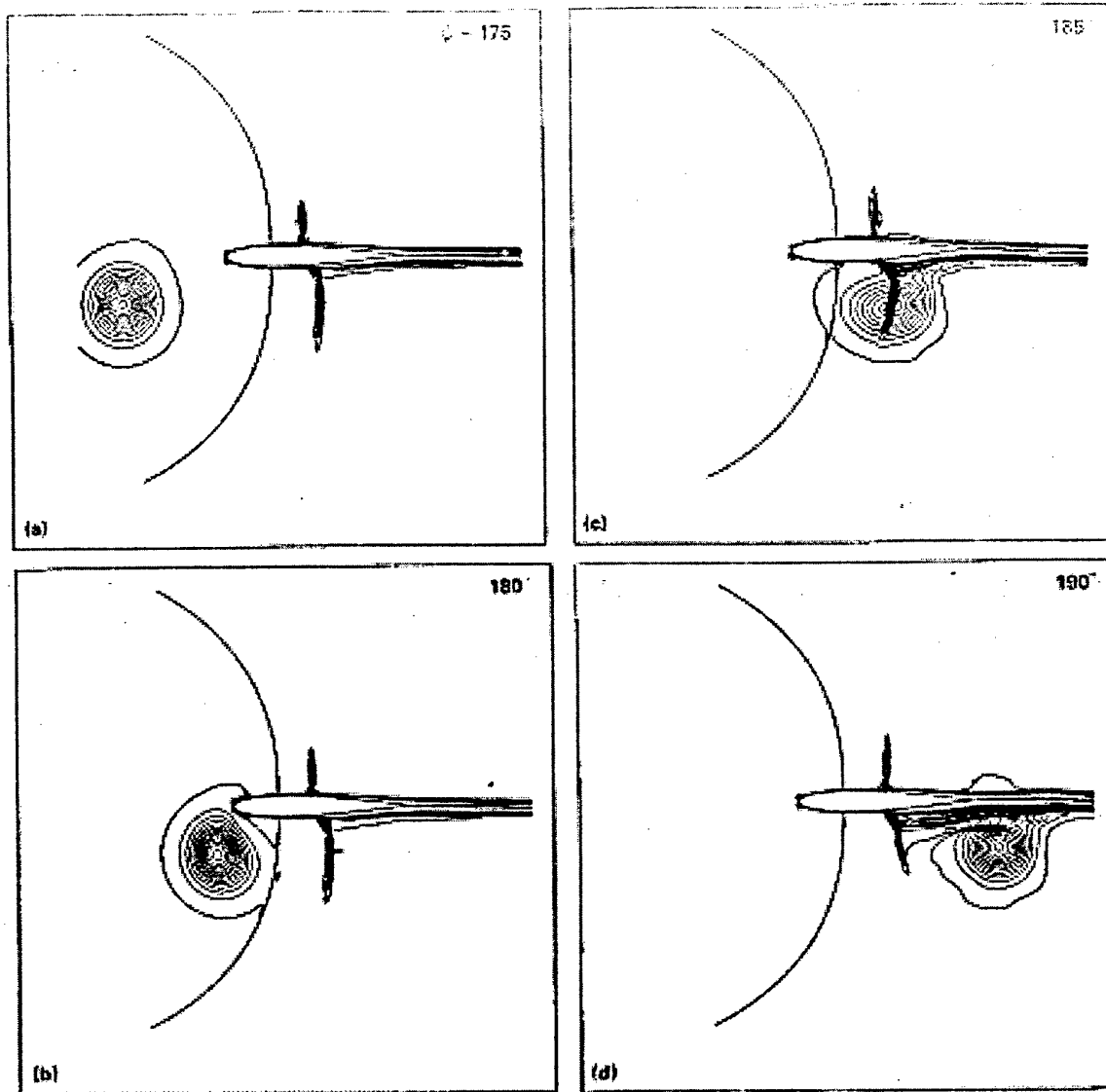


Figure 15. A two-dimensional, transonic BVI computed using a high-density grid and high-order method. [10]

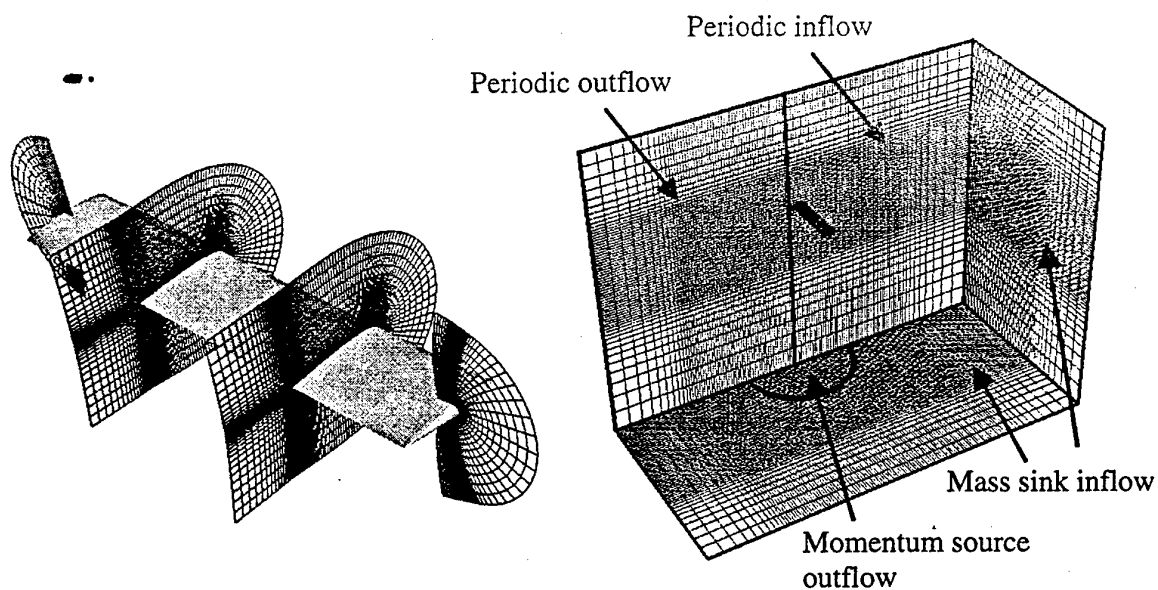


Figure 16. Grid system used to compute hover flow on a 2-bladed rotor. [13]

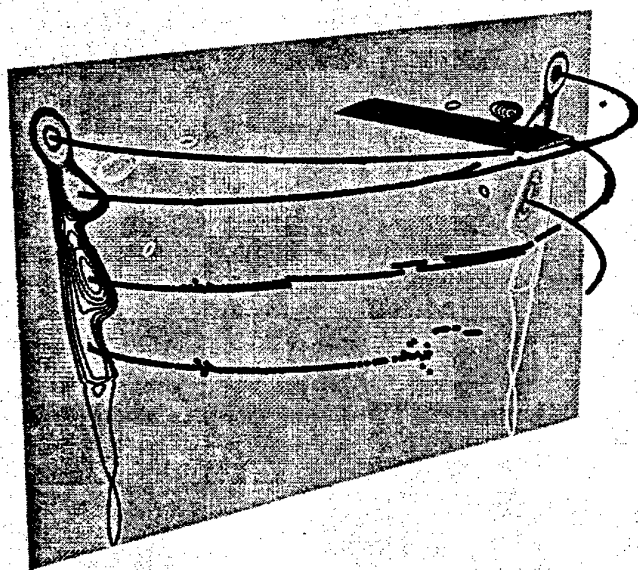


Figure 17. Vorticity contours for the 2-blade rotor. [13]

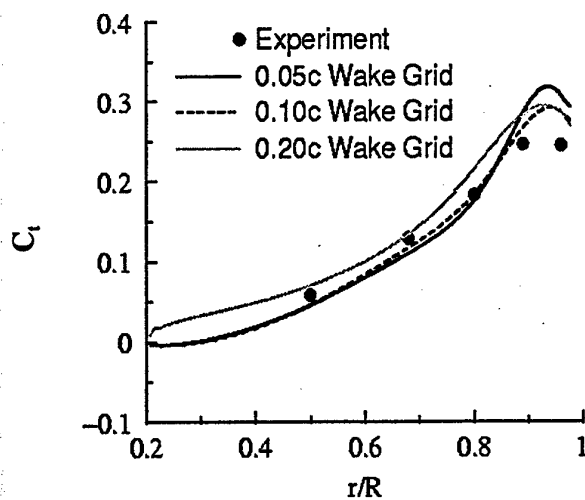


Figure 18: Spanwise lift distribution for the 2-blade rotor. [13]

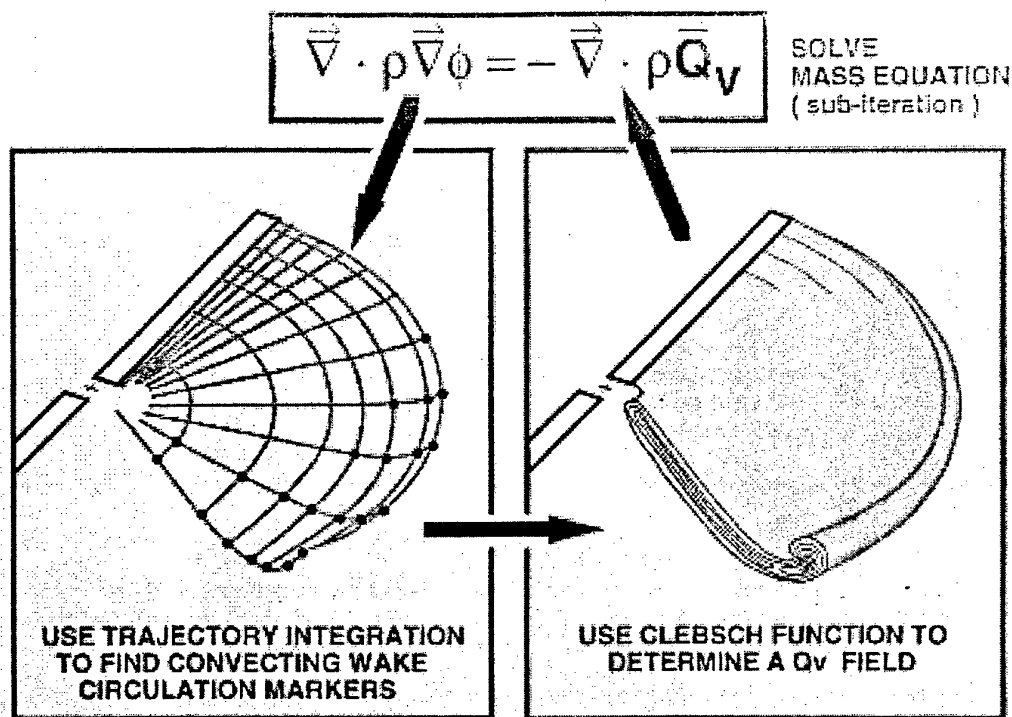


Figure 19. A schematic of the iterative solution process employed for the vortex embedding method.

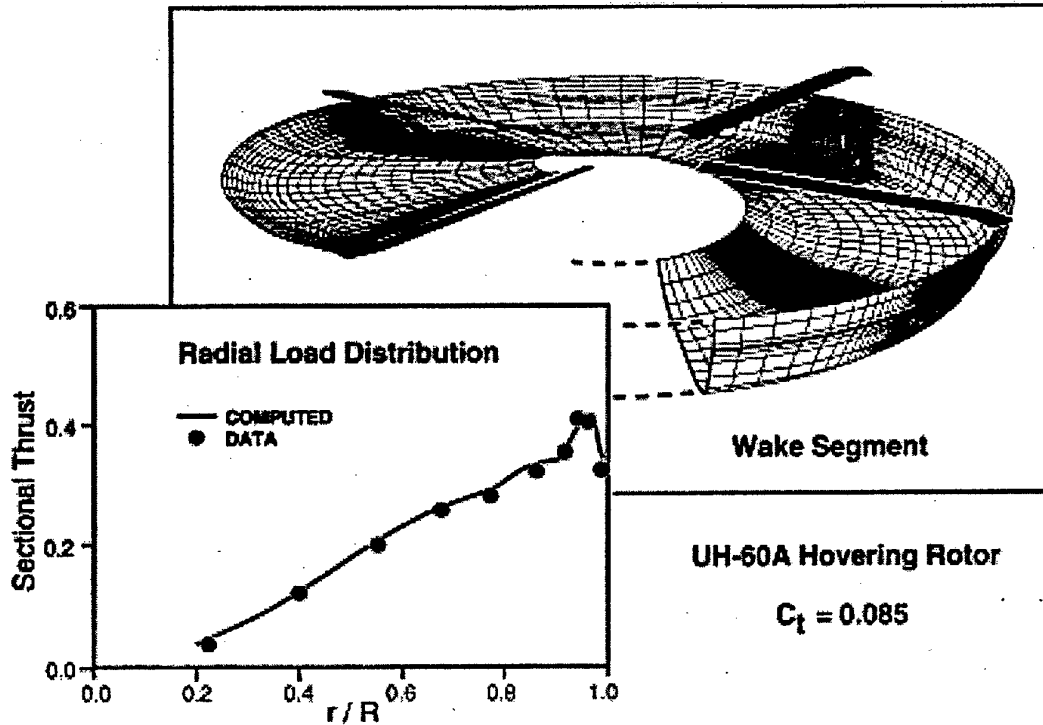


Figure 20. A typical wake marker sheet predicted by a vortex embedding solver - and a radial load distribution predicted by the same solution. [15]

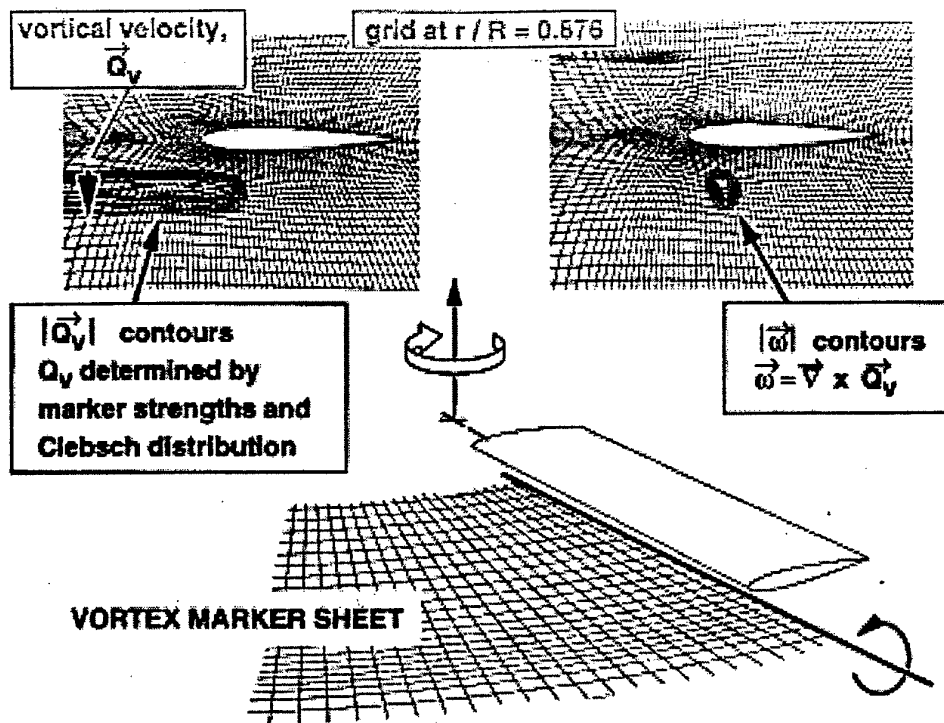


Figure 21. The convecting marker sheet used to represent a passing vortex for a vortex-embedded BVI solution. [16]

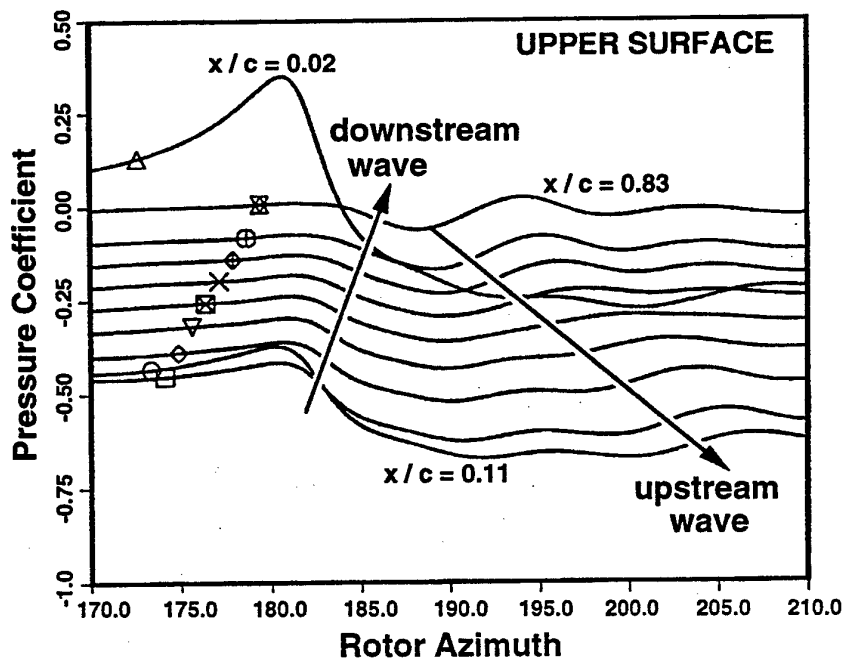


Figure 22. BVI-induced surface pressure-time histories computed using vorticity embedding scheme of fig. 21. Same case as for data in fig. 3. [16]

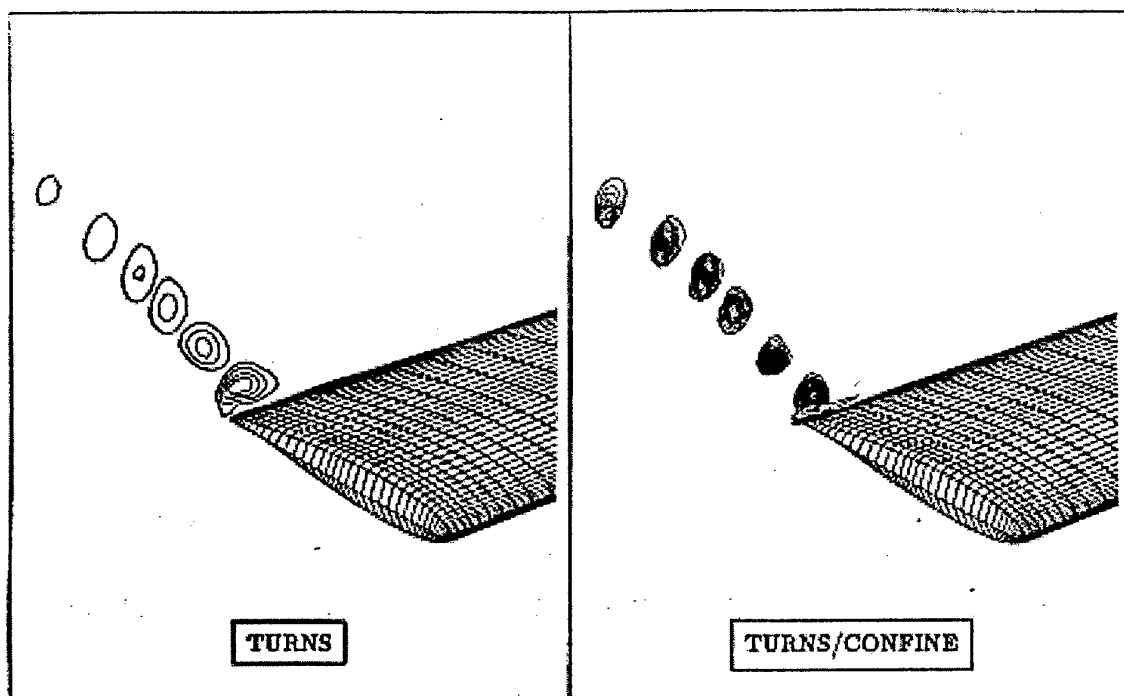


Figure 23. Wing-tip vorticity contours computed with a 3rd order upwind solver compared to an identical computation that uses confinement. [18]

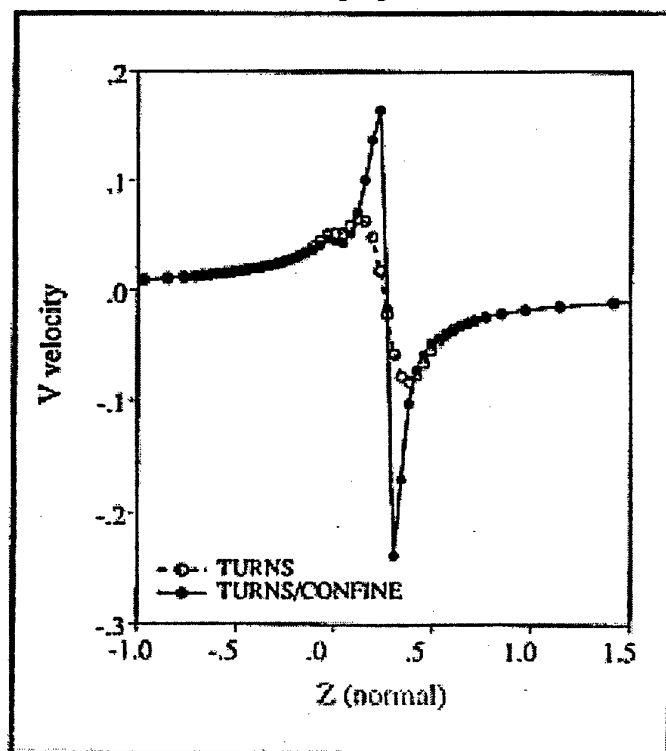


Figure 24. Tangential velocity distributions computed with a 3rd order upwind solver compared to an identical computation that uses confinement. [18]

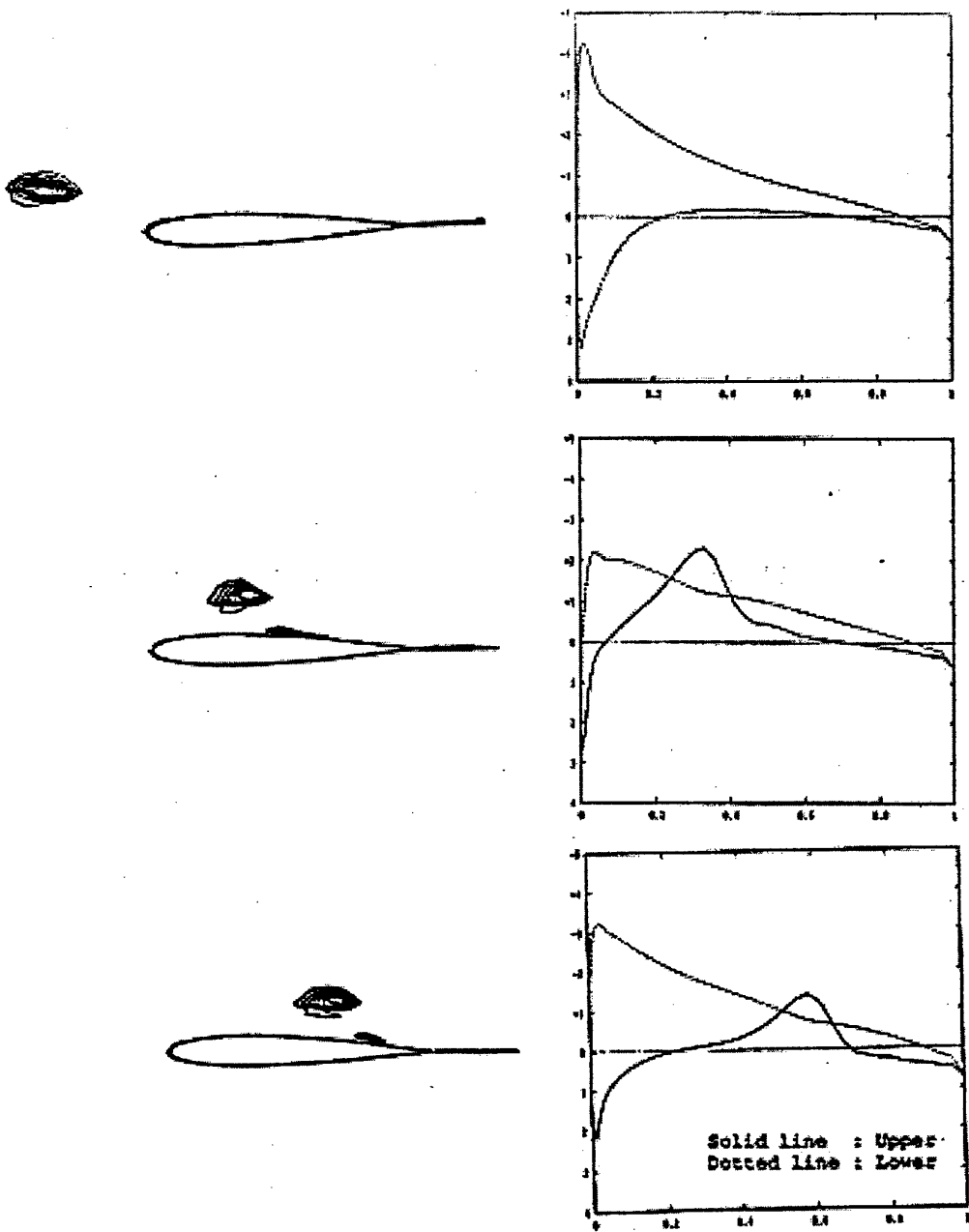


Figure 25. An inviscid computation of a BVI using vorticity confinement. [19]

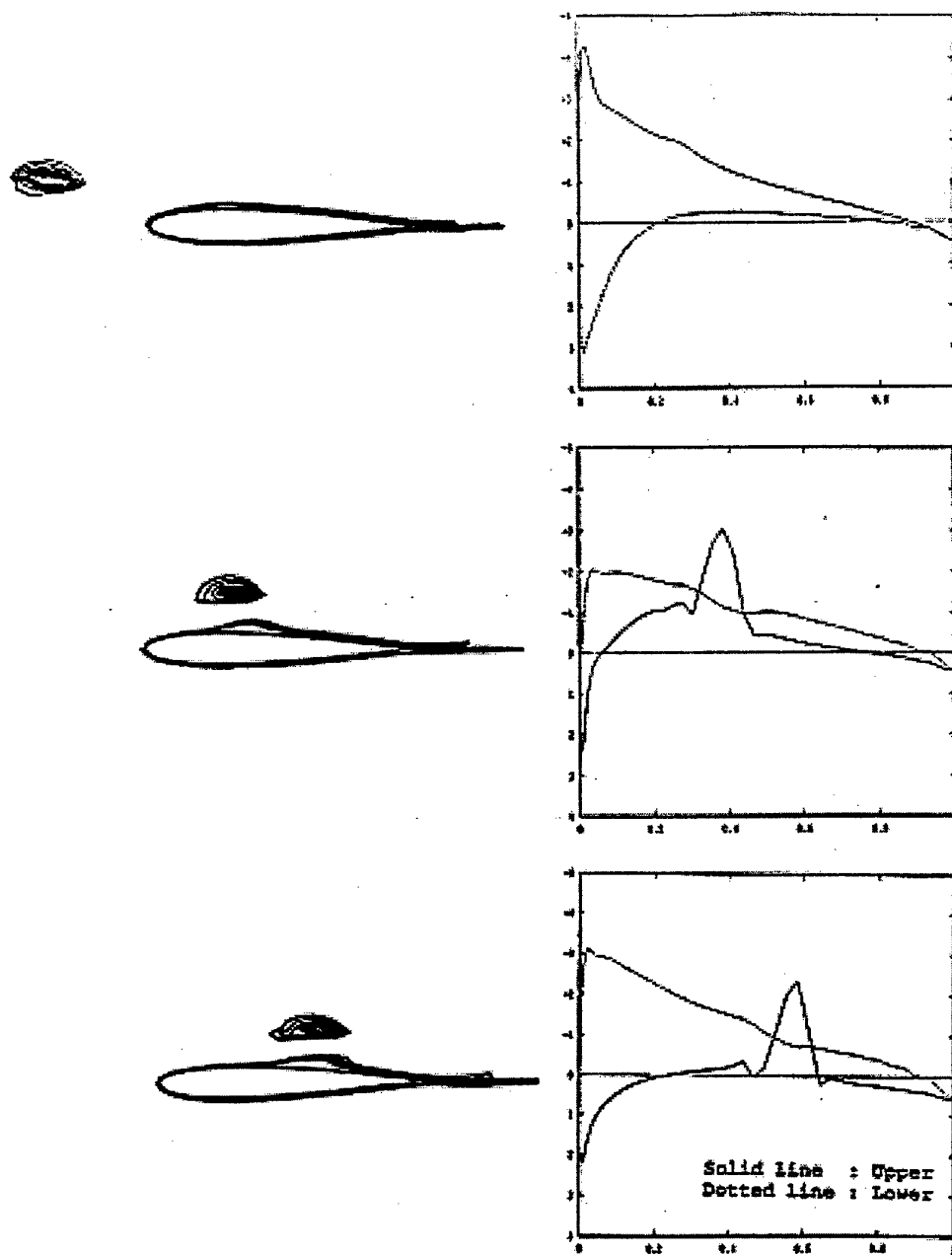


Figure 26. A low Reynolds Number computation of a BVI using vorticity confinement. [19]

Noise Levels Measurements at the INSEAN Circulating Water Channel with a Twin Screw Ship Model

Dr. Ing. Marcello Costanzo - INSEAN, Rome, Italy
C.F. Ing. Mauro Elefante - CEIMM, Rome, Italy

Summary

A twin screw ship model of 1:20.6 scale ratio was used in the INSEAN "Circulating Water Channel" to measure the noise due to cavitation on the four-blade propellers.

The Circulating Water Channel test section is 2.25 m depth, 3.60 m wide, 10 m long, and the maximum water speed is 5 m/s. The atmospheric pressure can be reduced till 35 mbar (3500 Pa) in the test section to keep the same "cavitation index" σ between ship and model.

The ship model is 5.232 meters length, with two propellers of 182 mm diameter; the hub diameter is 58 mm to look four controllable pitch blades.

Tests were conducted on ship model at the same "Froude" number and same "cavitation index" σ of the full-scale ship. In our case, that simulates ship speeds between 28 and 31 knots with corresponding propeller revolutions from 216 to 242 RPM, the water flow was in the range 3.2-3.5 m/s and propeller revolutions was set to 16.2-18.2 RPS. With the water temperature of 25.5-26.0 °C the pressure was reduced till 80 mbar (8000 Pa) to keep the same cavitation index. The acoustic pressure fluctuations are measured by miniature-hydrophone 8103B&K, with a nominal voltage sensitivity of 30 μ V/Pa. A B&K 2134-5765 analyzer have analyzed the signal in broad (1/3-octave) bands till 100 kHz.

It has been found that cavitation noise was rising up in the frequency range of 2 - 100 kHz, 20 dB up the background noise at one-meter distance. Sound pressure levels were higher increasing speed and decreasing reference pressure.

Some Notes on Underwater Acoustics

Sound waves are propagated pressure and density fluctuations in the medium caused by particle motions.

For small amplitudes the general wave equation can be expressed as follows:

$$\nabla^2 p - \frac{1}{c^2} \frac{\partial^2 p}{\partial t^2} = 0$$

Where $p = p(x, y, z, t)$ is the dynamic pressure and $c = c(x, y, z)$ is the speed of the sound and ∇ is the Laplacian operator.

It is worthwhile to consider some of the fundamental differences between the wave transmission in water and in air. The sound velocity in water is ≈ 4.4 times higher than in air. High frequencies in water are strongly attenuated. Background noise and reverberations are greater

then in air with stronger frequency spreading. Due to cavitation phenomena, water cannot support pressure below a certain minimum, so the size and depth of the projector limit the amount of energy that may be putted into the water.

The sound intensity is the measure of the rate of energy or power flow through a unit area. The intensity of an isotropic point source of known power "W", putted at the origin of a spherical coordinate system, is a function of the radial coordinate only.

$$I = \frac{W}{4\pi R^2}$$

where $4\pi R^2$ is the area of the sphere of radius "R" through the acoustic energy must flow. The relation between acoustic intensity and sound pressure levels can be expressed by

$$I = \frac{p^2}{\rho c}$$

where " ρc " is acoustic radiation resistance of the medium, " ρ " is its density and " c " is sound speed.

Till the acoustic radiation resistance in the water is $1.5 \cdot 10^6$ kg/m²s and in air is 420 kg/m²s, it results that the same sound pressure level corresponds to acoustic intensity in air 3570 times greater than in water.

$$\frac{I_{Air}}{I_{Water}} = \frac{\left(\frac{p^2}{\rho c}\right)_{Air}}{\left(\frac{p^2}{\rho c}\right)_{Water}} \approx \frac{1.5 \cdot 10^6}{420} \approx 3570$$

For the same reason if the acoustic intensity is the same in air as in water, the sound pressure level in water is approximately 60 times greater than the corresponding value in air.

$$\frac{p_{Water}}{p_{Air}} = \sqrt{\frac{\rho c_{Water}}{\rho c_{Air}}} = \sqrt{\frac{1.5 \cdot 10^6}{420}} \approx 60$$

Therefore the characteristics of a hydrophone or projector must be considerably different from those of a microphone or loudspeaker. The air - water interface represent a strong discontinuity and will act as a good reflector.

The consequence of the previous relations is that acoustic intensity and sound pressure levels due to an isotropic point source will vary according the following logarithmic expression:

$$10 \log I_2/I_1 = 20 \log P_2/P_1 = 20 \log R_1/R_2$$

that is good till the medium is without energy loss, where 1 and 2 indicate two points in the field at R_1 and R_2 the distances from the source.

In the sea, it's normally used the Thorp [1] equation to evaluate the attenuation coefficient "a" of sound pressure, in witch the frequency dependency is rising up:

$$a(f) = [0.1 f^2 / (1 + f^2) + 40 f^2 / (4100 + f^2) + 2.75 \cdot 10^{-4} f^2]$$

where "a" is the attenuation coefficient in dB per thousand yards and "f" is the frequency in thousand Hertz.

Getting Ready for Noise Cavitation Tests

To start the cavitation noise test as first has been chosen a ship model whose cavitation patterns are well known. A twin screw ship model was picked up from INSEAN laboratory with scale ratio $\lambda = 20,26$. Two inwards rotation propellers with four blades, able to be oriented in pitch, external diameter of 182.62 mm, hub diameter ratio of 32.4 %, pitch ratio $P/D_{0.7} = 1.495$ and expanded area - disk area ratio $A_e/A_o = 0.710$, supply the necessary thrust to reach 31 knots as full scale speed.

To minimizing the noise due to propulsion system the electric motor has been fitted in a special box supported by silent blocks on the hull. The reduction gear wheels were carefully chosen to warrant odd gear ratio, and the shafts were carefully aligned.

A self-propulsion test has been done in the INSEAN n°1 towing tank, useful to know the appropriate propellers rate versus speed. These kind of tests are normally done at the same relative speed as in full scale, at ship propulsion point. The model resistance is equal to the propeller thrust plus a towing force that takes account for the different resistance coefficient between model and ship, so the propeller works in the ship advance coefficient.

With these available data it's possible to have a prevision of back cavitation for our 4-blades propeller, using the "Burrill" diagram, in which are drawn the thresholds curves of 2.5 - 5 - 10 - 20 - 30 % of back cavitation in the $\sigma \perp \tau$ plane. The cavitation index is defined as $\sigma = (p_o - p_v)/q$ (with p_o the absolute pressure, p_v the water vapor pressure, q is the dynamic pressure at 0.7 tip radius), the propeller load coefficient defined as $\tau = (T/A_p)/q$ (with T the propeller thrust, A_p the projected area of the blades). The first diagram is relative to 28 knots ship (Fig. 1) speed, the second to 31 knots (Fig. 2). The labels that are shown near the marked points are the ambient pressure values during tests in INSEAN "Circulating Water Channel", and 80 mbar (8000 Pa) is the appropriate value to reach the same cavitation index σ for model and ship, while with 148 mbar (14800 Pa) the model cavitation index is $\sigma_{\text{model}} = 2.2 \sigma_{\text{ship}}$, until the water temperature during tests was 25.5 ± 0.2 °C.

As can be seen by these diagrams, with 148 mbar ambient pressure we are far away (28 knots) or very close (31 knots) the 2.5 % back cavitation (that means cavitation inception) threshold curve, while with 80 mbar ambient pressure we are below (28 knots) or upper (31 knots) the 10 % back cavitation threshold curve.

What about hydrophones and noise measurement equipment? The transducers, the conditioning amplifiers, the calibrator, the narrow band and the broad band analyzers, the noise generator and power amplifier are all built by Bruel&Kjaer.

Receiving transducers are the 8103 B&K miniaturized hydrophones, with a piezoelectric cylinder as active element. His frequency response in water is practically flat up to 150 kHz, and directivity patterns show that is omni-directional in all planes up to 100 kHz (± 4 dB). In addition are available transmitting transducers B&K 8104 hydrophones with voltage response of 12 dB/octave in the frequency range below the first resonance (70 kHz); they are coupled with white/pink noise generator and power amplifier to perform the acoustic characterization of the test section.

In the noise cavitation tests one receiving hydrophone has been looked in a Naca profile. This profile was built in fiberglass with the terminal transducer housing made by perspex. It was carefully fixed using rubber damping material to reduce any undesired vibration; it was looked in a vertical plane at 800 mm from the symmetry plane of the model. Other two hydrophones has been used, the first looked in a special perspex box on the stern shell, up to the starboard propeller, and the second looked in a special fiberglass box fitted on a perspex window in the propeller plane as shown in the sketch of fig. 3.

The receiving hydrophone B&K 8103 gets pressure information and send the electric signal by its own cable to the conditioning-preamplifier B&K 2650 directly connected with the broad band analyzer B&K 2134 expanded by B&K 5765 unit, useful till 160 kHz.

Cavitation Noise Measurements

Before cavitation noise was measured the background noise. To get this data the test section was set at atmospheric pressure and the model was lacking in propellers, the water flow was set at the appropriate speed to simulate the 28 knots (3.2 m/s) and 31 knots (3.5 m/s), coming from "Froude" number identity. The shafts were looked so that the pressure fluctuation measurement gets the background flow noise.

The second step was, always with the model lacking in propellers, at atmospheric pressure, at the same water speed as in previous case, to measure the background noise with the shafts rotating at the appropriate revolution rate, as obtained from the self propulsion test, so that the pressure fluctuation measurement gets the background flow noise with the rotating shafts noise.

Finally the absolute ambient pressure in the test section was reduced to reach the cavitation index identity. According to the previous paragraph data were kept at two cavitation index, at 148 mbar with σ model equal to 2.2 times σ ship, and at 80 mbar with σ model equal to σ ship.

The sketch with the broad band analysis are showed in fig. 4 and 5 for the two ship speed conditions, and can be seen that the background flow noise is quite big in the low frequency range, the shaft axis rotation noise can't be kept by the hydrophone fitted in the fin position.

It's important to note that the cavitation noise is in very good agreement with the percent back cavitation previsions done with the Burrill diagrams. They showed that at 148 mbar we were far away (28 knots) or very close (31 knots) the 2.5 % back cavitation (that means cavitation inception) threshold curve, while at 80 mbar we were below (28 knots) or upper (31 knots) the 10 % back cavitation threshold curve.

The same happens to the cavitation noise levels; they comes up from 2 kHz till 100 kHz from 110 dB to \approx 130 dB only in 31 knots speed condition if the pressure is 148 mbar. They come up either in 28 or in 31 knots speed, if the pressure is 80 mbar. The hydrophone is positioned in the fin, in a field point where the cavitation yields high frequency pressure fluctuations; this phenomena can be similar to the noise produced by a red-hot iron wetted by water. Cavitation generates different diameter vapor bubbles; they grow up and finally collapse. The broad band analysis can't give us much more detailed information, but it's the first step through the deeper investigation of the phenomena.

What does it happen nearer to the source? With our data it's possible to do only one comparison, at the pressure condition of 148 mbar and ship speed of 28 knots, that is shown in the graph of fig. 6.

In this graph are compared the results coming from fin hydrophone (Fin, circle symbol) and stern shell hydrophone (Tip, square symbol). In this last position, nearer to the source, the low

frequency pressure fluctuations appear, showing the shaft revolution rate frequency of 16 hertz, the blade frequency of 64 hertz, higher pressure fluctuations levels in the range 315 + 800 Hz. In the high frequency range the level at 10.000 Hz comes up. The hydrophone fitted on the window was too far from the source to be interesting in this report.

Full scale prevision method

The full-scale prevision method used here is described in the Cavitation Noise Proceedings of 1987 ITTC [3]. The first step is to calculate the contribution due to the propeller, keeping away the background noise. This kind of operation is done for each frequency band making a logarithmic subtraction. The result is shown in fig. 7, where are reported the propeller induced pressure fluctuations measured by the fin hydrophone. These data are referred to the 80 mbar measurements, at the same cavitation index between model and ship.

Second step is to correct these levels taking account of the limited dimensions of the circulating water channel test section. The result is shown in fig. 8. This correction is done using the acoustic calibration of the test section, previously done and described in [4].

Third step is to consider the scale ratio effects.

The frequency will be scaled according the following relation:

$$fp / fm = np / nm$$

where f and n are indicating frequency and revolution rate, p and m are indicating prototype and model scale.

The pressure levels are scaled according the following relation:

$$\Delta L(p) = 20 \log[(D_p / D_m)^x (r_m / r_p)^x (\sigma_p / \sigma_m)^{y/2} (n_p D_p / n_m D_m)^y (\rho_p / \rho_m)^{y/2}]$$

where D is the propeller diameter, r the hydrophone distance, σ the cavitation index, n the revolution rate, ρ the water density, while the exponent x, y and z are normally equal to x=1, y=2 and z=1.

Applying this equation and considering that the cavitation index for model and ship are normally the same in the circulating water channel, it will be:

$$\Delta L(p) \approx 20 \log[(\lambda)^z (\lambda^{-1})^x (\lambda^{1/2})^y] \approx 20 \log \lambda$$

The result is shown in fig. 9.

Conclusions and next develop

It's possible to say now that the cavitation noise pressure levels are fully measurable. The background noise is not so high and the pressure fluctuation frequency due to cavitation is in high range values. With the broad band analysis is not possible to say much more. Our suggestion is that full scale prevision must be deeper studied.

To have more details and deterministic phenomena description we will develop new analysis methods:

- phase average analysis, sampling pressure data according the propeller position;

- triggered narrow band analysis.

We are already working in this direction and it's possible to show the test run result, with shaft rotation rate of 10.7 revolutions per second in fig 10 and 11.

References

- [1] Aldo De Dominicis Rotondi, "Principi di Elettroacustica Subacquea " Elettronica San Giorgio ELSAG S.p.A. GENOVA ITALIA
- [2] A. de Bruijn, "Scale model experiments on the propeller noise of " CONFIDENTIAL c/o "TECHNISCH PHYSISCHE DIENST TNO-TH" di Delft per conto della Nederlands Scheepsbouwkunding Poefstation di Wageningen
- [3] I.T.T.C. 1987 Report of the Cavitation Committee pagg. 184-192
- [4] Del Vescovo D., Cavazza P. Poggi F. "Analisi preliminare per la valutazione del rumore indotto da cavitazione tramite misure in un canale a circolazione d'acqua depressurizzabile" INSEAN 1988
- [5] C.F. (GN) Lucio ACCARDO e C.C. (GN) Alberto GUAZOLINO, "Rilievi di Rumore Presso il Tunnel del C.E.I.M.M. Annali N°20 1992
- [6] Ing. R. Vergara della TECNAV, "Rilievi di Rumore nel Canale di Circolazione INSEAN; Rapporto sulla campagna sperimentale effettuata nel periodo aprile 1992 + luglio 1993" del 31.7.93
- [7] Ing. R. Vergara della TECNAV, "Procedura di previsione della rumorosità al vero" 11 gennaio 1994 conv. 68 NR del 2.4.92
- [8] Ing. R. Vergara della TECNAV, "Campagna sperimentale per la riduzione del rumore irradiato dal sistema propulsivo dei modelli" 10 dicembre 1994 conv. 103 NR del 23.02.94
- [9] Ing. M. Costanzo INSEAN "Caratterizzazione Acustica del Canale di Circolazione" del 4/4/97 Rapporto Tecnico Insean N° 3/97

- [10] Ing. R. Vergara TECNAV, "Rilievi Post Operam di Rumore di Fondo" preparata per l'Insean nel 3/7/97 nell'ambito della convenzione 1688/G.O. - CED 1862
- [11] Friesch, J "Correlation Investigations for Higher Order Pressure Fluctuations and Noise for Ship Propellers" Third International Symposium on Cavitation 1998
- [12] Ukon, Y. - Kudo, T. - Kurobe, Y. " Measurements of Pressure Fluctuations Induced by a Cavitating Propeller in a Cavitation Tunnel and it's Correlation between Model and Full Scale" Third International Symposium on Cavitation 1998

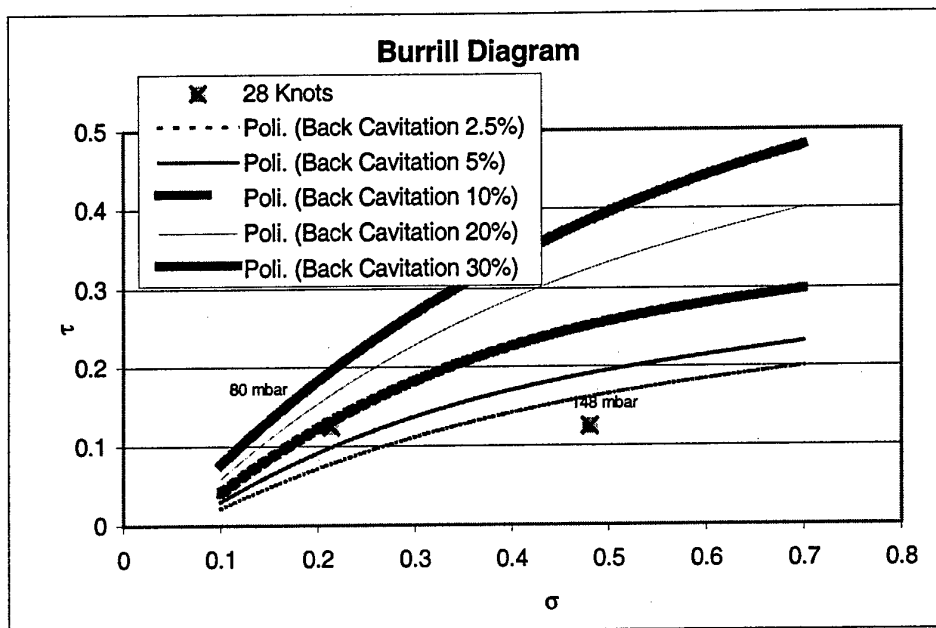


Figure N° 1

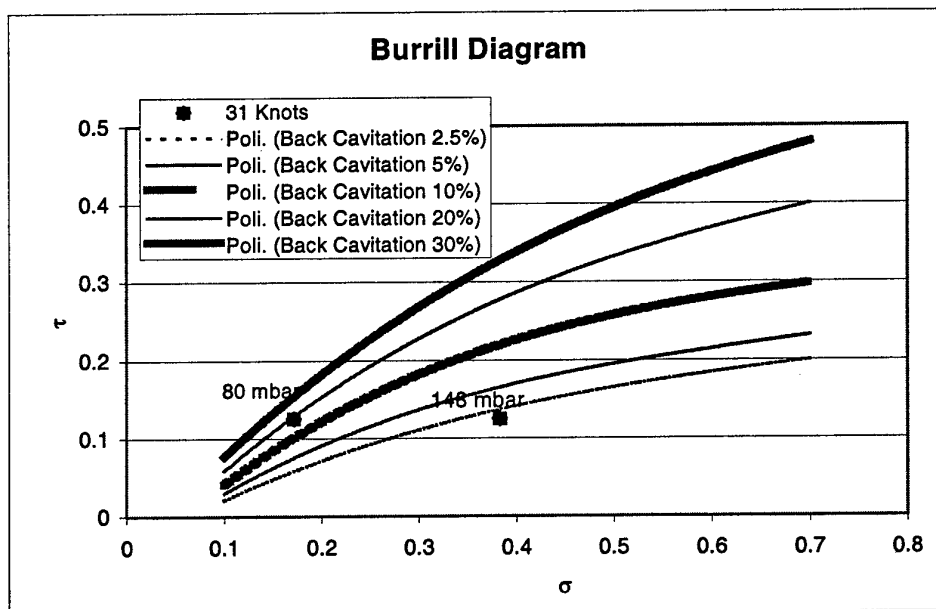


Figure N°2

Sketch of test section with fittings particulars during "Noise Cavitation Test"

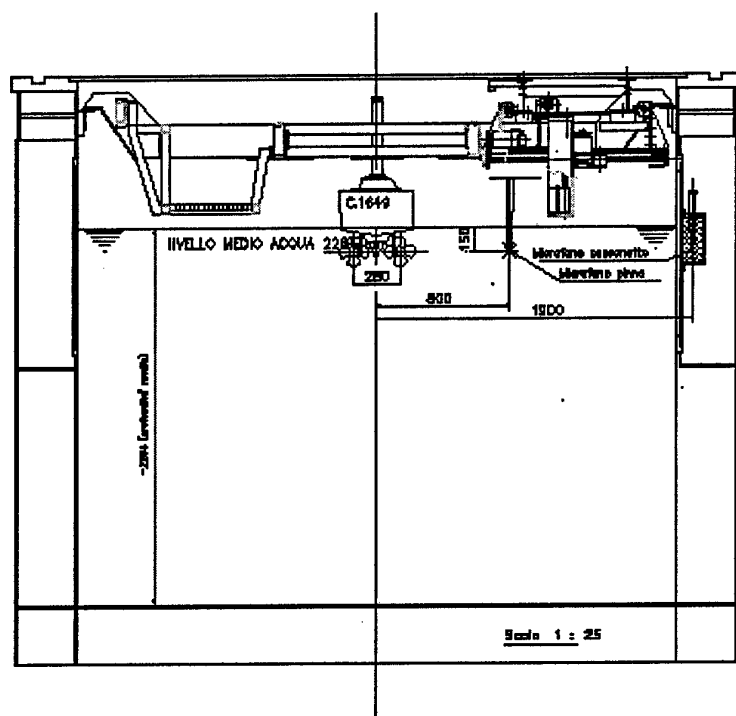


Figure N° 3

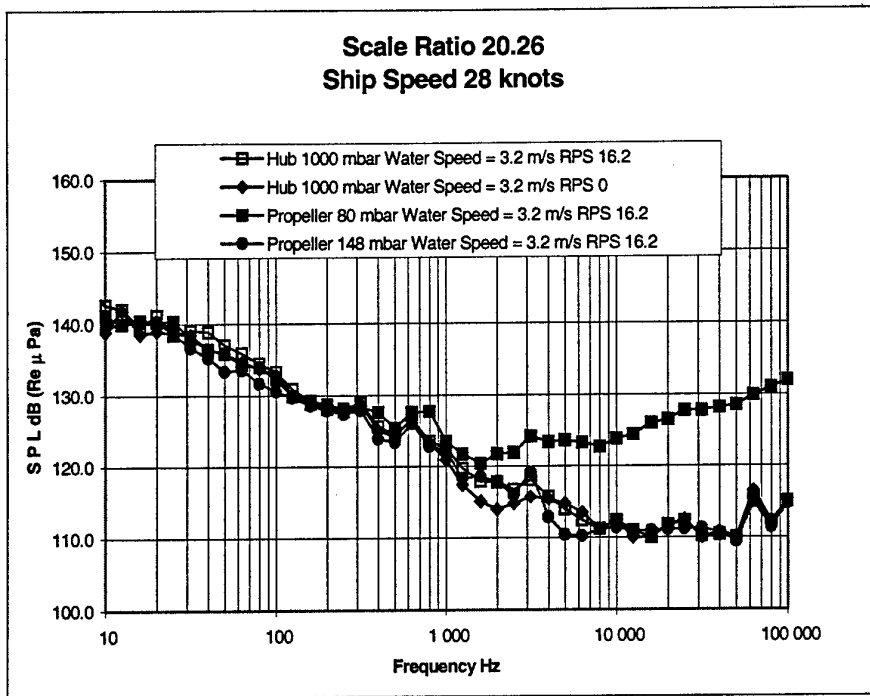


Figure N° 4

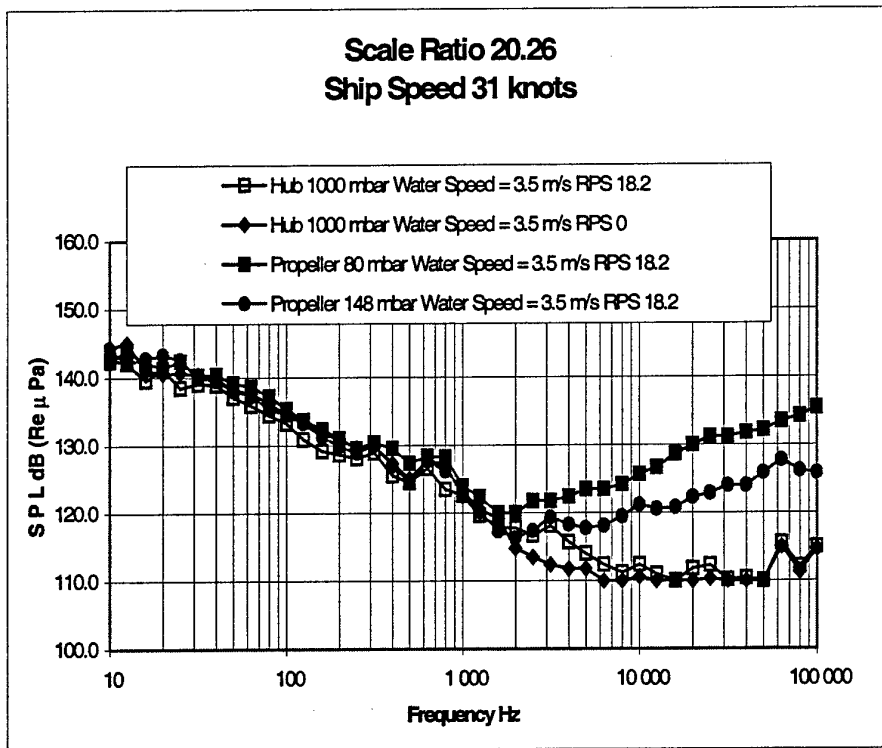


Figure N° 5

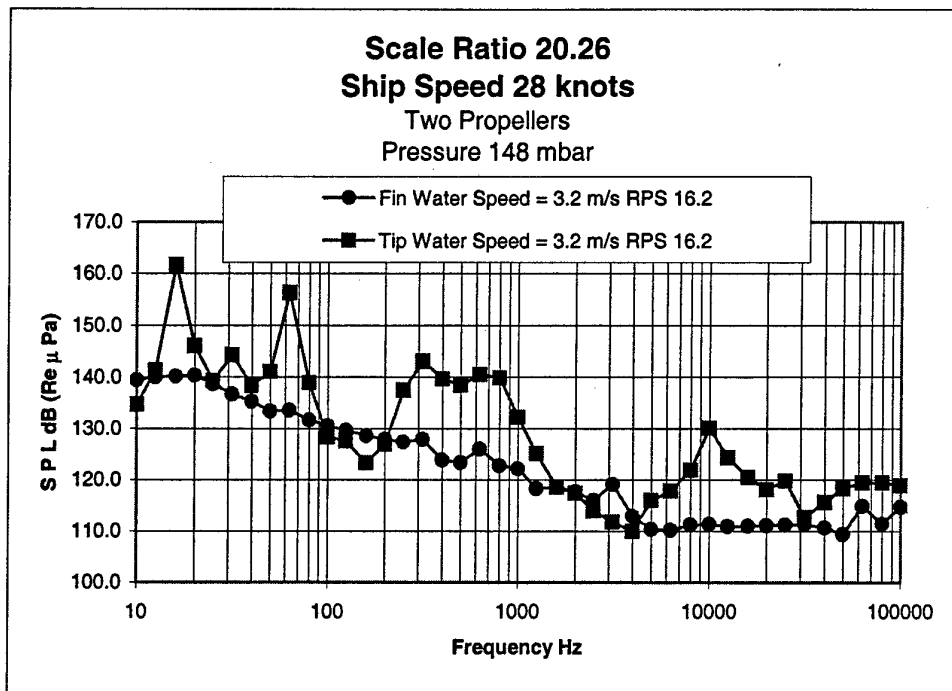


Figure N° 6

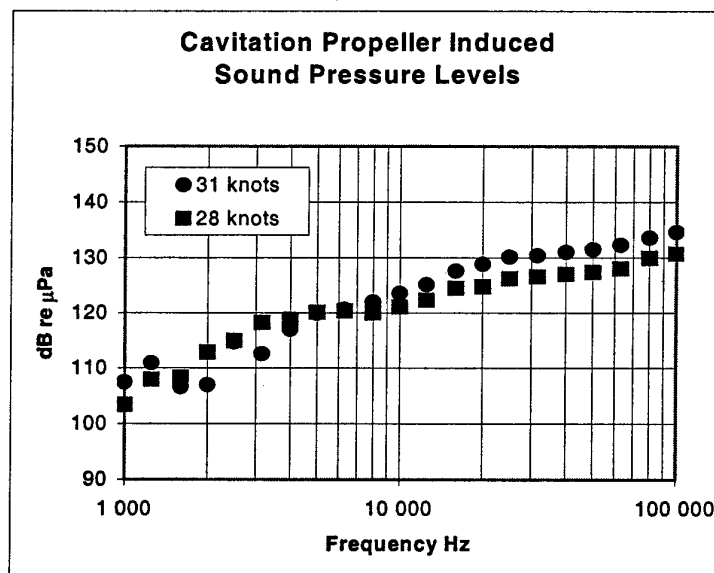


Figure N° 7

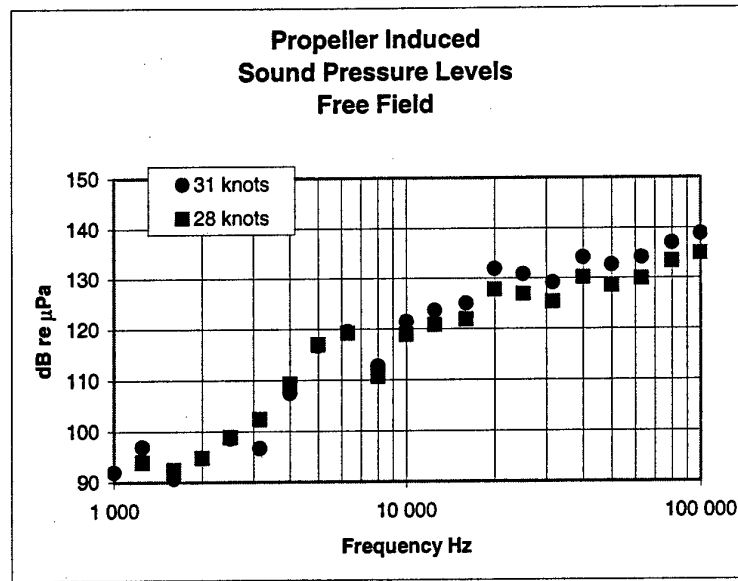


Figure N° 8

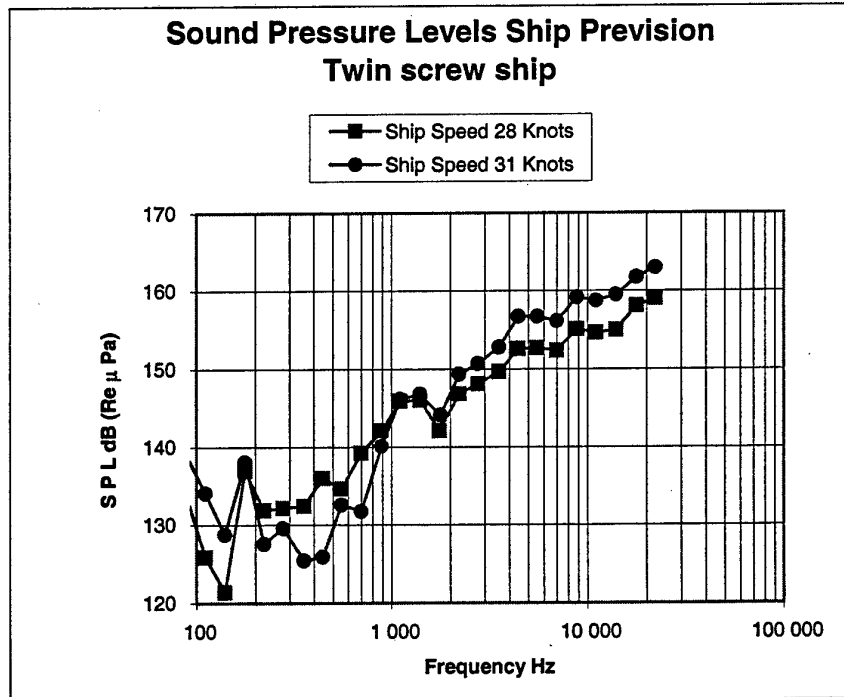


Figure N° 9

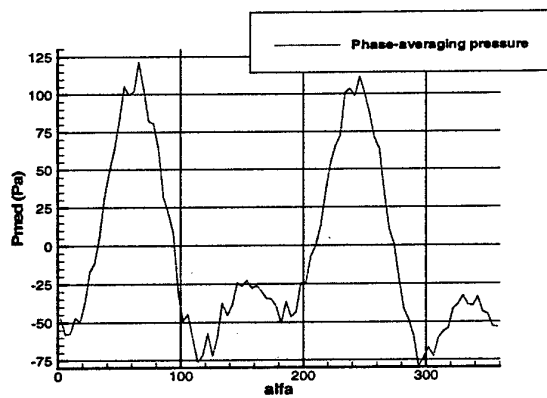


Figure N° 10

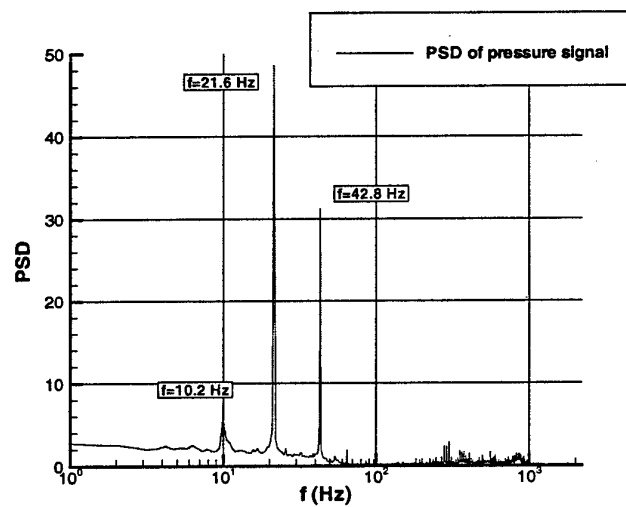


Figure N° 11

Noise Reduction Potential of Swept Propeller Blades

Dipl.-Ing. R. Drobietz, Dr.-Ing. G. Neuwerth
Institut für Luft- und Raumfahrt, RWTH Aachen
Prof. Dr.-Ing. D. Jacob

This project is aimed at the investigation of the noise reduction potential of propellers of General Aviation Aeroplanes due to a sweep of the blades. Both, the noise emission and the propeller thrust characteristics are investigated by experimental and theoretical means.

A code has been developed which computes the aerodynamic properties of propellers using a Prescribed-Wake-Method. The results are used in the implemented aeroacoustic subroutine which is based on the Ffowcs Williams / Hawkings-equation. The combination with an evolution algorithm allows the computational optimisation with respect to thrust and noise taking many different influencing parameters into account.

The experimental investigations were conducted with model propellers of a 1:2 scale of standard General Aviation propellers in the open test section of the subsonic wind tunnel of the Department of Aerospace Engineering. The propeller noise was quantified by measuring the emitted sound power level. The propeller thrust was determined by the application of the momentum theory on a cylindrical control volume including the propeller stream. Four different configurations of swept propellers were investigated and compared with an unswept reference blade.

A blade configuration has been found, which emits less noise at a better figure of merit than the reference blade. This configuration is characterised by a forward swept shape and an increased twist compared to the reference. Furthermore it has been observed, that a blade sweep alone does not lead to a clear reduction of the overall emitted sound power level at equal thrust. However, a forward swept blade shows a clearly reduced noise radiation in upstream direction compared to a straight propeller blade. Therefore, the time the observer is exposed to noise during over flight is shortened with forward swept blades.

Introduction

Due to the growing public complaints on aircraft noise, General Aviation aeroplane noise certification limits have become more strict in 1999 in Germany. The "Landeplatz-Lärmschutz-Verordnung" from January 5th 1999 states that General Aviation aeroplanes have to have noise levels of at least -5 dBA below the noise certification limit to avoid temporal restrictions of their flight operations. Aeroplanes constructed in the year 2000 and later will face intensified restrictions with an increased noise control limit determined at -7 dBA below certification limit. In comparison with the previous increased noise control limit of -4 dBA below certification limit this means a clearly tightened situation for the pilots and a demand on the General Aviation Industry.

The main noise sources of a General Aviation Aeroplane are the propeller and the engine. The presented project deals with the investigation of the propeller noise reduction due to a sweep of the blades.

For an observer in the propeller plane, for example, the periodic sound pressure time signature of a propeller is characterised by a strong peak of negative pressure (figure 1). This peak is generated at a specific angular position when the blade approaches the observer with maximum velocity.

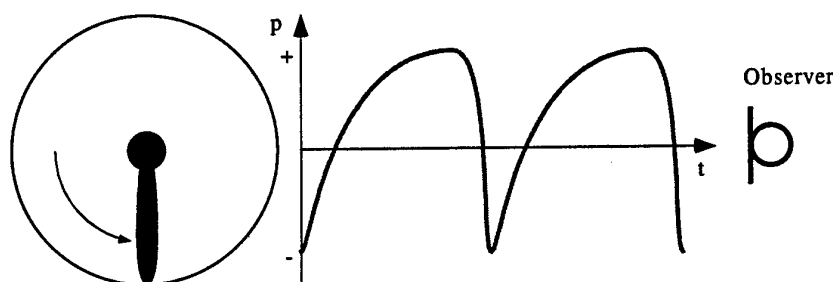


Fig. 1: Qualitative sound time signature at an observer point in the propeller plane

Sound pressure signals of propellers in the time domain can theoretically be divided in many discrete signals, each signal being generated by a different radial blade element. At the point of observation all signals can be summed up to the total noise time history of the blade (figure 2).

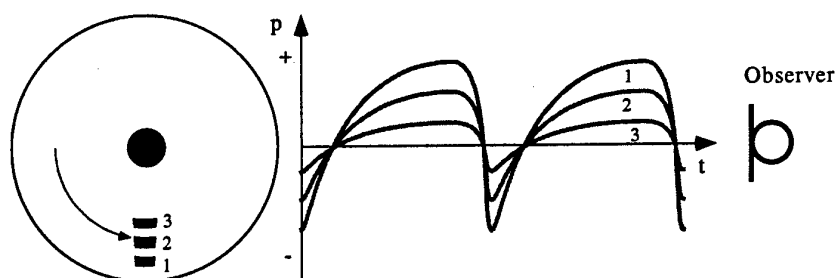


Fig. 2: Sound time signatures of three radial blade elements

For straight propeller blades every radial blade element passes the specific angular position at the same time, resulting in the synchronous generation of the peaks, which are superposed to a peak of high amplitude in the total noise time history at the observer point. Swept propeller blades have the advantage, that there is a time lag between the sound pressure signatures of the different radial blade elements, because the elements do not pass the specific angular position synchronously. This leads to a phase shift when the discrete signals are summarised to the total sound pressure time signal at the observer location (figure 3). The result is a lower amplitude of the negative sound pressure peak.

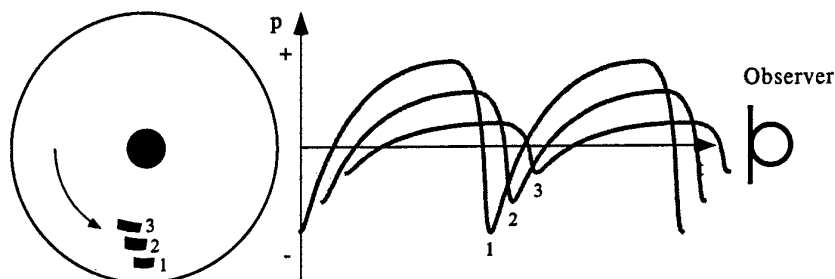


Fig. 3: Phase shift of the sound time signature of three radial blade elements of a swept propeller blade

Besides the noise emission the propeller figure of merit plays an important role in propeller design criteria. Therefore, the theoretical and experimental investigations have to concentrate on both, the noise emission and the figure of merit.

The developed numerical algorithms and the experimental set up are described in the following paragraphs. Finally, theoretical and experimental results are discussed.

Aerodynamic and Aeroacoustic Calculation Methods

An easy method to calculate the aerodynamic performance of a propeller is the combination of blade element and momentum theory [1]. The blade element theory, however, is based on the assumption that the behaviour of one element is not affected by the adjacent elements of the same blade. In spite of these simplifications the theory leads to appropriate results for straight propeller blades. First experimental data, however, have shown clear differences in the flow field of swept and non-swept blades, indicating that the assumptions of simple blade element theory are no longer valid. Therefore, theoretical investigations of the flow field around swept propellers require three dimensional methods.

The three dimensional vortex method developed within this research project replaces the propeller blades by a bound vortex system and a set of trailing vortices forming a helical surface. The bound vortices are located along the quarterchord line of the blade. The blade is divided in a number of radial blade elements. The strength of the bound vortex within each element is constant, while a stepwise jump between adjacent blade elements is assumed. The trailing vortex is carried downstream by the flow, forming a half-infinite filament following a helical path. The strength of the half-infinite helical filaments equals the difference of the adjacent bound vortices. Each helical filament is modelled by a series of straight vortices. The path of the vortex segments follows the local flow direction at its radial station and a prescribed wake contraction. The vortex layer of the outer wake region is concentrated to a single tip vortex (figure 4).

The Biot-Savart-law is then used to calculate the velocities at the blade induced by each bound and trailing vortex segment. These velocities combined with the relative airflow due to forward speed and rotation lead to the total airspeed and the flow direction in the disc plane. This implies an angle of attack at each blade element and hence the radial circulation distribution. This leads to a new estimate of the strength of the bound vortices and a new trailing vortex system. The iteration process can be repeated until a converged flow field is found.

Similar methods are described in Ref. [2, 3, 4, 5].

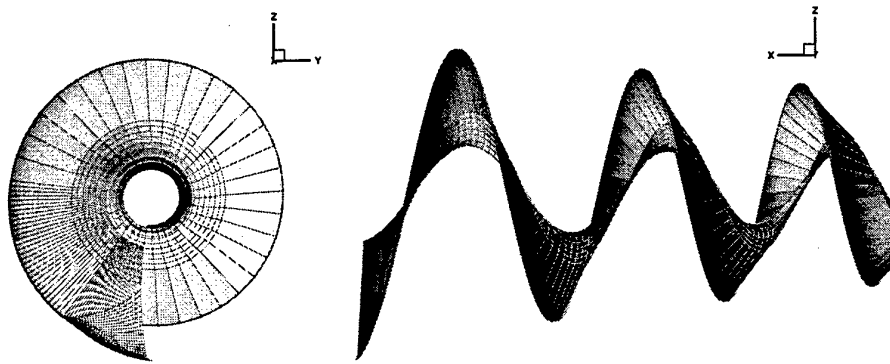


Fig. 4: Surface panels modelling the trailing vortex sheet

On the basis of the induced velocities obtained in the propeller disc the pressure distribution on the blade surface is calculated based on two dimensional airfoil theory [6]. The blade surface is numerically modelled by discrete surface panels (figure 5). The surface pressure and the thickness distribution are needed for the evaluation of sound emission using the Ffowcs Williams / Hawkings-equation [7].

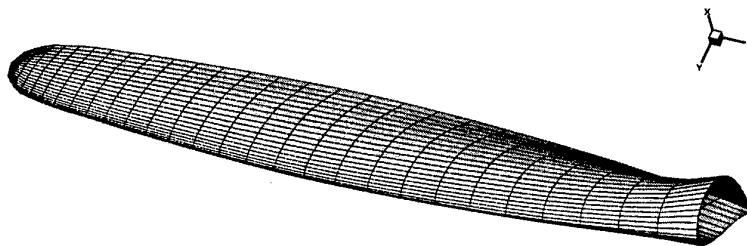


Fig. 5: Surface panels modelling the blade contour

Optimisation Algorithm

The optimisation of the sound emission and the figure of merit of a propeller is a complex problem because of the many influencing and interacting parameters, as for example the number of blades, the rotational velocity, the propeller diameter, the radial distribution of blade thickness, chord length, twist and blade sweep. The number of blades, the rotational velocity and the propeller diameter can be described by one value, but all other characteristics describing the blade geometry are formed by a series of data points. The radial blade thickness, chord length and twist are evaluated by the use of a cubic spline algorithm based on 9 data points. The blade sweep is generated by a Lagrange interpolation polynomial based on 5 data points.

Because all of these parameters have an interacting influence on sound emission and figure of merit a multiparametric optimisation algorithm is required. Therefore, a multimembered evolution algorithm has been chosen as optimisation strategy. Evolution strategies imitate the natural evolution process. They are very robust concerning the convergence behaviour, even for

highly complicated multiparametric systems, and they do not need any information on the inner mathematical connections of the system that has to be optimised.

The strategy is based on the two main principles of natural evolution: mutation and selection. In an initialising step the first parent generation consisting of 15 configurations is generated stochastically. Every configuration is described by a specific number of object parameters defining the blade geometry. The offspring generation consisting of 100 configurations is built up using global recombination and stochastic mutation. The object parameters are varied within defined boundary conditions. After rating the offspring generation the best 15 configurations of the whole population are selected and taken as the next parent generation. The process is repeated until a break criterion is reached. Further information about the evolution algorithm can be found in [8].

Experimental set up

All experiments took place in the subsonic Göttinger-type wind tunnel of the Department of Aerospace Engineering. The wind tunnel features an open test section with a diameter of 1.50 m and a length of 3 m. Therefore, experimental investigations are limited to scaled propellers. In the present study the scale factor was set to 1 : 2, leading to a diameter of 0.915 m for the tested propellers.

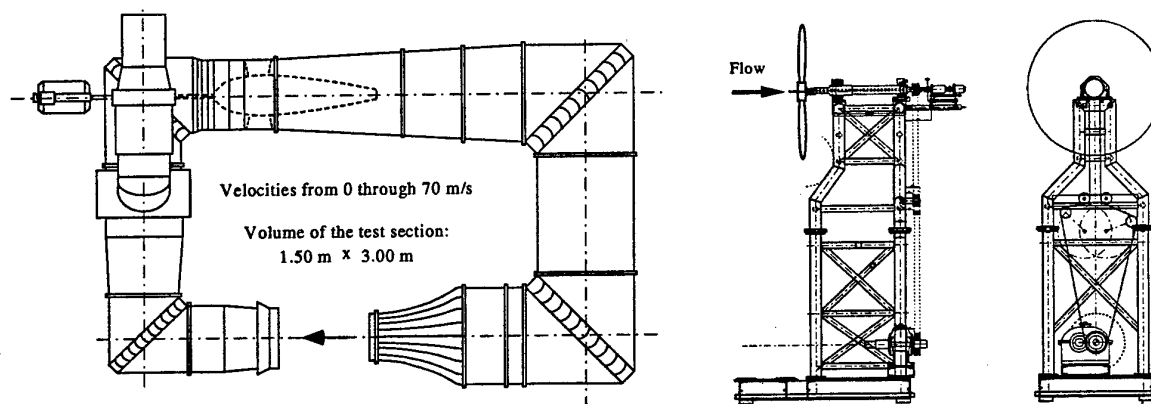


Fig. 6: Wind tunnel and Propeller Test Facility of the Institut für Luft- und Raumfahrt, RWTH Aachen

The model propellers run on a specific propeller test facility which was placed in the centre of the test section (figure 6). The propellers were driven through a belt by an electric motor seated underneath the test facility outside the propeller flow. An aerodynamic nacelle was placed over the shaft and bearings to reduce unwanted drag and turbulence in the wake.

For the assessment of the propeller performance, thrust and power had to be determined. The power was simply calculated using the electrical power consumed by the motor. The thrust was evaluated using momentum theory on a cylindrical control volume including the propeller stream. The sum of internal forces acting on the fluid within the control surface produced a

change in the flux of momentum. The flux of momentum was determined by measuring the velocities along the control volume by the use of a hot wire probe and a pitot tube. For the calculation of the thrust it was assumed that the static pressure along the control surface can be approximated to be equal in front and behind of the propeller as long as the control volume is chosen big enough. Furthermore the velocity direct downstream the propeller disc was measured.

The noise emission of the propeller configurations was determined by measuring the overall sound power level with a rotating microphone in the wind tunnel room, which acted as a reverberation chamber. Additionally, the directivity pattern of sound radiation of the propeller configurations was measured. However, only near field data have been recorded because the microphone had to be positioned inside the flow. This is caused by the fact that sound is deflected at the shear layer around the test section stream tube. Moreover the reflections of the sound at the wind tunnel walls would have led to significant deviations in the sound pressure level spectrum.

Theoretical Design Process

The theoretical investigation included a series of optimisation processes with different preconditions. The primary goal of the optimisation process was the reduction of noise emission. In this case the most appropriate quality criterion is the overall sound power level. But, an optimisation process requires the computation of about 4000 different configurations, in combination with the overall sound power level as quality criteria this would have led to a computation time of about 20 days for one optimisation process. Therefore, the sound pressure level at one observation point was chosen as quality criterion. This led to a computation time of about 24 hours for one optimisation process on a common PC. Tests with observer positions at different radiation angles have not resulted in different optimum configurations, so that finally a position at an azimuthal radiation angle of 110° in the far field was determined. The azimuthal radiation angle is defined to be zero in upstream direction, 90° in the propeller disc and 180° in downstream direction.

For each quality criterion the number and the combination of object parameters was varied. The process was started using the blade sweep as the only object parameter. In a second approach, a parallel variation of blade sweep and twist was investigated. The boundary conditions of the object parameters were always set such that the optimisation process results in a reasonable blade shape.

Forward sweep was determined in theoretical investigations as the optimum configuration concerning the noise reduction for uniform inflow. Increasing sweep leads to additional noise reduction. However, the maximum sweep is limited by structural aspects. Furthermore, a combination of varied blade sweep and twist was investigated.

In a second optimisation the configuration with the best figure of merit was sought. In a third optimisation a combination of a low noise emission and a good figure of merit was chosen as quality criterion. It will be discussed in detail that forward sweep leads to a reduction of the figure of merit.

Figure 7 shows the reference blade and 4 swept configurations which were numerically developed and then tested in the wind tunnel.

All propellers, reference and swept configurations, are three-bladed-propellers. Diameter, radial thickness and chord are identical for all configurations. Configurations 1, 3 and 4 have also the same twist distribution as the reference blade, so that only the sweep is different. Configuration 2 features sweep and increased twist. Configurations 2 and 3 have the same sweep. While configurations 1 through 3 are swept forward, configuration 4 is swept backward. The sweep of configuration 4 is equal to the sweep of the configurations 2 and 3, mirrored at the blade centre line.

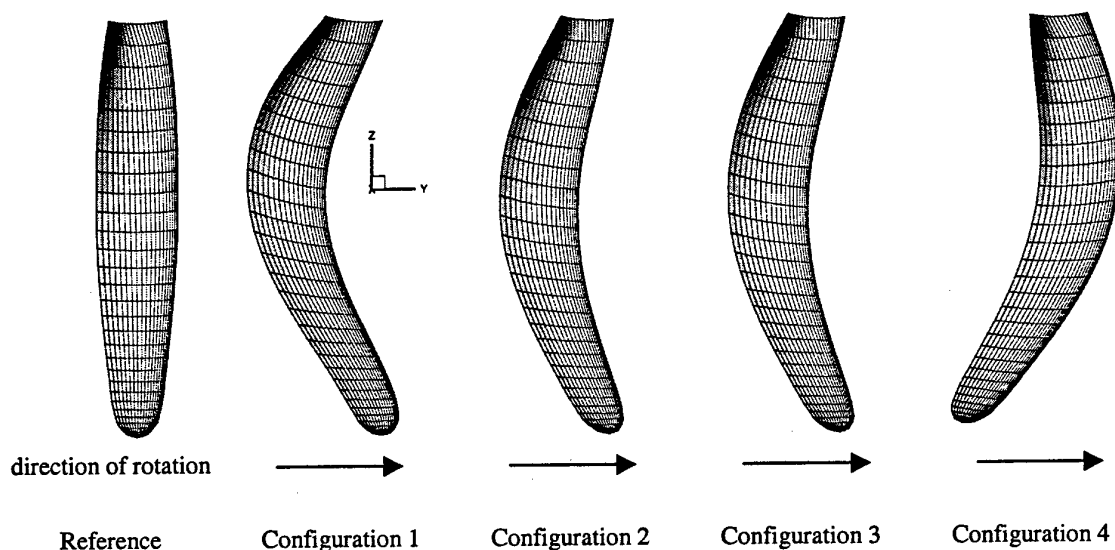


Fig. 7: Comparison of the reference and the swept configurations

The comparison of the calculated sound pressure level versus the azimuthal radiation angle of the reference blade and the swept configurations 1 through 4 is shown in figure 8.

First of all, it is obvious that there is a remarkable difference in sound radiation when the radiation in upstream direction at azimuth angles from 0 through 90° is compared to the radiation in downstream direction at azimuth angles from 90 through 180° . In contrast to the downstream directed radiation there is a big influence of the sweep of the blades on the sound radiation to the front. It can be seen that the forward swept blades are clearly quieter than the reference blade. At an azimuthal radiation angle of 60° , for example, the sound pressure level of configuration 1 falls more than 10 dBA below the level of the reference blade. Unfortunately the influence of the blade sweep decreases with increasing radiation angle. In the direction of maximum emitted sound at the radiation angle of 110° the difference in sound pressure level is less than 1 dBA. Therefore, the difference in the overall sound power level is only 1.3 dBA for configuration 1.

Secondly, the backward sweep of configuration 4 has a negative influence on the noise emission over the whole angle area.

Finally, configuration 2 shows the lowest noise emission. The overall sound power level is 1.9 dBA lower than the reference level. This result can be explained by the increased twist of configuration 2. An increased twist leads to higher blade loadings in the inner blade regions and

decreased surface pressures in the tip region. This reduces the sound sources in the area of maximum rotational velocity.

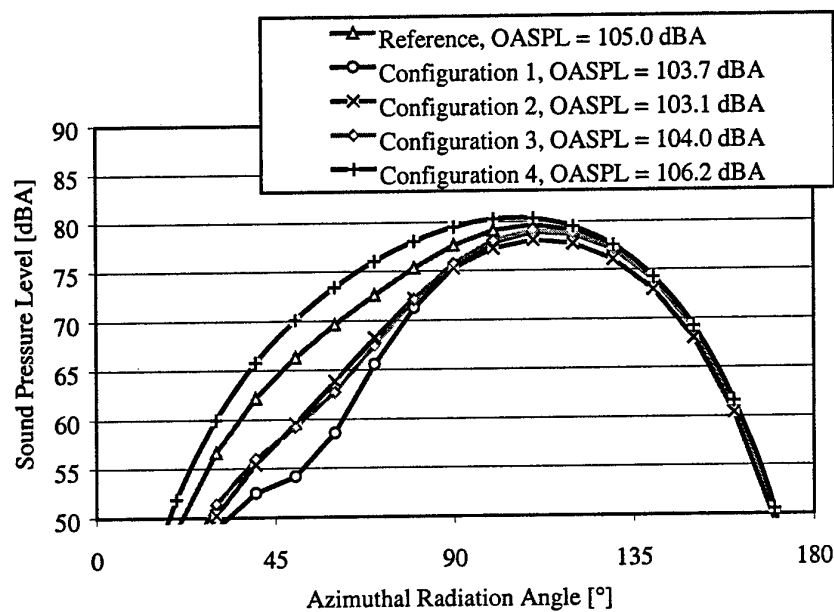


Fig. 8: Calculated far field sound pressure level vs. azimuthal radiation angle; comparison of the reference and the 4 swept configurations at equal thrust

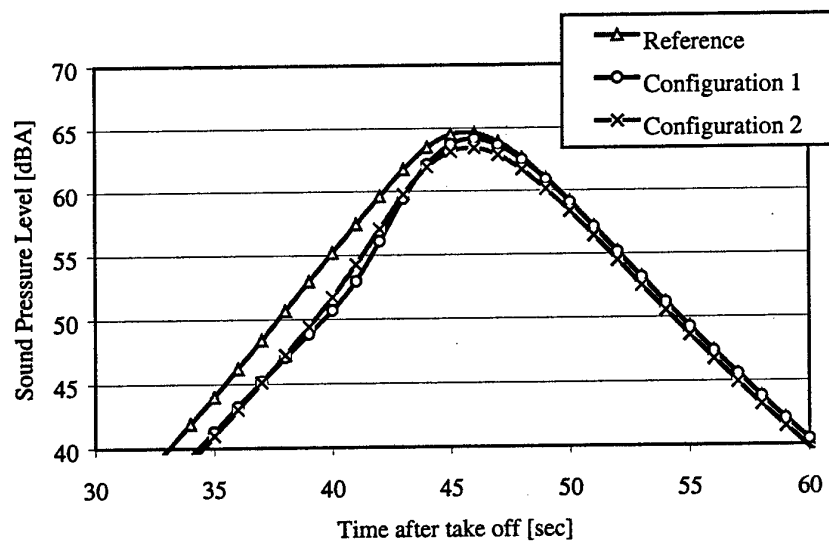


Fig. 9: Calculated sound pressure level during over flight; original three-blade-propeller at 2450 rpm, motor power 150 kW

Figure 9 shows the calculated sound pressure level during the flight over an observer located on the ground. The recorded noise increases when the aeroplane approaches the observer and reaches a maximum approximately at shortest distance between noise source and observer. For the approaching aeroplane the sound pressure level is reduced by about 4 dBA for forward swept blades and time of noise affection on an observer during over flight is shortened.

In figure 10 the figures of merit of the reference blade and the swept configurations are compared. Obviously, the figure of merit of the forward swept configurations is worse than that of the reference configuration, while it is better for the backward swept configuration 4. The differences of about 1 through 3% arise from the fact that the forward sweep also shifts the trailing vortices of the blade tip region to the front. This results in a reduced distance between the blade and the trailing vortices, and therefore the induced axial velocities at the blade are increased. Increased axial velocities at equal pitch cause a loss of lift at increasing drag and therefore the figure of merit declines. The opposite effect is obtained for blades with backward sweep. This is also confirmed in figure 11, where the radial distributions of the axial velocity in the propeller disc are compared for all configurations at an equal thrust of 400 N.

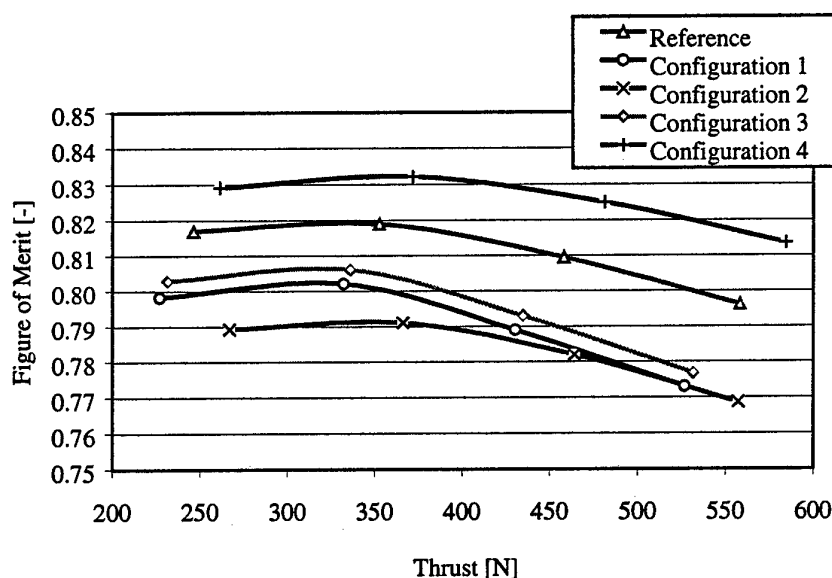


Fig. 10: Calculated figure of merit vs. thrust; comparison of the reference and the 4 swept configurations

Configuration 2 achieves a worse figure of merit than configuration 3. Figure 11 shows the higher loading of the inner blade region of configuration 2 because of the increased twist. The changed loading can be derived from the increased induced velocities in the inner blade region and decreased induced velocities in the blade tip region compared to the other configurations.

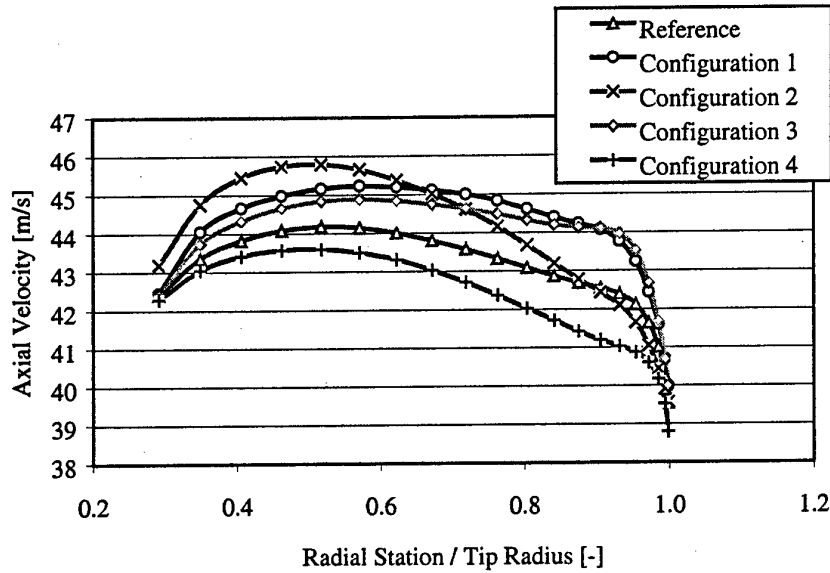


Fig. 11: Calculated axial velocity in the propeller disc vs. radial station; comparison of the reference and the 4 swept configurations at equal thrust of 400 N

Validation of Theoretical Predictions by Experimental Results

The calculated overall sound power levels were validated by measured data. In figure 12, for example, the good agreement of a measured and a calculated overall sound power level spectrum is shown.

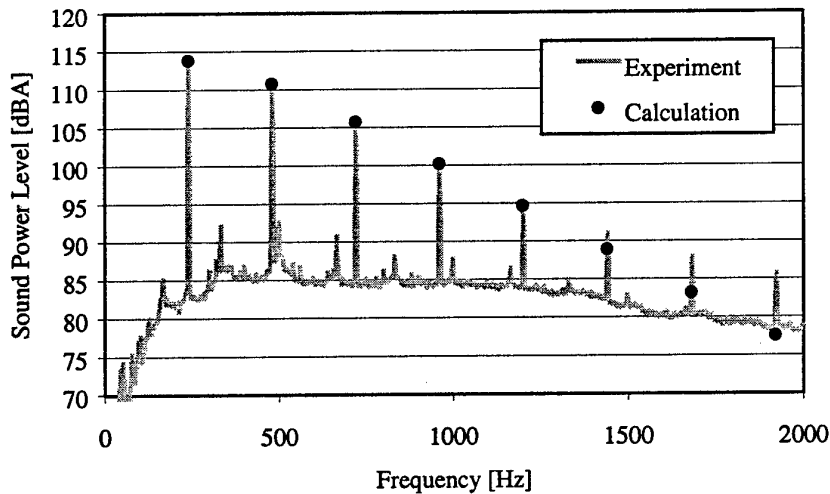


Fig. 12: Overall sound power level spectrum, reference blade at 4800 rpm; comparison of experiment and calculation at equal thrust

Figure 13 shows the measured radial distribution of the axial velocity 70 mm downstream the propeller disc for all configurations. It should be mentioned here that a large velocity gradient exists between a position in the nominal propeller disc and a position 70 mm downstream the propeller disc. Therefore, a direct comparison of the calculated and measured radial distributions of axial velocities in the propeller disc (figures 11 and 13) is not possible. However, a qualitative analysis leads to following conclusions:

At first, the comparison of the configurations 3 and 4 with the reference configuration confirms the theoretical prediction that a forward sweep leads to higher induced velocities and a backward sweep leads to lower induced velocities, especially in the inner blade region.

Secondly, the centre point of the thrust generating area of configuration 2 is shifted inboard caused by the increased twist.

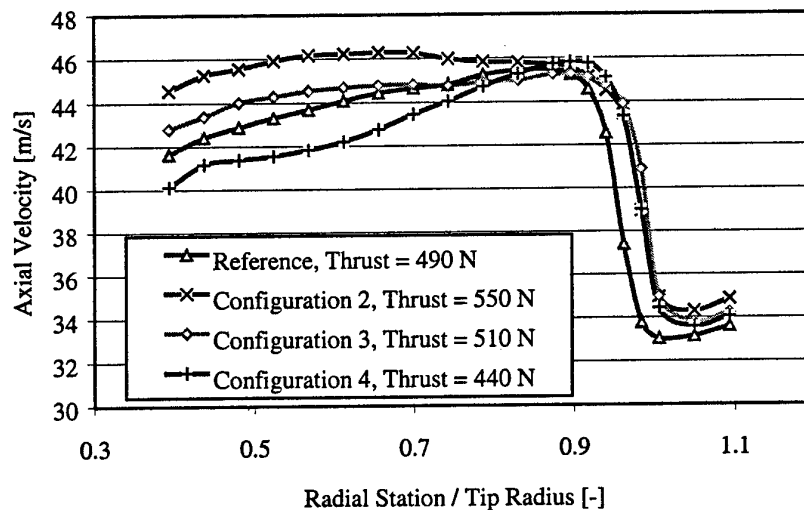


Fig. 13: Measured axial velocity 70 mm behind the propeller disc vs. radial station; comparison of all configurations at 4200 rpm

Experimental Results

As the aim of the experimental tests was to get similar flow conditions as in original flight cases, the wind tunnel velocity was set to 38 m/s. Considering the scale factor of 1 : 2 of the model propellers, the rpm should have been twice of that of the original propeller, assuming commonly settings this would have been 4800 rpm. Unfortunately this propeller frequency led to serious vibrations of the test facility, so that for the most of the tests the number of revolutions was set to 4200 rpm. Configuration 1 is missing in the analysis of the experimental results because it was destroyed by vibrations that arose during a test at 4800 rpm.

Figure 14 shows the measured overall sound power level versus the thrust at 4200 rpm. As predicted by the theoretical investigations configuration 2 shows a decreased overall sound power level of 1 to 1.5 dBA in comparison with the reference configurations. Configuration 3,

however, shows only a small deviation from the reference. It must be noted here that the advantage of less sound radiation of a swept blade is combined with a loss of thrust. To compensate this loss of thrust the pitch and therefore also the motor power have to be increased. Because the additional motor power leads to an increase of noise emission again, the initial advantage of the forward sweep becomes negligible. Configuration 4 shows better acoustic attributes for light disc loading than for heavy disc loading.

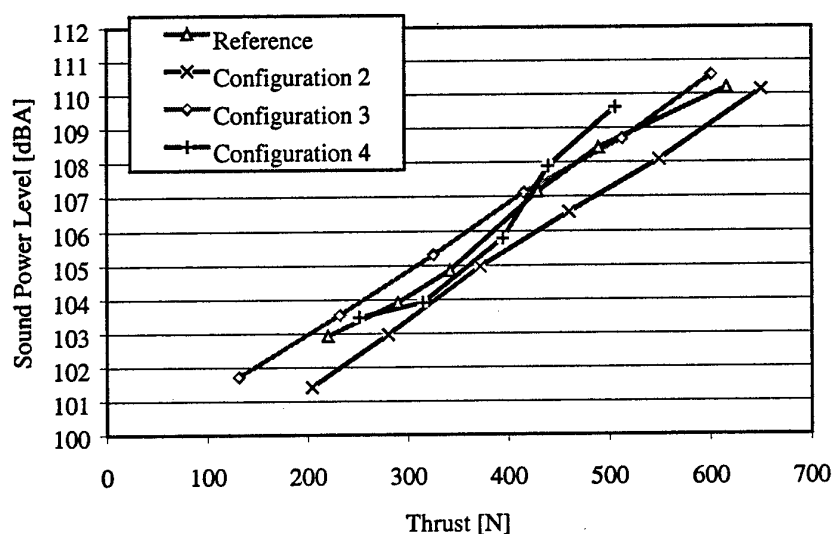


Fig. 14: Measured overall sound power level vs. thrust at 4200 rpm; comparison of the reference blade and swept configurations

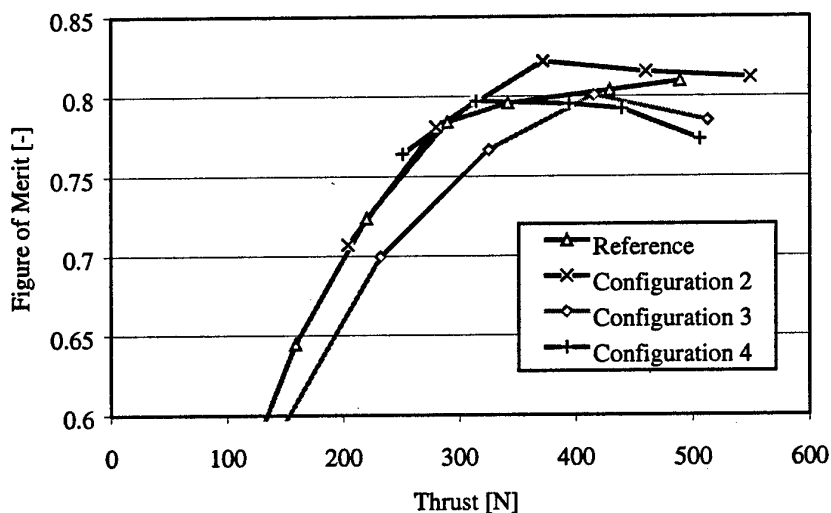


Fig. 15: Measured figure of merit vs. thrust at 4200 rpm; comparison of the reference blade and swept configurations

Figure 15 shows the measured figure of merit versus the thrust. The most interesting result is that configuration 2 operates at a better efficiency than the reference configuration. Therefore, a configuration has been found, which emits less noise at a better figure of merit. Configuration 3 shows a worse figure of merit than the reference for all blade loadings. This confirms theoretical predictions. Configuration 4 operates at a better figure of merit than the reference at light blade loadings. Obviously, the backward swept configuration shows unwanted attributes for heavily loaded blades. This cannot be explained in detail at the moment.

Conclusions

Four swept propeller configurations have been numerically designed and tested in the wind tunnel. The following conclusions can be drawn from the previously described results:

At first, a blade shape has been found, which emits less noise at a better figure of merit than the reference blade. This blade shape is characterised by a forward swept contour and an increased twist compared to the reference. The reduction of the maximum emitted sound pressure level is about 2 dBA.

As a second point, a blade sweep alone does not lead to a clear advantage in comparison with the straight reference concerning the overall emitted sound power level, because the reduction of noise emission is combined by a parallel loss of thrust.

Finally, a forward sweep of the blade leads to a changed directivity pattern of noise emission. Especially the noise radiation in upstream direction is reduced.

Acknowledgement

The presented research project is embedded in the "Luftfahrtforschungsprogramm" of the Federal Government of Germany.

References

- 1 H. Glauert: "Airplane Propellers", in "Aerodynamic Theory", edited by W. Durand, Div. L, Vol. 4, Julius Springer, Berlin, 1935
- 2 S. P. Fiddes, K. Brown, P. C. Bunniss: "Optimum Propellers Revisited – Beyond Blade Element Theory", ICAS-94-6.1.1, pp. 172-182
- 3 J. L. Hess, W.O. Valarezo: "Calculation of Steady Flow About Propellers Using a Surface Panel Method", Journal of Propulsion and Power, Vol. 1, No. 6, pp. 470-476
- 4 E. Quin, G. Yang, F. Li: "Numerical Analysis of the Interference Effect of Propeller Slipstream on Aircraft Flowfield", Journal of Aircraft, Vol. 35, No. 1, Jan.-Feb. 1998
- 5 C. N. Adkins, R. H. Liebeck: "Design of Optimum Propellers", Journal of Propulsion and Power, Vol. 10, No. 5, Sept.-Okt. 1994
- 6 H. Schlichting, E. Truckenbrodt: „Aerodynamik des Flugzeuges“, Springer Berlin, 1960
- 7 J. E. Ffowcs Williams, D. L. Hawkings: „Sound Generation by Turbulence and Surfaces in Arbitrary Motion“, Phil. Trans. Roy. Soc. (London), Ser. A, 264, 321-342, 1969
- 8 V. Engler, D. Coors, D. Jacob: "Optimization of a Space Transportation System Including Design Sensitivities", Journal of Spacecrafts and Rockets, Vol. 35, No. 6, pp 785-791

Tilt Rotor Aeroacoustic Model Project

Jeffrey L. Johnson
Aerospace Engineer
Aerospace Computing, Inc.
Los Altos, CA

Larry A. Young
Aerospace Engineer
NASA Ames Research Center
Moffett Field, CA

Summary

A new tiltrotor aeroacoustic research facility, the Tilt Rotor Aeroacoustic Model (TRAM), is being developed by NASA and the U. S. Army. The TRAM Project will enable new insights into the fundamental aeroacoustics of proprotors and tiltrotor aircraft, leading to improved acoustic prediction methodologies and noise reduction techniques. An overview of NASA's goals in understanding and reducing the technology barriers for civil tiltrotor aircraft is provided as well as a description of how TRAM will support these goals. TRAM is capable of being configured as an isolated rotor or as a complete full-span dual rotor aircraft model. The TRAM test stands and their modular, compatible sub-systems are described in detail. Sample results from an isolated rotor test recently completed at the Duits-Nederlandse Windtunnel are presented. The current status of the full-span model development is described.

Nomenclature

C_T	Rotor thrust coefficient
M_{tip}	Hover tip Mach number
α_s	Rotor shaft angle, deg
θ	Rotor collective, deg
μ	Rotor advance ratio
ψ	Rotor azimuth angle, deg

Introduction

The purpose of this paper is to describe a new tiltrotor aeroacoustic research facility: the Tilt Rotor Aeroacoustic Model (TRAM). The paper will provide a detailed description of the two TRAM test stand configurations and their sub-systems, provide a sample of recently acquired isolated rotor results, and describe the current state of the full-span model development and its future research potential.

The U. S. Government has long held an interest in developing high-speed rotorcraft for both military and civilian applications and has studied numerous concepts since the 1950's. Starting with the first successful in-flight conversion by the XV-3 in 1958 and followed by the very successful XV-15 flight research vehicle (1970's) and the V-22 Osprey development (late 80's and 90's), the tiltrotor concept has clearly established itself as a viable high-speed rotorcraft design. Figure 1 shows these three aircraft in flight.

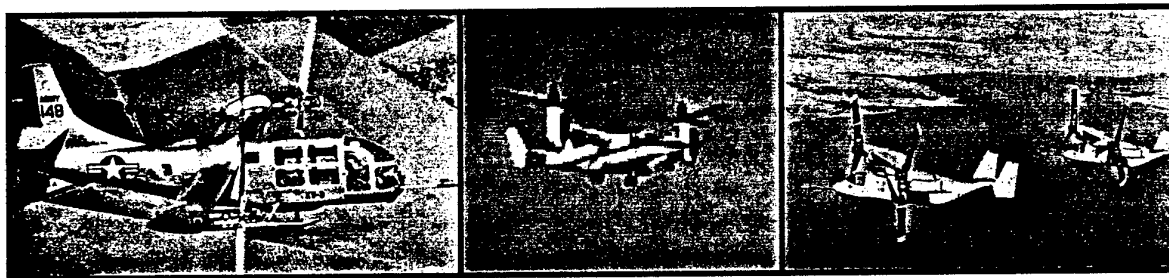


Figure 1. The XV-3, XV-15 and V-22 Osprey tiltrotor aircraft

Over the past two decades, as V-22 Osprey development progressed, many have become convinced that tiltrotor aircraft have civil transport applications. The Civil Tiltrotor Development Advisory Committee (CTRDAC), Ref. 1, studied the technical feasibility and financial viability of developing a civil tiltrotor aircraft. In their report to Congress, the Committee concluded that the civil tiltrotor concept is technically feasible, a market exists and the civil tiltrotor has the potential of relieving congestion at major airports. In addition, the report describes some of the barriers to be overcome for successful implementation of a civil tiltrotor. These include development of infrastructure, understanding safety and community acceptance requirements, integration into the air traffic control system and economics. NASA, through the Advanced Subsonic Transport and the Aviation Systems Capacity programs, initiated the Short Haul (Civil Tiltrotor) [SH(CT)] program to address the concern about tiltrotor noise, as well as operating efficiency and safety, for civil applications.

The SH(CT) program quickly recognized that reducing noise would be fundamental to passenger and community acceptance of the civil tiltrotor. Therefore, studying tiltrotor aeroacoustics in order to understand tiltrotor noise mechanisms and developing advanced low-noise rotors has been a high priority within the SH(CT) program.

As described in Ref. 2, the SH(CT) program outlines three areas for tiltrotor noise reduction: noise abatement, noise reduction through innovative proprotor designs (including active rotor control strategies), and improved noise prediction methodologies. Reference 2 also provides an overview of tiltrotor research conducted in these three areas through 1996.

Need for Tiltrotor Aeroacoustic Wind Tunnel Testing

For over 50 years the helicopter has evolved into a highly successful vehicle fulfilling a variety of useful VTOL missions in both civil and military air transport. Throughout this period, much effort has been spent studying helicopter noise mechanisms in order to devise techniques for reducing noise generated by this class of rotorcraft. Despite many years of investigation and numerous successes, rotorcraft aeroacoustic research continues to be a challenging field. Tiltrotors, in addition to being more complex aerodynamically (and hence, aeroacoustically), have had relatively less acoustic research effort than conventional helicopters. Although tiltrotor and helicopter rotors have common noise sources (such as blade-vortex interaction noise, high-speed impulsive noise and broadband noise), the aerodynamics of a tiltrotor blade can be vastly different than a conventional helicopter blade.

Compared to a helicopter blade, tiltrotor blades have thicker airfoils with higher built-in twist and operate at higher tip speeds with higher loading. These differences result in very different blade load distributions. Hence, existing analytical and empirical models developed for helicopter rotors do not necessarily apply to tiltrotors. In particular, the wake geometry models for helicopters are inadequate for tiltrotor wake systems. In descent conditions, tiltrotor blades can undergo negative tip loading over a substantial region of the rotor disk compared with conventional helicopter blades. The negative tip loading causes dual vortices, of opposite sign, to be shed from a single blade. The dual vortices greatly complicate the wake geometry and present a challenge to the analyst trying to model the wake. In addition, the dual-rotor arrangement over the wing results in aerodynamic interaction between the rotor and wing/fuselage. This interaction is evident during hover where the downwash from the rotors creates a download on the wing and a vertical inboard upwash and subsequent reingestion of a portion of the rotor wake into the disk. This phenomenon is known as the 'fountain effect.' Finally, tiltrotors operate in a wide range of conditions compared with helicopters because the rotor position relative to the fuselage can vary over 90 deg - from hover to propeller mode.

For all of the above reasons, less is understood about the aeroacoustics of tiltrotors than helicopters. Improved understanding of tiltrotor aeroacoustics requires primarily two key types of experimental data: blade airloads and rotor wake measurements. This data will be essential to validating acoustic prediction codes.

NASA is currently developing a new generation of aeroacoustic and aeromechanics prediction tools, some of which are uniquely tailored for tiltrotors. In order to validate this new predictive capability it is important to acquire a fundamental database of tiltrotor acoustics and aerodynamics. Further, because of unique configuration of the rotors in relation to the wing and fuselage, it is important to not only measure isolated rotor characteristics, but full-span dual-rotor airframe representative data as well.

TRAM Program Overview

The TRAM program was initiated to provide the data necessary to confirm performance and aeroacoustic prediction methodologies and to investigate advanced low-noise tiltrotor technologies. To accomplish these noise reduction goals, wind tunnel testing of moderate- to large-scale tiltrotor models is required.

Primary TRAM program goals are:

- Use the V-22 aircraft as the baseline for development of a high fidelity, small-scale aeroacoustic model. Fundamental to this design is a pressure-instrumented rotor having kinematic and dynamic similarity to the V-22 aircraft.
- Develop a hardware-compatible isolated rotor and full-span (dual-rotor, complete airframe representation) test stand to study important interactional aeroacoustic phenomena. The two TRAM configurations are not independent test stands, but share common modular sub-assemblies.
- Incorporate into the test stands (and associated auxiliary test equipment) a comprehensive suite of high-precision, high-bandwidth instrumentation to adequately characterize tiltrotor aerodynamics and acoustics. This includes the acquisition of unsteady rotor airloads, wing static airloads, acoustics, rotor and airframe performance data, rotor wake vortex trajectory and vortex velocity measurements.

The TRAM baseline rotors and airframe are based on a 1/4-scale V-22 Osprey tiltrotor aircraft. Selection of the V-22 as a baseline was dictated by two primary considerations. First, the gross weight of the V-22 is close to the proposed 40-passenger civil tiltrotor studied by the CTRDAC and others. Therefore, the civil tiltrotor propotor performance characteristics will be similar to those of the V-22. Second, as the first production tiltrotor aircraft, many V-22's will be flying and providing valuable operational data in the years ahead. This will create opportunities for comparisons between wind tunnel test results and full-scale flight vehicle data.

The 1/4-scale model size was selected with consideration of the test section size of the two facilities where TRAM would primarily be tested. For isolated rotor testing, the TRAM was intended to be tested in the open-jet test section of the Duits-Nederlandse Windtunnel and, for the full-span dual rotor model, the 40- by 80-Foot Test Section of the National Full-Scale Aerodynamic Complex (NFAC). The next section describes the TRAM model.

Tilt Rotor Aeroacoustic Model Description

TRAM is configured as either an isolated rotor model or a full-span dual rotor aircraft model. Figures 2 and 3 show the isolated rotor and full-span TRAM configurations respectively.

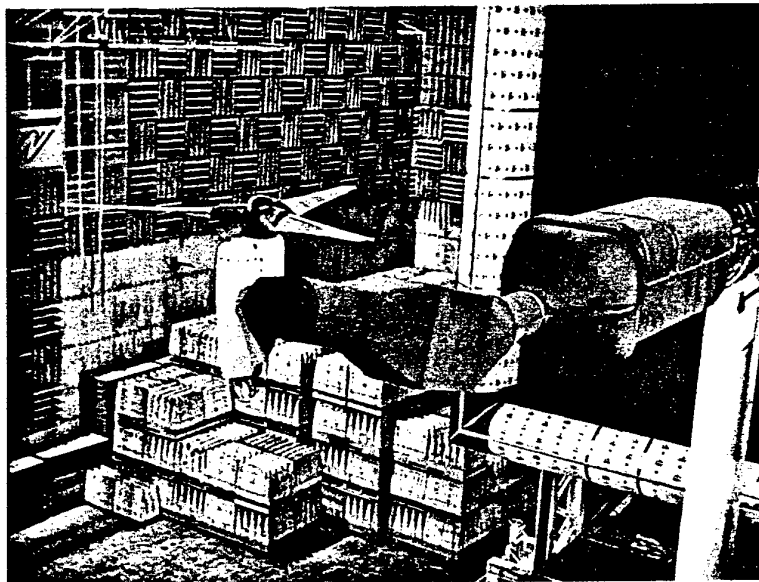


Figure 2. Isolated rotor TRAM configuration

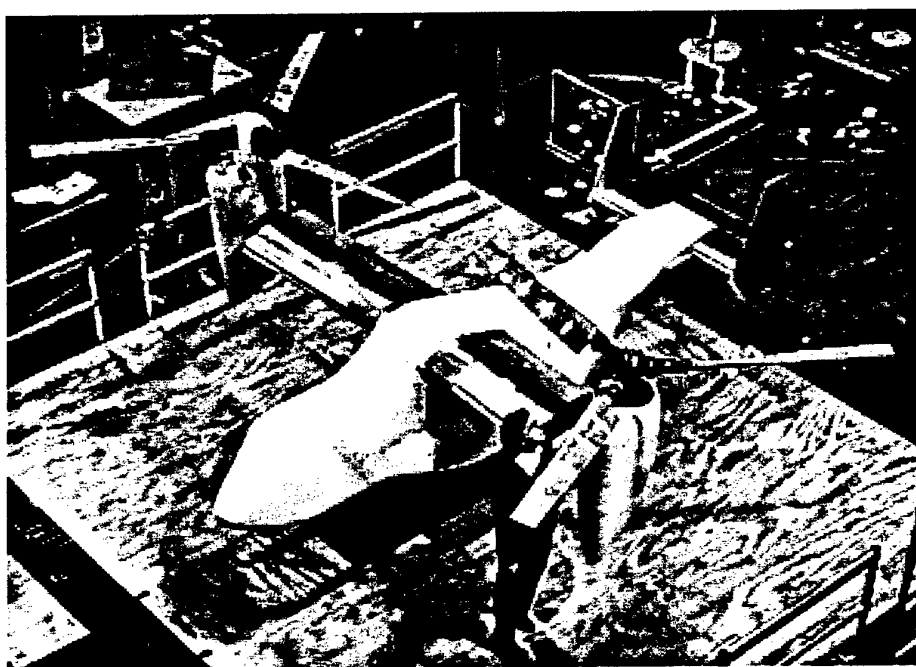


Figure 3. Full-span TRAM configuration

The TRAM can be configured as an isolated rotor or dual-rotor full-span aircraft model. This makes it uniquely suited for identifying and studying tiltrotor aerodynamics and acoustics in a rigorous experimental manner. The drive train, nacelle assembly, hub and rotor components from the isolated rotor model are also used to make up the right-hand rotor and nacelle assembly on the full-span model. Each rotor is powered by an electric motor designed to deliver up to 300 hp at 1588 rpm.

The right hand rotor has a set of pressure-instrumented blades and a set of strain-gauged blades, the left-hand rotor blades have only strain gauge instrumentation. The TRAM blades and hub

retention system are fabricated with composite materials and are structurally tailored to match fundamental frequencies of the full-scale aircraft. The hub and control system is kinematically similar to the full-scale aircraft. Both left-hand and right-hand rotor forces and moments are measured with strain-gauged balances located in each pylon assembly. The overall aerodynamic loads on the full-span model are measured with a strain-gauged balance located in the fuselage.

One of the TRAM characteristics that provides tremendous research capability for developing a tiltrotor aeroacoustics database, together with its data acquisition and recording system, is its ability to simultaneously acquire blade pressure and microphone data at extremely high rates. TRAM acquires 150 blade pressure measurements and up to 20 microphone measurements at 2048 samples per rotor revolution. Since the TRAM rotor spins at 26.5 revs per second, the data acquisition rate is more than 54,000 samples per second per channel. A state-of-the-art signal conditioning and data acquisition system was specifically designed to accommodate TRAM data rate requirements.

A detailed description of both the isolated rotor model and full-span model and their systems is provided in the Appendix.

TRAM Isolated Rotor Testing

In order to gain a further understanding of tiltrotor aeroacoustics, NASA and the U. S. Army conducted the TRAM isolated rotor test program in the Duits-Nederlandse Windtunnel (DNW). This isolated rotor test was the first comprehensive aeroacoustic test for a tiltrotor in forward flight. Rotor noise, rotor performance, rotor airloads, wake geometry and wake velocities were measured. An overview of TRAM DNW isolated rotor testing is provided in Ref. 3. A description of the DNW and its rotary-wing test capability is found in Ref. 4. A short summary of this test program is provided below.

The TRAM isolated prop rotor was tested in the 8-by-6 meter open-jet test section of the DNW (Fig. 4). Two tunnel entries were conducted with the TRAM isolated rotor test stand and the 1/4-scale V-22 rotor. The first tunnel entry, in December 1997, focused on test stand risk-reduction and envelope expansion. The second entry in April-May 1998 was devoted to acquiring a high quality isolated rotor aeroacoustic database.

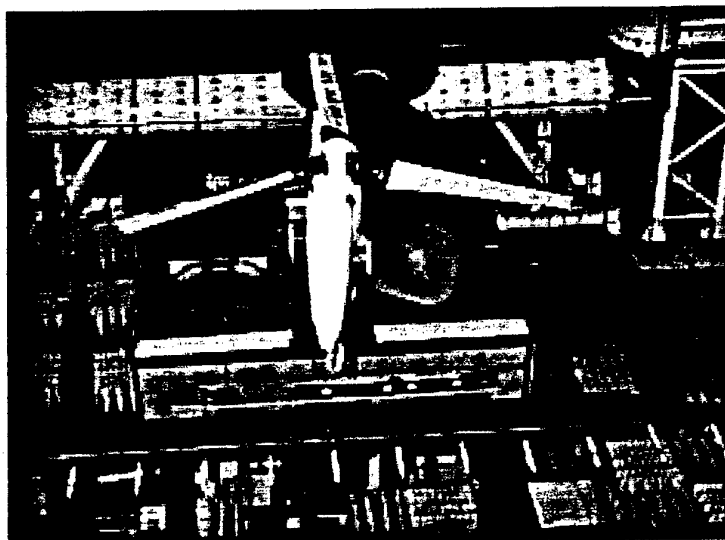


Figure 4. TRAM isolated rotor configuration and the DNW acoustic traverse

The TRAM DNW test focused primarily on low-speed helicopter-mode test conditions. Test objectives were, in order of importance:

- Perform detailed acoustic survey of blade vortex interaction (BVI) phenomena in helicopter-mode descent including rotor noise trends as a function of advance ratio, rotor shaft angle, tip Mach number and thrust coefficient.
- Acquire broadband noise data in hover and low-speed helicopter-mode flight
- Acquire performance, airloads, wake vortex and trailed tip vortex velocity measurements for helicopter-mode flight.
- Obtain proprotor airplane-mode performance and airloads measurements up to the maximum DNW open test-section tunnel speed, $\mu = 0.375$ at $M_{tip} = 0.59$.

Because of time and load limit constraints, transition flight ($-15 < \alpha_s < -75$ deg) measurements were not made. Data were acquired to meet all other test objectives.

The 1/4-scale V-22 proprotor was tested at a reduced tip speed of 0.63 hover tip Mach number because of operational considerations (the nominal design tip speed of the V-22 Osprey aircraft is $M_{tip} = 0.71$). All airplane-mode proprotor data were acquired at 0.59 hover tip Mach number (equivalent to the V-22 aircraft in airplane mode).

Among the most important information acquired during the TRAM DNW isolated rotor test was the high-fidelity acoustic data from the 1/4-scale V-22 rotor. The acoustic data were acquired using a combination of in-flow traversing and out-of-flow fixed microphones. Thirteen microphones were equally spaced on a traversing microphone wing (also shown in Fig. 4). In addition, two microphones were placed outside the test section flow, one above the model and another located adjacent to the hub on the advancing side of the rotor.

Acoustic data were acquired for a range of advance ratios ($\mu=0.125, 0.15, 0.175, 0.2$), rotor shaft angles ($\alpha_s = -14$ to $+12$ deg) and thrust sweeps ($C_T=0.009$ to 0.014). A detailed discussion of the 1/4-scale V-22 TRAM acoustic results can be found in Ref. 5.

Figure 5 is a representative contour plot of BVI acoustic data acquired with the acoustic survey in helicopter-mode operation. The contours represent 2 dB differences in BVISPL (Blade Vortex Interaction Sound Pressure Level), a noise metric defined as the acoustic energy between the 7th and the 50th blade harmonics. Prominent in Fig. 5 is the BVI 'hot spot' (marked with an 'X') on the advancing-side of the rotor.

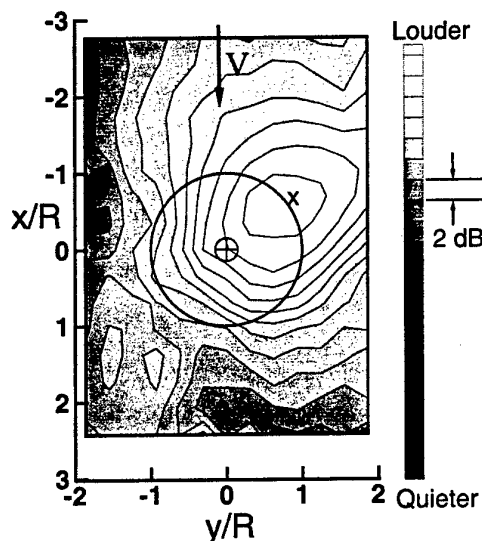


Figure 5. Acoustic survey of proprotor in helicopter-mode (BVI descent condition)

One example of the BVISPL acoustic trend with increasing advance ratio, for constant α_s and C_T , is presented in Fig. 6. As expected, the maximum noise levels increase with increasing advance ratio.

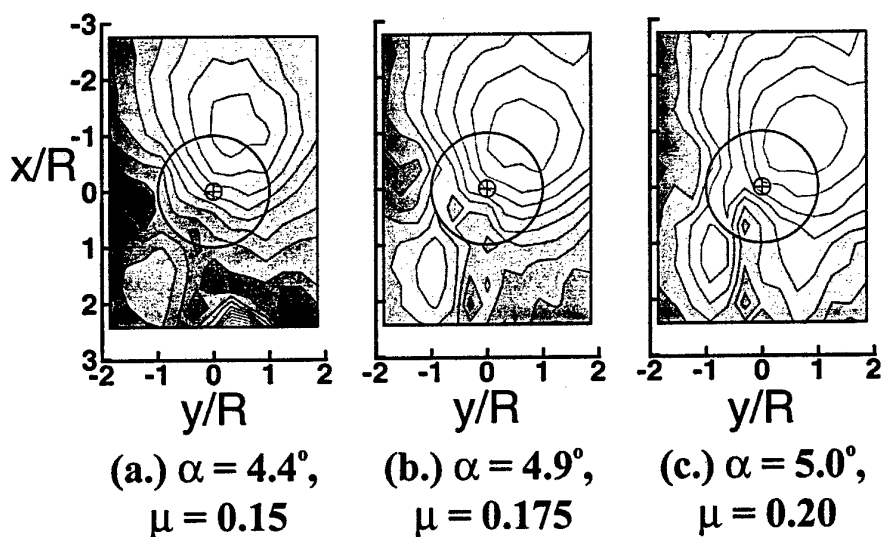


Figure 6. BVISPL directivity trend with increasing rotor advance ratio

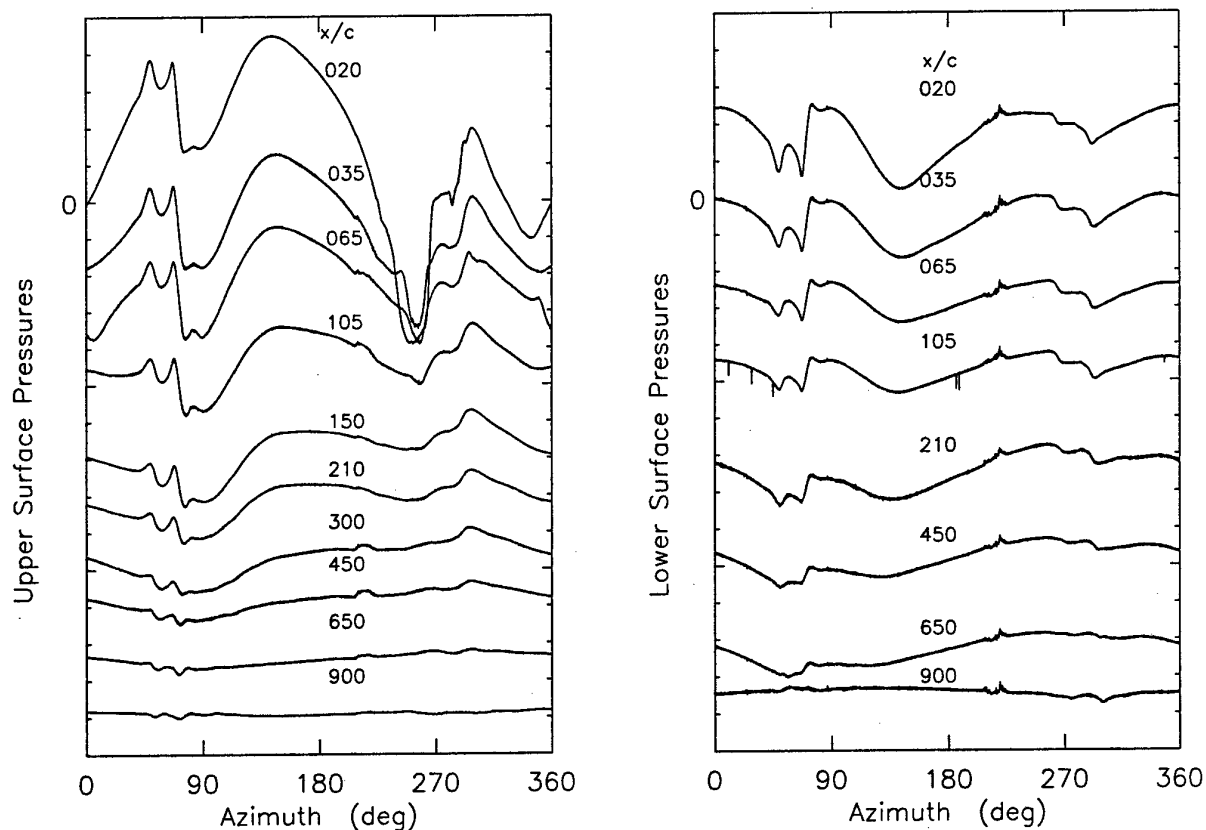


Figure 7. Sample TRAM DNW blade pressure data at $r/R = 0.93$

Figure 7 represents a very limited sample of the over seventy-five gigabytes of high-fidelity airloads data acquired during the test. A detailed description of the blade pressure data and

analysis of these results will be presented in Ref. 6. The airloads data, which will provide new insights into tiltrotor noise mechanisms, will be an important validation data set for a new generation of aeroacoustic prediction tools and will hopefully inspire new noise reduction strategies for tiltrotor aircraft.

Laser light sheet (LLS) flow visualization and 3-D vortex trajectory measurements were made for the 1/4-scale V-22 rotor. Two-dimensional vortex velocity measurements, using the particle image velocimetry (PIV) technique, were also acquired. Figure 9 is a representative laser light sheet flow visualization image. The rotor blade position is $\psi=45$ degrees, at $\mu=0.15$ and the visible vortices are on the advancing-side of the rotor.



Figure 8. Laser Light Sheet Flow Visualization of Trailed Tip Vortices

Acquisition of a series of laser-light sheet pictures enabled the determination of the three-dimensional vortex filament trajectories on the advancing-side of the rotor. Both clockwise (negative circulation) and counterclockwise vortices (positive circulation) were observed in the laser-light sheet pictures. The rotation directions of the observed advancing-side vortices can be seen in Fig. 8.

Reference 7 presents additional flow measurements findings from the DNW test with respect to the LLS images, the vortex trajectories, and PIV results. One important observation made during the DNW test was the confirmation of paired (one positive, one negative) vortices present on the advancing side of the proprotor in BVI descent conditions.

The TRAM DNW isolated rotor tests were successful in obtaining comprehensive acoustic and airloads data for the 1/4-scale V-22 rotor. The DNW data will enable substantial improvements in the predictive capability for tiltrotor aircraft.

The Future: Full-Span TRAM Testing

After the completion of the TRAM isolated rotor tests, the model was returned to NASA Ames Research Center for refurbishment and integration into the full-span TRAM. The development

of full-span TRAM is well underway and plans are for completion of dual-rotor operational checkout by the end of this year. When model development is completed, the full-span TRAM will support the goals of understanding the interactional aeroacoustics of tiltrotor aircraft and demonstration of potential noise reduction technologies.

Due to three-dimensional unsteadiness observed in the 'fountain flow' it is believed that some tiltrotor acoustic sources can only be studied with a full-span dual rotor model (Ref. 8). Studying the noise generating mechanisms and directivity characteristics of these three-dimensional phenomena will be possible with full-span TRAM.

The 1/4-scale V-22 pressure instrumented rotor will be tested on the full-span TRAM in the NASA Ames 40- by 80-Foot Wind Tunnel in late 1999. Figure 9 shows the full-span TRAM model being assembled. The test section of the 40- by 80-Foot Wind Tunnel has recently been modified with a new acoustic liner which is designed to have a minimum of 90% acoustic energy absorption from 80 Hz to 20 kHz (Ref. 9).

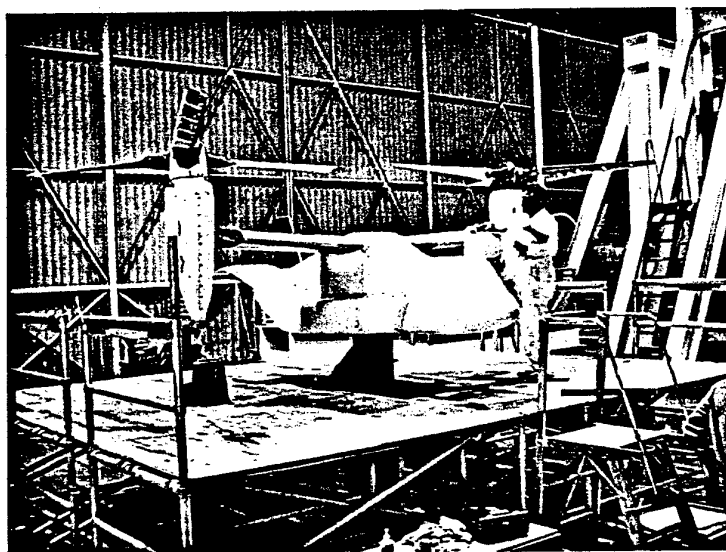


Figure 9. Full-span TRAM assembly and functional testing

Two microphone survey arrays will be placed under the model on both sides of the full-span TRAM to assess asymmetric effects and to study rotor-on-rotor -- as well wing-on-rotor -- aeroacoustic influences. Flow conditions tested during the isolated rotor test will be matched to the full-span model testing for correlation and comparison purposes. Figure 10 shows a comparison between the survey area for the DNW isolated rotor tests and the planned full-span TRAM V-22 rotor test planned for the 40- by 80-Foot Wind Tunnel.

The majority of the test matrix for the full-span TRAM will include helicopter-mode and transition testing conditions at full tip speed ($M_{tip} = 0.71$) for a range of shaft angles and forward speeds. Airplane mode data will also be collected. As with the isolated rotor test, acoustic data, airloads, and flow measurements (both LLS and PIV) will be acquired. Plans are also underway to include the acquisition of wing and fuselage pressure measurements.

Full-span TRAM testing will provide the ability to make comparisons between isolated rotor and dual-rotor with airframe in order to assess interactional aerodynamic and aeroacoustic effects.

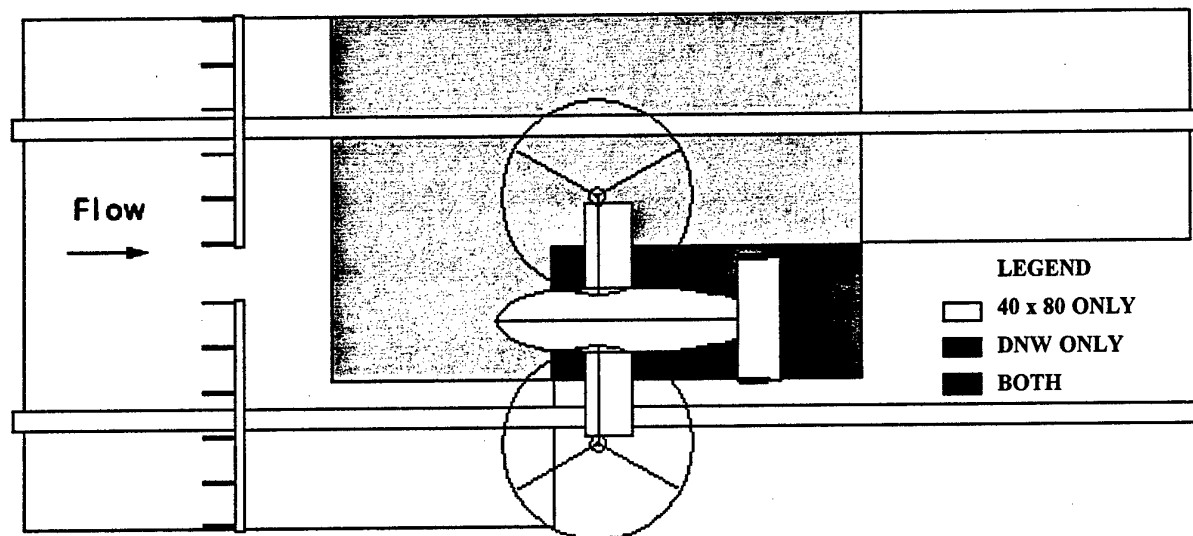


Figure 10. Comparison of acoustic survey area for the isolated rotor vs. full-span TRAM tests

Conclusion

NASA and the U.S. Army have made a major infrastructure investment in tiltrotor test technology through the continuing development of the TRAM. This investment has begun to pay-off through acquisition of fundamental aeroacoustic and aeromechanics data from a 1/4-scale V-22 isolated rotor tested in the DNW on the TRAM isolated rotor configuration. The isolated TRAM rotor data will provide much needed insight into the tiltrotor aeroacoustic problem and enable substantial improvements in the predictive capability for tiltrotor aircraft.

Test preparation is currently underway to assess the key interactional aerodynamics and acoustic effects with the TRAM full-span model. The TRAM will provide a wind tunnel demonstrator platform for future tiltrotor noise reduction technologies. Additional in-depth tiltrotor experimental investigations with the full-span (dual-rotor and complete airframe) TRAM configuration are planned in the near future.

Acknowledgments

The work reported in this paper was performed under the auspices of the Tilt Rotor Aeroacoustic Model (TRAM) Project and the NASA Short Haul Civil Tiltrotor program [SH(CT)]. The TRAM and SH(CT) programs are managed at NASA Ames Research Center by the Army/NASA Rotorcraft Division and Advanced Tiltrotor Technology Project Office,

respectively. Other major funding partners and research participants in the experimental research effort were the U.S. Army Aeroflightdynamics Directorate (AFDD) located at Ames, NASA Langley Research Center Fluid Mechanics and Acoustics Division and The Boeing Company (Mesa, Arizona). In addition, the outstanding support provided by the Duits-Nederlandse Windtunnel staff during the execution of the wind tunnel test was critical to the success of the test.

The authors wish to thank Dr. Gloria Yamauchi for contributions to this paper. The authors also wish to acknowledge the dedication and hard work by all members of the TRAM Development and TRAM DNW test teams.

The TRAM DNW test team also extend their thanks to the staff of the Dutch Nationaal Lucht-en Ruimtevaartlaboratorium (NLR), and U.S. Army European Research Office (ERO) for their technical and programmatic contributions to the TRAM development and the DNW wind tunnel access, respectively.

References

1. F. E. Kruesi (Chair), Civil Tiltrotor Development Advisory Committee Report to Congress, Volume I and II (in accordance with PL102-581), December 1995.
2. Marcolini, M.A., Burley, C.L., Conner, D.A., and Acree, Jr., C.W., "Overview of Noise Reduction Technology in the NASA Short Haul (Civil Tiltrotor) Program," SAE Technical Paper #962273, SAE International Powered Lift Conference, Jupiter, Florida, November 18-20, 1996.
3. Young, L. A., Booth, E. R., Yamauchi, G. K., Botha, G., Dawson, S., "Overview of the Testing of a Small-Scale Proprotor" 55th Annual Forum of the American Helicopter Society, Montreal, Canada, May 25-27, 1999.
4. Van Ditshuizen, J.C.A., "Helicopter Model Noise Testing at DNW -- Status and Prospects," Thirteenth European Rotorcraft Forum, Arles, France, September 1987.
5. Booth, E. R., McCluer, M., Tadghighi, H., "Acoustic Characteristics of an Isolated Tiltrotor Model in the DNW," 55th Annual Forum of the American Helicopter Society, Montreal, Canada, May 25-27, 1999.
6. Swanson, S. M., McCluer, M. S., Yamauchi, G. K., Swanson, A. A., "Airloads Measurements from a 1/4-Scale V-22 Tiltrotor Wind Tunnel Test," Submitted for presentation at the Twenty-Fifth European Rotorcraft Forum, Rome, Italy, September 14-16, 1999.
7. Yamauchi, G. K., Burley, C. L., Mercker, E., Pengel, K., JanikiRam, R., "Flow Measurements of an Isolated Model Tilt Rotor," 55th Annual Forum of the American Helicopter Society, Montreal, Canada, May 25-27, 1999.

8. George, A. R.; Smith, C. A.; Maisel, M. D., Breiger, J. T., "Tilt Rotor Aircraft Aeroacoustics," Presented at the 45th Annual Forum of the American Helicopter Society, Boston, MA, May 22-24, 1989.
9. Soderman, P. T., "Design of a Deep Acoustic Lining for the 40- by 80-Foot Wind Tunnel Test Section," 5th AIAA/CEAS Aeroacoustics Conference, Seattle, WA, May 10-12, 1999.
10. Versteeg, M. H. J. B., Slot, H., "Miniature Rotating Amplifier System for Wind Tunnel Application Packs 256 Pre-conditioning Channels in 187 Cubic Inch," Presented at the 17th International Congress on Instrumentation in Aerospace Simulation Facilities (ICIASF), Naval Postgraduate School, Monterey, California, September 29-October 2, 1997.

Appendix – Descriptions of the Isolated Rotor and Full-Span TRAM

TRAM can be configured as an isolated rotor model or as a full-span, dual rotor aircraft model. The rotors and airframe are based on a 1/4-scale of the V-22 Osprey tiltrotor aircraft. The following sections describe the isolated rotor model, the full-span dual rotor model, and components and systems common to both configurations. These common components include the blades, hub, transmissions and drive shaft components, rotor balance and rotating amplifier system.

Isolated Rotor Configuration

The TRAM isolated rotor test stand is comprised of two major elements: the rotor and nacelle assembly and the motor mount assembly. The rotor and nacelle assembly is attached to the acoustically treated isolated rotor test stand at a mechanical pivot or 'conversion axis' (Fig. 2). This conversion axis allows the nacelle to be manually rotated in 5-degree increments from airplane to helicopter mode.

The isolated rotor test stand drive train arrangement is shown schematically in Fig. A1.

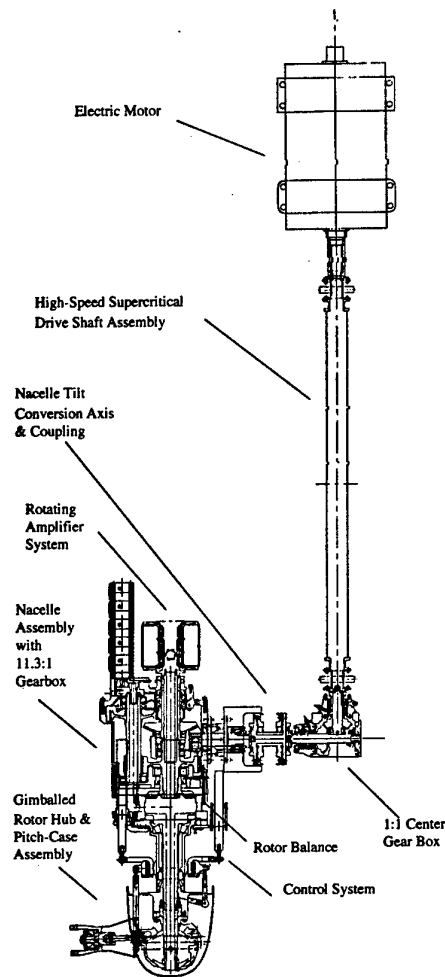


Figure A1. Schematic of the TRAM isolated rotor configuration and key sub-systems

An electric motor provides power to the rotor via a super-critical driveshaft and two gearboxes. The nacelle assembly contains a reduction gearbox that reduces speed by 11.34:1. The case of the nacelle gearbox is designed to carry the structural loads of the rotor through the conversion axis to the model support. Rotor shaft angle changes are accomplished during testing by pitching the entire test stand using the wind tunnel sting pitch mechanism. During the isolated rotor test, the DNW sting automatically maintained the hub on tunnel centerline as the model was pitched. The motor mount and model support assembly is acoustically treated with foam panels. The nacelle assembly is not acoustically treated but is geometrically scaled to the V-22 aircraft.

Full-Span TRAM Description

The full-span TRAM basic model consists of a steel and aluminum frame with fiberglass skins, a steel wing and an aluminum empennage, and dual rotors. The wing was not designed to be aeroelastically scaled with respect to the V-22 aircraft. The model structure is designed for testing up to 300 knots (maximum speed of NFAC). The full-span TRAM is equipped with remotely adjustable flaperons and one elevator. The rudders are ground-adjustable but are nominally zero degrees for most wind tunnel testing. The wind tunnel mounting strut and the

tunnel turntable provide angle-of-attack and yaw control. Nacelle tilt settings on the full-span TRAM are accomplished manually, as on the isolated rotor configuration. The left-hand wing and flaperons are currently being modified to include chordwise distributions of static pressure taps at five wing span locations. Figure A2 shows the major components of the full-span model.

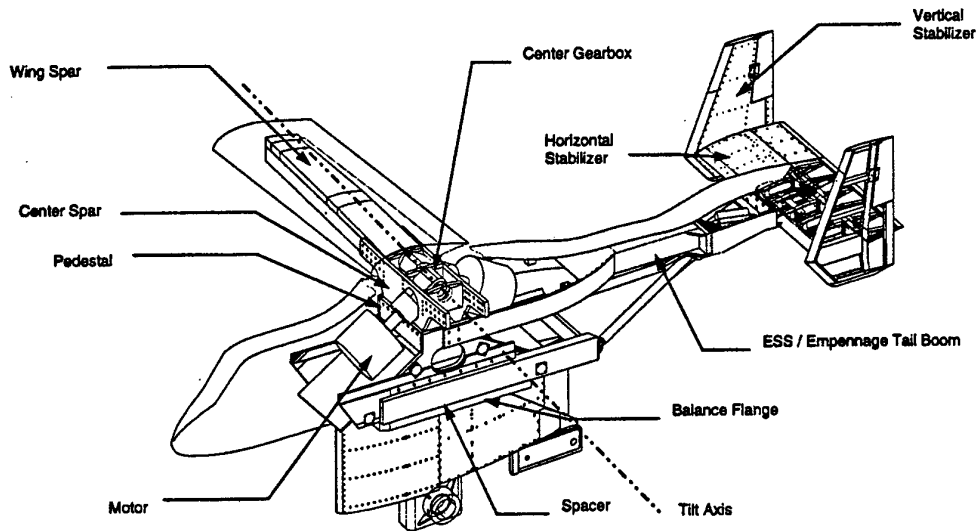


Figure A2. Full-span TRAM components

One of the unique features of the full-span TRAM (as compared to the isolated rotor configuration) is a fuselage balance that measures the total model aerodynamic loads. This fuselage balance is a six-component strain-gauged balance located in the fuselage. The fuselage balance maximum design loads are provided in Table A1.

Table A1. TRAM fuselage balance design limits

	Design Limit
Thrust Force	+4000, -8500 lbs.
Side Force	± 1500 lbs.
Drag Force	+2000, -6000 lbs.
Pitch Moment	+100,000, -150,000 in-lbs.
Roll Moment	$\pm 35,000$ in-lbs.
Yaw Moment	$\pm 40,000$ in-lbs.

Two tandem mounted high-speed electric motors are housed in the fuselage and a series of gearboxes and drive shafts transmit power through the wing into transmissions in the nacelles. The motors and drive train are designed to deliver up to 300 HP to each rotor. Similar to the isolated rotor configuration, each nacelle contains a gearbox to reduce the speed and transmit power to the rotor hub. The purpose of the TRAM drive train is to transmit power from the two electric motors in the fuselage, through the wing, to the nacelle mounted rotors. All of the components from the motors to the input of the nacelle transmission are designed to operate at

18,000 rpm. The center-mounted gearboxes are 1:1 right angle transmissions that turn the drive train into the wings. These two gearboxes are connected together so the two rotors are mechanically linked for safety, similar in purpose to the cross-shaft in the wing of the full-scale aircraft. The drive shafts in the wing are designed to operate above their first fundamental frequency of approximately 6600-rpm. A flail damper system is incorporated at the shaft mid span for safety in case the shaft deflection goes divergent during transition through the critical speed. The supercritical drive shafts are supported on each end by dual-diaphragm couplings. These couplings are designed to permit angular deflections up to four degrees at 18,000 rpm. The angular deflection is required to accommodate the wing dihedral and nacelle cant angles, the combination of which result in an approximately 3.5 degree coupling deflection. The nacelle transmission has three stages of gear reduction which combine to reduce the 18,000-rpm input to 1588-rpm output (11.34:1).

The two electric motors are solid-state controlled permanent magnet motors providing each rotor with 300 HP at 1588 rpm. Although this level exceeds 1/4 scale V-22 power requirements, extra capacity was designed into TRAM for future testing. These power requirements, combined with the relatively small space available in the 1/4 scale model, dictated that the motor and a large portion of the drive train operate at 18,000 rpm. This speed is necessary to transmit the required power, with adequate safety margins, through the 1/4 scale wing to the rotors. A transmission in the nacelle is then required to reduce speed to 1588 rpm at the rotor. This rotor speed for the TRAM matches the full-scale aircraft tip speed of 0.71 ft/s. The TRAM electric motors are based on a unique permanent magnet design in combination with advanced high-speed PWM (pulse width modulated) switching technology for motor control. This approach allows for high power capability in a package small enough to fit inside the TRAM fuselage. Figure A3 shows one of the electric motors.

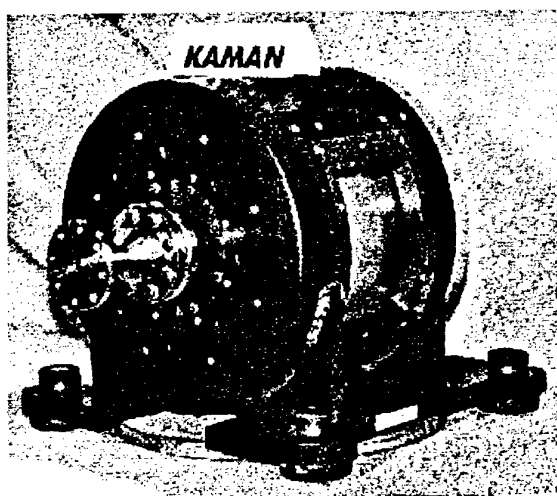


Figure A3. TRAM electric motor (one of two required to power full-span TRAM)

Over 700 data, health monitoring and 'Safety-of-Flight' (SOF) instrumentation channels are incorporated into this model. Health and SOF monitoring systems, utility and fixed-wing control console workstations were developed to support efficient and safe wind tunnel testing.

The right-hand rotor hub and control system, blades, rotor balance, rotating amplifier system and slinging are the same components used in the isolated rotor model and will be described in the following sections. The corresponding left-hand components (except for the rotating amplifier system and slinging) are mirror images of the right-hand components.

Components Common to the Isolated Rotor Configuration and the Full-Span TRAM

Rotor Hub and Control System

The TRAM baseline gimbaled rotor hub incorporates a constant velocity joint (spherical bearing and elastomeric torque links) and is dynamically and kinematically similar to the V-22 aircraft. The rotor control system is comprised of three electromechanical actuators, a rise-and-fall swashplate, and rotating and nonrotating scissors allowing full proprotor collective and cyclic control. A remotely mounted rotor control console allows pilot inputs to be made from the wind tunnel control room. The two rotors can be controlled independently or linked-together. Figure A4 shows a schematic of the TRAM hub.

Rotor Blades

The composite-material rotor blades have both strain-gauge and pressure transducer instrumentation. The rotor diameter is 9.5 feet (2.9 m). All blades, whether strain-gauged or pressure-instrumented, have the same mass distribution properties and can be readily interchanged per rotor. The blades have high fidelity scaling with respect to the V-22 rotor for blade/airfoil contours. Additionally, the first elastic modes (flapwise, chordwise, and torsional) of blades were dynamically scaled to V-22 aircraft frequencies.

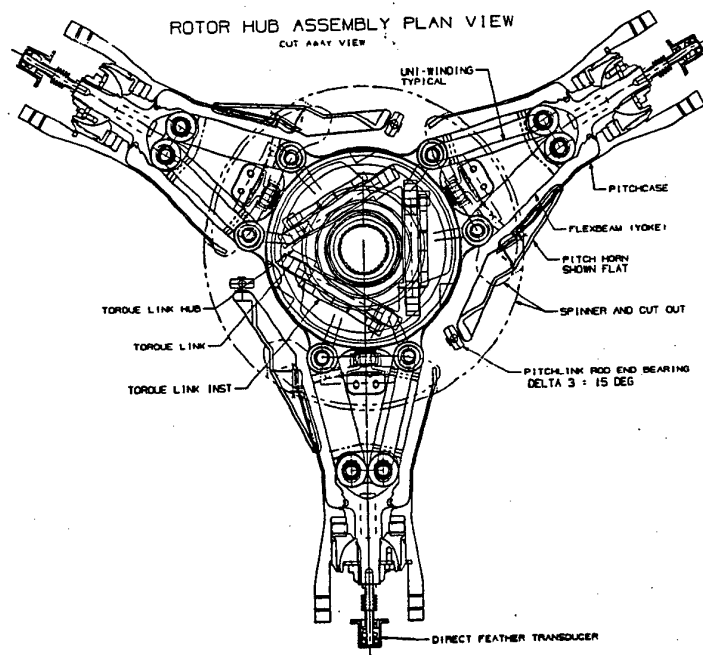


Figure A4. TRAM hub schematic

Two blades of the right-hand rotor blade inventory are pressure-instrumented. Three right-hand strained gauged blades were fabricated so that researchers have a choice of two right-hand rotor

sets: 1) a pressure-instrumented set consisting of two pressure-instrumented blades and one strain-gauged blade, or 2) a set made up of three strain-gauged blades. The left-hand blade inventory consists of only strain-gauged blades (three plus one spare). Each strain-gauged blade was fabricated with 14 strain gauge (full-bending) bridges installed: five flapwise bending-moment, five chordwise bending-moment and four torsion.

Rotor pressure-instrumentation consists of 150 dynamic transducers distributed over two rotor blades on the right-hand rotor only. The transducers are flush-mounted with a pressure range of 25 psi absolute. Three transducer model types were installed: pipette, B-screen, and flatpack. All transducer types have the same electrical specifications with a vendor-quoted, flat-response characteristic of less than 0.5 dB out to 60 kHz. Figure A5 shows the distribution of the transducers over the two blades.

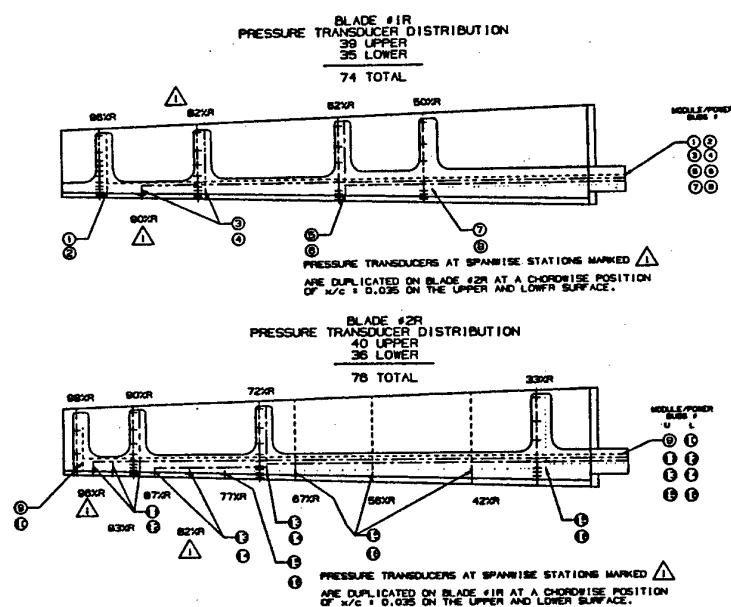


Figure A5. Pressure-instrumented blade transducer locations

Rotor Balance

The full-span TRAM incorporates two identical six-component strain-gauged balances, one in each nacelle. The TRAM isolated rotor configuration uses one of the two rotor balances. The balance design is comprised of four strain-gauged posts instrumented with primary and backup sets of gauges, which allow the measurement of the rotor aerodynamic forces and moments. A flexible coupling provides transmission of torque to the rotor hub through a load path independent of the rotor balance. Therefore, this coupling is instrumented to measure torque and any residual thrust carried by the drive system. Data reduction software corrects the rotor balance thrust measurement for this residual thrust component.

The rotor balances incorporate a fail-safe retention design. In the event a balance flexure breaks the rotor is captured. A heater system is integrated into each rotor balance. Heater coils on metric and non-metric sides are close-loop controlled to maintain constant balance temperature during a data acquisition run in the tunnel. Each flexure has eight thermocouples installed to record the rotor balance distributed temperature characteristics during a run. The rotor balances are mounted in the model with ceramic insulators on both the metric and non-metric sides to stabilize the heat transfer throughout the balance. The base of the rotor balance is mounted to the nacelle transmission (non-metric side) and the static mast is mounted to the metric side of the balance. The rotor balance maximum design loads are provided in Table A2.

Table A2. Rotor balance design load limits

	Design Limit
Thrust Force	+3000, -500 lbs.
Side Force	+750, -750 lbs.
Drag Force	+750, -750 lbs.
Pitch Moment	± 2400 in-lbs.
Roll Moment	± 2400 in-lbs.
Yaw Moment	N/A
Torque*	+15,600 in-lbs.

*Torque measured by flex coupling, rotor balance yaw moment is the residual torque.

Rotating Amplifier System (RAS) and Slip-Ring Assembly

All rotating data channels were amplified by a rotating amplifier system (RAS) developed by the Nationaal Lucht-en Ruimtevaartlaboratorium (The Netherlands National Aerospace Laboratory, NLR) to enhance transducer signal-to-noise ratios before entering the slipring (Ref. 10).

Early in TRAM development, it was anticipated that the blade pressure transducers would be susceptible to electromagnetic interference (EMI) noise from the model's electric drive motors and from passing the signals from the rotating frame, through sliprings, to the non-rotating side of the model. In order to mitigate the effect of these noise sources on blade pressure data quality, a compact precision amplifier system was developed to boost the signal levels in the rotating frame prior to passing the signals through the slipring. Another advantage of a rotating amplifier system is the reduction in the number of rings in the slipring since the amplifier converts each channel to single-ended output. The RAS was designed to provide signal conditioning and amplification of 256 channels and to provide up to 128 unmodified or 'pass-through' channels. The pass-through channels are used for safety-of-flight monitoring of critical blade and hub structural components.

The entire RAS system is contained in a cylindrical housing 7.0 inches (178 mm) in diameter and 5.6 inches (142 mm) in height. The RAS cylindrical housing is divided into 16 'pie' shaped modules each containing 16-hybrid amplifier cards. The RAS design utilizes hybrid circuitry to perform signal conditioning and amplification; the hybrid circuitry minimizes the size of each

amplifier card. Photographs of the RAS modules, housing and hybrid amplifier cards are shown in Figure A6. Each card has four selectable gain and three resistor calibration (Rcal) settings. The settings are programmable via an RS 232 link to a PC. Software has been developed to permit adjustment of the gain settings during a wind tunnel run to permit maximum signal resolution for each test condition.

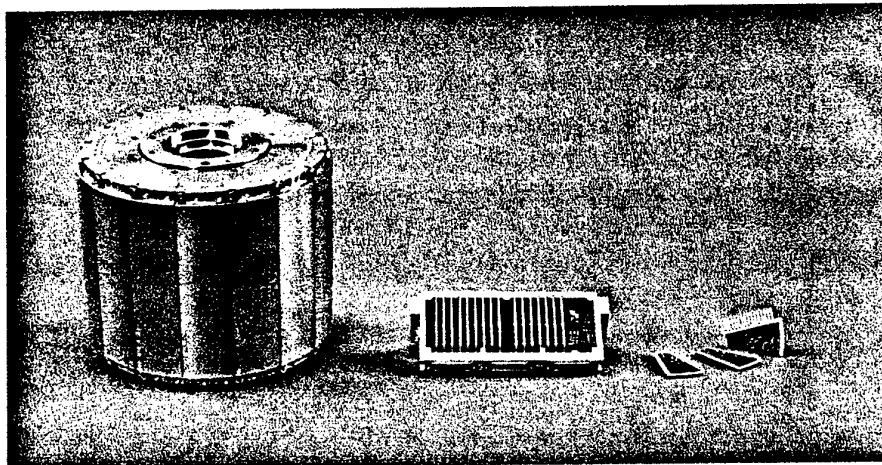


Figure A6. Photograph of RAS and components

The Mechanism of Noise Intensification and Suppression for a Propeller in a Short Duct

V.F. Kopiev and A.A. Maslov

*Central Aero and Hydrodynamics Institute (TsAGI), State Scientific Research Center,
Acoustic Division, Radio 17, 107005 Moscow, Russia*

The mathematical model of a ducted eight-bladed propeller in a subsonic flow is analyzed in the linear approximation. A system of two integral equations for simultaneous evaluation of aerodynamic loads on the blades and duct surface is used. It is shown that the duct presence can substantially affect the acoustic characteristics of the system at the expense of useful interference of the acoustic fields produced by equivalent sources located on the propeller and on the duct. The effect of the duct chord shape and of axial position of the propeller in the duct under conditions of the thrust constancy is investigated. These results are compared with the respective data for an open propeller. It is shown that the system allows a possibility of considerable noise suppression and optimization of sound field directivity in the task of exterior and interior noise.

INTRODUCTION

The development of efficient fuel-saving turboprop engines has designated noise control among principal design considerations. A promising direction of solving concomitant acoustical problems seems to be along the lines of optimal and more complex aerodynamic configurations, rather than a single propeller. Among them, special interest is directed to a system of a propeller in a duct. Even a short shroud cowling a propeller may provide new possibilities in noise control due to an advantageous directional redistribution of the sound field, interference of noise from the sound sources on the duct and the propeller, arrangement of a sound absorbing lining in the duct, etc.

For a relatively wide and thin bladed prop-fan operating without transonic zones, a theoretical analysis of aerodynamics and noise may be conducted with good accuracy in the linear approximation. An approach used earlier to determine aerodynamic loads on propeller blades [1] and based on the method of the potential of perturbations was developed recently for a ducted propeller operating at subsonic relative flow velocities [2].

We present simultaneous calculations of aerodynamic loads and sound field produced by a modeled eight-blade ducted propeller on the base of theory developed in [2]. The effect of duct chord inclination (weak diffuser or contractor) and of its shape (straight, concave or convex) on acoustic characteristics of the system is investigated. We also consider the effect which a propeller excursion along the duct axis has on the sound field directivity pattern. The configuration are considered under condition of thrust constancy which is easy to realize owing to the task linearity.

AERODYNAMIC LOADS ON BLADES AND DUCT

Consider a propeller of blade radius $R^{(B)}$ with N_B blades rotating with a constant angular velocity Ω in a short cylindrical duct (ring) in an ideal gas. The velocity of an incoming flow V is constant and directed along the propeller axis. Denote $M = V/a_0$, $M_T = \Omega R^{(B)}/a_0$, where a_0 is

the velocity of sound in stationary gas. Perturbations induced by the blades are assumed as small and isentropic.

Let r, θ, z represent a cylindrical system of coordinates tied with the rotating propeller, as shown in Fig. 1. The duct radius may slightly vary about its average value R along the z coordinate, but it remains constant along θ for any particular z . The model has a clearance between the duct and the blade tip, $R > 1$. For a point on the duct, stationary in this coordinate system, the velocity of the main incoming flow is $(M^2 + M_T^2 R^2)^{1/2}$. Analysis is conducted with the linear theory of compressible fluid where the blades and duct are assumed to be infinitely thin surfaces, velocity is subsonic. The finite thickness of blades and duct could be readily taken into account, but this would leave us with cumbersome expressions.

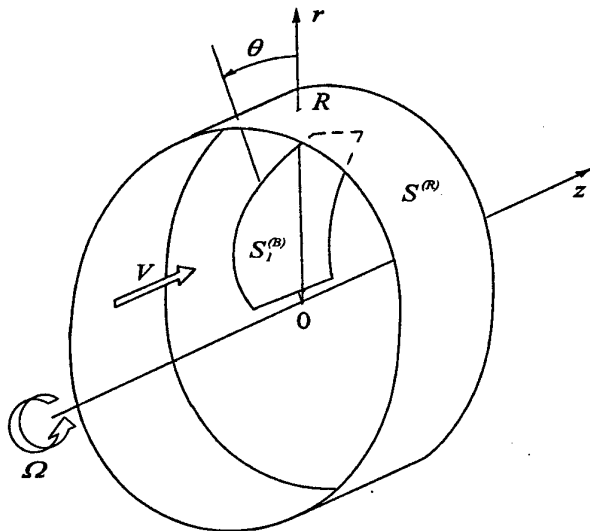


Fig. 1. Cylindrical coordinate system tied with a ducted blade.

The aerodynamic loads on blades and duct and the flow perturbations are stationary in a system of coordinates tied with the blade. Therefore, in this system of coordinates, the blade and duct surfaces may be modeled by acoustic dipoles with a time-invariable intensity; the density of these dipoles is to be determined. The derivation of equations for the distribution of aerodynamic loads on blades and duct is given in [2]. The resulted system of integral equations for the unknown distributions $\Delta P^{(B)}(x, r)$ and $\Delta P^{(R)}(z, \theta)$ of aerodynamic load on blade and duct surfaces is

$$w^{(B)}(x, r) = \frac{1}{2M_T} \left[\sum_{n=1}^{N_B} \iint_{S^{(B)}} \Delta P^{(B)}(x', r') K_n^{(BB)}(x', r', x, r) dx' dr' + \right. \\ \left. + R \iint_{S^{(R)}} \Delta P^{(R)}(z', \theta') K^{(BR)}(z', \theta', x, r) dz' d\theta' \right] \quad (1)$$

$$w^{(R)}(z, \theta) = \frac{1}{2M_T} \left[\sum_{n=1}^{N_B} \iint_{S_n^{(B)}} \Delta P^{(B)}(x', r') K_n^{(RB)}(x', r', z, \theta) dx' dr' + \right. \\ \left. + R \iint_{S^{(R)}} \Delta P^{(R)}(z', \theta') K^{(RR)}(z', \theta', z, \theta) dz' d\theta' \right] \quad (2)$$

$$\frac{w^{(B)}(x, r)}{M_r} = \frac{\partial f^{(B)}(x, r)}{\partial x}, \quad \frac{w^{(R)}(z, \theta)}{M} = \frac{df^{(R)}(z)}{dz} \quad (3)$$

Here $w^{(B)}$ and $w^{(R)}$ are the normal velocities on blade and duct satisfying the no-flow conditions (3), $f^{(B)}(x, r)$ and $f^{(R)}(z)$ are the given equations of the blade surface and duct chord. The expressions for the velocity components $K_n^{(BB)}$ and $K_n^{(RB)}$ induced by the unit blade dipole on the blade and duct respectively, and for components $K^{(BR)}$ and $K^{(RR)}$ induced by the unit duct dipole on the blade and duct are presented in [2]. Eqs. (1) - (2) are the integrals for the full normal velocities $w^{(B)}$ and $w^{(R)}$ expressed through the unknown densities $\Delta P^{(B)}(x, r)$, $\Delta P^{(R)}(z, \theta)$, $M_r = U(r)/a_0$. The equations (1) and (2), augmented by the conditions (3), represent a closed system of integral equations for the unknown distributions $\Delta P^{(B)}(x, r)$ and $\Delta P^{(R)}(z, \theta)$ of aerodynamic load on the blade and duct surfaces. This system extends the approach of Hammond et al. [1] for the unshrouded propeller to a ducted propeller. Note that this approach based on using pressure rather than velocity potential as an independent variable does not require that the vortex sheet behind the blade should be considered, because in contrast to the potential, the pressure in the sheet is continuous.

The system (1) - (3) is solved numerically. It is worth noting that the nuclei $K_1^{(BB)}$, and $K^{(RR)}$ vanish at lines along the relative velocity from the incoming flow to points x, r and z, θ , respectively. Therefore, to compile an effective solving algorithm, one would have to evaluate the analytical form of the singularities of these nuclei [2]. Solving this system of equations we obtain the stationary distributions $\Delta P^{(B)}$ and $\Delta P^{(R)}$ on the blade and duct surfaces in coordinate system tied with rotating blades. In the linear approximation, the sound field of a ducted propeller is defined by the total radiation of dipoles distributed over the blades and the duct, which occur in the main reference system.

SOUND FIELD

In the frequency approach (see, e.g., [3,4]) the distributions of surface sources obtained in a rotating coordinate system (which are steady in this system) are Fourier-transformed in a main coordinate system into periodic sources in the form of a series in individual harmonics. In a cylindrical stationary coordinate system r, θ, z , where $\theta = \theta + \Omega t$, the stationary distribution of the above singularities will spin with an angular velocity Ω . We reexpand this nonstationary periodic (with period $2\pi/N_B\Omega$) field of sources in a Fourier series. This transformation represents the part of sources associated with aerodynamic load on the blades in the form of a distribution of stationary acoustic monopoles over the volume $D^{(B)}$ swept by the blades. For the m th harmonic, this distribution is the harmonic intensity $Q_m^{(B)}(r, \theta, z) \exp(-i\omega_m t)$, where $\omega_m = mN_B\Omega$ is the frequency of the m th harmonic. Early we found [5] the complex volume

density of the source in the form

$$Q_m^{(B)}(r, \vartheta, z) = -\frac{1}{2\pi} \left(\frac{U}{Vr} \right)^2 \left[\frac{r^2 \Omega}{U} \frac{\partial (\Delta P^{(B)})}{\partial x} \left(\frac{U}{V} z, r \right) + i m N_B \Delta P^{(B)} \left(\frac{U}{V} z, r \right) \right] \times \\ \times \exp \left[i m N_B \left(\frac{\Omega z}{V} + \vartheta \right) \right] \quad (4)$$

As for the other part of the source associated with dipoles placed on the duct surface $S^{(R)}$, the above map ping into a stationary coordinate system and expansion into a Fourier series transforms this part, for each harmonic, into a surface (rather than volume on the same surface $S^{(R)}$) distribution of stationary dipoles with intensity harmonically varying in time.

In order to determine the sound field due to the derived distribution of the sources, we resort to the Green's function for the convective equation for a homogeneous subsonic flow [6],

$$G = \frac{1}{4\pi R^*} \exp \left[i \frac{k}{1-M^2} (R^* - M(z-z')) \right] \quad (5)$$

where $R^* = [(z-z')^2 + (1-M^2)(r^2 + (r')^2 - 2rr' \cos \vartheta')]^{\frac{1}{2}}$; $k = \omega_m / a_0$, r', ϑ', z' are the coordinates of the source in the cylindrical stationary system of coordinates; and $r, 0, z$ are the coordinates of the observation point (we select $\vartheta = 0$ for this point). Then, for the component of the m th harmonic caused by the load on the blades we obtain

$$p_m^{(B)}(r, 0, z) = N_B \iiint_{D^{(B)}} Q_m^{(B)}(r, \vartheta, z) G(r, z; r', \vartheta', z') dz' d\vartheta' r' dr' \quad (6)$$

For the component due to dipoles on the duct, we have

$$p_m^{(R)}(r, 0, z) = \iint_{S_R} Q_m^{(R)}(\vartheta', z') \frac{\partial G}{\partial r'} \Big|_{r'=R} R dz' d\vartheta' \quad (7)$$

where

$$\frac{\partial G}{\partial r'} \Big|_{r'=R} = \frac{1}{4\pi (R^*)^2} (R - r \cos \vartheta) \left(i k - \frac{1-M^2}{R^*} \right) \exp \left[i \frac{k}{1-M^2} (R^* - M(z-z')) \right]$$

The complex amplitude of the m th harmonic for $m \geq 0$ equals the sum of complex expressions (6) and (7):

$$p_m = p_m^{(B)} + p_m^{(R)} \quad (8)$$

Equations (1) – (3) for the aerodynamic load and equations (8) for the sound are used for simultaneous aerodynamic and acoustical computations of a ducted propeller.

DUCT PROPELLER CONFIGURATION

Consider a specific configuration outlined in Fig.2. This is a propeller with eight straight blades. The blade tip radius $R^{(B)}$ is 1 m, the blade length is 0.8 m, and the chord is constant over the span and equal 0.4 m. The effects of the central hub are not taken into account. We assume that, in each cross section, the blade chord is a straight line, and the twist and the blade angle setting are selected so that $\partial f^{(B)} / \partial x \equiv \alpha_p$ is the *const* over the entire blade surface. As an initial configuration we center the propeller in a 1-m-long duct with the clearance between a blade tip and the duct equal to 0.05 m. Mach number of the incoming flow is 0.6.

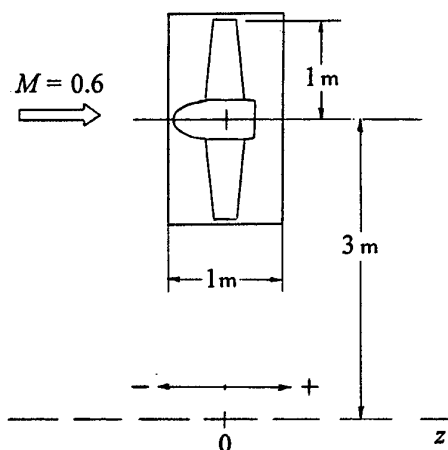


Fig. 2. Schematic diagram of a ducted propeller with computation parameters.

For a propeller speed of 1800 RPM, in the coordinate system tied with the blade, the relative velocity is $0.857M$ at the blade tip and $0.879M$ at the duct. The computational accuracy of load distributions is within 5%. Accordingly, the accuracy of sound pressure levels in the near field amounts to 0.5 dB.

NUMERICAL RESULTS FOR DUCTED PROPELLER

First of all, it is interesting to see the significance of the duct effect on the propeller sound field characteristics, variations in propeller thrust also need to be taken into account. Therefore, in sound field calculations, we simultaneously computed the thrust. The calculated levels of the first noise harmonic ($m=1$) of the considered ducted propeller and the unshrouded propeller are compared in Fig. 3 (solid curves). The sound field was determined on a line parallel to the propeller axis and offset by a distance of 3 m (Fig.2). In this case we consider a "simple" duct with the straight noninclined chord. At an almost invariable thrust (attributed to the simplest form

of duct chord), we found a considerable reduction of noise in the area upstream of the ducted propeller and some increasing downstream.

In order to clarify the reasons behind this effect, we calculated the first harmonic of the noise produced separately by the sources on the blades $p_1^{(B)}$ and on the duct $p_1^{(R)}$ (Fig. 3, dashed lines). The duct presence makes almost no effect on the sound generated by equivalent sources located on the blades (the respective sound field coincide almost completely). Consider the sound field produced separately by equivalent sources appear on the duct. The duct sources are not independent but are generated by the rotating propeller. Therefore, the sound field from the propeller and duct sources must interfere and this interference result is presented by a solid line in the same figure. The sound field interference leads to the situation when the resulting noise in the propeller region and upstream appears to be reduced by more than 10 dB.

Consider the effect of duct chord shape. First consider a straight chord shape inclined to the propeller axis at the positive angle (contractor) or at negative angle (diffuser), Fig.4. The predicted results for different angles α_R are presented in this figure. It is easy to see that a weak contractor duct ($\alpha_R > 0$) provides an additional noise reduction in comparison with an unshrouded propeller and a propeller in a straight duct. If the angle α_R would increase the sound pressure maximum decrease and then begin to increase in the upstream direction. A weak diffuser duct appears to be substantially worse compared with a propeller in a straight duct and with increasing $|\alpha_R|$ the noise becomes greater even than for the unshrouded propeller.

Consider the effect of the duct chord curvature (Fig.5). Concave and convex parabolic configurations are studied. The curvature effect is weaker than that of inclination. Nevertheless it is clear that the convex profile causes a slight noise reduction (mainly upstream) and the concave one - on the contrary.

It is interesting to consider the effect of two positive factors - a combination of a weak contractor and convex chord shape. Despite the task linearity these two effects act not independently and resulting noise (amplitude of pressure) is different from the algebraic sum of two effects. Nevertheless the resulting curve appears to be close to optimum one, since this form of duct leads to a substantial noise reduction both in the propeller zone and upstream or downstream. This remarkable curve presented by a dark line on Fig.6.

Consider at last a case when the duct is shifted relatively to the propeller axis. For definiteness we consider a contractor duct. The most optimum curve is obtained near the central location of propeller (Fig.7). If the duct is shifted forward or backward the noise increases especially downstream. As it was shown for the "simplest" duct considered in [2], noise increasing becomes very pronounced for greater values of shift.

CONCLUSIONS

It is shown that the duct presence around the propeller even without application of duct liners, can significantly affect the acoustic characteristics of the system and provide a substantial noise reduction. This effect connected with a useful interference of sound generated by equivalent sources of two type (propeller and duct) and can be revealed only at the complete task solutions with a simultaneous account for the influence of propeller and duct on each other.

According to the duct chord shape and mutual location of propeller and duct, the noise can substantially increased or decreased and it is desirable to take into account the presence of such

effects. At the same time the whole task optimization can be realized only with account for the propeller arrangement relative to the fuselage (so, for rear arrangement the value of noise downstream is not important) and with considering a more real configuration of the propulsor itself with account for the blade thickness and the duct wall thickness, liner presence etc. Generalization of the results obtained in application to such situations requires an insignificant modification of numerical codes and seems will not bring to considerable problems.

REFERENCES

1. Hammond, C.E., Runyan, H.L., and Mason, J.P., Application of Unsteady Lifting Surface Theory to Propellers in Forward Flight, *AIAA*, Pap. no. 74-419, 1974.
2. Maslov, A.A., Simultaneous evaluation of the aerodynamic characteristics and sound field of a ducted propeller, *Acoust. Phys.* 1997, vol.43, No.2, pp.179-185.
3. Gutin, L.Ya., On the Sound Field of a Rotating Propeller, *Zh. Tekh. Fiz.*, 1936, vol. 6, no. 5, pp. 899-909.
4. Hanson, D.B., Near-Field Frequency Domain Theory for Propeller Noise, *AIAA J.*, 1985, vol. 23, no. 4, pp. 499 - 504.
5. Kopiev, V.F., Maslov, A.A., and Chernyshev, S.A., Prop-Fan Sound Field Shielding by the Fuselage Boundary Layer, *DGLR/AIAA*, Pap. no. 92-02-068, 1992.
6. Blokhintsev, D.I., *Akustika neodnorodnoi dvizhushcheysya sredy* (Acoustics of an Inhomogeneous Moving Fluid), Moscow: Nauka, 1981.

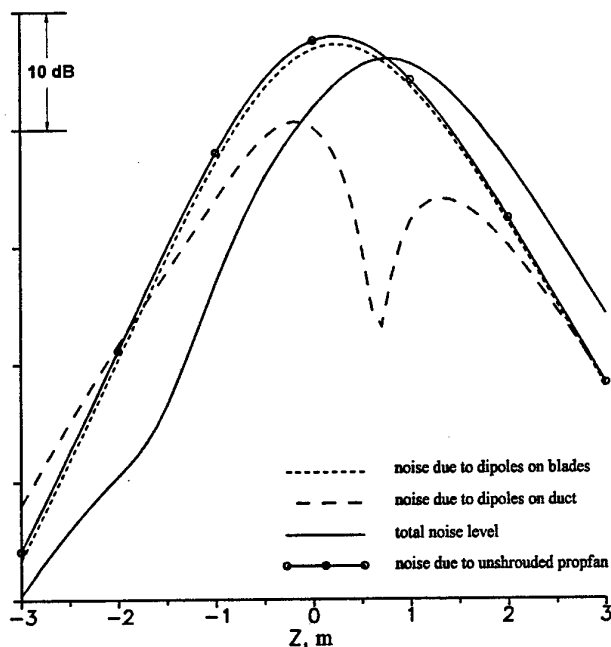


Fig. 3. Sound pressure levels of the first noise harmonics due to shrouded and unshrouded propellers.

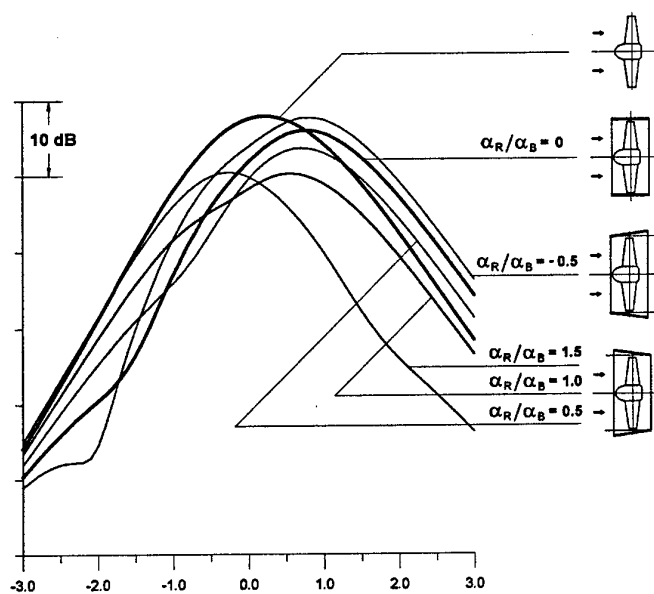


Fig.4. The effect of duct chord inclination compared with unshrouded propeller and a propeller in a straight duct.

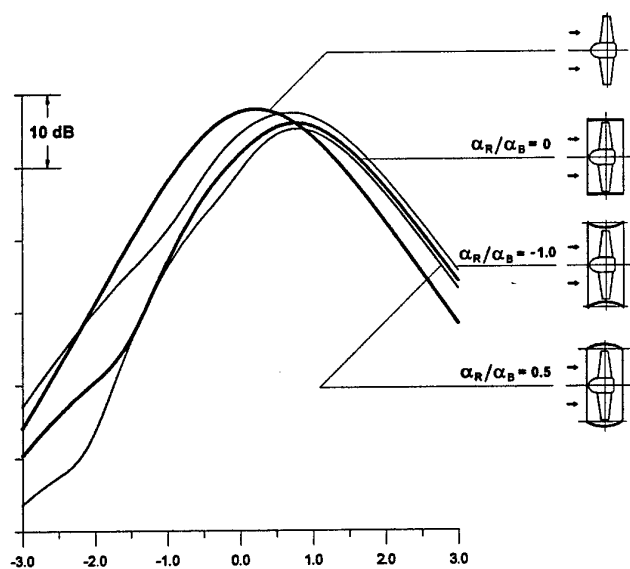


Fig.5. The effect of duct chord curvature compared with unshrouded propeller and a propeller in a straight duct.

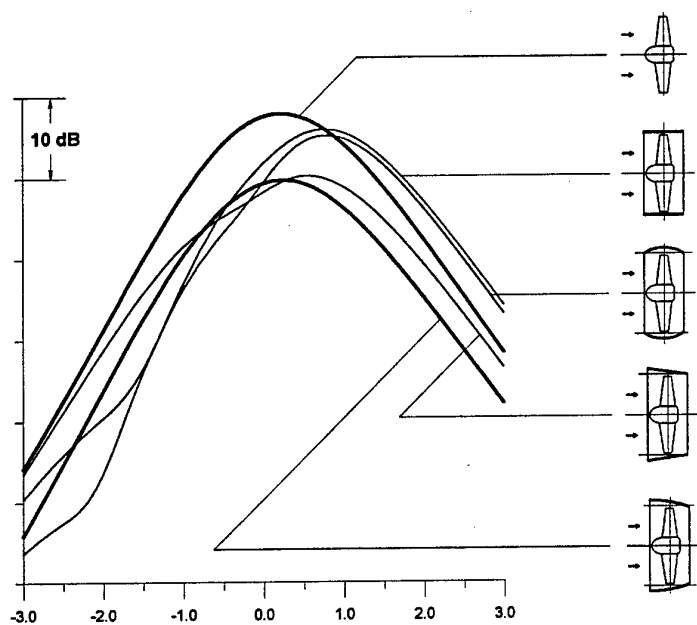


Fig.6. Combination of curvature with inclination compared with separate effects. Contractor with convex give the noise reducing in all directions.

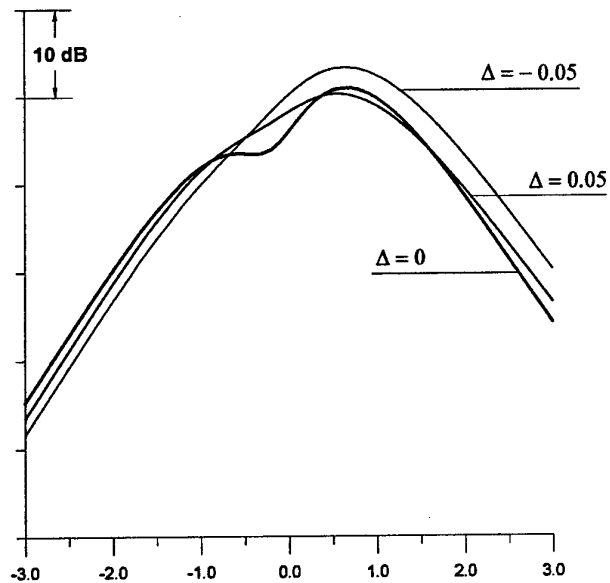


Fig 7. The effect of duct shifting relatively the propeller axis.

RESEARCH OF PROPFAN ACOUSTIC CHARACTERISTICS

V.M.Kuznetsov, L.S.Krymova, S.Yu. Makashov

Central Aerohydrodynamics Institute (TsAGI), Acoustic Division
107005, Radio Str.,17, Moscow, Russia

Recently increasing level of requirements for improving passenger aircraft ecology characteristics determines the urgency of solving the tasks of further noise level reduction in the airport vicinity and comfort improvement in aircraft cabins. The community noise levels of modern Russian airplanes with propeller power plants and turbojet by-pass engines, f.i. Il-114, Tu-204, comply with the regulating requirements of ICAO Standard, Annex 16, Chapter 3. As for the noise inside cabin, the national Standard GOST-20296-81 is in force in Russia. All passenger airplanes being under development in Russia are designed with account for obligatory provision of interior noise levels allowed by this GOST. Of special interest is the problem of providing noise comfort inside cabins for propeller-powered and propfan-powered airplanes [1,2].

As the experience of air vehicle service in the last decade shows, propeller application as propulsion system provides a higher degree of aircraft power efficiency in comparison with turbojet by-pass engines at flight cruise $Mach < 0.75$. In the fifties it was designed and introduced in service for Tu-114 a power plant with coaxial (on the same axis) two propellers AB-60K with dural blades. Efficiency η of these propellers at flight $M=0.75-0.8$ is $\eta=0.83-0.78$, and of experimental propellers $\eta=0.86-0.82$ (Fig.1). In the 1960's for transport aircraft An-22 a power plant with coaxial propellers AB-90 was designed which provided a larger thrust at take-off. Aircrafts Tu-114 and An-22 with four engines on wings were in service for many years. Such an extended experience of introducing in service and of wide-spread use of power plants with coaxial propellers in aviation is available only in Russia.

The experimental research of acoustic characteristics of aircraft with four power plants of this type placed on the wing were carried out. Thus, the analysis of measurement results of acoustic loading on the fuselage surface showed that the acoustic loading on the fuselage surface in the propeller zone were determined completely by propeller noise. With a distance from the propeller zone in the longitudinal direction forward and backward the contribution into the loading levels of other noise sources of the power plant increases; in the fuselage nose part a considerable contribution into the loading levels is made by engine compressor and in

the tail part - by the exhaust jet [3]. The largest overall level of loading on the fuselage in the propeller zone at the operation regime of 0.7 nominal is ~ 143 dB. With a distance from the propeller the overall loading levels determined by propeller coincide but still remain rather high (Fig.2). Thus, in the fuselage nose part the measured loading level is $L=132$ dB and in the tail part it is 125 dB. From the loading level distributions on the fuselage surface along the line of maximum clearance at the frequencies of the first four harmonics of BPF at the power plant operation regime of 0.7 nominal it was found that in the most loaded fuselage part the acoustic loading was determined by the levels at BPF; in the nose and tail fuselage parts - by the levels at the second harmonic frequency. For the coaxial propellers with equal blade numbers in the front and rear rows the second harmonic frequency coincides with the first combination frequency determined by aerodynamical interaction of the blades of front and rear propellers.

The following distributions of overall levels of acoustic loading in the lateral fuselage cross-section in the propeller zone were determined. The increase of power supplied to propeller causes approximately an identical loading level increase at all the points of this section. In this case approximately the identical power variation from 0.4 nominal to 0.7 nominal and from 0.7 nominal to one nominal causes an essentially different increase of overall loading levels (by 14 dB and 4 dB, respectively) (Fig.3). A contribution of separate power plants into the acoustic loading levels on the left fuselage board surface was also determined. The maximum acoustic loading levels on the wing surface are 142 dB at the power plant operation regime of 0.7 nominal and the loading spectra are characterized by high levels of the highest harmonics.

The analysis of the sound field structure in the maximum loading zone showed that the acoustic loading correlation radius (at the frequencies of the first eight harmonics) for the external engine functioning is 0.5-0.8 wavelength and for the internal one it is 0.2-0.4 wavelength. The analysis of the sound pressure impulse form at the different points of the fuselage surface showed that in the nose and tail parts away from the noise source the reflected signals were compatible in level with the direct ones.

Measurements in the far field on the arc of the circle with radius $R=30$ m showed that the maximum levels of propeller noise were observed at the angle $\varphi=140^\circ$ to the axis and were 127 dB at the regime of 0.7 nominal.

Outstanding possibilities of using propeller power plants with the aim of fuel economy and aircraft take-off-landing performance improvement are offered by application of propfans

which are characterized by a larger number of more wide swept blades with thin supercritical profiles.

Russian-Ukrainian aircraft An-70 (Antonov) with a propfan power plant, first designed on a global scale, made several test flight series [4,5]. Its design started in the 1980's with the aim of replacing transport aircraft An-12 with a propeller power plant. Coaxial propellers SV-27 made of composite materials and with 4,5 m diameter are designed in Design Bureau in Stupino (Russia). Propfan is formed by a front 8-bladed propeller and a rear 6-bladed propeller.

Turbo-propfan engine D-27 with a power of about 14000 h.p. producing thrust of the order of 120 kN is developed in Design Bureau in Zaporozhie (Ukraine) in cooperation with Russian institutes of scientific research. The wing of An-70 which has a large aspect ratio and supercritical profile is blown over by an air flow from propfans closely located. Such arrangement was investigated by Antonov Design Bureau in co-operation with Central Aerohydrodynamics Institute by name of Zhukowsky N.E. (Russia). An-70 wing provides a high value of the lift/drag ratio and very good take-off-landing characteristics of the aircraft. Due to the supercirculation phenomenon generated at streamlining deflected flaps by an air flow from propfans, the wing lift at aircraft take-off and landing substantially increases. Besides, the main undercarriage wheels provide a low specific loading on the runway surface. An-70 with propfans SV-27 and engine D-27 possesses extremely high take-off-landing characteristics. Serial production of An-70 is planned to be realized in Ukraine and in Russia.

The power plant with propfans for this aircraft has been tested since the beginning of 1990's on flying laboratory Il-76 in the Institute of Flight Tests in Zhukowsky [6]. Measurements of acoustic loads are made under the air field conditions and in forward flights with constant velocity. The engine with a front 8-bladed propeller and a rear 6-bladed propeller is mounted instead of by-pass turbojet engine D-30 KP under the flying laboratory wing [7,8]. This laboratory together with the equipment for recording the acoustic loading was presented at a number of international exhibitions.

For using the power plants with propfans on passenger airplanes it is necessary to solve the tasks of complying with the regulating requirements on noise and vibration inside cabins because the maximum noise levels of the propeller power plant are observed in the range of lower frequencies in comparison with those of by-pass turbojet engine. For example, the noise levels inside passenger aircraft cabin with a propeller power plant on the wing are, in practice,

higher along the whole cabin than those observed in the case of mounting by-pass turbojet engines in the rear aircraft part [9,10,11]. The major degree of noise effect in the passenger cabin in the case of propeller power plant is observed in the frequency range of $f < 200-300$ Hz where the acoustic efficiency of traditional thermo-soundinsulating structures for aircrafts is not high (Fig.4). The excess of the interior noise levels allowed by Russian GOST is determined by high levels of acoustic loading on the fuselage surface observed at the frequencies $f = 100-150$ Hz, i.e. at those corresponding to the fundamental harmonics of propeller rotation noise.

For evaluating the possibilities of noise reduction due to replacement of a propeller power plant by a propfan a series of experimental investigations of acoustic loads produced by a full-scale front single 8-bladed propeller from the coaxial propfan on the serial transport aircraft surface was carried out. Acoustic load measurements were conducted on the ground ($H=0$) and also in aircraft flight at $H=4.0$ km with velocity $V \approx 400$ km/h. The power plant operation regime corresponded to 0.85 of the design regime.

This experimental 8-bladed propfan in the process of measurements was mounted on the left plant instead of the serial propeller AB-68DM. Its diameter was 4,7 m and a number of revolutions per minute was 1075, location of the propeller (relative clearance) was $\bar{z} = 0.15$, experimental propfan diameter was 4,2, a number of revolutions was the same and the clearance value was $\bar{z} = 0.22$.

The data obtained permitted evaluating the effect of replacing propeller by propfan on the acoustic loading, determining the conditions required for similar evaluations. The measurements show that there is no complete similarity in distributions of overall levels and harmonics of propeller and propfan revolution noise on the fuselage surface under conditions of air field and flights. Under flight conditions the maximum acoustic loading produced by a serial propeller is concentrated close to the propeller revolution plane; in tests under the air field conditions the acoustic loading is distributed along the fuselage more uniformly. Compare now the dependencies of revolution noise harmonic levels for a serial propeller and for an experimental propfan from number mk in the most loaded zone of the aircraft fuselage surface, obtained under air field and flight conditions (Fig.9,10). The levels of the first two revolution noise harmonics for the serial propeller on the aircraft surface at flight and air field conditions are actually in agreement. Beginning with the third harmonic ($mk=12$) the acoustic load levels measured in flight are lower than those on the ground and with the harmonic number increase this difference becomes larger. This can be explained by the ground presence

and, as a consequence, by non-steady loading generation due to which the harmonical component levels actually do not vary with number mk . In flight the effect of the ground and of the non-steady loading connected with it is absent and therefore the first four-five noise harmonics of serial propeller ($mk=16-20$) revolution are determined by steady loads affecting the propeller blades.

In tests of the experimental propfan the non-steady loading makes a substantial contribution both under air field and flight conditions, therefore the noise harmonic levels of propfan revolutions decreases but the velocity of falling of the highest harmonics levels under air field conditions is equal to 6-8 dB per one harmonic and at flight it is still larger.

Thus due to the absence of a complete similarity in distribution of overall levels of noise harmonics produced by propeller and propfan revolutions on the aircraft surface under air field and flight conditions, it seems impossible to make any predictions relating to the expected levels of acoustic loading on the aircraft surface in flight on the basis of data obtained in the air field tests.

Evaluate the efficiency of using an experimental 8-bladed propfan on the aircraft instead of a serial 4-bladed propeller and consider distributions of the overall levels and noise harmonic levels produced by their revolutions at the same values of mk under flight and air field conditions (Fig.5,6). At flight conditions the acoustic loading is concentrated close to the revolution plane. This effect is observed for both propellers. The overall levels of acoustic loading produced by the experimental propfan is lower than the loading levels produced by the 4-bladed propeller and in the zone of cockpit this difference is ≈ 10 dB and in the most loaded zone $\Delta L=3$ dB (Fig.7). The levels of harmonic components at similar mk produced by propeller and propfan are actually the same. The propfan efficiency is determined by doubling a blade number and, as a consequence, by doubling the fundamental frequency of the experimental propfan revolutions, i.e. efficiency is associated with the absence of noise components characteristic of the serial propeller rotation which determine the overall level of acoustic loading.

In tests under air field conditions the overall levels of acoustic loading along the fuselage surface are distributed more uniformly than in flight tests and the acoustic loading levels produced by a propfan are lower than those produced by a serial propeller by $\Delta L=8-13$ dB (Fig.8).

Thus, the acoustic loading levels along the fuselage surface produced by an experimental propfan are considerably lower than those produced by a serial propeller.

Consider the results of experimental research relating to acoustic loading produced by an experimental coaxial propfan on the flying laboratory (FL) surface at flight. The flying laboratory was designed on the basis of a serial aircraft with four by-pass turbojet engines but on the left half-wing of which an unducted turbopropfan with a coaxial propfan was placed instead of the second power plant. The propfan has a different number of blades in the front propeller ($k=8$) and in the rear propeller ($k=6$). Measurements of acoustic loading produced by the propeller in forward flights of the flying laboratory are made at heights $H=0.5, \dots, 8$ km at flight Mach numbers $M_f=0.32 \dots 0.49$ for different regimes of turbopropfan operations (in this case the power supplied to the propfan varied within the limits of 1660-5520 kWt. The acoustic loading was measured on the left board of the FL in seven cross-sections of the fuselage surface. The measurements were conducted with the use of half-inch microphones of B&K which were mounted flush with the fuselage surface and the information was recorded by a 14-channel storing device KS-616W Sony. Repeatability of measurement results under different conditions (air field and flight) and accuracy of the acoustic loading measurement result analysis in narrow frequency bands ($\Delta f=4$ Hz) is ± 2 dB.

Since the measurements of acoustic loading produced by the propfan were made at FL flights with four functioning power plants (3 turbojet by-pass engines + turbopropfan), the interference levels on the fuselage surface produced by turbojet by-pass engines were evaluated. As a result of measurements in forward flights of FL at heights $H=7.5-8.0$ km with three turbojet by-pass engines (turbopropfan is cut-off, propfan is weathervaned), it was found that the acoustic interference of turbojet by-pass engines did not affect the acoustic loading levels produced by propfan. This gave a possibility of analyzing three sources of harmonic noise of the coaxial propfan: rotation noise of the front (8-bladed) propeller (L_8), rotation noise of the rear (6-bladed) propeller (L_6) and the noise determined by aerodynamical interaction of propeller blades in coaxial arrangement with an unequal number of the front and rear propeller blades (L_c).

Considering contributions made by different noise sources of the coaxial propfan with a different number of the front and rear propeller blades into distribution of the overall levels of acoustic loading produced by propfan along the fuselage surface at FL flights at different height and at the same power supplied to propfan, we note that the maximum acoustic loading of the fuselage surface is observed in the zone of propfan location, is determined by the noise of 6- and 8- bladed propeller rotation (Fig.11,12) [12]. In the fuselage surface sections far away from propfan location the acoustic loading levels are determined by the levels of components at combination frequencies of the aerodynamical interaction between the

front and rear propeller blades. This conclusion follows from the dependency determining contributions of different sources of the harmonic noise (L_8 , L_6 , L_c) into distribution of the overall levels of acoustic loading along the fuselage surface produced by coaxial propfan in the forward flight of FL at constant flight velocity.

The acoustic loading level distribution at BPF and the distribution of four harmonics of the 6-bladed propeller rotation noise along the FL fuselage surface in flight at constant velocity show that the overall levels of 6-bladed propeller are determined by the levels at the fundamental frequency of propeller rotation noise. A similar dependency is obtained for the 8-bladed propeller. The overall levels at measurement points far away from the zone of PF location are determined by the levels of the component at combination frequency $f_{\text{front}}+f_{\text{rear}}$.

The analytical method of predicting the noise of coaxial propeller revolutions which permits improving the aeroacoustical and geometrical parameters of propellers was developed [13]. At high transonic velocities one of the principal noise sources is the variable pressure field which is formed due to affecting the medium by stationary aerodynamic loading on blades.

The prediction method consists in determining the aerodynamic parameters of propeller blade in each design cross-section at the current radius with a successive integration of the expressions obtained. On the basis of using this method of prediction the influence of the peripheral Mach number, blade number and geometrical parameters of blades on the levels of harmonical components of blades is investigated.

Analysis of the available results of experimental research of the acoustic characteristics of singular and coaxial propfans at flight conditions, using the methods of predicting the expected acoustic loading produced by propfan on the aircraft fuselage surface in flight permitted evaluating the expected acoustic loading of hypothetical transport aircraft surface in cruise flight at $H=9.0$ km. The maximum acoustic loading of the fuselage surface in the region of propfan location is produced at the fundamental harmonic of the 8-bladed propeller rotation noise. The maximum acoustic loading in the region of cockpit location is observed at the combination frequency ($f_{\text{front}}+f_{\text{rear}}$) determined by aerodynamic interaction between the front and rear propellers of propfan.

One of the most important problems for the aircraft with propfans is providing a high level of acoustic comfort in the passenger cabin [14,15,16]. Traditional thermo-soundinsulating board structures are made according to the scheme of double-walled structure

where the role of the first wall is fulfilled by the fuselage skin and the second wall is usually a trim panel. The soundinsulating ability of the structure can be strengthened at the expense of varying a degree of filling the space between the fuselage skin and trim panels with the layers of soundabsorbing materials and of varying a degree of contracting these layers. The most complete effect of the second wall in this case is provided by the respective vibroisolation of trim panels from the fuselage structure. In the range of low sound frequencies $f < 300$ Hz, i.e. where the maximum acoustic radiation of PF is observed these structures possess a weak soundinsulation ability, since the second wall effect is revealed slightly. Increase of the soundinsulating board structure at the expense of increase of its surface mass or of the distance between the fuselage skin and trim panels is unacceptable.

At present the most reasonable ways of improving the soundinsulating structure efficiency are, in our opinion, the following: increase of sound energy losses between the skin and trim panels due to a local increase of soundabsorption; attenuation of the radiating ability of trim panels; variation of elasto-inertial features of fuselage panels; using the resonance soundabsorbers for providing the effective acoustic energy absorption in a narrow band of low sound frequencies.

It is quite possible that the fruitful cooperation between Russian and Western experts in the aviation acoustics field can lead to designing a passenger aircraft with propfan power plant with high levels of the acoustic comfort in passenger cabins.

References

1. V.M.Kuznetsov, A.G. Munin. The investigations on aviation acoustics in Russia. CEAS/AIAA 95-003, First Joint CEAS/AIAA Aeroacoustics Conference, München, Germany, 1995, 15p.
2. V.M.Kuznetsov, A.G.Munin. Civil aircraft noise problems in connection with more stringent community noise standards. Proceedings of the Int. EAA/EEAA Symposium "Transport Noise and Vibration", Tallinn, 1998, p.339-344.
3. P.S.Antohin, Yu.B.Arihov, G.M. Gerasimova. Experimental investigations of acoustic characteristics of aircraft with four power plants. Reports of IX technical-scientific conference on aviation acoustics. TsAGI publ. department, Moscow, 1989, p.92-95.
4. Air Cosmos/Aviation magazine '1391, 1992, September, p.50
5. Flight International. 1994, February, p.34-35.

6. V.M.Kuznetsov, A.G.Munin. Aircraft noise control in Russia. Proceedings of the Second International Symposium "Transport Noise and Vibration", St.- Petersburg, Russia, 1994, p.7-12.
7. V.M. Kuznetsov, V.I.Ganabov, L.S.Krymova, S.Yu. Makashov. Acoustic characteristics of propfans. AIAA 93-4444, 15th AIAA Aeroacoustics Conference, Long Beach, CA, 1993, 7 p.
8. A.G. Munin, V.M. Kuznetsov, L.S. Krymova, M.P. Lavrukchina, S.Yu. Makashov, Yu.L. Vaznov, V.A. Sophin, A.Yu. Karjagina. Acoustic loading produced by the propfan on flying laboratory surface. Reports of IX technical-scientific conference on aviation acoustics. TsAGI publ. department, Moscow, 1989, p.69-72.
9. V.M. Kuznetsov, S.Yu.Makashov. Acoustic loading of surfaces due to aerodynamic noise sources. Third Int. Congress on air and structure-borne sound and vibration, 1994, Montreal, Canada, 1253-1256.
10. V.M.Kuznetsov, A.G.Munin. Aviation acoustics. TsAGI - principal stages of scientific activities. Moscow. Nauka.Fizmatlit, 1996, p.556-559.
11. V.M.Kuznetsov, A.G.Munin. Acoustics of passenger airplanes of new generation. Proceedings of the 12-th International FASE Symposium "Transport Noise and Vibration", St.-Peterburg, Russia, 1996, p.133-134.
12. V.M. Kuznetsov, L.S. Krymova, G.M. Gerasimova, M.P. Lavrukchina. On reduction of acoustic loadings produced by counter-rotating propfans. The Reports of X scientific-technical conference on aviation acoustics, TsAGI. Publ.department, Moscow, 1992, p.65-68.
13. Yu.V. Vlasov, V.M. Kuznetsov, A.G.Munin et.al. Propeller noise. Proceedings of Central Aerohydrodynamic Institute. Basic problems of aeroacoustics. TsAGI. Publ.department, Moscow, 1996, 56 p.
14. F.B.Metzger. Past, present and future of cabin noise control in propeller prop-fan driven airplanes. Noise-93. Int. Noise and Vibration Control Conf. 1993, St.Petersburg, Russia, 7p.
15. A.G.Munin, V.M.Kuznetsov. The noise must be turned down. Airspace Journal, July-August 1997, p.40-41.
16. L.S. Krymova, V.M. Kuznetsov, M.P. Lavruhina, S.Yu. Makashov. Acoustic loading produced by propfans on aircraft surface. Reports of scientific seminar "Aviation acoustics". TsAGI publ. department. Moscow, 1999, p.21-22.

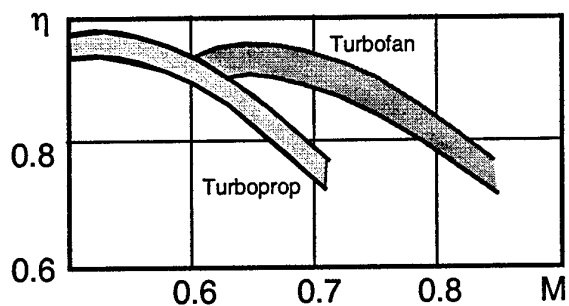


Fig. 1. Effect of flight velocity (Mach number) on the power plant efficiency.

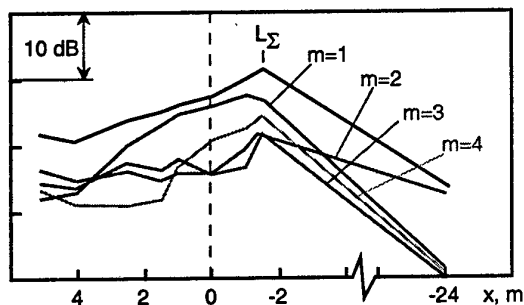


Fig. 2. Distribution of sound pressure levels along the fuselage.

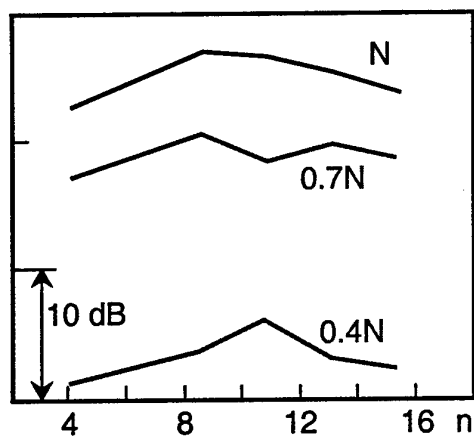


Fig. 3. Overall sound pressure levels in the front propeller rotation plane at different engine regimes.

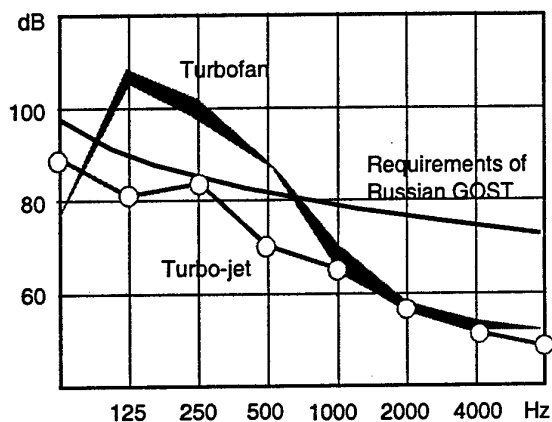


Fig. 4. Sound pressure levels inside the cabin in the vicinity of the propeller plane.

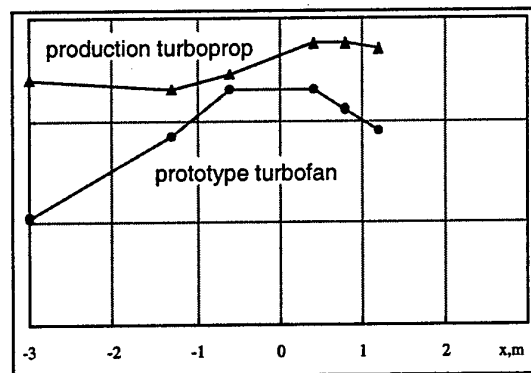


Fig. 5. Sound pressure levels of production and prototype engines at $mk=8$.

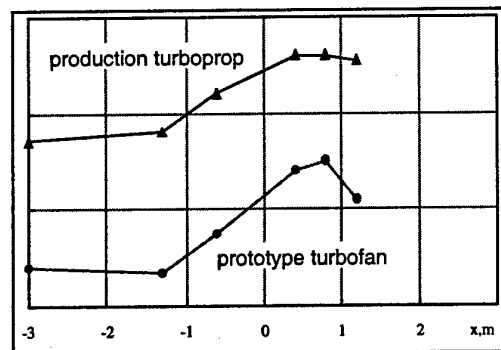


Fig. 6. Sound pressure levels of production and prototype engines at $mk=16$.

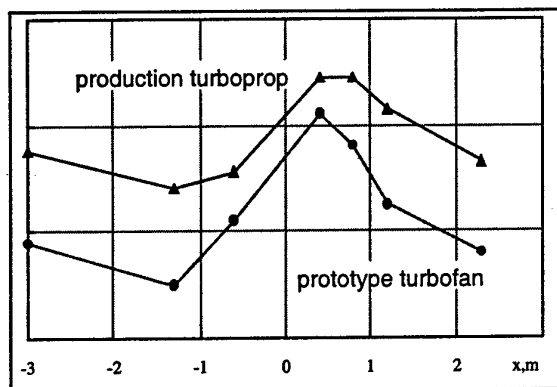


Fig. 7. Overall sound pressure levels of production and prototype engines under flight conditions.

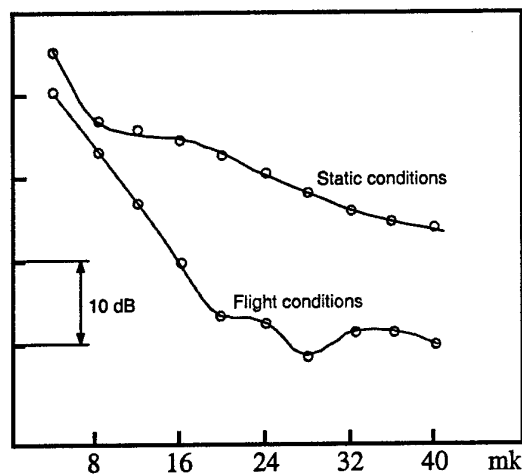


Fig. 10. Sound pressure levels depending on harmonics number for prototype turbopfan.

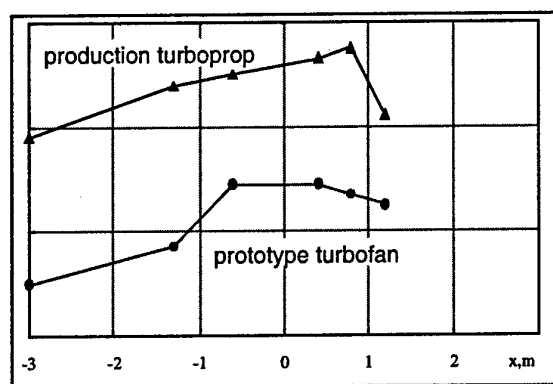


Fig. 8. Overall sound pressure levels of production and prototype engines under static conditions

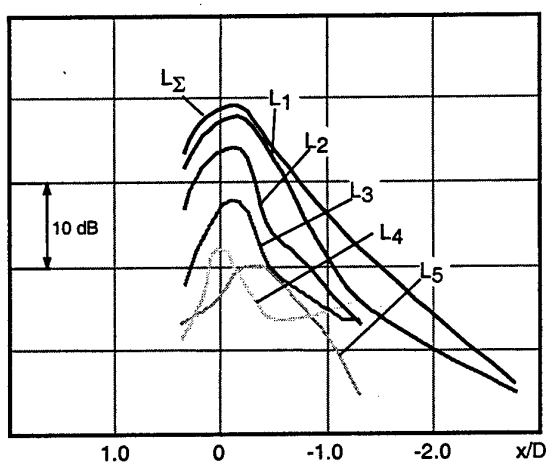


Fig. 11. Sound pressure levels produced by 6-blade (rear) propeller of propfan.

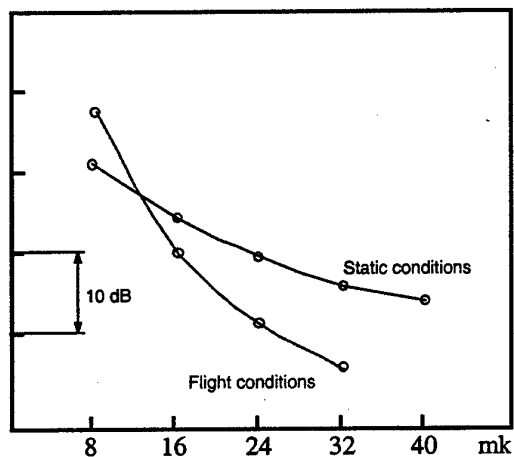


Fig. 9. Sound pressure levels depending on harmonics number for production turboprop.

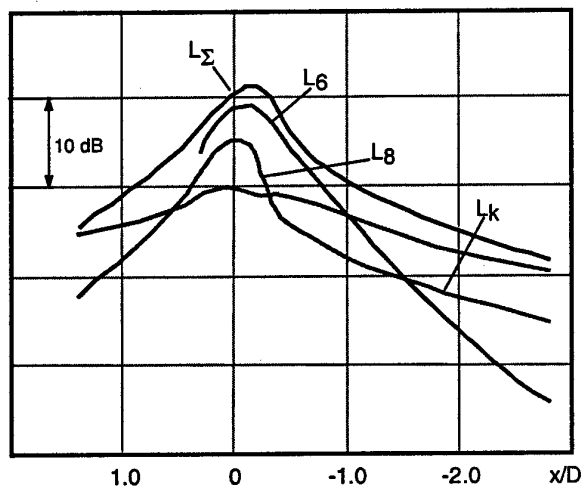


Fig. 12. Sound pressure levels produced by (6+8)-blade counterrotation propfan.

"Smart" Blade Effects on the Aeroelastic Characteristics of Helicopter Rotors

Fred Nitzsche

National Research Council Canada / Institute for Aerospace Research
Ottawa, ON, K1A 0R6, Canada

Solaiman A and Fred F. Afagh

Carleton University
Ottawa, ON, K1S 5B6, Canada

Abstract

In the present study, the three-dimensional, non-linear, aeroelastic stability of a reduced-scaled model of a helicopter rotor blade subject to harmonic parametric excitation in the rotating frame is investigated. The analyses are conducted using Floquet's theory for the stability of periodic systems. Using a square-wave (on-off) control law with frequencies 3, 4 and 5/rev, the stability margins of a "smart" blade incorporating a harmonic parametric excitation device under development at the National Research Council of Canada are obtained for the hover condition and compared with a baseline case. The results indicate that the stability of the periodic system is greatly affected when the actuation is performed. The analyses demonstrate that significant shifts in the modal frequency associated with the aeroelastic modes of the blade result from actuation, suggesting the feasibility of tailoring the forced frequency response of the blade and actively control phenomena such as the noise generated by blade vortex interaction in helicopter rotors.

Nomenclature

a	Lift-curve slope
A	Section area, $\iint_A d\eta d\zeta$
B	Number of blades
c	Blade chord
c_{d_0}	Drag coefficient
E	Young's modulus
G	Shear modulus
I_y, I_z	Area moments of inertia, $\iint_A \zeta^2 d\eta d\zeta, \iint_A \eta^2 d\eta d\zeta$
J	Area polar moment of inertia corrected for warping, $\iint_A (\hat{\eta}^2 + \hat{\zeta}^2) d\eta d\zeta$
k_A^2	Area radius of gyration, $\iint_A (\eta^2 + \zeta^2) d\eta d\zeta / A$
k_m^2	Mass radius of gyration, $k_{m_1}^2 + k_{m_2}^2$
$k_{m_1}^2, k_{m_2}^2$	$\iint_A \rho \zeta^2 d\eta d\zeta / m, \iint_A \rho \eta^2 d\eta d\zeta / m$
L_v, L_w	Aerodynamic forces in the v - and w -directions per unit of length

m	Mass per unit of length, $\iint_A \rho d\eta d\zeta$
M, C, K	Generalized mass, damping and stiffness matrices
M_ϕ	Aerodynamic moment in the ϕ -direction per unit of length
P, Q	Matrix of periodic coefficients, transition matrix solution
R	Rotor radius
t	Time
T	Period of actuation
u, v, w	Blade extensional, lead-lag and flap bending displacements (along x, y, z)
U	Matrix of non-rotating eigenvectors
v_i	Rotor induced velocity
x, y, z	Undeformed blade coordinate system (x is the elastic axis)
X	Vector of generalized displacements
β_{pc}	Pre-cone angle
γ	Lock number, $3\rho_\infty acR/m$
ϕ, ϕ_0	Twist displacement, twist displacement at steady-state (trim) condition
ρ, ρ_∞	Structural mass density, air density
η, ζ	Principle coordinate system of the blade cross section
σ	Rotor solidity, $Bc/\pi R$
ψ	Azimuth angle
λ	Eigenvalue of the transition matrix
ω, ξ	Frequency, damping of the aeroelastic mode
ω_{NR}^2	Matrix of non-rotating eigenvalues squared
Ω	Rotor spin velocity
θ	Blade pitch angle
$()'$	Derivative with respect to x
$(\dot{ })$	Derivative with respect to t or ψ
$(-)$	Non-dimensionalized quantity

Introduction and Background

The excellent mission characteristics of helicopters cannot be exploited more extensively, especially in the civilian market, due to the high exterior noise level generated by the aircraft. The most important component of the external noise occurs during maneuvering flight and landing, when the rotor blades interact more strongly with the vortices shed by the tip of preceding blades, resulting in the phenomenon known as blade vortex interaction (BVI). This interaction leads to an impulsive change in the blade loading that generates a pressure perturbation in the flow field above and below the rotor disk. The perturbation that propagates as a sound wave below the rotor disk is particularly annoying because it eventually reaches the ground in the form of a strong slapping noise whose frequency spectrum is periodic and most intense between the 6th and the 40th harmonic of the rotor frequency (Ref. 1).

It has been shown that the BVI noise intensity depends strongly on the rotor speed, vortex strength, blade-vortex miss distance, blade local angle-of-attack at the moment of blade-vortex

interaction, age of the vortex, alignment of the vortices structure with respect to the blade span, and airfoil shape (Ref. 2-8).

Figure 1 depicts a two-dimensional model of a free vortex passing underneath a blade element. The vortex moves with the free flow towards the airfoil until the actual interaction starts. The free vortex is assumed to have the constant circulation Γ . The higher the circulation of the vortex, the steeper is the velocity gradient induced by the vortex on the blade element. Also, the shorter the miss distance r , the larger would be the velocity gradient. The BVI phenomenon can be closely related to the aerodynamic response of the airfoil to a gust. It is worthwhile to point out the fact that a simple change in the reference coordinate system will pose the problem in terms of the effect of a fast moving airfoil on a stationary vortex structure. Sharp-edged gusts generate compressible waves that are similar in nature to the BVI-related acoustic waves.

According to Fig. 1, the bound circulation of the blade element Γ_0 produces the pressure coefficient distribution c_{p_0} when the vortex is far away. At the instant of time t_1 the core of the free vortex is located directly underneath the leading edge of the airfoil. The leading edge of the free vortex induces a downwash on the airfoil that reduces the pressure coefficient to c_{p_1} . At the instant of time t_2 the core of the free vortex has moved a short distance downstream. Its trailing edge now induces an upwash on the airfoil, increasing the pressure coefficient to c_{p_2} . Since the interval $\Delta t = t_2 - t_1$ is very small, the variation on the pressure distribution causes a pulse-type perturbation on the fluid flow (a dipole perturbation to a first approximation) that propagates above and below the airfoil. In a typical helicopter rotor operation, the flow on the lower side of the airfoil is close to transonic. The flow acceleration, is induced by the proximity of the vortex, is directly proportional to its strength and inversely proportional to the blade-vortex miss distance. This vortex generates a supersonic region bounded by a strong shock wave on the lower side of the airfoil. The whole structure consisting of the supersonic region, shock wave and vortex moves with the mean flow in the downstream direction. The induced velocity also moves the stagnation point from the nose towards the upper side of the airfoil increasing the stagnation pressure at the upper side of the leading edge of the airfoil by almost 50%. As the vortex passes, the stagnation point briefly migrates to the lower side and then back to its original position. The unsteady pressure fluctuation in the nose region causes the emission of the compressible wave that starts to travel in the upstream direction. When the vortex separates from the supersonic pocket in the lower side region of the airfoil close to its tail, the supersonic pocket breaks down immediately. Since a low-pressure region is present downstream the shock, when the supersonic pocket breaks down a weak transonic shock wave is released. Both the compressible and the transonic waves are the two members of the perfect dipole pressure perturbation that would be expected for low Mach numbers. In the high Mach number case, a deviation of the ideal dipole occurs as the largest amplitudes of pressure perturbation are not normal to the airfoil, but oblique and slightly rotated towards the direction of motion of the airfoil.

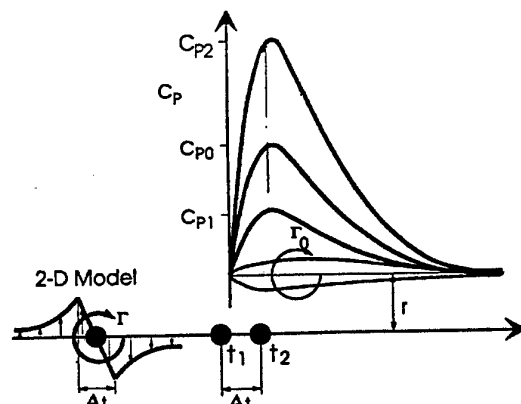


Figure 1: Basic mechanism of BVI noise generation.

The interval Δt is directly proportional to the age of the vortex. Vortices originated from earlier passages of the blades have larger cores that produce smoother pressure gradients, as well as spectra of BVI-related noise with less intense poorer harmonic-content.

BVI normally occurs along large sections of the blade span. The free vortices emanating from the tip of the blades have spiral trajectories that roll outwards, and eventually interact with the following blade in a formation almost parallel to its leading edge. When this situation occurs, high levels of BVI noise are generated because the phenomenon is produced in unison along a large section of the blade span. In general, these critical conditions are observed in two distinct regions in the advancing and retreating sides of the rotor.

Attenuating BVI by Individual Blade Control

As explained in the previous section, BVI noise is generated by the interaction of a blade with the free vortices produced at the tip of the blades during previous passages. This is a phenomenon that cannot be avoided due to the continuity laws of the bound circulation in a finite wing. The phenomenon becomes more intense when the blade operates close to its own wake, as in the case of a landing or maneuvering flight. However, both the strength and the trajectory of the vortices may be altered by suitable aerodynamic design. Alternatively, active control techniques may be used to change the angle-of-attack of the following blades with respect to the mean flow either increasing the blade-vortex miss distance or controlling the local angle of attack. The latter approach to the problem is more flexible because it can be adaptive and work efficiently under different flight conditions.

Studies indicate that there is considerable reduction of the transonic wave strength, when the angle of attack of the airfoil is modified during the BVI process (Ref. 9). Hence, a very efficient way of attenuating BVI can be achieved by active control. In fact, further wind tunnel experimental results in the HELINOISE program proved that the individual blade control (IBC) technique reduces both vibration and BVI noise in a rotor model (Ref. 10).

The present paper deals with the development of a "smart" hingeless helicopter blade for which the spectrum associated with the forced aeroelastic response of the blade may be tuned by superimposing a harmonic parametric excitation in the rotating frame. One may control the

frequency response associated with the local angle of attack of the blade rotor in the rotating frame according to the IBC concept proposed by Kretz (Ref. 11) and Ham (Ref. 12). The final objective of such an approach is to synthesize a suitable control system that breaks down the effect of the parallel vortex structures and, hence, minimizes BVI noise. In the present paper, the aeroelastic stability analysis of a rotor blade under parametric harmonic excitation is investigated.

Blade Equations of Motion for Parametric Harmonic Excitation

The main objective of this study is to investigate the aeroelastic stability of the rotating blade system undergoing parametric harmonic excitation using a device that modifies the impedance of the blade structure (Ref. 13). As an initial attempt only hover flight conditions are considered. Moreover, the rotor is modeled as a long, straight, slender, homogeneous isotropic beam with a constant axial twist for which the offsets between the tension, elastic, mass and aerodynamic axes are negligible.

The non-linear terms in the perturbed equations of motion are linearized about the trim (steady state) displacements. This allows the use of the conventional Floquet's theory for the stability analysis of linear periodic systems.

Using two complimentary methods: (1) the variational method based on Hamilton's principle, and (2) the Newtonian method, Hodges and Dowell derived the non-linear flap-lag-torsion equations of motion of a twisted non-uniform rotor (Ref. 14). Later, Hodges and Ormiston simplified these equations for a uniform rotor blade and investigated the associated stability problem (Ref. 15). The main parameters influencing the stability were found to be the structural coupling between the flap and lag bending as well as the torsion stiffness. The harmonic parametric excitation proposed in the present work required further elaboration (Ref. 16). For this, the flap, lag, and torsion stiffness as well as the mass radii of gyrations of the cross section were assumed to be functions of x , the axial coordinate that defines the distance of a given cross section from the hub. The latter functions were then incorporated into the equations defining the linear perturbations about the equilibrium position to investigate the stability of the IBC system.

The blade elastic displacements considered in the analysis are the axial u , the transverse v , and the transverse w , associated with the lead-lag bending, the flap bending, and the twist ϕ (Figure 2). In the derivation of the equations of motion, an ordering scheme based on the restriction that the squares of the bending slopes, torsion deformation, chord/radius and thickness/radius ratios were small compared to unity was adopted according to Hodges and Dowell (Ref. 14). Finally, the model can be simplified by solving for u in terms of the local tension, and assuming that the radial displacement of the rotor blade is a purely geometric consequence of the transverse bending deflections of the blade. It should be noted that such an assumption is valid only for sufficiently large values of dimensionless radial stiffness.

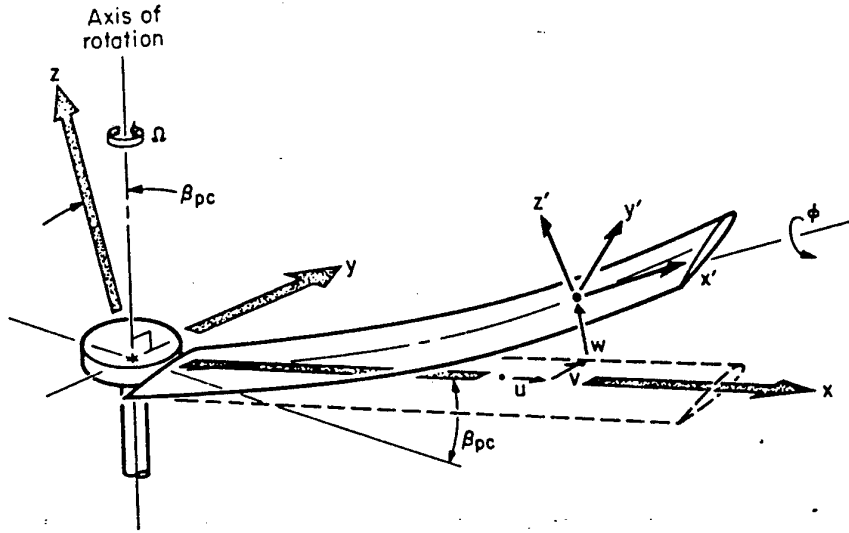


Figure 2: Blade definitions (Ref. 15).

The following three equations for v , w , and ϕ can be derived (Ref. 15):

$$\begin{aligned}
 & -\frac{m\Omega^2}{2} \left[v'(R^2 - x^2) \right]' - 2m\Omega \left(v' \int_x^R \dot{v} dx \right)' + [EI_z - (EI_z - EI_y) \sin^2(\mathcal{R}\theta)] v'''' \\
 & + (EI_z - EI_y) \frac{\sin(2\mathcal{R}\theta)}{2} w'''' + (EI_z - EI_y) \left[-\sin(2\mathcal{R}\theta) (\phi v'')'' + \cos(2\mathcal{R}\theta) (\phi w'')'' \right] \\
 & - 2m\Omega \beta_{pc} \dot{w} - 2m\Omega \int_0^x (v' \dot{v}' + w' \dot{w}') dx + m(\ddot{v} - \Omega^2 v) = L_v
 \end{aligned} \quad (1)$$

$$\begin{aligned}
 & -\frac{m\Omega^2}{2} \left[w'(R^2 - x^2) \right]' - 2m\Omega \left(w' \int_x^R \dot{v} dx \right)' + [EI_y + (EI_z - EI_y) \sin^2(\mathcal{R}\theta)] w'''' \\
 & + (EI_z - EI_y) \frac{\sin(2\mathcal{R}\theta)}{2} v'''' + (EI_z - EI_y) \left[\cos(2\mathcal{R}\theta) (\phi v'')'' + \sin(2\mathcal{R}\theta) (\phi w'')'' \right] \\
 & + 2m\Omega \beta_{pc} \dot{v} + m\ddot{w} = L_w - m\Omega^2 \beta_{pc} x
 \end{aligned} \quad (2)$$

$$\begin{aligned}
 & -\frac{m\Omega^2}{2} k_A^2 \left[\phi'(R^2 - x^2) \right]' - GJ\phi'' + mk_m^2 \ddot{\phi} + m\Omega^2 (k_{m_2}^2 - k_{m_1}^2) \phi \cos(2\theta) \\
 & + (EI_z - EI_y) \left[(w''^2 - v''^2) \frac{\sin(2\mathcal{R}\theta)}{2} + v'' w'' \cos(2\mathcal{R}\theta) \right] = M_\phi - m\Omega^2 (k_{m_2}^2 - k_{m_1}^2) \frac{\sin(2\theta)}{2}
 \end{aligned} \quad (3)$$

where \mathcal{R} is a coupling parameter that can be assigned any arbitrary value between 0 to 1, representing the completely uncoupled and coupled cases, respectively.

The aerodynamic loads applied to the rotor blade used in this study are based on Greenberg's extension of the Theodorsen's theory (Ref. 17). This model is valid for a two-dimensional airfoil undergoing sinusoidal motion in pulsating incompressible flow. The basis of this formulation is

strip theory in which only velocity components in the directions perpendicular to the spanwise axis of the blade influence the aerodynamic loads. A quasi-steady approximation of the unsteady theory for low reduced frequencies is employed, in which the Theodorsen lift-deficiency function is taken to be unity. The classical blade element momentum theory is used to calculate the steady inflow for the rotor. The aerodynamic loads are, thus, expressed as:

$$L_v = \frac{\rho_\infty a c}{2} \left\{ v_i^2 - \Omega^2 x^2 \frac{c_{d0}}{a} - \Omega x v_i (\theta + \phi) - \left[2\Omega x \frac{c_{d0}}{a} + (\theta + \phi) v_i \right] \dot{v} + [2v_i - \Omega x (\theta + \phi)] \dot{w} \right\} \quad (4)$$

$$L_w = \frac{\rho_\infty a c}{2} \left\{ -\Omega x v_i + \Omega^2 x^2 \left(\theta + \phi + \int_0^x v' w'' dx \right) - \Omega^2 x v (\beta_{pc} + w') + \Omega^2 \frac{x c}{2} (\beta_{pc} + w') \right. \\ \left. + [2\Omega x (\theta + \phi) - v_i] \dot{v} - \Omega x \dot{w} + \frac{3xc}{4} \Omega \dot{\phi} - \frac{c}{4} \ddot{w} \right\} \quad (5)$$

$$M_\phi = -\frac{\rho_\infty a c}{2} \left(\frac{x c^2}{8} \Omega \dot{\phi} \right) \quad (6)$$

where v_i is the induced inflow velocity that is taken to be steady and uniform along the blade radius and equal to the value of the non-uniform inflow given by blade momentum theory at 0.75 radius. The value of the blade angle at that particular position is equal to the pitch angle plus the equilibrium elastic twist at 0.75 radius. Thus:

$$v_i = \text{sgn}[\theta + \phi_0(0.75R)] \Omega R \frac{\pi \sigma}{8} \left(\sqrt{1 + \frac{12}{\pi \sigma} |\theta + \phi_0(0.75R)|} - 1 \right) \quad (7)$$

The non-linear, equations of motion with variable coefficients (Eqs. 1-3) are solved by Galerkin's method. To this end, once these equations are appropriately non-dimensionalized, in order to apply Galerkin's method, the flap, lead-lag and twist displacements are prescribed as a series in generalized coordinates and mode shape functions:

$$\bar{v} = \sum_{j=1}^N V_j(\psi) \Psi_j(\bar{x}), \quad \bar{w} = \sum_{j=1}^N W_j(\psi) \Psi_j(\bar{x}), \quad \phi = \sum_{j=1}^N \Phi_j(\psi) \Theta_j(\bar{x}) \quad (8)$$

where the non-dimensional quantities defined in Eq. 8 are:

$$\psi = \Omega t, \quad \bar{x} = \frac{x}{R}, \quad \bar{v} = \frac{v}{R}, \quad \bar{w} = \frac{w}{R} \quad (9)$$

The assumed comparison functions,

$$\Psi_j(\bar{x}) = \cosh(\beta_j \bar{x}) - \cos(\beta_j \bar{x}) - \alpha_j [\sinh(\beta_j \bar{x}) - \sin(\beta_j \bar{x})] \\ \Theta_j(\bar{x}) = \sqrt{2} \sin(\gamma_j \bar{x}) \quad (10)$$

are the non-rotating, uncoupled natural modes of a uniform cantilevered beam for which the constants α_j, β_j and γ_j are tabulated (Ref. 18). Substitution of Eq. 8 into Eqs. 1-6, considering the expressions shown in Eq. 10, yields $3N$ equations of motion in terms of the generalized coordinates V_j, W_j and Φ_j , where N is the number of natural modes of the uniform beam retained. The resulting non-linear ordinary differential equations of motion are linearized for small perturbations about an equilibrium or trim condition. To achieve this, the generalized coordinates were decomposed into steady-state equilibrium quantities and small perturbations as follows:

$$V_j(\psi) = V_{0j} + \Delta V_j(\psi), \quad W_j(\psi) = W_{0j} + \Delta W_j(\psi), \quad \Phi_j(\psi) = \Phi_{0j} + \Delta \Phi_j(\psi) \quad (11)$$

This procedure led to two sets of equations of motion. By substituting the steady-state equilibrium quantities of the generalized displacements into the non-linear equations of motion, a first set of non-linear algebraic equilibrium equations was obtained. The second set of equations was available by substituting both the steady state and perturbation quantities of the generalized displacements into the original equations, subtracting the equilibrium equations obtained above, and neglecting all the non-linear products of the perturbation quantities. A set of $3N$ linear differential equations on the perturbation quantities for which the coefficients were functions of the equilibrium solution was obtained. The latter equations define the blade motion about the equilibrium or trim displacements:

$$[M]\{\ddot{X}\} + [C]\{\dot{X}\} + [K]\{X\} = \{0\} \quad (12)$$

where the matrices are defined by Hodges and Ormiston (Ref. 15). It is desirable to reduce the order of the system by transformation to modal coordinates. The real-valued, free-vibration eigenvalue problem associated with the non-rotating blade was solved:

$$[M_s][U][\omega_{NR}^2] = [K_s][U] \quad (13)$$

where the subscript s is applied to the corresponding matrices without the aerodynamic contribution. Hence the stability of the perturbed motion about the equilibrium condition is determined by the eigenvalues of the square matrix of dimension $2m$:

$$\begin{Bmatrix} \dot{\tilde{X}} \\ \ddot{\tilde{X}} \end{Bmatrix} = \begin{bmatrix} 0 & I \\ -\tilde{M}^{-1}U^T K U & -\tilde{M}^{-1}U^T C U \end{bmatrix} \begin{Bmatrix} \tilde{X} \\ \dot{\tilde{X}} \end{Bmatrix} \quad (14)$$

where m is the number of modes retained and \tilde{M} is the diagonal matrix:

$$[U]^T [M][U] = [\tilde{M}] \quad (15)$$

Another consequence of coordinate transformation $X = U\tilde{X}$ is that only the eigenvectors of the modal matrix U that correspond to the desired frequencies can be selected. For the present study, $N=6$ and $m=4$ (including the first lead-lag, first and second flap, and first torsion eigenvectors).

The aerodynamic term in the mass matrix known as the apparent mass was of a smaller order of magnitude and thus neglected in the present analysis, i.e. $M \approx M_s$.

The harmonic parametric excitation introduces a periodic change in the matrices defined in Eq. 12. A variation in the amplitude of these matrices, according to a square-wave form, will be added, representing actuation and de-actuation of the IBC system in an on-off configuration. Over one normalized period of the blade rotation, 2π , it will be assumed that the control system is activated at a frequency of n/rev . Hence,

$$([M] + [\Delta M])\{\ddot{X}\} + ([C] + [\Delta C])\{\dot{X}\} + ([K] + [\Delta K])\{X\} = \{0\} \quad (16)$$

where the new matrices for a particular actuator are defined by A and Afagh (Ref. 16), and

$$[\Delta M] = [\Delta C] = [\Delta K] = [0]; \quad 2j\frac{\pi}{n} \leq \psi \leq (2j+1)\frac{\pi}{n} \quad (j = 0, 1, 2, \dots) \quad (17)$$

yielding the set of linear periodic differential equations and solution:

$$\begin{Bmatrix} \dot{\tilde{X}} \\ \ddot{\tilde{X}} \end{Bmatrix} = [P(\psi)] \begin{Bmatrix} \tilde{X} \\ \dot{\tilde{X}} \end{Bmatrix} \Rightarrow \begin{Bmatrix} \tilde{X}(T) \\ \dot{\tilde{X}}(T) \end{Bmatrix} = [Q(0, T)] \begin{Bmatrix} \tilde{X}(0) \\ \dot{\tilde{X}}(0) \end{Bmatrix} \quad (18)$$

Floquet's method for periodic systems was used in the present study to perform the stability analysis (Ref. 19). The eigenvalues of the transition matrix $Q(0, T)$ over one complete period of actuation, from $\psi = 0$ to $\psi = T = \pi/n$ were examined:

$$\begin{aligned} \bar{\xi}_k &= (1/2T) \ln [\text{Re}^2(\lambda_k) + \text{Im}(\lambda_k)] \\ \bar{\omega}_k &= (1/T) \tan^{-1} [\text{Im}(\lambda_k) / \text{Re}(\lambda_k)] \end{aligned} \quad (19)$$

The real part of the k^{th} eigenvalue of the transition matrix represents the non-dimensional growth/decay rate of the aeroelastic response to the system. A positive value indicates instability. The imaginary part of the same eigenvalue is associated with the non-dimensional frequency. Since the function \tan^{-1} is multi-valued, the latter can be obtained only as a principal frequency plus or minus an integer multiple of $2\pi T$. In the following section, numerical results are obtained considering the principal value of the modal frequencies.

Numerical Results

The aeroelastic stability analysis of a reduced-scale blade model based on the EUROCOPTER BO105 helicopter rotor was performed. The rotor was adapted to have an IBC system using the harmonic parametric excitation device developed at the National Research Council Canada ("Smart" Spring). The parameters of the rotor model analyzed are listed in Table 1.

Table 1: Rotor Model Analyzed

Parameter	Value
a	$2\pi \text{ rad}^{-1}$
B	4
c	0.121 m
c_{d_0}	0.01
$EI_y/m\Omega^2 R^4$	0.0017 ⁽¹⁾
$EI_z/m\Omega^2 R^4$	0.0222 ⁽²⁾
$GJ/m\Omega^2 R^4$	0.001 ⁽³⁾
R	2.0 m
\mathfrak{R}	1.0 (fully coupled)
β_{pc}	0°
γ	5.0
σ	0.077
Ω	110 rpm

⁽¹⁾ Corresponding to a normalized lead-lag frequency 0.7/rev at 110 rpm.

⁽²⁾ Corresponding to a normalized first flap bending frequency 1.14/rev at 110 rpm.

⁽³⁾ Corresponding to a normalized torsion frequency 3.9/rev at 110 rpm.

In the following simulations, the IBC actuator was placed at the inner sections of the blade covering 15% of the blade radius (between stations $\bar{x} = 0.05$ and $\bar{x} = 0.20$). In Tables 2 to 5, the complex roots associated with the evolution of the non-dimensional frequency (imaginary part) and non-dimensional damping (real part) versus the pitch angle of the first lead-lag, first flap, second flap and first torsion aeroelastic modes of the blade are shown, respectively. These tables display the baseline case corresponding to the blade without the harmonic parametric excitation device, a "non-activated" case for which only the static contribution of the actuator is included in the analysis, and the cases corresponding to actuation at 3, 4 and 5/rev in a square-wave form, respectively.

Table 2: Root loci for the 1st lead-lag mode

θ (rad)	Baseline	Non-activated	Activated (3/rev)	Activated (4/rev)	Activated (5/rev)
0.0	-0.0011+0.656i	-0.0011+0.775i	-0.0011+0.718i	-0.0011+0.718i	-0.0011+0.718i
0.1	-0.0567+0.605i	-0.0466+0.766i	-0.0182+0.668i	-0.0203+0.664i	-0.0201+0.658i
0.2	-0.158+0.422i	-0.197+0.696i	-0.191+0.586i	-0.186+0.583i	-0.205+0.569i
0.3	0.456 (D); -1.41	0.319 (D); -1.47	-0.0823; -1.09	-0.0006; -1.14	-0.340+0.205i

Table 3: Root loci for the 1st flap mode

θ (rad)	Baseline	Non-activated	Activated (3/rev)	Activated (4/rev)	Activated (5/rev)
0.0	-0.324+0.971i	-0.329+1.07i	-0.326+0.951i	-0.339+0.971i	-0.334+0.962i
0.1	-0.269+0.958i	-0.274+1.05i	-0.338+0.953i	-0.309+0.958i	-0.353+1.07i
0.2	-0.175+0.989i	-0.130+1.05i	-0.144+0.963i	-0.138+0.983i	-0.133+1.01i
0.3	-0.0955+0.926i	-0.0377+0.926i	-0.184+0.868i	-0.247+0.853i	-0.0374+1.01i

Table 4: Root loci for the 2nd flap mode

θ (rad)	Baseline	Non-activated	Activated (3/rev)	Activated (4/rev)	Activated (5/rev)
0.0	-0.758+1.91i	-0.816+1.98i	-0.785+1.77i	-0.786+1.97i	-0.787+2.22i
0.1	-0.720+1.89i	-0.787+1.97i	-0.728+2.00i	-0.743+1.83i	-0.747+1.78i
0.2	-0.682+1.72i	-0.754+1.82i	-0.708+1.89i	-0.711+1.79i	-0.712+4.45i
0.3	-0.434+1.16i	-0.440+1.34i	-0.173+1.30i	-0.108+0.911i	-0.501+0.957i

Table 5: Root loci for the 1st torsion mode

θ (rad)	Baseline	Non-activated	Activated 3/rev	Activated 4/rev	Activated 5/rev
0.0	-0.304+2.76i	-0.362+3.23i	-0.318+3.17i	-0.322+2.99i	-0.325+3.07i
0.1	-0.386+3.02i	-0.619+4.10i	-0.494+2.96i	-0.507+2.97i	-0.459+3.20i
0.2	-0.536+3.54i	-1.06+4.90i	-0.804+4.77i	-0.813+4.96i	-0.799+4.73i
0.3	-0.784+4.01i	-1.02+4.71i	-0.990+4.72i	-1.01+0.565i	-1.05+0.444i

The results indicate that the blade is always stable, except for the divergence condition achieved for the lead-lag mode when $\theta = 0.3$ radians (root identified in Table 2 by the letter "D"). For this unlikely high value of the commanded pitch angle (approximately 17 degrees), activation of the IBC controller actually stabilized the blade at the zero frequency (in the 3 and 4/rev cases) and at a low frequency (in the 5/rev case). The tables also indicate that in general, especially for the more feasible values of the pitch angle, activation of the IBC controller improves the system stability margins.

Although at this point no definite conclusion can be drawn regarding the blade forced frequency response when excited by BVI, the results demonstrate that the aeroelastic modal frequencies considerably change with respect to the baseline case when IBC is activated. As a result, a significant impact on the frequency response of the blade can be expected. In Figure 3, a comparison is provided involving the evolution of the torsion mode (non-dimensional frequency and damping) with the commanded pitch angle for the case of IBC activation at 3/rev.

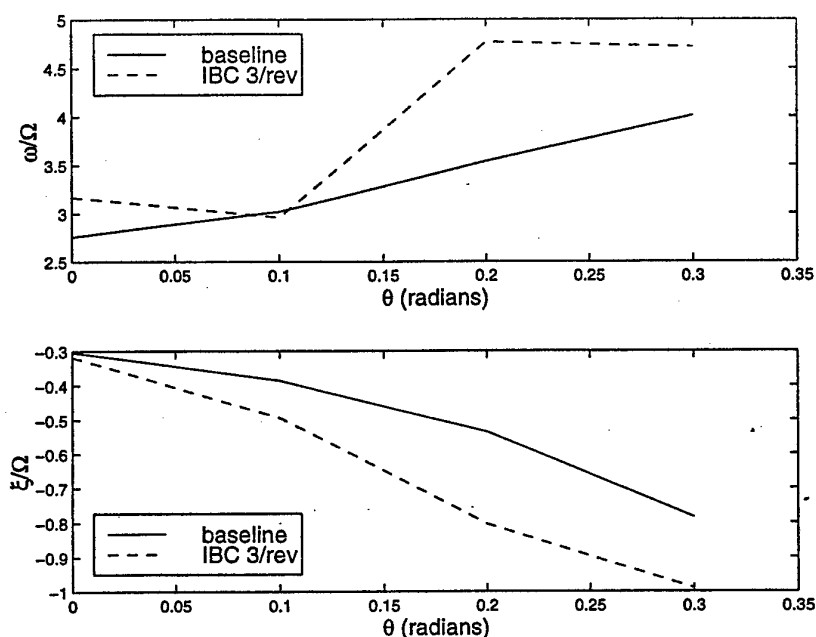


Figure 3: Effect of IBC operating at 3/rev (on-off control law) on the stability of the first torsion aeroelastic mode of the blade. "Smart" blade with actuation device extending from stations 5 to 20% along the blade.

Conclusions

It was observed in the previous section that the harmonic parametric excitation device affected the aeroelastic stability of the system. Unstable conditions associated with the basic blade that was encountered for large values of the pitch angle could be stabilized using IBC. However, one may expect that IBC will not always be beneficial to the overall stability of the system. As noted by Bolotin (Ref. 20), one may expect that the harmonic parametric excitation when approaching the frequency associated with the structural modes cause stability problems.

The present analysis also demonstrates that the dynamic characteristics of the "smart" helicopter blade may be significantly changed. In the simulations presented in this work, data associated with a typical rotor model were employed, more importantly indicating the feasibility of the solution when a carefully engineered project is conducted.

References

1. Johnson, W., *Helicopter Theory*, Princeton University Press, 1980, pp. 903-905.
2. Spettstösser, W.R., Niesl, G., Cenedese, F., Nitti, F. and Papanikas, D.G., "Experimental Results of the European HELINOISE Aeroacoustic Rotor Test in the DNW," Paper B8, *Proceedings: 19th European Rotorcraft Forum*, Cernobbio, Italy, September 14-16, 1993.
3. Yu, Y.H., Gmelin, B., Heller, H., Philippe, J.J., Mercker, E. and Preisser, J., "HHC Aeroacoustics Rotor Test at the DNW - The Join German/French/US HART Project," Paper

- 115, *Proceedings: 20th European Rotorcraft Forum*, Amsterdam, The Netherlands, 4-7 October, 1994.
4. Kube, R., Spettstösser, W.R., Wagner, W., Seelhorst, U., Yu, Y.H., Boutier, A., Micheli, F. and Mercker, E., "Initial Results from the Higher Harmonic Control Aeroacoustic Rotor Test (HART) in the German-Dutch Wind Tunnel," AGARD Report CP-552, NATO, August 1995, pp. 25/1-11.
5. Swanson, S.M., Jacklin, S.A., Niesl, G., Blaas, A. and Kube, R., "Effect of Individual Blade Control on Noise Radiation," AGARD Report CP-552, NATO, August 1995, pp. 19/1-12.
6. Schultz, K. -J., Spettstösser, W.R., Junker, B., Wagner, W., Schöll, E., Arnaud, G., Mercker, E., Pengel, K. and Fertis, D., "A Parametric Wind Tunnel Test on Rotorcraft Aerodynamic and Aeroacoustics (HELISHAPE) - Test Procedures and Representative Results," Paper 52, *Proceedings: 22nd European Rotorcraft Forum*, Brighton, UK, 17-19 September, 1996.
7. VanDerWall, B.G., "The Impact of Rotor Angle of Attack on BVI Trajectories and Rotor Load Characteristics, Paper 40, *Proceedings: 20th European Rotorcraft Forum*, Amsterdam, The Netherlands, 4-7 October, 1994.
8. Ehrenfried, K. and Meier, G.E.A., "Numerical Investigation of the Basic Mechanisms of BVI-Noise Generation," Paper B9, *Proceedings: 19th European Rotorcraft Forum*, Cernobbio, Italy, September 14-16, 1993.
9. Nellessen, D., Britten, G. and Ballmann, J., "Numerical Simulation of Individual Blade Control," Paper 84, *Proceedings: 22nd European Rotorcraft Forum*, Brighton, UK, 17-19 September 1996.
10. Kube, R. and Schultz, K. -J., "Vibration and BVI Noise Reduction by Active Rotor Control: HHC Compared to IBC," Paper 85, *Proceedings: 22nd European Rotorcraft Forum*, Brighton, UK, 17-19 September 1996.
11. Kretz, M., "Research in Multicyclic and Active Control of Rotary Wings," *Vertica*, Vol. 1, No. 1/2, 1976, pp. 95-105.
12. Ham, N.D., "Helicopter Individual Blade Control at MIT 1977-1985", *Vertica*, Vol. 11, No. 1/2, 1987, pp. 109-122.
13. Nitzsche, F., "Modelling an Adaptive Impedance Boundary Condition Device for Helicopter Individual Blade Control," *Proceedings: SPIE Vol. 3039*, 1997, pp. 216-226.
14. Hodges, D.H. and Dowell, E.H., "Non-Linear Equations of Motion for the Elastic Bending and Torsion of Twisted Nonuniform Rotor Blades," NASA TN D-7818, December 1974.
15. Hodges, D.H. and Ormiston, R.A., "Stability of Elastic Bending and Torsion of Uniform Cantilever Rotor Blade in Hover with variable Structural Coupling," NASA TN D-8192, April 1976.
16. A, S. and Afagh, F.F., "Helicopter Individual Blade Control Strategies using "Smart" Structures," Final Report, PWSGC Contract No. 31184-6-0296/001/ST, Carleton University, Ottawa, Canada, June 1999.
17. Greenberg, J.M., "Airfoil in Sinusoidal Motion in Pulsating Stream," NACA TN 1326, 1947.
18. Chang, T-C and Craig, R.R. Jr., "On Normal Modes of Uniform Beams," ERML 1068, University of Texas (Austin), 1969.
19. Dugundji, J. and Wendell, J.H., "Some Analysis Methods for Rotating Systems with Periodic Coefficients," *AIAA Journal*, Vol. 21, No. 6, 1982.
20. Bolotin, V.V., *Dynamic Stability of Elastic Systems*, Holden-Day Inc., 1964.

Study of noise and aerodynamics of advanced propellers (SNAAP Project)

A.Paonessa and A.Cafiero
Alenia - Aerospazio Pomigliano d'Arco (Napoli) - Italy

ABSTRACT

The project was performed within the European IMT programme and started on 1993 and completed its activities on 1996 after 42 months involving 15 organisations located in 7 different European countries:

Coordinator : Alenia

Partners : Aerospaziale, Dornier, Fokker, NLR, Dowty, Ratier-Figeac, Onera, Cira, UCG, IBK, TCD, IST

Subcontractor : ARA, DNW

Recent progress in aerodynamics, aeroelasticity, materials and structures has enabled the design of innovative propeller configurations which operate at the same cruise speeds as jet-propelled aircraft. The inherently high propulsive efficiency of these advanced propellers and propfans allows fuel savings with a corresponding reduction in exhaust emissions. The major drawback is the level of noise emitted by propellers operating at high rotational speeds. This is partly due to a lack of detailed information on the understanding of the physical phenomena involved so that commensurate progress in the aeroacoustics of advanced propellers is now essential.

The work described in this report is a first response to the above needs, and has been performed by a European Consortium under the financial support of the European Union. It represents a first joint European study on aircraft propeller aerodynamics and acoustics.

INTRODUCTION

In response to current economic and environmental crises, propulsion systems to be adopted during the next future on short range aircraft must offer substantial reductions in fuel consumption along with low noise emission. Furthermore improved passenger comfort and reduced environmental noise are becoming a strong requirements by airliners to the aircraft industry.

So that the long-term objective of this project is to enable the European aircraft industry to design quieter propeller-driven aircraft.

The major drawback is the level of noise emitted by propellers operating at high rotational speeds. The focus of the concluded program was on the understanding and

prediction of noise generated by the propeller. Realistic measurements are necessary to understand the noise generation and propagation phenomena.

The project IMT/SNAAP (Study of Noise and Aerodynamics of Advanced Propellers) started officially on January 1, 1993 and it was planned to last 36 months, but a 6 months of prolongation was necessary to complete the activities.

To achieve the objectives of the project, rigorously controlled experiments were essential and these were performed satisfactorily in two wind tunnels.

To ensure the general applicability of the theoretical and computational methods, two advanced model **propellers** have been designed and manufactured. These are composite six bladed propellers, one for a cruise Mach number of 0.7 with helical tip Mach number of 0.88 and the second a swept blade configuration with a cruise Mach number of 0.8 and a helical tip Mach of 1.1. The aero-design of the LSP (Low Speed Propeller) has been developed by Dornier during the project, while the aero-design for the HSP (High Speed Propeller) was available from the GEMINI project, and was given to the consortium by Aerospatiale.

Both the propeller models were manufactured by NLR, which replaced the subcontractor Hoffman Propeller during the first period of the project.

Testing have been conducted in two wind tunnel facilities. The ARA transonic wind tunnel and DNW subsonic wind tunnel have been used to perform aerodynamic and acoustic measurements at speeds typical of cruise missions of the aircraft and at low speeds typical of take-off and approach operation of the aircraft, respectively.

Numerical **codes** for the prediction of both aerodynamic and acoustic properties have been developed in parallel to the experimental programme. In particular one aerodynamic code have been produced by UCG, and gives input to two acoustic codes developed by ONERA and CIRA. Those three codes have been integrated in only one code (SNAAP_code).

Comparison between theoretical and experimental data have been made, to correlate the results, and to validate the code.

During the 42 months of activity the overall program progressed extremely well, even if some technical difficulties were encountered.

The excellent co-operation and strong contribution of all the participants allowed the respect of the project goals, and even if some delays occurred, the normal on going of the project was not influenced, and the results expected from the project have been fully obtained.

Here a summary of the activity performed in the several tasks of the project is reported.

TECHNICAL DESCRIPTION

Task 1 - Experimental data requirements

Was required to define testing laws and philosophy, such as scaling parameters, aerodynamics data and acoustics data to be investigated and identify the procedures. Two types of aircraft flight conditions have been simulated to define the condition at which the propellers have been tested: take-off (low Mach number, high angle of attack) and cruise (high Mach number, low angle of attack).

The targets of the scaling process were:

- to save the full scale helical tip Mach number
- to save full scale blades loading

A propeller diameter of 90 cm came out from a parametric study for both models.

Task 2 - Design and manufacture of two instrumented composite propeller models

Has been identified as the critical path of the project. The main objective was to provide two non-assembled propellers based on existing hub and spinner and new-instrumented composite blades.

The two-instrumented models are two 6-bladed propellers. The first one a Low Speed Propeller (LSP) is an advanced subsonic propeller for a cruise Mach number of 0.7 and helical tip Mach number of 0.88; the second one an High Speed Propeller (HSP) is a transonic one with a cruise Mach number of 0.78 and helical tip Mach number of 1.1. Both the propeller models have a diameter of 90 cm.

The composite blades, made of carbonfibers and epoxy resin, are equipped with pressure sensors (static and dynamic) and stress gages for monitoring; the mastery of this high technology conception has been a key element for the project global success.

In the following table a summary of the instrumentation implemented into the blades is reported:

LSP and HSP		
Sensors	Total n.	Blade n.
Static taps	165	4,5,6
Kulites	30	1,2,3
Strain Gauges	6	1,2

Task 3 - Adaptation of each advanced propeller model on test rig and installation in the wind tunnel:

Consisted of the commissioning of the SNAAP model and rig systems. The purpose of the commissioning was to ensure as far as possible that all the model and rig systems were functioning properly and safely, and ready for the two sets of wind tunnel test. It included checks on as much of the instrumentation as possible. All the commissioning work was undertaken at ARA Ltd, Bedford, UK, in the Powerplant Test House (PTH), and involved personnel from ARA, Dornier and DAP. The first period of commissioning began in July 1994, but was prematurely terminated by some serious problems, which are described below. After corrective actions had been successful and commissioning was successfully completed, and the model and rig moved into the ARA tunnel ready for testing to start.

The resulting delay to the programme was therefore approximately 6 months, however it was of the utmost importance to ensure that all systems were functioning properly before entry into the wind tunnels.

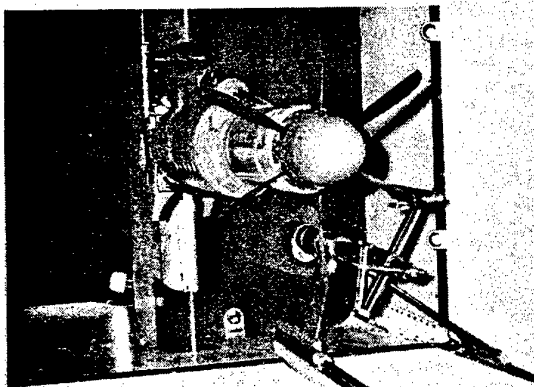
Task 4 - Wind tunnel testing and data reduction:

The purpose of the task 4 was to prepare and perform SNAAP experimental activities.

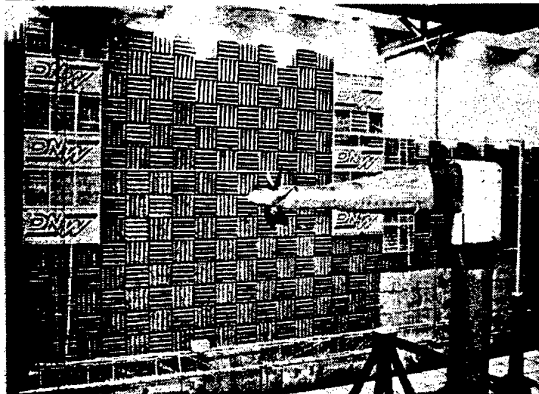
Two wind tunnel facilities have been used: ARA transonic wind tunnel, to simulate the cruise condition of the aircraft (high flight Mach numbers), and DNW low speed wind tunnel to simulate take-off, climb and approach conditions (low Mach numbers). Both wind tunnel tests have been safely conducted to a successful end.

Both SNAAP propellers (LSP and HSP) were tested in both tunnels. ARA was aiming at measurement of noise and performance at high speed and DNW at low speed.

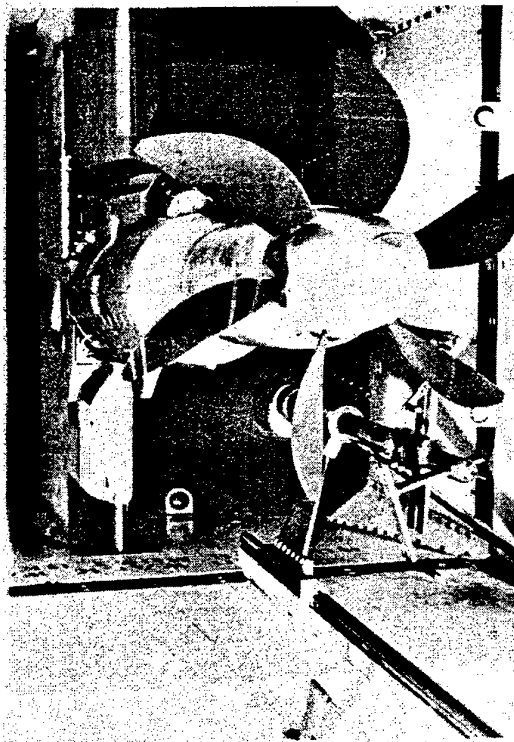
LSP in ARA TWT



LSP in DNW wind tunnel



HSP in ARA TWT



In the following the conditions at which the propellers have been tested are reported:

LSP at ARA

$\beta=61.8, 54.9$

Mach=0.60, 0.65, 0.70

$\alpha=0, 1.5, 3$

rpm=several from 2989 to 498.

LSP at DNW

$\beta=36.0, 39.0, 41.1$

Mach=0.10, 0.15, 0.20

$\alpha=0, 7.5, 15.0$

rpm=several from 1594 to 4544.

HSP at ARA

$\beta=40.39, 51.63, 40.39$

Mach=0.20, 0.5, 0.6, 0.74, 0.76, 0.78

$\alpha=0, 1.5, 3, 5, 10$

rpm=several from 4200 to 5143.

HSP at DNW

$\beta=35.0, 40.4$

Mach=0.10, 0.15, 0.20

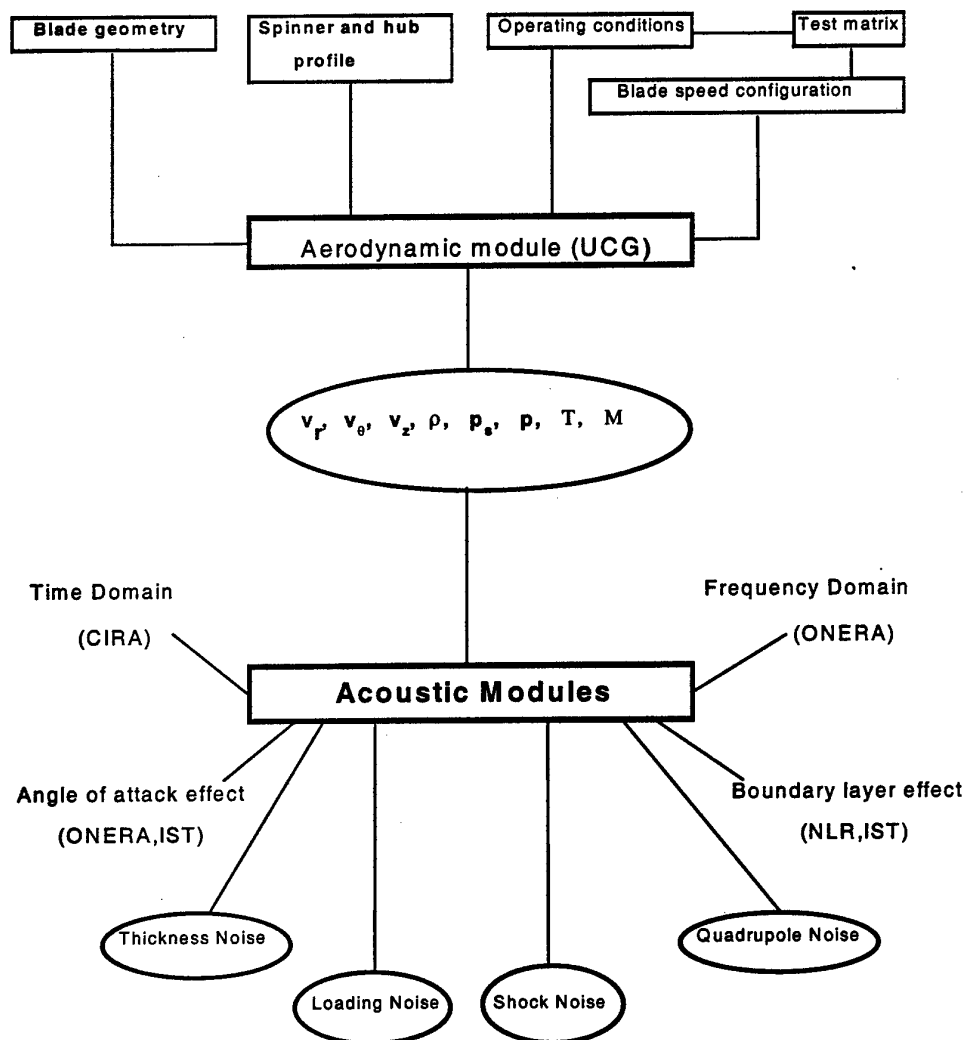
$\alpha=0, 5, 10, 15$

rpm=several from 3533 to 4796.

The data measured have been used to validate computer codes developed within the project

Task 5 - Theoretical/Numerical prediction codes and data correlation, which was considered the main part of the project, deals with the theoretical/numerical activity. The identification of the noise sources on advanced propellers and propfans, modelling the mechanism responsible for the sound generation and its propagation, and the development and validation of an aero-acoustic code capable of prediction of propeller noise, are the main goals of the project. Aeroacoustic codes have been produced and some of them validated with experimental data.

The structure of the main SNAAP code is reported in the following chart:



The activity was addressed to:

- ◆ Generate or improve code module
- ◆ Pre-test validation of the module
- ◆ Post-test validation
- ◆ Code integration
- ◆ Code validation

The code produced consists of several computer programs, which are linked together by a simple procedure. The aerodynamic module of this code, based on a 3D Euler equation, works within limits clearly investigated along the project: it cannot include non-axial inflow angles, and it is unable to converge below Mach 0.2.

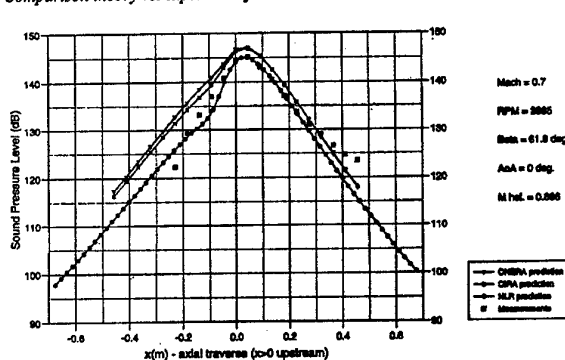
Two acoustic modules developed and validated within the project, are included in the code. Those modules use two different approaches one in the time domain, the other in the frequency domain; both use the input from the unique aerodynamic module.

Furthermore other acoustic tools have been developed within the project and are now available: one to predict the installation effect, due to the aircraft fuselage; another to identify the noise source using fluctuating pressure records.

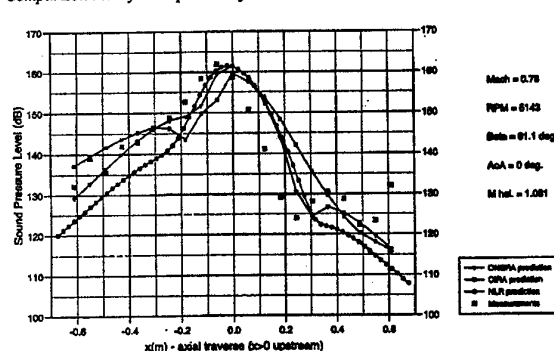
In addition some empirical methods or simplified models to account the scattering effect of the fuselage and of the angle of attack on the noise have been developed.

In the following figures comparisons between theory and experimental for the LSP and HSP at ARA and DNW are reported:

Comparison theory vs. experiment for LSP at ARA - case 7 - IBPF

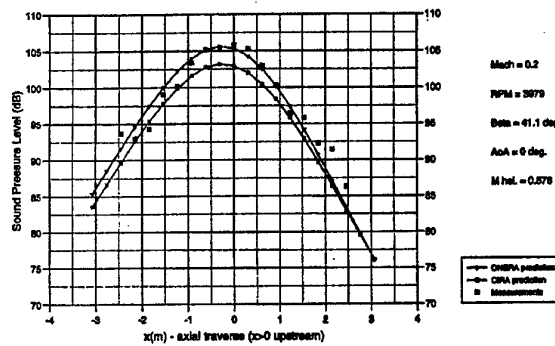


Comparison theory vs. experiment for HSP at ARA - case 1 - IBPF



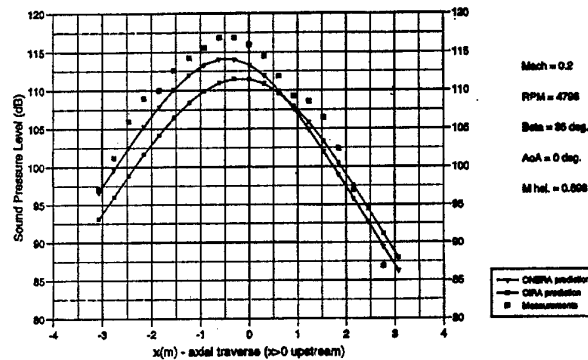
Comparison theory vs. experiment for LSP in DNW - case 1 - IBPF

99-AMV-1999



Comparison theory vs. experiment for HSP in DNW - case 11 - IBPF

99-AMV-1999



RESULTS AND CONCLUSIONS

As a research programme, SNAAP project has provided a complete database from propeller wind tunnel basic tests i.e. without installation effect. Sophisticated techniques like blade fitted and inflow sensors adapted to acoustic measurements have been used.

In addition aerodynamic and acoustic prediction codes have been developed and their validity investigated.

The achieved results are the fruit, of an extensive work program performed in different tasks mainly addressed to:

- Define the parameters and the conditions to be tested in the wind tunnel.
- Design and manufacture the test articles (two instrumented composite propellers)
- Prepare the tests
- Perform the tests
- Prepare theoretical/numerical tools for the predictions of the noise generated from the propellers.

In this way a first complete process for the development and validation of tools needed for the predictions of the noise generated from the propellers, in several operating conditions, was performed.

Herewith main results and conclusions of the project are reported.

To define the conditions at which the propellers should have been tested was not extremely complicated, since operating conditions of aircraft driven by these kind of propellers are well known. Two types of flight conditions have been simulated: typical take-off with low flow Mach number and high angle of attack; and typical cruise with high flow Mach number and low angle of attack.

The scaling parameters were obtained taking into account limitations due to the capability of the ARA rig, and to the dimensions of the testing room at ARA.

Very much care was put on the definition of the parameters to be investigated during the tests; aerodynamic parameters such as steady and unsteady pressure, and the locations of 30 Kulite miniature pressure sensors for dynamic pressure measurements and pressure tubes for static pressure measurements were the output of several discussions and updating between the partners. As well as the locations of the microphones in the wind tunnel areas.

The design and the manufacturing of the composite instrumented blades was a really challenge. Manufacturing of such instrumented propeller blades was new in Europe. The activity has been completed in 10 months; two sets of 8 blades were delivered for wind tunnel tests. Despite several in-use troubles, the propeller assemblies have been completed and tested with success. The achievement of this big challenge is the result of a team effort wherein NLR and DORNIER tremendous implications have been particularly noticeable.

Although actual work started with one-year delay, the task of the wind tunnels testing met its targets beyond expectations. Both propeller were tested in two wind tunnel, first in the transonic wind tunnel of ARA for the near field noise at High Mach numbers. Afterwards they were tested in DNW open test section at low speed for far field noise. Both the activities have been safely conducted to a successful end. The amount of data accumulated is unique on European scene and meets the 99 % of our objectives, which is a very impressive result for such a challenging experimental exercise.

An aeroacoustic code has been produced within the research programme, and its validity investigated. The code consists of several computer programs, which are linked together by a simple procedure.

The aerodynamic module developed by UCG has shown results which generally match quite well the experimental data, even if some mismatches have been outlined, some surely due to some simple mistake in the experimental data processing, some others due to uncertainties coming from the prediction methodology. It must be clearly noted that the prediction module only works within limits clearly investigated along the project: it cannot include non-axial in-flow angles; it was shown unable to converge below Mach 0.2.

Two acoustic modules have been produced and validated with experimental results. Those modules use the aerodynamic input provided by the aerodynamic code. When "classical noise terms" are calculated (thickness, loading,...) the aero input does not influence so much the noise output. So that in take-off conditions, the predictions are satisfactory but only with no in-flow angle of attack.

In cruise conditions, the prediction tool can provide very helpful results for a large range of "not-too-high" flight Mach number. But when higher in-flow Mach number causes helical tip speed to be significantly supersonic, some numerical problems may arise in the loading noise calculation. In addition, quadrupole noise prediction is very critical to a correct representation of high pressure gradients in the volume around the blades and the subsonic/supersonic transition flow on the blade surface.

It will be difficult to conclude about the validity of the prediction codes at high helical tip Mach numbers, before the quadrupole noise source can be extracted from experimental data.

Empirical methods or simplified models to account the scattering effect of the fuselage and the influence of the angle of attack on the noise have been developed by IST.

An acoustic tool to predict the installation effect, due to the aircraft fuselage has been produced by NLR. It was not possible to validate this code because installation effect measurements have not been done during the wind tunnel tests. This will be one of the objectives of the next IMT/APIAN project.

A useful tool to identify the noise source using fluctuating pressure records (Kulite signals) has been produced by TCD.

The main conclusion of such a programme consists in how its results will be used by industrial partners for their product development processes: propeller design, choice of a propeller, aircraft noise prediction, cabin noise control.

ACKNOWLEDGEMENTS

The work described in this report has been performed with the financial support of the European Community under

Contract Number: AER2-CT92-0038

Project Number: AERO 2026

Title: Study of Noise and Aerodynamics of Advanced Propellers

The financial support provided by the Commission of the European Union and the interest and encouraging discussions with Mr J. M. Martin Hernandez are gratefully acknowledged by the Consortium.

A SUBSONIC PROPELLER ACOUSTIC SCALING LAW

H. V. L. Patrick[†]

and

G. Tchotchoua*

Abstract

The acoustic scaling laws for subsonic propellers are investigated. Using an integral solution of the Ffowcs Williams-Hawkins equation, while ignoring the quadrupole term, and making some simple assumptions for the time derivatives, forces, and blade geometry, simplified expressions for the free-field thickness and loading acoustic pressure are developed. Assuming the propeller observer geometry, tip Mach number, and forward Mach number are conserved, it is concluded that the difference in non-weighted overall sound pressure level in decibels is simply equal to twenty times the logarithm (base 10) of the ratio of the prototype to model propeller diameters. This simple relationship is applicable to the total, as well as thickness and loading noise components. Of course, the operating Reynolds number of the propeller blades must be sufficiently high for linear scaling of aerodynamic performance characteristics. The NASA Aircraft Noise Prediction Program - Propeller Analysis System (ANOPP-PAS) using the compact chord approximation option is used for the propeller noise predictions to ascertain the validity of this relationship. This paper is an extension of AIAA/CEAS 5th Aeroacoustics Conference Paper 99-1882, Bellevue, Washington, USA, May 10-12, 1999.

Aeroacoustic Similarity and Scaling Laws for Propellers

The aeroacoustics scaling laws are based on conservation of momentum and mass concepts using the Ffowcs Williams-Hawkins equation (FW-H) [1]. Williams and Hawkins developed the original derivation, and Farassat introduced the embedding process [2]. This process results in an equation that is useful for computational aeroacoustics and generates theoretical values that compare reasonably well with experimental data. The FW-H equation considers a body whose surface is described by the equation $f(x,t)=0$ where the x -frame is fixed to the undisturbed medium and t is the time. The equation of the surface $f=0$ is defined such that $f>0$ is outside the body and $f<0$ is inside the body. The general FW-H equation to determine the acoustic pressure for a surface is given as Equation 1,

$$\frac{1}{c^2} \frac{\partial^2 p}{\partial \tau^2} - \nabla^2 p = \frac{\partial}{\partial \tau} \left\{ \rho v_n |\nabla f| \delta(f) \right\} - \frac{\partial}{\partial y_i} \left[P_{ij} \frac{\partial}{\partial y_j} \delta(f) \right] + \frac{\partial^2 T_{ij}}{\partial y_i \partial y_j} \quad (1)$$

[†]Associate Professor, Aerospace Engineering Department, Embry-Riddle Aeronautical University, Daytona Beach, Florida, USA.

*Graduate Research Assistant, Aerospace Engineering, Mechanics and Engineering Science Department, The University of Florida, Gainesville, Florida, USA.

where p is the acoustic pressure, ρ and c are the density and speed of sound of the undisturbed medium, respectively, v_n is the local normal velocity of the blade surface, and δ_f is the Dirac delta function. The Laplacian operator ∇^2 and the gradient $|\nabla f|$ of the function define the blade surface. The compressive stress tensor is represented by the P_{ij} term and is the force acting on the fluid due to surface pressure distribution and viscous stress on the surface of the body. The source terms of the right hand side of the equation are known as the thickness, loading, and quadrupole terms respectively.

The stress tensor term T_{ij} is a quadrupole noise source that represents noise due to transonic effects, which generally can be neglected for air flowing over blade airfoils for a Mach number less than unity, resulting in Equation 2.

$$\frac{1}{c^2} \frac{\partial^2 p}{\partial t^2} - \nabla^2 p = \frac{\partial}{\partial t} \{ \rho_0 v_n |\nabla f| \delta_f \} - \frac{\partial}{\partial t} [p \hat{n}_i |\nabla f| \delta_f] \quad (2)$$

Based upon this relationship a more simplified integral representation of the FW-H equation is developed by F. Farassat [2] and is designated as Formulation 1A. When given the body geometry, motion, and surface loading, this formulation becomes a solution to the FW-H equation and related acoustic problems. The NASA propeller noise prediction computer code ANOPP-PAS [3] uses this formulation.

Formulation 1A is valid for arbitrary blade motion and geometry. To derive the required formulation, the equation needs to be converted from Cartesian ground fixed frame of reference to a blade fixed frame of reference. The formal solution to the wave equation is used to give the integral representation of the FW-H equation. After quite a few conversions and transformations, the result of Equation 2 is given by Equations 3, 4, and 5 [3];

$$4\pi p'_L(\vec{x}, t) = \frac{1}{c} \int_{f=0} \left[\frac{\dot{l} \cdot \hat{r}}{r(1 - M_r)^2} \right]_{\tau} dS + \int_{f=0} \left[\frac{l_r - l_i M_i}{r^2(1 - M_r)^2} \right]_{\tau} dS \quad (3)$$

$$+ \frac{1}{c} \int_{f=0} \left[\frac{l_r(r\dot{M}_i \hat{r}_i + cM_r + cM^2)}{r^2(1 - M_r)^3} \right]_{\tau} dS$$

$$4\pi p'_T(\vec{x}, t) = \int_{f=0} \left[\frac{\rho_0 v_n (r\dot{M}_i \hat{r}_i + cM_r + cM^2)}{r^2(1 - M_r)^3} \right]_{\tau} dS \quad (4)$$

$$4\pi p'(\vec{x}, t) = p'_L(\vec{x}, t) + p'_T(\vec{x}, t) \quad (5)$$

where τ is a solution of retarded time equation, $g = \tau - t + r/s = 0$, Equation 3 denotes the loading noise, Equation 4 the thickness noise and Equation 5 the total noise neglecting quadrupole terms.

There are several approximate representations of Equations 3 and 4. Point source formulation is obtained if each blade is replaced by a single point source involving both the thickness and loading effect [3]. Let L_i be the net force by each blade on the fluid and ψ be the net volume of each blade. Then the loading and thickness noise components are respectively given by Equations 6 and 7;

$$4\pi p'_L(\vec{x}, t) = \left\{ \frac{1}{cr(1-M_r)^2} \left[\hat{r}_i \dot{L}_i + \frac{\hat{r}_i L_i}{(1-M_r)} \left[\dot{M}_r + \frac{c}{r}(1-M^2) \right] - \frac{c}{r} M_i L_i \right] \right\} \Big|_{\tau=\tau^*} \quad (6)$$

$$4\pi p'_T(\vec{x}, t) = \left\{ \frac{\rho\psi}{r(1-M_r)^5} \left[\begin{aligned} &(1-M_r)(\ddot{M}_r - 3\frac{c}{r}\vec{M} \cdot \dot{\vec{M}}) + 3(\frac{c}{r}M_r)^2 \\ &+ 3(\dot{M}_r - \frac{c}{r}M^2)^2 + \frac{c}{r}(\dot{M}_r - \frac{c}{r}M^2)^2 \\ &*(1+4M_r+M_r^2) \end{aligned} \right] \right\} \Big|_{\tau=\tau^*} \quad (7)$$

where,

r is the distance from source point at emission time to observer;

M_r is the source Mach number component in the direction of radiation vector;

\hat{r} is the unit vector from source point at emission time to observer;

\dot{L}_i is the rate of change of the force per unit distance (time derivative) as seen from the ground fixed frame;

M is the source Mach number.

τ^* is the solution to retarded time equation, $g=0$, for given observer time, seconds.

The following assumptions are made:

1. Propeller observer distance r is sufficiently large that $\omega \gg \frac{c}{r}$, which satisfies the far-field noise definition where $kr \gg 10$, and $k=\omega/c$ is the wave number.
2. Let ω be the angular velocity of the propeller, then the magnitude of time derivatives in Equations 6 and 7 can be represented by the following relations:

$$\ddot{M}_r \approx \omega^2 M_r$$

$$\dot{M}_r \approx \omega M_r$$

$$\dot{L}_i \approx \omega L_i$$

Based on these assumptions, Equation 6 and 7 are simplified and result in the formulations expressed in Equations 8 and 9.

$$4\pi p'_L(\vec{x}, t) \approx \left\{ \frac{1}{cr(1-M_r)^2} \left[\hat{r}_i \omega L_i + \frac{\hat{r}_i L_i \omega M_r}{(1-M_r)} \right] \right\} \Big|_{\tau=\tau^*} = \left\{ \frac{\hat{r}_i \omega L_i}{cr(1-M_r)^3} \right\} \Big|_{\tau=\tau^*} \quad (8)$$

$$4\pi p'_T(\vec{x}, t) \approx \left\{ \frac{\rho\psi}{r(1-M_r)^5} \left[(1-M_r)\omega^2 M_r + 3(\omega M_r)^2 \right] \right\} \Big|_{\tau=\tau^*} = \left\{ \frac{\rho\psi\omega^2 M_r (1+2M_r)}{r(1-M_r)^5} \right\} \Big|_{\tau=\tau^*} \quad (9)$$

Consider some retarded time τ^* corresponding to some characteristic acoustic pressure P in the pressure time history. The angular velocity ω is equal to $2\pi n$ where n is propeller rotational speed in revolutions per second units. The definition of thrust T is given by

$T = \rho n^2 d^4 C_T$ where C_T is the thrust coefficient, and $L_i \propto \rho n^2 d^4$. The net volume is given by $\psi \propto d^3$. Then Equations 8 and 9 can be put into coefficient format as shown in the following relations, i.e. Equations 10 and 11:

$$P_L(\bar{x}) \propto \frac{\rho n^3 d^4}{cr} \Rightarrow P_L(\bar{x}) = C_{NL}(M_i, M_F, r, \varphi) \frac{\rho n^3 d^4}{cr} \quad (10)$$

$$P_T(\bar{x}) \propto \frac{\rho n^3 d^4}{cr} \Rightarrow P_T(\bar{x}) = C_{NT}(M_i, M_F, r, \varphi) \frac{\rho n^3 d^4}{cr} \quad (11)$$

$$\approx C'_{NT}(M_i, M_F, r, \varphi) \frac{\rho n^3 d^4}{cr}$$

where coefficients C_{NL} and C_{NT} denote loading and thickness acoustic pressure coefficients respectively. Equation 5 states that the total acoustic pressure is the sum of the loading and thickness components, which is now expressed in Equation 12.

$$P(\bar{x}) = P_L(\bar{x}) + P_T(\bar{x}) \quad (12)$$

Consider two geometrically similar propellers with diameter d and d_1 operating under the following conditions:

1. Tip Mach number M_i is the same for both propellers.
2. Forward Mach number M_F is the same for both propellers.
3. Propeller-observer distance r and visual radiation angle φ is the same for both propellers.
4. Blade tip speed is the same for the two propellers ($nd = n_1 d_1$).

Then the values in the square brackets in Equations 1 and 2 should be the same for both propellers and, therefore, the ratio of acoustic pressures is proportional to the ratio of the propeller diameters. Thickness, loading and total acoustic pressures exhibit this dependency. Note that for the first two conditions, i.e. M_i and M_F are the same for both geometrically similar propellers of diameter d and d_1 , it follows that these propellers operating at the same advance ratio, $J = V/nd$, are in similar conditions from an aerodynamics point of view.

These last three equations state that if two geometrically similar propellers with diameter d and d_1 operate at the same:

1. tip Mach number M_i ($nd = n_1 d_1$),
2. forward velocity Mach number M_F ,
3. propeller observer angle φ ,
4. and observer distance r ;

the difference in its far field thickness, loading and total noise levels are the same and equals:

$$\Delta L = L_d - L_{d_1} = 20 \log_{10}(d/d_1) \quad (13)$$

where L_d and L_{d_1} are the decibel levels of the acoustic mean square pressure of the prototype and model propellers respectively and both measured at observer distance r .

Verification of Results

The NASA Aircraft Noise Prediction Program - Propeller Analysis System (ANOPP-PAS) [3] using the compact chord approximation option is used for the propeller noise simulations to ascertain the validity of Equation 13. The Hartzell round tip 2.03-m diameter propeller (F8475D-4) is chosen for these theoretical propeller noise validations. These propeller experimentally measured radiated noise characteristics are well documented and described in DNW Propeller Noise Tests reported in Reference 4. The full-scale model is based on BN-2 experiment operational conditions listed in Table 1 of this reference.

Table 1. Operational conditions at the BN-2 experiment.

Rotational Speed	2100 RPM
Flow velocity	40.2 m/s
β_{75} pitch angle	19.9 deg.
Power	123.8 kW
Thrust	2270 N
Advance Ratio	0.1779
3/4 span airfoil attack angle	6.410 deg
Helical Mach number	0.6682.

The assumed prototype source observer geometry is based on an observer distance r of 30.5 m and observer angle ϕ of 90° . Only total noise level is considered because it contains both the loading and thickness components.

Table 2 presents the decibel noise levels with respect to $20 \mu\text{Pa}$, for the thickness L_{thick} and loading L_{load} components as well as the total L_{total} overall sound pressure levels (OASPL). These are the noise levels predicted at 30.5 m and in the plane of propeller rotation, i.e. ϕ is 90° . Also presented are the differences between the scaled and prototype noise levels for each component, i.e. ΔL_{thick} , ΔL_{load} , and ΔL_{total} . The column furthest to the right lists the results of calculations using Equation 13 $[20\log(d/d_1)]$ and the next column lists the differences $[\Delta L_{\text{total}}]$ calculated using the ANOPP-PAS propeller noise prediction program. Comparison of these two columns reveals miniscule differences between the two methods. For example, the half-scale case indicates a ΔL_{total} of 5.99 dB and $20\log(d/d_1)$ of 6.02 dB. This comparison indicates that the far-field prototype propeller noise can be accurately scaled from model acoustic measurements using the simple relationship given by Equation 13. This result is based upon the scaled and prototype propellers being tested in the same free-stream and propeller tip Mach numbers, as well as the same propeller observer geometry.

Table 2. Predicted noise levels presented as a function of scaling factors for $r = 30.5 \text{ m}$, $\phi = 90^\circ$.

d_1/d	L_{thick}	L_{load}	L_{total}	ΔL_{thick}	ΔL_{load}	ΔL_{total}	$20\log(d/d_1)$
1.0	82.73	92.60	92.76	--	--	--	--
0.75	80.23	90.12	90.27	2.50	2.48	2.49	2.50
0.5	76.61	86.62	86.77	6.02	5.98	5.99	6.02
0.25	70.69	80.65	80.80	12.05	11.96	11.95	12.04

Shown in Table 3 are the ANOPP-PAS predicted overall-sound pressure level (OASPL) results at different source to observer distances r in the propeller plane of rotation, i.e. $\phi = 90^\circ$. The OASPL of the total noise L_{total} in decibels with respect to $20 \mu\text{Pa}$ is listed for prototype and

one-quarter scale of geometrically similar Hartzell model F8475D-4 propellers, at observer distances from 5 m to 50 m in 5 m increments. Also shown for both the full and 1/4-scale propeller's, are the thickness noise L_{thick} and loading noise L_{load} components, as well as the differences between the two cases for thickness noise ΔL_{thick} , loading noise ΔL_{load} and total noise ΔL_{total} . In the last column is listed the value obtained from using Equation 13, i.e.

$$\Delta L = 20\log(d/d_1) = 20\log(1/0.25) = 20\log(4) = 12.04 \text{ dB.}$$

Table 3. Noise levels for full and 1/4- scale propellers at different observer distances $\phi = 90^\circ$.

r in m	$\omega/r/c$	Full scale			0.25 scale			ΔL_{thick}	ΔL_{load}	ΔL_{total}	20log4
		L thick	L load	L total	L thick	L load	L total				
5.00	3.23	98.76	108.72	108.86	86.41	96.39	96.54	12.35	12.33	12.32	12.04
10.00	6.46	92.48	102.39	102.53	80.37	90.34	90.49	12.11	12.04	12.05	12.04
15.00	9.69	88.92	98.81	98.96	76.85	86.81	86.96	12.07	11.99	12.00	12.04
20.00	12.92	86.41	96.28	96.44	74.34	84.31	84.46	12.06	11.97	11.98	12.04
25.00	16.16	84.46	94.33	94.49	72.41	82.37	82.52	12.05	11.96	11.97	12.04
30.00	19.39	82.87	92.74	92.89	70.83	80.79	80.94	12.04	11.95	11.95	12.04
35.00	22.62	81.53	91.40	91.55	69.49	79.45	79.60	12.04	11.95	11.95	12.04
40.00	25.85	80.37	90.23	90.39	68.32	78.29	78.44	12.05	11.94	11.95	12.04
45.00	29.08	79.35	89.21	89.36	67.30	77.26	77.41	12.05	11.94	11.95	12.04
50.00	32.31	78.43	88.29	88.45	66.39	76.35	76.50	12.04	11.94	11.95	12.04

Inspection of Table 3 indicates that for both the full and one-quarter scale cases, that the loading noise dominates the thickness noise, and that noise level inaccuracy increases with decreasing distance but there is only a 0.3 dB at an observer distance of 5 m. Comparing ΔL_{thick} , ΔL_{load} and ΔL_{total} with $20\log(4)$, reveals that Equation 13 is valid for all free-field radiated noise distances considered.

Wind Tunnel Scaling Considerations

It is important to indicate that Equation 13 is applicable for predicting the OASPL of the thickness, loading and total propeller noise components but because of the equal tip Mach number assumption, there is a shift in blade passing frequency (BPF) components. It is well known that propeller noise is dominated by loading and thickness noise components that consist of BPF and harmonics, which are readily identifiable in a frequency spectrum [5]. For example, a two-bladed propeller rotating at 2,400 rpm results in a BPF of 80 Hz. For a one-third-scale model propeller of the prototype, the BPF would be three times higher, or 240 Hz, to satisfy the tip Mach number assumption. This frequency-shift means that only non-weighted OASPL can be scaled from model to prototype propellers. To accurately scale A-weighted noise levels, all tonal levels of the model BPF and multiples in the frequency spectrum must be frequency shifted in the manner indicated, to the prototype case and then the A-weighted corrections applied. After this frequency shift has been applied, then the total A-weighted OASPL of the prototype can be obtained by adding the tones logarithmically.

Reynolds number (Re) scaling of the model and prototype propellers exhibit the scaling dependency where $Re_1/Re = d_1/d$. It is important to note that scaling with both Reynolds and tip Mach number results in irreconcilable differences. When scaling propeller parameters with tip Mach number it is important to assure that boundary layer

transition from laminar to turbulent flow on the model occurs at the same percentage of chord that occurs on the prototype, which then ultimately satisfies the Reynolds number scaling requirement. This reconciliation between Re and M_t scaling can be satisfied by using boundary layer trips, but can cause noise problems associated with the trip. It is generally accepted that maintaining a Re no lower than $0.75(10)^6$ at the three-quarter radial position of model propeller blade [6], will satisfy the boundary layer transition concern. This Re requirement means that general aviation propellers should not be scaled smaller than approximately one-third unless appropriate boundary layer trips are installed. From a fundamental fluid mechanics point of view, Re scaling assures that boundary layer separation is not occurring on the model in a manner that is different than that occurring on the prototype. This requirement is essentially satisfied if no appreciable boundary layer separation is occurring on either the model or prototype except possibly near the trailing edge.

When measuring propeller noise characteristics in an anechoic wind tunnel the observer distance r_1 is obviously different than for the prototype case r , though both must be measured at the same observer angle ϕ . To correctly compare measurements at the model observer distance r_1 with measurements at the prototype distance r , it is assumed that spherical acoustical expansion is applicable, and the inverse square law as expressed in Equation 14 is valid;

$$\Delta L_r = 10 \text{Log}(r/r_1)^2 = 20 \log(r/r_1) \quad (14)$$

where ΔL_r is the difference in decibel noise level measured at two different distances. This ΔL_r is in addition to the decibel difference denoted in Equation 13. When performing acoustic pressure measurements in an anechoic wind tunnel, it is important that the microphone be located in the far-field, which is satisfied by the criteria that $kr > 10$.

Conclusions

Based upon a simplified integral solution of the Ffowcs Williams-Hawkins equation, expressions for the free-field thickness and loading acoustic pressure of subsonic propellers are developed. Assuming that the propeller observer geometry, tip Mach number, and forward Mach number are conserved between prototype and model propeller's, it is concluded that the difference in overall sound pressure level in decibels noise are related as shown in Equation 13,

$$\Delta L = L_d - L_{d_1} = 20 \log\left(\frac{d}{d_1}\right) \quad (13)$$

where ΔL is the decibel difference in noise levels, L_d is the prototype decibel noise level, L_{d_1} is the model decibel noise level, d is the prototype propeller diameter, and d_1 is the model propeller diameter. This relationship is valid for free-field measurements, and is applicable to the propeller thickness and loading noise components as well as the total propeller noise.

The NASA Aircraft Noise Prediction Program - Propeller Analysis System (ANOPP-PAS) using the compact chord approximation option was found to produce propeller noise predictions that validate this relationship. This paper is an extension of AIAA/CEAS 5th Aeroacoustics Conference Paper 99-1882, Bellvue, Washington, USA, May 10-12, 1999.

References

1. Ffowcs Williams, J.E. and D.L. Hawkings, "Sound Generation by Turbulence and Surfaces in Arbitrary Motion," Proc. of Roy. Soc., A264, 1969, pp. 321-342.
2. Farassat, F., "Theory of Noise Generation from Moving Bodies with an Application to Helicopter Rotors," NASA TR-451, December 1975.
3. Padula, S. L., "11.1 Subsonic Propeller Noise Module. Aircraft Noise Prediction Program Theoretical Manual, Propeller Aerodynamics And Noise." William E. Zorumski and Donald S. Weir, eds., NASA TM-83199, Part 3, June 1986.
4. Dobrzynski, W., H. Heller, J. O. Powers and J. E. Densmore, "DFVLR/FAA Propeller Noise Tests in the German-Dutch Wind Tunnel DNW," FAA Report N0. AEE 86-3, 1986
5. Patrick, H. V. L., R. W. Finn, and C. K. Stich, "Two and Three-Bladed Propeller Design for the Reduction of Radiated Noise," AIAA Paper No. 97-1710, 1997, 3rd AIAA/CEAS Conference, May 12-14, 1997, Atlanta, Georgia.
6. Metzger, F. B, "Personal Communication," 1998.

FIRST PRINCIPLES BASED METHODS FOR THE PREDICTION OF LOADING OVER FIXED AND ROTARY WING GEOMETRIES

Lakshmi N. Sankar
School of Aerospace Engineering
Georgia Institute of Technology, Atlanta, GA 30332-0150

Nathan Hariharan
CFD Research Corporation, Huntsville, AL 35805

Chee Tung
NASA Ames Research Center
Moffett Field, CA 94035

First-principles based techniques for the prediction of fixed and rotary wing wake geometry are described. It is demonstrated that fifth order accuracy schemes do substantially better than third order spatial accuracy schemes in capturing the details of the vortex core structure. It is demonstrated that the use of embedded grids can further enhance the resolution of the tip vortex, particularly if the boundary conditions and the order of interpolation accuracy are carefully maintained to be fifth order. A hybrid approach where the costly Navier-Stokes analysis is confined to small viscous regions near the blade surface is also described. Sample applications of this method to the vortex wake behind a fixed wing, and the surface pressure distribution over a rotor are presented.

Introduction

The earliest methods for modeling rotors were based on an extension of Prandtl's lifting line theory for wings. In these techniques, the individual blades were modeled as line vortices, and the wake was modeled as a deformed helix. During 1970s and 1980's, these methods were augmented by modern CFD techniques. Caradonna and Isom applied the transonic small disturbance theory to lifting rotors [1]. Chang[2] modified the full potential flow solver FLO22 for isolated wings to model rotors. Egolf and Sparks[3] modified Chang's work by embedding the vortex element associated with the tip vortex with the potential flow field. Their approaches solved either the steady or quasi steady form of the potential flow equation. Sankar et al [4,5], Strawn[6], Bridgeman et al. [7], Strawn and Caradonna[8] developed unsteady full potential flow based rotor solvers. Ramachandran et al.[9,10] solved the full potential equation and included the rotor wake effects using a Lagrangean based approach for tracking the vortex filaments.

During the late 1980's, Euler methods matured to a point where calculation of the rotor flow field in hover and forward flight was feasible. These methods solved the mass, momentum and energy conservation equations in a time dependent fashion using finite-difference or finite-volume methods. These solvers did not include viscous effects but could analyze the transonic flow with non-isentropic shocks. Sankar et al.[11], Agarwal and Deese [12], and Hassan et al. [13] developed Euler solvers for isolated rotors. Again, the wake effects were modeled as an inflow angle of attack table supplied from a separate comprehensive analysis. In Ref. 14, Wake and Sankar developed a Navier-Stokes code to analyze rotor flow fields in hover and forward flight.

During the 1980s, a new class of Euler and Navier-Stokes methods were developed in an effort to capture the rotor wake from first principles without any need for external wake models. Removing the need for external information that depends on rotor geometry is a big step in the true simulation of the rotor flow field. These first-principles based solvers are particularly useful in analyzing new or complex rotor blades where no experimental data are available. Strawn and Barth[15], Srinivasan and McCroskey[16], Srinivasan et al.[17-19], Duque[20-21] all solved the hovering rotor flow fields by capturing the rotor wake in an Eulerian fashion, and from first principles. Hariharan [22] developed high order accuracy schemes for capturing rotor wakes. Bangalore [23] studied the use of high lift devices such as slats to enhance the maneuverability of rotorcraft.

Recently, a new class of methods has become available, which combine the simplicity of Lagrangean wake methods for capturing trailing vortices, the efficiency of potential flow methods and the accuracy of Navier-Stokes methods. These methods are discussed in references 24-26.

Scope of the Present Work

The present work is organized as follows. A compressible Navier-Stokes solver that is second or third order accurate in time, and fifth order accurate in space is briefly described. An overset grid approach is next described, which allows sharp gradients in the flow field such as shocks and vortices to be captured on a locally embedded fine grid. Next, a hybrid formulation, where the time consuming calculations are confined only to small regions surrounding the rotor is discussed.

A number of results are presented for rotors in hover, and for a wing in forward flight. The surface pressure distributions, and the velocity field in and around the tip vortices are presented and compared with measurements.

Because the mathematical formulation behind this work is well developed, and has been extensively documented [22-23], the present formulation is very briefly discussed. The emphasis of this work is on the predictive capabilities of the approaches described here.

Mathematical and Numerical Formulation

Navier-Stokes Analysis:

The three-dimensional compressible Navier-Stokes equations are solved in an integral form in the present study. These equations may be formally written as:

$$\frac{\partial}{\partial \tau} \iiint_V q \cdot dV + \oint_S [\bar{F} - q \cdot \bar{V}_G] \cdot \bar{n} dS = \iint_S \bar{R} \cdot \bar{n} dS \quad (1)$$

Here, the symbol V refers to the control volume on which the governing equations are applied in the above integral form. The symbol τ represents time; The quantities F and G are inviscid and viscous fluxes evaluated at the boundaries S of the control volume. Finally, V_G is the velocity of the grid surfaces in an inertial coordinate system. All the motions of the blade such as pitching, flapping and the rotations about the rotor shaft enter the calculations through this term. This is in contrast to calculations in a rotational frame, where the centrifugal, angular acceleration and Coriolis terms are explicitly represented.

A fifth order accurate essentially non-oscillatory (ENO) scheme is used in the present work to compute the flow properties q to the left and right side of each of the six cell face S. An

adaptive stencil is used, which uses only the smoothest part of the flow properties information in the cell, and its neighbors.

The semi-discrete form of the equations may be written as:

$$\frac{d(qV)}{dt} = R \quad (2)$$

Here the symbol V represents the cell volume. At any time step 'n+1', this equation is solved using an implicit iterative scheme of the form:

$$\left[\frac{1}{\Delta t} - \frac{\partial R}{\partial (qV)} \right] \Delta(qV) = \left[R - \frac{\partial (qV)}{\partial t} \right]^{n+1} \quad (3)$$

where the objective of the iteration is to drive $\Delta(qV)$ to zero, thereby satisfying equation (2). The left side matrix is approximately factored into several smaller tridiagonal factors facilitating the inversion. Of course, when the iterations converge, the factorization errors disappear. If only a single iteration is done, then the present scheme reduces to a classical non-iterative ADI scheme.

It may also be noted that matrix equation (3) may be solved using multigrid techniques. The left side operator as well as the right side "Residual" may be injected onto coarser grids and then inverted. This multigrid approach has been used in some wing-alone calculations, but were not used in this study.

Hybrid Navier-Stokes/Full Potential Approach:

In this approach, the above Navier-Stokes calculations are done only in a small region surrounding the rotor blade. At node points away from the viscous region, the following simplified form of the governing equations is used:

$$\frac{\partial \rho}{\partial t} + \nabla \cdot (\rho \nabla \phi) = -\nabla \cdot (\rho \bar{q}_v) \quad (4)$$

Here, the quantity $\nabla \phi$ represents the irrotational portion of the velocity field. For a lifting rotor, the presence of the rotor wake leads to pockets of rotational flow in the vicinity of the tip vortices trailing from the rotor. In the present work, these rotational effects are modeled by tracking the vortical elements leaving the Navier-Stokes zone with markers, and applying the Biot-Savart law to find the induced velocity field q_v associated with these vortical elements. Finally, the isentropic energy equation is used to compute the density ρ in terms of the velocity potential, and the rotational component.

Overset Grid Scheme:

In rotary wing in forward flight applications, it is difficult to know the vortex trajectory a priori. As a result, the grid in the vicinity of the vortices is not likely to be adequately clustered. In other instances, for example in rotor airframe interaction applications, a single body-fitted grid around the rotor and the airframe can not be generated. For these reasons, an overset capability has been implemented in the present method. In this approach, independent curvilinear refined grids are placed on top of existing grids. The base grid and the overset grid will not coincide as in conventional patched grids. Thus, information between the base grid and the

overset grid must be exchanged by three-dimensional interpolation. Efficient 3-D interpolation techniques and search procedures that identify holes and fringe points have been developed.

Results and Discussion

In this section, a number of results are presented to demonstrate the capabilities of the present approach.

Fixed Wing Tip Vortex Generation Process:

A NACA0015 wing tested by McAlister et al. [27], has been studied. This experimental data is quite extensive and includes velocity profiles across the cross-section of the tip vortex at various stations downstream of the wing. A C-grid consisting of 121 points in the streamwise direction, 25 points in the spanwise direction and 31 points in the normal direction was constructed. The angle of attack of the wing was set at 12 degrees and the free stream Mach number was 0.18.

Figure 1 presents the surface pressure distribution comparison between the two schemes, at two spanwise stations. The solution computed by the fifth order scheme is found to be superior at all the stations, comparing better with the experimental values. At the inboard stations the suction peak is picked up better by the fifth order scheme, and the overall agreement with experiment is better. Very close to the tip (97% semi-span), the difference between the third and the fifth order scheme is even more marked. The fifth order scheme correctly predicts the rear bump in the suction side, caused by the formation of the tip vortex and the subsequent roll-up over the wing upper surface.

To study of tip vortex evolution in detail, the inviscid calculations were repeated with 40 points in the spanwise direction, retaining the same number of points in the other two directions. Figure 2 shows the velocity (V_z) profile normal to the wing plane across the tip vortex core at two streamwise locations behind the trailing edge. The fifth order solution is again found to be superior to the third order solution. Immediately behind the trailing edge ($x/c = 0.1, 0.2, 1.0$) the fifth order solution agrees very well with the experiments.

Around $x/c > 2$ the velocity peaks captured by the fifth order scheme starts to diminish when compared to experiments. The grid stretching in the streamwise direction becomes too large to produce the exact peak.

An embedded grid shown on Figure 3 removes this difficulty. The normal velocity field was accurately computed up to six chords away from the rotor as shown in Figure 4. The fifth order scheme with an embedded grid was also able to capture the axial component of velocity inside the vortex core, as shown in Figure 5.

Rotary Wing Analysis- Forward Flight

The full Navier-Stokes analysis has been applied to wings in hover and forward flight. Sample results from the Ph. D. Dissertation of Bangalore [23] for a UH-60A rotor in forward flight is given in Figure 6. These calculations involving four blades required 1.2 Million grid points, and were done using a distributed computing strategy. Although the surface pressure distribution over most of the rotor is in good agreement, the integrated loads shown in Figure 7 do not agree with the measurements well. Considerable additional work is needed in the areas of

tip vortex modeling and 3-D dynamic stall modeling to improve agreement between the analyses and the measurements.

Hybrid Analysis:

As discussed earlier, the CPU time for first principles based analysis can be reduced by a factor of 2 or more if most of the flow field is modeled using potential flow techniques. The resulting hybrid solver has been validated for a typical current generation rotor, the four bladed UH-60A rotor. The blade has an aspect ratio of 15.3 and a maximum twist of 13° . The blade has a rearward sweep of 20° starting from a rotor radius of 93%. The blade is made up of two airfoil sections, SC1095 as the main airfoil and SC1095R8 section in the midspan [28].

Figure 8 shows the surface pressures at two radial stations. The results are in agreement with the experimental measurements. In these studies, the wake marker locations were iteratively adjusted until the wake filaments were force free, as in conventional free wake analyses. These calculations required only 50% of CPU time required by a full blown Navier-Stokes analysis.

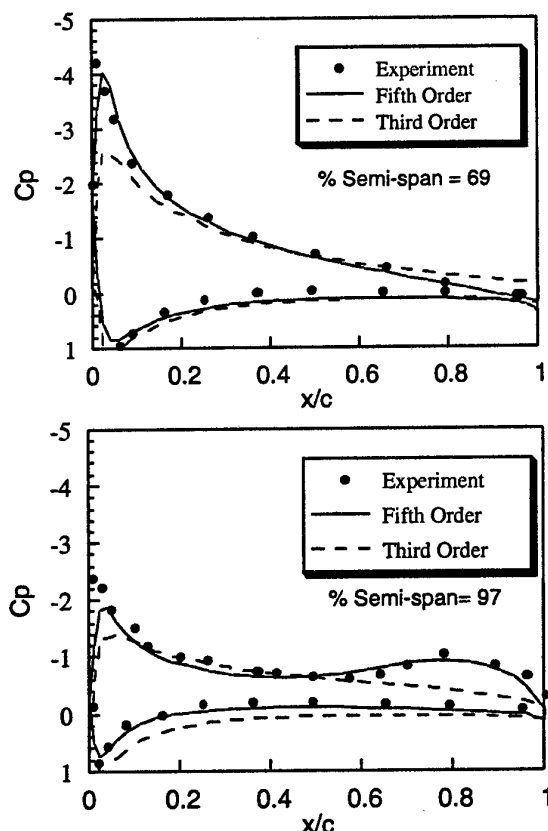


Figure 1. Surface Pressures over a Rectangular Wing Tested by McAlister, $\alpha=12^\circ$, $M_\infty=0.18$.

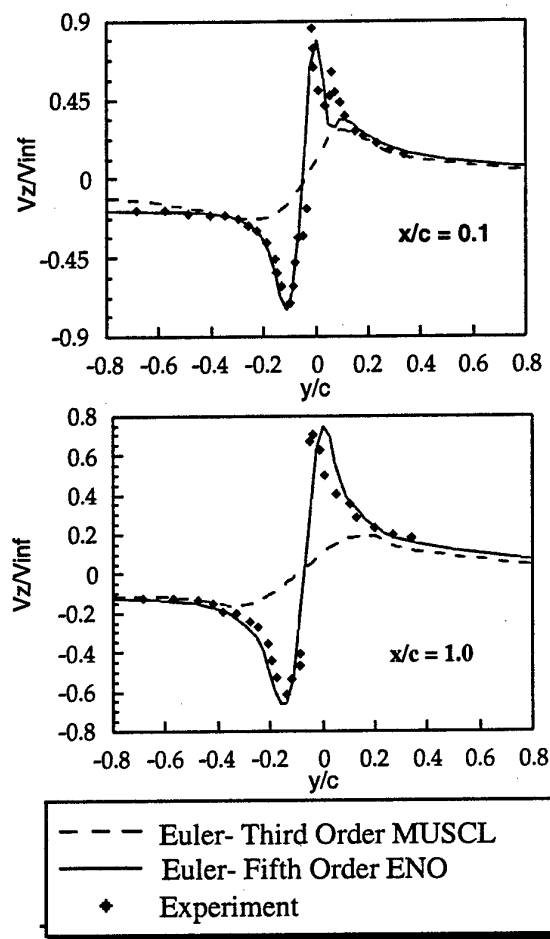


Figure 2. Variation of the Component of Velocity normal to the Wing Planform across the Vortex Core

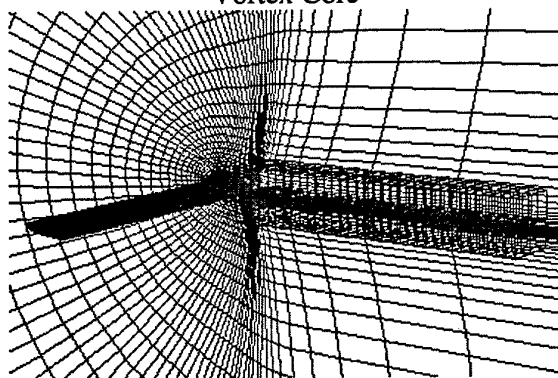


Figure 3. Embedded grid for Improved Resolution of the Tip Vortex

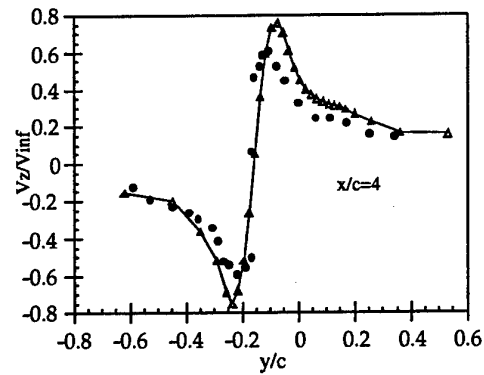


Figure 4. Variation of Normal Component of Velocity inside the Vortex Core (Embedded Grid)

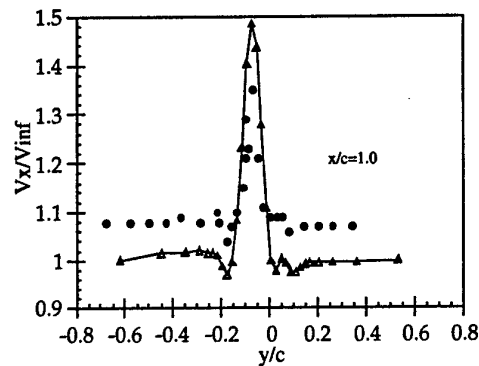


Figure 5. Variation of Axial Velocity within the Vortex Core with the Embedded Grid.

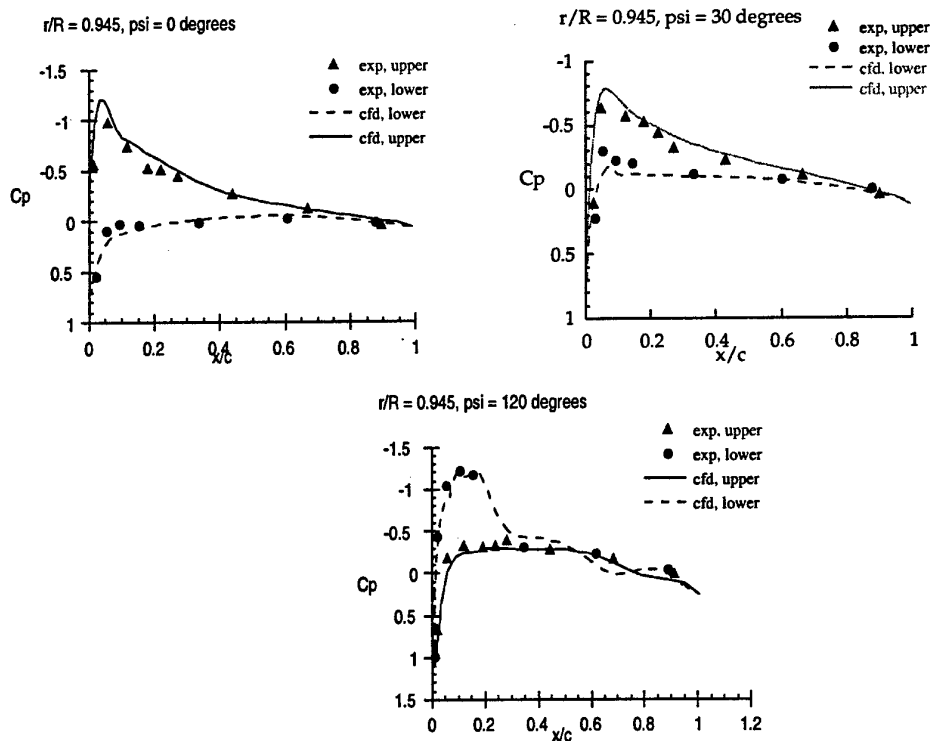


Figure 6: Surface pressure distribution, 95 % radial station at selected azimuthal locations, $M_{tip} = 0.628$, advance ratio=0.3

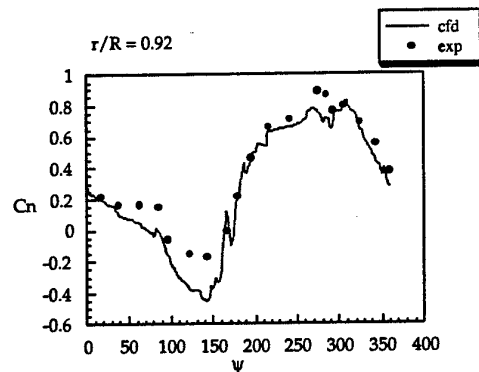


Figure 7. Variation of Normal Forces at 92% for the UH-60A Rotor

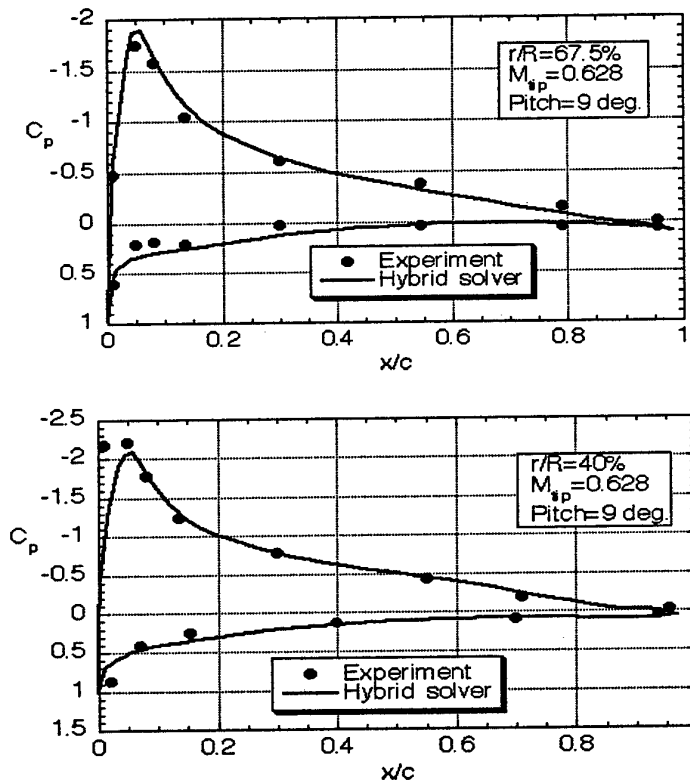


Figure 8. Surface C_p over UH-60A Rotor; Hybrid Method

Acknowledgments

This work was supported by the National Rotorcraft Technology Center and by the U. S. Army Research Office under their Rotorcraft Center of Excellence program, and by the National Rotorcraft Technology Center.

References

1. Caradonna, F. X. and Isom, M. P., "Subsonic and Transonic Potential Flow over Helicopter Rotor Blades, AIAA Journal, No. 12, Dec 1972, pp. 1606-1612.
2. Chang, I. C., "Transonic Flow Analysis for Rotors, " NASA TP 2375, July 1984.
3. Egolf, T. A. and Sparks, S. P., "A Full Potential Rotor Analysis with Wake Influence using an Inner-Outer Domain Technique, " 42nd Annual AHS Forum, June 1986.
4. Sankar, L. N. and Prichard, D., "Solution of Transonic Flow past rotor blades using the Conservative Full Potential Equation, " AIAA Paper 85-5012, October 1985.
5. Sankar, L. N., Malone, J. B. and Tassa, Y., "A Strongly Implicit Procedure for Steady Three-dimensional Transonic Potential Flow, " AIAA Journal, Vol. 20, No. 5, 1982.
6. Strawn, R.C., "Numerical Modeling of Rotor Flows with a Conservative form of the Full Potential Equation, " AIAA Paper 86-0079, July 1986.
7. Bridgeman, J. O., Strawn, R. C. and Caradonna, F. X., "An Entropy and Viscosity Corrected Potential Method for Rotor Performance prediction, " 44th Annual AHS Forum, June 1988.
8. Strawn, R. C. and Caradonna, F. X., "Conservative full potential model for unsteady transonic rotor flows, " AIAA Journal, Vol. 25, February 1987, pp. 193-198.
9. Ramachandran, K., Tung, C. and Caradonna, F. X., "Rotor hover performance prediction using a free-wake computational fluid dynamics method, " Journal of Aircraft, Vol. 26, December 1989, pp. 1105-1110.
10. Ramachandran, K., Moffitt, R. C., Owen, S. J. and Caradonna, F. X., "Hover Performance Prediction using CFD, " 50th Annual AHS Forum, June 1994.
11. Sankar, L.N., Wake, B.E. and Lekoudis, S.G., "Solution of the Unsteady Euler equations for fixed and rotor wing configurations, " Journal of Aircraft, Vol 23, No.4, April 1986, pp283-289.
12. Agarwal, R. K. and Deese, J. E., "An Euler solver for calculating the flow field of a Helicopter Rotor in Hover and Forward Flight, " AIAA 19th Fluid Dynamics, Plasma Dynamics and Laser Conference, June 1987.
13. Hassan, A. A., Tung, C. and Sankar, L. N., "An Assessment of Full Potential and Euler Solutions for Self generated Blade-Vortex Interactions, " 46th Annual AHS Forum, May 1990.
14. Wake, B.E. and Sankar, L.N., "Solution of Navier-Stokes equations for the flow over a rotor blade", AHS Journal, April 1989.
15. Strawn, R.J and Barth, J.T "A finite-volume Euler solver for computing rotary-wing aerodynamics on unstructured meshes", presented at the 48th Annual AHS Forum, Washington D.C, June 1992.
16. Srinivasan, G. R. and McCroskey, W. J., "Navier-Stokes Calculations of Hovering Rotor Flow fields, " Journal of Aircraft, Vol. 25, No. 10, October 1988, pp. 865-874.
17. Srinivasan, G.R., Baeder, J. D., Obayashi, S. and McCroskey, W. J., "Flow field of a Lifting Rotor in Hover : A Navier-Stokes Simulation, " AIAA Journal, Vol. 30, No. 10, October 1992.
18. Srinivasan, G.R and Baeder, J.D "TURNS: A free wake Euler/Navier-Stokes numerical method for helicopter rotors", AIAA Journal, Volume 31, Number 5 May 1993.
19. Srinivasan, G.R, Raghavan, V., Duque, E.P.N and McCroskey, W.J "Flow field analysis of modern helicopter rotors in hover by Navier-Stokes method", presented at the AHS International Technical Specialists meeting on Rotorcraft Acoustics and Rotor Fluid dynamics, Oct 1991, Philadelphia, PA.

20. Duque, E. P. N., " A Numerical Analysis of the British Experimental Rotor Program Blade, " 45th Annual AHS Forum, Boston, MA, May 1989.
21. Duque, E. P. N. and Srinivasan, G. R., "Numerical Simulation of a Hovering Rotor using Embedded Grids, " 48th Annual AHS Forum, Washington D.C., June 1992.
22. Hariharan, N., Sankar, L. N., "Higher Order Numerical Simulation of Rotor Flow Field," AHS Forum and Technology Display, Washington, DC., May 1994.
23. Bangalore, A., Computational Fluid Dynamic Studies of High Lift Rotor Systems Using Distributed Computing, " Ph. D Thesis, Georgia Institute of Technology, Atlanta, GA, May 1994.
24. Mello, O. A. F., "An Improved Hybrid Navier-Stokes/Full Potential Method for Computation of Unsteady Compressible Flows, " Ph. D Thesis, Georgia Institute of Technology, Atlanta, GA, November 1994.
25. Berezin, C. R. and Sankar, L. N., "An Improved Navier-Stokes/Full Potential Coupled Analysis for Rotors, " Mathematical Computational Modeling, Vol. 19, No. 3/4, 1994, pp. 125-133.
26. Moulton, M. A., Hafez, M. M. and Caradonna, F. X., "Zonal procedure for predicting the hovering performance of a helicopter, " ASME Journal, Vol. 184, 1984.
27. McAlister, K. W., Takahashi, R. K., "NACA 0015 Wing Pressure and Trailing Vortex Measurements," USAAVSCOM TR-91-A-003, 1991.
28. Lorber, P. F., Statuter, R. C., Landgrebe, A. J. "A Comprehensive Hover Test of the Airloads and airflow of an Extensively Instrumented Model Helicopter Rotor," Proceedings of 45th Annual Forum of the AHS, MA, May 1989.

NOISE FROM WIND TURBINES

D. Theofiloyiannakos
Center for Renewable Energy Sources
19th Km Marathonos Av. GR-19009
Pikermi, Greece

S.G. Voutsinas
National Technical University of Athens
P.O.box 64070, Zografou,
Athens, Greece

1. INTRODUCTION

Wind energy has made tremendous progress in the last 20 years, achieving a world-wide operational wind power capacity of 9200 MW. For wind turbine manufacturers, the basic aim of research and development is to be able to manufacture ever more cost effective machines, which are also acceptable from an environmental point of view.

Sound insulation plays a minor role in most wind modern turbines on the market today, although it can be useful to minimise some medium and high-frequency noise. It is more efficient to attack noise problems at the source. Sound emissions from wind turbines may have two different origins: Mechanical noise and aerodynamic noise.

Mechanical noise, i.e. metal components moving or knocking against each other may originate in the gearbox, in the drive train (the shafts), and in the generator of a wind turbine. The noise is transmitted along the structure of the turbine and radiated from surfaces such as the tower, blades or nacelle. Aerodynamic noise is mainly associated with the interaction of turbulence with the blade surface and is the dominating noise mechanism.

2. MEASUREMENTS

2.1 Wind tunnel measurements

Wind tunnel measurements can provide unique information about the the different noise generating mechanisms, which can be studied separately and the flow parameters can be varied and measured. However, care has to be taken because acoustic measurements in wind tunnels are subject to certain interference effects including wind noise, flow-sensor interaction noise, flow induced sensor vibration, etc.

Serious attention has to be paid to the influence of tunnel background noise being of the same order with the noise generated by the interaction of wind flow with an airfoil. Order tracking techniques are not suitable in this case. Although in practice it is difficult, an attempt should be made to position the microphones as close as possible to the airfoil and as far as possible from the tunnel background noise sources. Multiple microphone correlation techniques have resulted to a reduction of tunnel background noise of 5-10 dB. A reduction of more than 10 dB can be achieved for frequencies above 2 KHz, by applying an acoustic antenna using a 'delay and sum' beam-forming algorithm and assuming wave fronts at the microphone positions.

Four different self-noise mechanisms have been studied in wind-tunnel experiments: blunt-trailing-edge noise, trailing-edge noise, inflow-turbulence noise and tip noise. In case full-scale conditions cannot be met, serious attention should be paid to scaling-effects.

2.2 Full scale measurements

2.2.1 Emission measurement

Wind Turbine's noise emission assessment is done by measurements at locations close to the machine, in order to avoid errors due to sound propagation, but far enough away to allow for the finite source size. A reference distance R_0 based on the WTGS dimensions is used.

A wind speed of 8 m/s at reference conditions (10 m height, roughness length equal to 0,05 m) is used in the calculation of the apparent sound power level to provide a uniform basis for the comparison of apparent sound power levels from different WTGS.

Noise assessment provides the value of the apparent A-weighted sound power level, its variation with wind speed and the directivity of an individual WTGS. The frequency analysis include octave or third octave band sound pressure levels and narrow band spectra.

Measurements are obtained with a microphone positioned on a board placed on the ground to reduce the wind noise generated at the microphone and to minimise the influence of different ground types.

Sound pressure levels and wind speeds are measured simultaneously over short periods of time (not less than 1 min) and cover as broad a range of wind speeds, between cut-in and the wind speed where rated power is obtained, as practically possible. The range should be at least 4 m/s (wind speed at 10 m height and roughness length of 0,05 m). With the WTGS stopped, and using the same measurement setup, the background noise shall be measured immediately before or after each measurement series of WTGS noise. In total at least 30 measurements are needed, covering corresponding ranges of wind speed as stated above.

The measured wind speeds are adjusted to corresponding wind speeds at a reference height of 10 m and a reference roughness length of 0,05 m. The sound level at the acoustic reference wind speed of 8 m/s is determined based on a derived regression line correlating the sound levels and wind speeds. The apparent A-weighted sound power level, L_{WA} , is calculated from the background corrected sound pressure level, $L_{Aeq,c}$ as follows:

$$L_{WA} = L_{Aeq,c} - 6 + 10 \log(4\pi R^2 / S_0) \quad (1)$$

where R is the slant distance in meters from the rotor centre to the microphone and S_0 is the reference area (1 m²). The 6 dB constant accounts for the approximate pressure doubling that occurs for the sound level measurements on a ground board.

The directivity is determined by comparing the A-weighted sound pressure levels at three additional positions around the turbine with those measured at the reference position. The downwind measurement position is identified as the reference position. The horizontal distance R_0 from the wind turbine tower vertical centreline to each microphone position measured with an accuracy of + 2 % and with a tolerance of 20 % is given by:

$$R_0 = H + D/2 \quad (2)$$

where H is the vertical distance from the ground to the rotor centre, and D is the diameter of the rotor.

The test anemometer and wind direction transducer are mounted in the upwind direction of the WTGS at a height between 10 m and rotor centre. The transducers are placed in an allowable region at a distance between 2D and 4D from the rotor centre. The use of power measurements

and the WTGS power curve is the preferred method of wind speed determination, provided the WTGS operates below the maximum power point during the noise measurement series. The power curve gives the relation between the wind speed at rotor centre height and the electric power that the turbine produces for standard atmospheric conditions of 15 °C and 101,3 kPa. The electric power measured during the noise measurements must be converted to these standard atmospheric conditions and the wind speed at rotor centre height obtained from the power curve must be adjusted for a height of 10 m and the reference roughness length conditions, by assuming logarithmic wind profile. The same adjusting should be applied if an anemometer is used between 10 m and rotor centre height. Measurement by an anemometer at between 10 m and rotor centre height is also appropriate during background sound measurements, when the wind turbine is parked, and the turbine has been used as an anemometer during the turbine noise measurements.

Tonality assessment

For a fixed speed WTGS, 2 one-minute, RMS averaged narrowband spectra are obtained for the analysis of tonality. For a variable speed WTGS, 12 ten-second, RMS averaged narrowband spectra are obtained. These spectra are energy averaged to produce a single, long term spectrum and are obtained for integer wind speed bins covering at least 4 m/s including the acoustic reference wind speed. Data in each wind speed bin are analyzed for tones.

The effective noise bandwidth should be less than the values shown in table 1.

Table 1 -- Effective noise bandwidth

Tone frequency, Hz	Less than 2000	2000 - 5000
Effective noise bandwidth	2 to 5 Hz	2 to 12.5 Hz

The bandwidths of the critical bands are:

$$\text{Critical Bandwidth} = 25 + 75(1 + 1.4(f/1000)^2)^{0.69} \quad (3)$$

where f is the frequency of the tone, in Hz. The critical band is positioned with centre frequency coincident with the tone frequency. If more than one tone is present within the same critical band, the critical band is placed so that tonality content is maximised. For tones with frequencies between 20 Hz and 70 Hz the critical band is 20 Hz to 120 Hz.

Within each critical band, every spectral line is classified as tone, masking, or neither as follows:

- Determine action level by one of two ways: a) As the energy average of all spectral lines below $L_{70\%} + 6$ dB, where $L_{70\%}$ is the energy average of the 70% of spectral lines in the critical band with the lowest levels; b) If the masking level within a critical band has a steep gradient, the action level is determined by a linear regression through all spectral lines defined as masking.
- A line is regarded as a 'tone' if its level is greater than the action level plus 6 dB;
- The adjacent lines to a 'tone' are also classified as 'tones' if their levels are greater than the action level plus 6 dB and less than or equal to 10 dB below the level of the 'tone';
- A line is regarded as neither 'masking' or 'tone' if its level is greater than the action level plus 6 dB but 10 dB below the level of the 'tone';
- A line is regarded as masking if its level less than the action level plus 6 dB.

The total masking noise level within the critical band L_{pn} corrected for the bandwidth of the critical band shall be obtained from the averaged long-term spectrum and is determined by:

$$L_{pn} = L_{pn,avg} + 10 \log(\text{critical bandwidth} / \text{effective noise bandwidth}) \quad (4)$$

where $L_{pn,avg}$ is the energy averaged measured masking noise level obtained from the long-term averaged spectra, and determined by averaging the masking noise spectrum separate from any tones within the critical band.

If more than one tones are present within the same critical band, the overall tone level is determined by energy summing the level of each individual tone within the critical band.

The difference between the tone level and the level of the masking noise, ΔL , is describing the tonal content of the corresponding critical band.

The tone level, $L_{pt,ave}$, is determined from the analysis of the long-term spectra and

$$\Delta L_{tn,ave} = L_{pt,ave} - L_{pn} \quad (5)$$

Additionally, tonal content can be described using the max tone level $L_{pt,max}$, determined from the analysis of the short term spectra (approximating time weighting F) as the arithmetic average of the highest 10 % of the tone levels. The difference between the tone level, $L_{pt,max}$ and the level of the masking noise in the corresponding critical band, is given by:

$$\Delta L_{tn,max} = L_{pt,max} - L_{pn} \quad (6)$$

This will, in general, differ from the tonality defined above using the average rms tone level. $\Delta L_{tn,max}$ is related to the frequency dependent audibility criterion defined as:

$$\Delta L_{tn,crit} = -2 - \log(1 + (f/502)^{2.5}) \quad (7)$$

Note that this criterion curve has been determined from listening tests, and reflects the subjective response of a 'typical' listener to tones of different frequencies. According to the criterion, a 'typical' listener would consider such tones as being 'audible'. In excess of 6.5 dB, a 'typical' listener would consider such tones as being 'prominent'.

2.2.2 Immission measurements

Immission measurements can be carried out with a free-standing microphone at a height of 1.2-1.5 m (preferred method) or a microphone mounted on a vertical board.

The main difficulty in Immission measurements is that in many cases, the noise level of a wind turbine generator is of the same magnitude with the background noise level. This means, that it is particularly important to correct the measured levels, while taking into account the effect of the background noise. For this reason, while the combined noise of the wind turbine generator(s) and all other sources (L_{s+b}) is measured at the receiver site, the wind speed is measured at the same time at two locations: at the wind turbine generator and at the receiver site. A set of triple data is obtained: wind speed at the receiver site, wind speed at the wind turbine generator site and noise level at the receiver site. In a similar way, we measure only the background noise (L_b) with the wind turbine generator(s) stopped and at the same time the wind speed at the receiver site. The two noise levels are plotted on a chart as the relation of the wind speed at the receiver site. Next, the background noise level curve is approached with the use of the regression method a second degree polynomial function $L_b(v)$. For any measurement of the combined noise (L_{s+b}) the relevant value of background noise is defined by the curve. Based on this value, the correction of

the combined noise is being performed and the noise level of the wind turbine generator only is assessed (L_s).

The corrected noise levels (from the wind turbine generator only) are then plotted on a new chart as the function of the wind speed at the wind turbine generator site and at a height of 10 m. The points of noise level are approached with a straight line (method of the minimum squares) and the level at reference speed is read from the chart. Usually the reference wind speed is 8 m/s at the location of the wind turbine generator and height of 10 m.

The tonality assessment is similar with the one described above for the Emission measurement. Often during Immission noise measurements, it is necessary to use a secondary windscreen in order to obtain an adequate signal-to-noise ratio at low frequencies in high winds. For example, it could consist of a wire frame of approximate hemispherical shape, at least 450 mm in diameter, which is covered with a 13 mm to 25 mm layer of open cell foam with a porosity of 4 to 8 pores per 10 mm. If a secondary wind screen is used, its frequency response must be documented.

3. STANDARDS AND ACTUAL INDUSTRIAL STATUS

The purpose of the relative standards, is to provide a uniform methodology that will ensure consistency and accuracy in the measurement and analysis of acoustical emissions by wind turbine generator systems.

- EN 61400-11:1998, "Wind turbine generator systems- Part 11: Acoustic noise measurement techniques".

The basic standard dealing with the measurement of the source strength of a wind turbine. The tonal assessment procedure introduced, at present not yields consistent results and is currently under revision

- MEASNET, Version 1, 10/98, "Measnet measurement procedure: Acoustic Noise Measurement Techniques"

This standard is based on the method described in EN document 61400-11 and introduces some modifications for the assessment of tonality.

- IEA Recom/tions, part 4 (1994) "Recommended practices for wind turbine testing. Part 4: Measurement of noise Emission from wind turbines".

This guide is the basis for the above mentioned standards.

- IEA Recom/tions, part 10 (1997) "Recommended practices for wind turbine testing. Part 10 : Measurement of noise immission from wind turbines at noise receptor locations".

This guide recommends measurement techniques and methods which will enable a characterisation of the noise immission from a wind turbine or a group of wind turbines at a noise receptor location .

- CLC/BTTF-2-WG4, 3. Draft Declaration of Sound Power Level and Tonality Values of Wind Turbines.

The intention of this document is to determine declared noise emission values from a sample of turbines of the same type. The declaration is to increase the reliability of wind farm planning and shall facilitate the comparison of sound power levels and tonalities of different types of wind turbines. At present wind turbine noise specifications tend to be based on a single instance of particular make and model of turbine and these are taken to be representative of these turbines as a whole. Clearly this is unlikely to be the case, as there will be individual variation between different turbines.

Today the sound power levels of representative W/Ts (500-700 KW size) are between 96 and 102 dB(A) with an average of about 100 dB(A).

While at many modern W/Ts, the emission of mechanical noise is reduced to acceptable levels by structural dynamics analysis and use of quieter gearboxes, the tonality is still a problem for the new generation of large W/Ts.

Within the process of aerodynamic noise generation a large number of complex flow phenomena play an important role. Wind turbines engineers use techniques such as stall, which aircraft designers try to avoid. Wind turbine blades are prone to stalling even at low wind speeds close to the root of the blade where the profiles are thick.

Most of the noise originates from the trailing (back) edge of the blades. Care is also taken for the tip of the blade, since it moves substantially faster than the root of the blade. Careful design of trailing edges and tips and careful handling during blades' mounting, are essential.

A number of technologies known from the aircraft industry are applied to improve the performance of wind turbine rotors. For example to avoid the stalling at low wind speeds, a stretch of about one metre along the back side near the root of the blade and equipped with a number of vortex generators, is installed on some of the newest rotor blades.

4. THEORETICAL WORK

4.1 Modelling of noise sources on wind turbines

Noise is identified to pressure fluctuations which propagate due to the compressibility of the air. Because wind turbines operate at low Mach numbers (0.2-0.3 at the tip), the assumptions of linear aeroacoustics are fulfilled. So the flow problem can be considered independently from any other effect. Based on time domain aerodynamic calculations, the aeroacoustic problem can then be processed. Considering the broadband noise as a whole, three main categories are distinguished (See Grosveld (1985), Lowson (1993), Hubbard & Shepherd (1991) and Brooks, Pope & Marcolini (1989)):

- 1) The discrete frequency noise at the blade-passing frequency and its harmonics due to:
 - (a) steady and other ordered sources on the blades, and
 - (b) wake interactions
- 2) The self-induced noise caused by:
 - (a) direct radiation from the attached to the rotor blade boundary layer,
 - (b) the separated flow on the blade (this includes the blade-tip noise),
 - (c) radiation due to trailing edge instabilities involving quasi-discrete frequencies.
- 3) The broadband noise due to inflow turbulence.

The noise associated with the first category is of low-frequency. To calculate the corresponding acoustic pressure distribution, the representation formula by Ffowcs Williams and Hawkings (1969) is used. It describes the generation of sound related to mass flow, forces acting on fluid and turbulent flows in the case of moving solid boundaries (i.e. the blades in the case of wind turbines).

As regards the high frequency part, closed form expressions give the sound pressure levels for the different types of noise that are identified. The relative importance of each source depends on many factors such as the design of the turbine, the site of installation and the operating conditions. Previous works (Grosveld (1985), Lawson (1993)) indicate that for almost all wind turbines operating under normal conditions, the most significant noise source is the self-induced noise of the blades. However it is pointed out that under certain conditions the noise due to inflow turbulence can become predominant.

In the model described in the sequel, detailed free wake aerodynamic calculations (Voutsinas, Triantos (1999)) provide the distributions of the angles of attack and the Reynolds numbers along the span of the blades. Then, for each spanwise section, the required boundary layer parameters are calculated. All these provide the necessary input data for the semi-empirical expressions of self-induced noise. Because all the results in Brooks et al (1989) refer to NACA 0012, their application to other airfoils requires suitable scaling. The prediction of turbulent inflow noise is based on Lawson's analysis (1993) using the ESDU data base (ESDU (1990)).

Formulation of the Aeroacoustic Model

Lighthill (1952) first combined the continuity and momentum equations to get a non-homogeneous wave equation for the pressure field $p(.,t)$ for which Ffowcs-Williams and Hawkings (1969) gave the following solution assuming that the acoustic sources contained in a volume V bounded by a surface S are compact.

$$4\pi(p - p_o) = \frac{\partial^2}{\partial x_i \partial x_j} \int_V \left[\frac{T_{ij}}{r} \right] dV - \frac{\partial}{\partial x_i} \int_S \left[\frac{F_i}{r} \right] dS + \frac{\partial}{\partial t} \int_S \left[\frac{\rho_s \dot{U}_s \cdot \dot{v}}{r} \right] dS \quad (8)$$

where $T_{ij} = \rho u_i u_j + (p - c^2 \rho) \delta_{ij}$ denotes the Lighthill tensor, ρ denotes the density of the fluid and c the speed of sound, \dot{U} denotes the velocity of the fluid, \dot{F} denotes the force per unit area (N/m^2) acting on the surface S , \dot{U}_s denotes the velocity of the solid surface, \dot{v} is the unit vector normal to the surface, r is the observer's distance and p_o is the uniform pressure of the fluid at rest. In (8) the brackets denote evaluation in retarded time.

For wind turbines, low-frequency noise is generated by: (a) the wakes of the blades giving a quadrupole contribution depending on vorticity, (b) the blades themselves giving the loading-noise and the thickness-noise terms and, (c) the tower giving contributions to all three terms.

Depending on the specific modelling of the wind-turbine configuration, the various contributions are included differently. The model used considers the blades as flexible thin-lifting surfaces. The flow displacement induced by the tower as well as the effects of the tower-wake are also taken into account. All these terms contain the effect of the structural flexibility of the blades. In addition there is also a part in the low frequency range that is due to the interaction between the inflow turbulence and the airfoil sections of the blades. This part is discussed later in the section.

The high frequency is related to the so-called *self-induced noise* which describes the noise due to the motion of the rotor blade through the air, independent to other interactions and ignoring the

local accelerations due to the rotational motion. Consequently, the noise radiated by every blade element of small but finite radial width, can be identified with that of a two-dimensional airfoil in turbulent flow with uniform mean velocity. The effective velocity, i.e. the velocity far upstream at the same radial position, as well as the angle of attack are provided by the aerodynamic model.

Substantial research work has been carried out on the subject at NASA Langley and summarised in Brooks et al (1989). For the case of the NACA 0012 airfoil, different noise sources were studied: (i) the sound radiation from the attached boundary layer, namely the trailing-edge noise (TBL-TE noise), (ii) the noise due to separation and the tip vortex noise and, (iii) the radiation due to trailing edge instabilities involving quasi-discrete frequencies, namely the laminar-boundary-layer-vortex-shedding noise (LBL-VS noise) and the trailing-edge-bluntness noise (TE-bluntness noise). The measured data were used to derive semi-empirical expressions which provide the far-field noise spectra.

The basic theoretical result on the trailing-edge noise is due to Ffowcs Williams and Hall (1970) who showed that the main effect is the interaction of the inflow turbulence with the trailing edge (See also Amiet (1975,1976) and Howe (1978)). The model gives a Ma^5 law for the noise radiation, instead of the classic Ma^8 law that applies in the case of sound radiation in free-space turbulent flows. The spectrum in a 1/3-octave representation is then given a closed form depending on the boundary layer displacement thickness δ^* , the directivity D and the corresponding Strouhal number:

$$SPL_{TBL-TE} = K + 10 \log \left(\frac{\delta^* Ma^5 LD}{r^2} \right) + g(St_{\delta^*}) \quad (9)$$

L being the local length scale. Also a Ma^5 correlation was given for the *laminar-boundary-layer-vortex-shedding* noise. Similar is the approach for the *trailing-edge bluntness* noise which is generated as a result of vortex shedding. Brooks et al.(1989) give a $Ma^{5.5}$ dependence which was found to better correlate with the measurements. Finally for the modelling of the *tip-vortex noise* (TIP) the approach given in Brooks et al (1989) is adopted (See also George (1984)). The flow around the tip of the blade consists of a vortex with a thick viscous core. The recirculating flow within the core is highly turbulent. The mechanism of noise production is due to the passage of this turbulent flow region over the edge and into the wake of the blade. The corresponding noise spectrum takes the form:

$$SPL_{TIP} = 10 \log \left(\frac{Ma^2 Ma_{max}^3 L^2 D}{r^2} \right) + 126 - 30.5(\log(St_L) + 0.3)^2 \quad (10)$$

in which case L is the core of the tip vortex and Ma_{max} denotes the local maximum Mach number defined by the tip velocity.

The basic disadvantage of the above methodology is that the closed-form expressions rely on experiments for the NACA 0012 airfoil at moderate Reynolds numbers for both tripped and untripped boundary layers. Therefore, the results obtained with the above expressions need scaling when used for another blade profile. For every type of self-induced noise, the ratio of the values of the corresponding boundary layer parameters for the specific profile and the NACA 0012 is used for scaling. An integral boundary layer method is used to calculate the necessary boundary layer parameters (Voutsinas and Riziotis (1999)). For this purpose a suitable numerical tool provides the boundary layer parameters for the NACA 0012 and any other type of profile.

Then a scaling parameter is calculated as the ratio between the numerical values corresponding to NACA 0012 and the other airfoil. This parameter acts as a "scaling factor" to the experimental boundary layer parameters involved in all the above semi-empirical expressions.

The last term is the *turbulent inflow noise*. The passing of the turbulent wind flow through the rotor plane of a wind turbine causes unsteady pressures on the blade that radiate noise. Noise radiation by turbulent ingestion is significant for the wind turbine noise and makes part of the model put forward by Grosveld (1985). Grosveld's prediction method indicates that turbulence ingestion is normally the most important source of noise at high power levels or wind speeds. The model adopted is the one proposed by Amiet (1975) as modified by Lowson (1993). Amiet gives two formulae which apply to the high and low frequencies respectively as follows:

$$SPL_{1/3}^H = 58.4 + 10 \log \left(\frac{\rho_o c^2 L L_i Ma^3 u^2 K^3}{(1 + K^2)^{7/3} r^2} \right), \quad SPL_{1/3}^L = 10 \log \left((10 S^2 Ma K^2 \beta^{-2}) \right) + SPL_{1/3}^H \quad (11)$$

where L_i is the inflow turbulence length scale, $K = \pi f x_c / U$ is the wave number defined with respect to the chord x_c , u is the rms value of the turbulent velocity, $\beta^2 = 1 - Ma^2$, and S^2 is the compressible Sears function given as $S^2 = (2\pi K / \beta^2 + (1 + 2.4K / \beta^2)^{-1})^{-1}$. The turbulence parameters appearing in the above expressions, are all calculated by means of the relations given in the widely accepted ESDU reports (1990). They basically depend on the ground roughness z_o . Figure 1 shows the predicted spectrum of a typical wind turbine compared with measurements and the predictions from a simplified calculation by Lowson. The difference of the two predictions is mainly on the aerodynamic model.

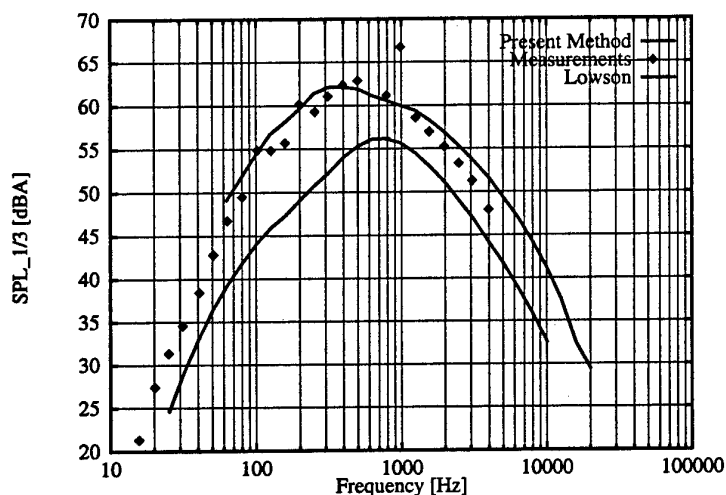


Figure 1: Typical spectrum of a wind turbine

4.2 Modelling of propagation

Investigations have shown, that methods developed to predict propagation of industrial sources, are insufficient for predicting the propagation of wind turbine noise, which exhibits some special features:

- The Height of the source is higher (30-80 m)
- The wind speed has a strong influence on the generation and propagation of the noise
- The distances usually affected are comparatively small (less than 1Km)

Propagation of noise emitted from wind parks can be considered as a wave propagation problem in an inhomogeneous medium which can be treated under quite general assumptions within the framework of linear acoustics. In order to solve the acoustic equation a variety of methods have been developed and widely used in underwater acoustics (Jensen et al (1994), Robinson, Lee (1994)). After some necessary modifications they can also be applied to propagation problems in atmospheric environment.

In particular, to exploit these models for wind energy applications, the following features must be included: (a) the spatial variability of the mean velocity field, (b) the stratification of the atmosphere, (c) the terrain orography and (d) the ground acoustic characteristics. Two methods of this kind have been recently set up. They consist of models which take into account the vertical profile of the mean wind velocity, the range dependence of the medium characteristics and the terrain effects through velocity variations and ground geometry.

The problem of wave propagation is usually decomposed in two parts: the "low" frequency part which is treated by solving directly the acoustic equation, and the "high" frequency part which is usually treated by a ray tracing approach. Two different codes representing the two different methodologies are used. The first is KRAKEN (Porter (1994)); it applies the methodology of normal modes (Jensen et al (1994), Robinson, Lee (1994)) which is able to give an exact representation of the acoustic field in a wide range of frequencies. For the high frequency part a model applying the very popular methodology of ray theory (Jensen et al (1994), Robinson, Lee (1994)) has been developed given the name AERAS (Belibassakis et al (1997)).

The Normal Modes Model

The KRAKEN model (Porter 1994) takes into account the stratification of the air and the ground, the attenuation of the noise in the air and the ground, the terrain geometry and the range dependence of the wind velocity profile. The equivalent sound speed, which is given as input, is obtained from the algebraic summation of the sound speed plus the wind velocity which varies with height. Consequently, for downstream propagation, it takes greater values than the reference sound speed, whereas the opposite applies for upstream propagation. The reference sound speed, i.e. the sound speed in quiescent air is taken equal to 343 m/s. The height of the computational domain is divided into a number of equidistant intervals so that the modes are adequately sampled. Usually 10 points per wavelength are sufficient. This means that the computational time increases with frequency. That is the reason why ray theory models are preferred for high frequencies.

When the terrain or the sound speed variation with range are taken into account, namely the environment is range dependent, the coupled modes theory should be used (Jensen et al (1994)). However, such a consideration increases substantially the computational time. The alternative is

to join the tower base with the measurement point via a straight line and then consider that the x-axis is aligned with that straight line. In addition, the sound speed profile is assumed constant with range. The investigation made proved that if the whole rotor disk is visible from the measurement point, the predictions received using that approximation do not present significant variations with those received using the coupled modes approach. So, in favor of time and simplicity, that approximation was adopted.

KRAKEN has the capability of using free, rigid and homogenous half-space options for boundary conditions. In the case of the atmospheric environment, the under-ground layer is modelled as an acoustic half-space with the characteristics of the specific acoustic material (density of the material, sound speed and attenuation into the material). The density of soil is taken equal to 2650 kg/m^3 (Hess et al (1989), Sabatier et al (1992)) and the sound speed into soil is taken equal to 2000 m/s . If there is information about the stratification of the ground (e.g. grass - soft soil - dry soil - stone), this can be taken into account as separate horizontal layers. The upper-air layer is modelled as a finite acoustic medium with constant characteristics up to a certain height. The height of the boundary layer is taken usually equal to 1000 m , whereas the height of the upper-air layer counts 1000 m additionally. Above that height vacuum is considered.

The AERAS Ray Theory Model

The AERAS model (Belibassakis et al(1997)) takes into account the terrain geometry, the air absorption and the range dependence of the wind velocity profile. The stratification of the atmosphere is not taken into account. The top boundary of the computational domain is considered absorptive, whereas the bottom boundary is considered as a material with complex impedance $Z = R + iX$. The rays are reflected from the material according to the reflection coefficient \mathfrak{R} which is given from the relationship (Chessell (1977)):

$$\mathfrak{R} = \frac{\sin \phi - |Z_0 / Z|}{\sin \phi + |Z_0 / Z|} \quad (12)$$

where ϕ is the angle of incidence and $Z_0 = \rho_0 c_0$ is the impedance of air; ρ_0 is the density of the air (g/cm^3) and c_0 (m/s) is the sound speed in quiescent air (343 m/s). If the density of the air is not given, it is set arbitrarily to 1.23 kg/m^3 .

Various relationships have been expressed in order to determine the real and imaginary parts of the impedance of the material. In the present model, two of these approximations were used. The one most common used is the one-parameter formula of Delany-Bazley (Chessell 1977, Delany, Bazley 1970):

$$R / \rho_0 c_0 = 1 + 9.08(f / \sigma)^{0.75}, X / \rho_0 c_0 = -11.9(f / \sigma)^{0.75} \quad (13)$$

where f is the frequency and σ is the flow resistivity of the material. The other approximation used is the two-parameter formula (2PA) described by Attenborough (1992):

$$R = 0.4342\sqrt{\sigma/f}, X = 9.6485\beta/f + R \quad (14)$$

where β is the rate of decay of the porosity (m^{-1}) and σ is again in cgs units (kNsm^{-4}). The values of σ and β are taken from Table II in (Attenborough (1992)) or Table III in (Martens et al (1985)) according to the ground classification. Flow resistivity ranges from 150000 Nsm^{-4} to 630000 Nsm^{-4} for the usual types of ground, whereas β varies between 50 and 200 m^{-1} . The choice of the parameters is not strictly determined, since the accurate ground classification according to the literature is not possible in most of the cases. There are more detailed impedance models, including three or four parameters (Sabatier et al (1992), Chessell (1977), Attenborough (1985)), however, the determination of more parameters demands additional experimental data which are usually not available.

All models take as input the attenuation (dB/m) which is due to the atmospheric absorption. Atmospheric absorption has been theoretically and experimentally studied and predicted, on the basis that air is composed of four gases (oxygen, nitrogen, water vapor and carbon dioxide). Diagrams of the absorption as a function of frequency, humidity, temperature and pressure have been extracted over the last thirty years and are available in the literature (Harris (1966), Evans et al (1971)). In the present model, the updated formulas for the calculation of the attenuation coefficient α due to atmospheric absorption, presented in Bass et al (1994), are used.

Figures 2 and 3 show typical propagation results for a flat terrain and a complex terrain case respectively. There is clear degradation of the predictions quality in the second case which indicates the difficulty in reproducing full scale measurements in complex terrains where there are a lot of uncertainties concerning the conditions of propagation.

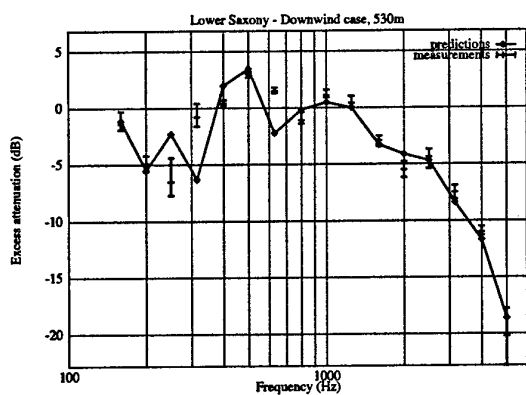


Fig. 2: propagation modelling in flat terrain

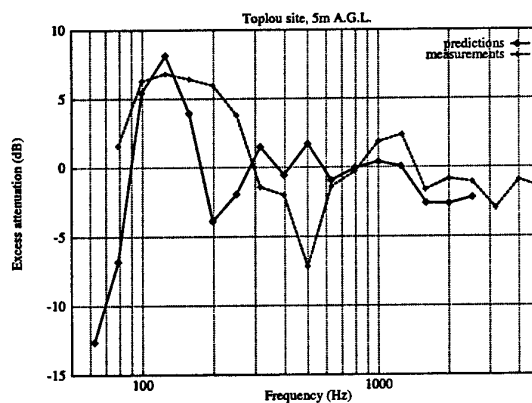
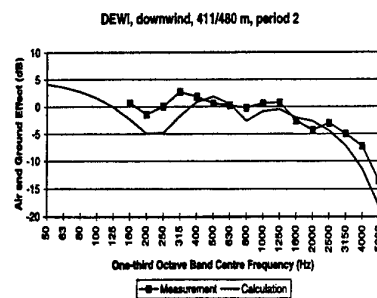
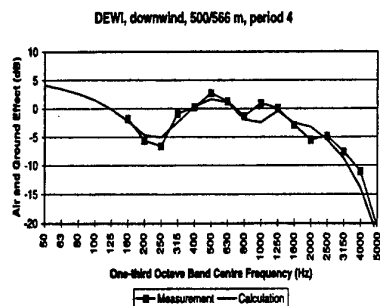


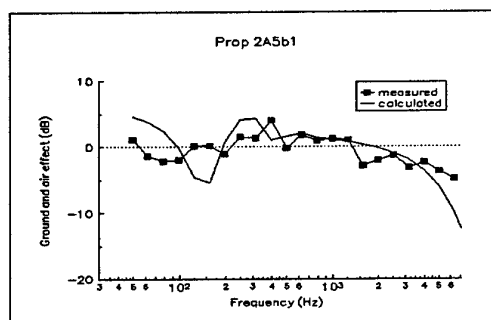
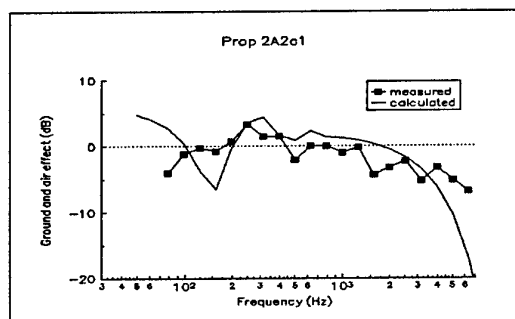
Fig. 3: propagation modelling in complex terrain

WiTuProp noise propagation model.

A new noise propagation model, WiTuProp, allows more accurate calculations and is available as a PC program. It is based on the so-called 'heuristic model', adapted and developed by DELTA Acoustics & Vibration. The real sound speed profile is approximated by a linear profile and the model can be used for any profile but the results are not reliable if it is very irregular. Such irregular profiles, however, are not important to wind turbine noise propagation.



Figures 4&5. Noise propagation prediction by WITUPROP model, for flat terrain



Figures 6&7. Noise propagation prediction by WITUPROP model, for complex terrain

5. RESEARCH AND INDUSTRIAL TRENDS AND PERSPECTIVE

The current trend in Wind turbine design and manufacturing, is towards large scale turbines (above 1 MW).

Theoretical (modelling) and experimental work is needed for the investigation of reducing broadband noise by better blade design. Full scale and wind tunnel measurements are basic for the study and validation of theories on noise generation and reduction.

The fluctuation strength of W/T's noise, is the second important influence (after tonality) on subjective unpleasantness. The guidelines for the quantification of the fluctuation strength, introduced in the IEC standard, are far from consisting a specific method with reliable and repeatable results.

Advanced noise propagation models have to be developed and applied for studies on the optimal positioning of W/Ts, taking into account wind effects and complex terrain. For the modification and validation of the models, there is a need for more data obtained from complex terrain sites..

6. REFERENCES

1. EN 61400-11:1998, "Wind turbine generator systems- Part 11: Acoustic noise measurement techniques".

2. MEASNET, Version 1, 10/98, "Measnet measurement procedure: Acoustic Noise Measurement Techniques"
3. IEA Recom/tions, part 10 (1997) "Recommended practices for wind turbine testing. Part 10 : Measurement of noise immission from wind turbines at noise receptor locations".
4. IEA Recom/tions, part 4 (1994) "Recommended practices for wind turbine testing. Part 4: Measurement of noise Emission from wind turbines".
5. CLC/BTTF-2-WG4, 3. Draft Declaration of Sound Power Level and Tonality Values of Wind Turbines.
6. IEC 1400-12 FDIS (1997): "Wind turbine generator systems, part 12: Power performance measurement techniques".
7. ETSU W/13/00386/REP, 1996, "Noise measurements in windy conditions"
8. D. Theofiloyiannakos, J. Kragh: "Investigation of the reduction of the wind induced microphone noise by the use of supplementary wind screens". Proceedings of the European Wind Energy Conference, EWEC'97.
9. S. Wagner, R. Bareib, G. Guidati : "Wind Turbine Noise", 1996, Ed. Springer
10. "Noise Immission from Wind Turbines", Final report on project JOR3-CT95-0065, AV 1121/98
11. Amiet, R.K., 1975, "Acoustic Radiation from an Airfoil in a Turbulent Stream, Journal of Sound and Vibration", 41 (4), pp 407-420
12. Amiet, R.K., 1976, "Noise due to turbulent flow past a trailing edge", Journal of Sound Vibration, 47(3), pp. 387-393.
13. Attenborough, K., 1985, "Acoustical impedance models for outdoor ground surfaces", J.Sound Vib. 99, pp 521-544.
14. Attenborough, K., 1992, "Ground parameter information for propagation modelling", J.Acoust.Soc.Am. 92(1), pp 418-427.
15. Bass, H.E., Sutherland, L.C., Zuckerwar, A.J., Blackstock, D.T. and Hester, D.M., 1994, "Atmospheric absorption of sound: Further developments", J. Acoust. Soc. Am. 97(1), pp 680-683.
16. Belibassakis K.A., Prospathopoulos I.M., Voutsinas S.G., 1997, "Numerical Modelling of Noise Propagation in the Atmospheric Environment and Application to Wind Energy Installations", EWEC 97 Proc., Dublin, Ireland.
17. Brooks, T.F., Pope D.S. & Marcolini M.A., 1989, "Airfoil Self Noise and Prediction", NASA Reference Publication 1218.
18. Chessell, C.I., 1977, "Propagation of noise along a finite impedance boundary", J.Acoust.Soc.Am. 62(4), pp.825-834.
19. Delany, M.E., Bazley, E.N., 1970, "Acoustical Properties of Fibrous Absorbent Materials", Appl.Acoust. 3, pp 105-116.
20. ESDU Data Sheets, 1990, "Characteristics of Atmospheric Turbulence near the Ground; Part II: Single Point Data for Strong Wings(neutral atmosphere)", Engineering Sciences Data Item No. 85020.
21. Evans, L.B., Bass, H.E., Sutherland, L.C., 1971, "Atmospheric Absorption of Sound: Theoretical Predictions", J.Acoust.Soc.Am. 51(5), pp 1565-1575.
22. Ffowcs Williams, J.E., Hawkins, D.L., 1969, "Sound Generation by Turbulence and Surfaces in Arbitrary Motion", Philosophical Transactions of Royal Society of London 264 (A1151), pp. 321-342.
23. Ffowcs Williams, J.E., Hall, L.H., 1970, "Aerodynamic Sound Generation by Turbulent Flow in the Vicinity of a Scattered Half Plane", Journal of Fluid Mechanics 40(4), pp. 657-670.

24. Grosveld, F.W., 1985, "Prediction of Broadband Noise from Horizontal Axis Wind Turbines", *Journal of Propulsion and Power*, 1(4), pp. 292-299.
25. Harris, M., 1966, "Absorption of Sound in Air versus Humidity and Temperature", *J. Acoust. Soc. Am.* 40(1), pp 148-159.
26. Hess, H.M., Attenborough, K., Heap, N.W., 1989, "Ground characterization by short-range propagation measurements", *J. Acoust. Soc. Am.* 87(5), pp 1975-1986.
27. Howe, M.S., 1978, "A review of the theory of trailing edge noise", *Journal of Sound Vibration* 61(3), pp. 437-465.
28. Hubbard, H.H., Shepherd, K.P., 1991, "Aeroacoustics of Large Wind Turbines", *Journal of the Acoustic Society of America* 89, pp. 2495-2508.
29. Jensen, F.B., Kuperman, W.A., Porter, M.B., Schmidt, H., 1994, "Computational Ocean Acoustics", American Institute of Physics, New York.
30. Lighthill, M.J., 1952, "On Sound Generated Aerodynamically; I. General Theory", *Proceedings of the Royal Society of London* 222A(1107), pp. 564-587.
31. Lowson M.V., 1989, ETSU/W/13/00284/REP
32. Lowson, M.V., 1993, "Assessment and Prediction of Wind Turbine Noise", ETSU W/13/00284/REP
33. Martens, M.J.M., van der Heijden, L.A.M., Walthaus, H.H.J., and van Rens, W.J.J., 1985, "Classification of soils based on acoustic impedance, air flow resistivity, and other physical soil parameters", *J. Acoust. Soc. Am.* 78(3), pp 970-980
34. Porter, M.B., 1994, "The Kraken Normal Mode Program", Saclant Undersea Research Centre Report.
35. Robinson, A.R., Lee, D., 1994, "Oceanography and Acoustics. Prediction and Propagation Models", American Institute of Physics, New York
36. Sabatier, J.M., Raspet, R., and Frederickson, K., 1992, "An improved procedure for the determination of ground parameters using level difference measurements", *J. Acoust. Soc. Am.* 94(1), 396-399.
37. Voutsinas, S.G., Rizziotis, V.A., 1999, "A Viscous-Inviscid Interaction Model for Dynamic Stall Simulations on Airfoils", AIAA 99-0038.
38. Voutsinas, S.G., Triantos, D.G., 1999, "Aeroacoustics of Full Helicopter Configurations using Vortex Particle Flow Approximation", to be presented in the same forum.

Aeroacoustics of Full Helicopter Configurations using Vortex Particle Flow Approximation

Spyros G. Voutsinas, Dimitris G. Triantos
National Technical University of Athens, Fluids Section,
PO Box 64070, 15710 Zografou, Athens, Greece

tel.: (+)301-7721096, fax: (+)301-7721057, e-mail: aiolos@fluid.mech.ntua.gr

Abstract

The aeroacoustic problem for complete rotorcraft configurations is formulated within the framework of linear acoustics. The assumptions associated to such an approach decouple the aerodynamics from the acoustics. First the aerodynamic problem is formulated by combining a boundary integral representation of the flow induced by the solid boundaries with a vortex particle approximation of the wakes. The loads and flow velocities are then introduced to the FW-H equation to give the acoustic pressure field. The flexibility of the method proposed in the present paper is such that the complete configuration is modelled and thus all possible interactions are accounted for. Predictions of aerodynamic pressures and of the acoustic pressure field are compared with wind tunnel measurements confirming the consistency and the reliability of the method.

1 Introduction

Noise is a major issue in rotorcraft industry the reduction of which is an important target for the next period [1-3]. In its general formulation the aeroacoustic problems associated to the generation and propagation of noise is extremely complicated and to a large extent still open. In order to arrive to tractable problems, the low frequency part of noise is usually considered independently within the framework of linear aeroacoustics. Within this context, approaches based on the Ffowcs-Williams Hawkins equation [4], [5] or Kirchhoff formulation [6] are extensively used. Both approaches are formulated through the use of a Green's function leading to an integral representation of the solution. Input to this representation are the results of a purely aerodynamic calculation which is performed first. This makes the aerodynamic calculations extremely important.

Flows with spatially distributed vorticity (free vorticity) and in particular problems with strong vortex-to-solid interactions are of major importance in aeronautical engineering. In rotorcraft concepts the main rotor is in close interaction with the body of the craft whereas on helicopters there is also a strong interaction with the tail rotor. For applications with engineering orientation, and in particular for flows involving several bodies moving independently, Vortex Methods (VM) seem to be the best choice, mainly due to their grid-free structure [7]. Field methods of CFD type, although in principle more accurate in terms of physical modelling, are to the authors' opinion still too heavy in computational terms. There is no doubt that CFD is the only way to get the flow details and from this point of view they are indispensable. However for

engineering applications less demanding methods could prove themselves to be equally or even more accurate especially when multi-component configurations are considered.

VM are relatively old. They were originally designed to approximate vortical flows of an incompressible and inviscid fluid occupying the entire space [8-11] although some vortex methods including solid boundaries did appear during the first decades of the 20th century. The Lifting Line and Lifting Surface theories are two of the oldest vortex methods that are still in some use. As numerical methods evolved, some of the simplifying assumptions regarding the fluid were alleviated and solid boundaries were added more systematically [12], [13]. In aeronautics most of the early developments concerned the application of various versions of the well known Vortex Lattice Method (VLM) [14-16]. According to the currently used terminology these methods as well as their subsequent improved versions, constitute examples of the Vortex Filament Method (VFM) [17-19]. During the same period, in addition to VFM a second class of three-dimensional vortex methods by the name Vortex Particle Methods (VPM) appeared. They were first introduced by Rehbach [20] who anticipated the theoretical studies that appeared later on [21], [22] and was partially ignored. The main difference between the VF and VP methods lies in the approximation of the vortical regions of the flow. More specifically Rehbach used three-dimensional point vortices instead of vortex filaments. This alternative approach is equivalent to a relaxation of the smoothness requirements for the approximation scheme permitting a more consistent treatment of the instabilities that a vortical flow exhibits. The basic idea of the whole scheme is as follows:

Assume the fluid incompressible and inviscid and the flow unsteady. Then, according to Helmholtz's decomposition theorem [23] the velocity field is made up of an irrotational part representing the disturbance due to the presence of the solid boundaries and a rotational part representing the disturbance due to the wakes. In order to determine the irrotational part, the non-penetration boundary condition is used. On the other hand the rotational part of the velocity field is determined directly as convolution of the vorticity contained in the wakes. As the fluid is assumed inviscid, there is no link between the irrotational and the rotational part of the velocity field. In order to bring these parts into contact, additional conditions are required. More specifically a mechanism is introduced that models the vorticity emission process observed in real flows. Such a mechanism is provided by the well-known Kutta condition. It is noted that the fulfilment of the Kutta condition, permits to define numerically the conversion of the bound vorticity into free vorticity, a production process already existing in all the traditional aerodynamic models.

Probably the most important feature of such a flow description is the flexibility in modelling multi-component configurations, with solid elements that move independently. This still holds even if a less simplified flow model is desired, namely the case of a fast rotating rotor over which weak shocks are formed and the case of a viscous fluid. In such cases the domain is decomposed in the near regions, which include all the "non-linearities (shock waves and boundary layers) and the outer region where the approach just described is still valid. This aspect is not considered in the present paper as it concerns a work still in progress.

At NTUA, a code named GENUVP (GENeral Unsteady Vortex Particle code) has been developed along these lines. So far it has been successfully applied to wind turbines, propeller powered aircraft, tilt-rotor aircrafts and recently to helicopters. Two options have been added which can be run in parallel: an aeroacoustic module which determines the low frequency noise based on the FW-H equation and an aeroelastic module using beam approximations of the rotor blades. In the present paper only the aeroacoustic part will be discussed.

2 Formulation of the problem and description of the model

2.1 The aerodynamic model

Consider the unsteady flow around a multi-component configuration consisted of N_s bodies. The bodies are allowed to move independently, a feature necessary for helicopter configurations. Let $\vec{u}(\vec{x};t), \vec{x} \in D, t \geq 0$ denote the velocity of the fluid where D denotes the flow field. Then according to Helmholtz decomposition theorem, \vec{u} can be split in two parts: an irrotational and a rotational one. Usually the presence of solid boundaries is included in the irrotational part whereas the wakes are, as expected, included in the rotational part. So,

$$(1) \quad \vec{u}(\vec{x};t) = \vec{U}_{ext}(\vec{x};t) + \vec{U}_{solid}(\vec{x};t) + \vec{U}_{wake}(\vec{x};t)$$

where \vec{U}_{ext} denotes a given external field possibly time varying, \vec{U}_{solid} denotes the velocity induced by the solid bodies and \vec{U}_{wake} denotes the velocity induced by the wake of the configuration.

Assuming the fluid incompressible and inviscid, \vec{U}_{solid} can be given an integral representation in terms of the normal and tangential to the solid boundaries velocities, $\vec{u} \cdot \vec{n}$ and $\vec{n} \times \vec{u}$ respectively:

$$(2) \quad \vec{U}_{solid}(\vec{x}_o; t) = \int_S (\vec{u} \cdot \vec{n})(\vec{x}; t) \frac{\vec{x}_o - \vec{x}}{4\pi|\vec{x}_o - \vec{x}|^3} dS + \int_S (\vec{n} \times \vec{u})(\vec{x}; t) \times \frac{\vec{x}_o - \vec{x}}{4\pi|\vec{x}_o - \vec{x}|^3} dS$$

The integrals are evaluated over all solid boundaries. In case of the presence of a vortex sheet the second integral should also include it. The non-entry boundary conditions over the solid boundaries determines the normal velocity $\vec{u} \cdot \vec{n}$ and therefore by applying (1) on the body surfaces, two integral equations are obtained for the two components of $\vec{n} \times \vec{u}$.

In the context of classical panel or boundary element methods, $\vec{n} \times \vec{u} = \sigma$ corresponds to a source distribution and $\vec{n} \times \vec{u} = \vec{\gamma}$ corresponds to a surface vorticity distribution often associated to the surface gradient of a dipole distribution μ : $\vec{\gamma} = \nabla \mu \times \vec{n}$. Then instead of solving two equations, only one equation is required, with respect to μ which can be

equal to $-\phi_s$, i.e. the surface potential when the interior of the body is considered as stagnant.

The above two formulations are called *direct* in order to distinguish them from the *indirect* ones in which the source and dipole distributions are introduced as jumps. Direct formulations in aerodynamics and aeroacoustics were introduced by Morino [24] whereas indirect methods were introduced by Hess [25]. In most panel approximations, wakes are introduced as vortex sheets, i.e. surfaces where either the potential or the tangential velocity exhibits a jump. In cases of free wakes, every vortex sheet is moving according to the mean flow defined on it. This means that the vortex sheet will deform according to the surface gradients of this mean flow. Due to the singular character of the associated equations, such an approach can become unstable. Exception to this rule, was Rehbach who first introduced the idea of approximating the surface vorticity of a wake as a collection of freely moving vortex particles. Vortex particles or vortex blobs can be considered as concentrated packages of vorticity: $\vec{\Omega} = \vec{\omega} \delta D$. For an incompressible fluid, $\vec{\Omega}$ will behave exactly as $\vec{\omega}$, the volume δD being invariant. For compressible fluid, extension is possible by considering $\vec{\omega} / \rho$. The concept of vortex blobs can be generalized to include also vortex filaments as well as surface vortex elements. It can be proved that packages of line vorticity $\vec{\Gamma} \delta \ell$, surface vorticity $\vec{\gamma} \delta S$ and volume vorticity $\vec{\omega} \delta D$ behave according to the same material evolution equations, namely:

$$(3) \quad \begin{aligned} \frac{d\vec{Z}}{dt} &= \vec{u}(\vec{Z}; t) \\ \frac{d\vec{\Omega}}{dt} &= (\vec{\Omega} \nabla) \vec{u}(\vec{Z}; t) \end{aligned}$$

where \vec{Z} denotes the center of the package. $\vec{\Omega} = \vec{\Gamma} \delta \ell$, $\vec{\gamma} \delta S$ or $\vec{\omega} \delta D$ denote respectively line, surface and volume elements respectively.

Based on this concept and discretizing the generalized vorticity by pointwise approximations:

$$(4) \quad \vec{U}_{wake}(\vec{x}_o; t) = \sum_{j \in J(t)} \frac{\vec{\Omega}_j(t) \times (\vec{x}_o - \vec{Z}_j(t))}{4\pi |\vec{x}_o - \vec{Z}_j(t)|^3} f\left(\frac{|\vec{x}_o - \vec{Z}_j(t)|}{\epsilon}\right)$$

where the summation runs the entire collection of generalized vortex blobs $J(t)$. In (4), $f(\cdot)$ is regularizing function which renders the velocity bounded. Following Beale & Majda [32],

$$(5) \quad f\left(\frac{r}{\epsilon}\right) = 1 - \exp\left(-\left(\frac{r}{\epsilon}\right)^3\right)$$

where ε denotes the cut-off length.

For an inviscid flow, vorticity can be released into the free flow, only along the edges of the solid boundaries which will include the trailing edge and possibly the tip of any lifting (blade like) body. Kelvin's theorem together with the divergence free condition for the generalised vorticity give the two necessary conditions for determining the amount of bound vorticity being shed and transformed into free vorticity. Figure 1 gives a close-up look of the situation at the trailing edge. Spanwise vorticity \tilde{a}_y is primarily determined by Kelvin's theorem, which ensures a zero pressure jump across the wake vortex surface. The streamwise vorticity \tilde{a}_x is determined by the spanwise gradient of the loading and can be determined by the divergence free condition for $\tilde{\gamma}$ written locally. These two conditions can be considered as the Kutta conditions for 3D unsteady flows.

In the method developed the wake retains its "surface" character only for the part generated during the current time step which is termed *near-wake*. Subsequently the surface vorticity is treated in particle form. From every panel of the near wake, one or more vortex blobs are generated depending on the length scale we wish to have. This is done by integration. For consistency reasons with the general invariance constraints, this integration must conserve the zero and first moments of vorticity. Higher order scheme can be formulated but such an analysis is beyond the scope of the present paper. The above considerations can be directly implemented in a time-marching scheme as follows:

For every time step,

- I) First the so-called "potential" calculations are performed in order to satisfy the non-penetration condition over the solid surfaces and the Kutta conditions along the near wakes. This part will determine the \vec{U}_{solid} term. At this stage any calculation related to applied results such as load estimation, aeroelastic interaction, acoustic pressure estimation is performed. Pressure is calculated according to Bernoulli's theorem. Viscous friction or even viscous effects in general can be included by coupling this calculation with appropriately defined integral boundary layer equations [31].
- II) Next the near wake is transformed into particles.
- III) Finally, in order to prepare the next step, all vortex particles are convected and deformed according to (3). At the end of this procedure, in the near-wake region a gap will appear which will be filled by the shed vorticity of the next step.

A word of caution must be mentioned: calculations based on vortex particle or vortex blob approximations can become very time consuming. There are ways to overcome this difficulty one of which is the use of the so-called vortex-in-cell or particle-mesh approximations [33]. Another equally important point concerns the case of strong vortex-to-solid body interactions. The only remedy to that is again to increase the panel resolution so that the trajectory of a vortex approaching a solid surface can be well approximated. This can again lead to an explosion of the required CPU time. A remedy, which we followed in GENUVP, is to calculate the basic surface integrals by means of

multi-pole expansions. Details on both of these computational tools are given in Voutsinas, Triantos [26].

2.2 The aeroacoustic problem.

The problem of the radiated acoustic field generated by a multi-component configuration is formulated within the context of linear aeroacoustics. Let $f(\vec{x}, t) = 0$ be the moving solid surface. The governing equation takes according to Ffwoes-Williams Hawkins [27] the following form:

$$(6) \quad \frac{1}{c^2} \frac{\partial^2 p'}{\partial t^2} - \nabla^2 p' = \frac{\partial}{\partial t} [\rho_o u_n |\nabla f| \delta(f)] - \frac{\partial}{\partial x_i} [l_i |\nabla f| \delta(f)]$$

Where p' is the acoustic pressure, c is the speed of sound and ρ_o is the density in the undisturbed medium, $u_n = u_i n_i$ is the local normal velocity on the solid surface, l_i is the local force per unit area on the solid surface (it is not just the pressure it might also contain skin friction terms), and $\delta(f)$ is the Dirac delta function. Equation (6) has been extensively investigated through the literature. Following Farassat [28], and neglecting the quadrapole term, the solution of equation (6) is expressed in terms of two integrals over $f(\vec{x}, t)$:

$$(7) \quad 4\pi p'(\vec{x}, t) = \frac{1}{c} \frac{\partial}{\partial t} \int_{f=0} \left[\frac{\rho_o c u_n + l_r}{r |1 - M_r|} \right]_{ret} dS + \int_{f=0} \left[\frac{l_r}{r^2 |1 - M_r|} \right]_{ret} dS$$

Where \vec{x} is the position vector of the observer, \vec{y} is the position vector of the solid surface $r = |\vec{x} - \vec{y}|$ is the radiation distance, $M_r = u_i \hat{r}_i / c$, $l_r = l_i \hat{r}_i$, and $\hat{r}_i = (x_i - y_i) / r$ is the unit vector at the radiation direction. The terms in brackets $[...]_{ret}$ are evaluated in the retarded time $\tau = t - r / c$. In practical computations the solid surface is divided into surface elements each one considered as point source. To each of these sources a volume V_k , a force vector $\vec{L}^k = L_i^k$ and a position vector \vec{y}^k are associated. Thus the radiated field can be synthesised as the sum of the acoustic pressure of all the point sources. Further more, equation (7) can be split into a thickness and a loading term. Following Farassat and Succi [29] the acoustic pressure is given as:

$$(8) \quad p'(\vec{x}, t) = \sum_k (p_L^k + p_T^k)$$

Where,

$$(9) \quad p_L^k = \frac{1}{4\pi} \left\{ \frac{1}{r} \frac{1}{(1-M_r)^2} \left[\frac{\hat{r}_i}{c} \frac{\partial L_i^k}{\partial \tau} + \frac{L_i^k \hat{r}_i}{(1-M_r)} \left(\frac{\hat{r}_i}{c} \frac{\partial M_i}{\partial \tau} \right) \right] + \right. \\ \left. \frac{1}{r^2} \frac{1}{(1-M_r)^2} \left[r_i L_i^k \frac{1-M_i^2}{1-M_r} - L_i^k M_i \right] \right\}_{ret}$$

is the acoustic pressure due to the point force L_i^k of the k th element corresponding to the loading noise term, and

$$(10) \quad p_T^k = \frac{\rho_o}{4\pi} \left\{ \frac{1}{1-M_r} \frac{\partial}{\partial \tau} \left[\frac{1}{1-M_r} \frac{\partial}{\partial \tau} \left(\frac{V_k}{r(1-M_r)} \right) \right] \right\}_{ret}$$

is the acoustic pressure due to the volume V_k of the k th element corresponding to the thickness noise term.

In the above formulation there are two time levels, the emission time denoted by (∂) and the observer time denoted by (t) . An acoustic signal generated by a moving point source located at $\vec{y}(\tau)$, travels with speed c and reaches the observer located at \vec{x} after a time interval of $|\vec{x} - \vec{y}|/c$. Based on this remark, an emission time algorithm is used in order to evaluate the retarded-time integrals. The algorithm is *source time dominant* and requires as input: a set of sources each one associated with a volume V_k , a time sequence of force vectors $\vec{L}^k(\tau)$, and a time sequence of position vectors $\vec{y}(\tau)$. Alternatively, to the sequence of position vectors an analytic expression of the motion of each source can be used. However in cases of complicated motion as for example in helicopter rotors a discrete sequence is more appropriate. In addition, the density and the speed of sound of the undisturbed medium as well as the observer position vector \vec{x} have to be defined. In case the observer is not still, an analytical expression of its motion or a discrete sequence of position vectors $\vec{x}(t)$ can be used.

The calculation procedure involves the following steps:

- A sequence of emission time steps (τ_i) is defined depending on the time step of the aerodynamic calculation. For every source k , at every time (τ_i) , p_L^k and p_T^k are evaluated using (9) and (10). This is straightforward since all quantities and derivatives in these formulas are expressed at emission time (∂) . Thus, a discrete sequence of "emitted" acoustic pressure $p_i^k = p^k(\tau_i)$ is created for each source.
- For every time (τ_i) the corresponding observer time (t_i) is calculated. The observer time (t) is the time that the acoustic signal generated at (∂) will reach the observer. Calculation of (t_i) is straightforward: $t_i = \tau_i + r_i^k/c$ for a stationary observer, or $t_i - \tau_i - |\vec{x}(t_i) - \vec{y}^k(\tau_i)|/c = 0$ for an observer in motion. Even in the later case determination of (t) is simple since the motion of the observer is usually simple and

therefore given by an analytic expression. Thus, the "emitted" sequence $p^k(\tau_i)$ is transformed into an "arrived" sequence $p^k(t_i)$, which is the acoustic pressure sequence that the observer will receive from the acoustic source k . It should be noted here, that the spacing of the source time sequence (τ_i) is not conserved in the observer sequence time (t_i) . Further more if supersonic motion of the source is in consideration the 'arrived' sequence $p^k(t_i)$ will not be a one valued function of (t) since the order in source time sequence (τ_i) will not be conserved in the observer sequence time (t_i) .

- The final step is to sum up the acoustic pressure sequences $p^k(t_i)$ of all sources. This is realised by creating a time sequence t^* , as equally spaced, in observer time level. At each time t_j^* of that sequence, interpolation of the pressure signature $p^k(t_i)$ of each source is performed, leading to a new sequence of acoustic pressure $p^k(t_j^*)$ for each source. This interpolation procedure is necessary since the observer time sequence derived in the previous step is not the same for all acoustic sources. The final acoustic pressure signature that the observer will receive, is the summation over all the acoustic sources

$$p'(\bar{x}, t_j^*) = \sum_k p^k(t_j^*).$$

This is a generalised weighted interpolation step. Simple linear interpolation was used in this work. Higher order schemes can be used when the input data set is not dense enough in time since there is risk of smoothing the acoustic pressure signature. The density of the interpolating sequence t_j^* can be several times larger than the density of the input sequence (τ_i) , however with the use of linear interpolation and by increasing the density more than four times did not give any significant difference in the resulting pressure signature. This means that in any case the aerodynamic time step which rules the density of the input information must be carefully selected.

The quality of the derived acoustic pressure signature is strongly dependent on the aerodynamic data that will be used as input. Thus aerodynamic input data must be, dense in time (small time step) and dense in space (fine discretization of the solid surfaces), in order to capture the acoustic signatures of local in time and space interactions (e.g. B.V.I. noise). The algorithm described above has the advantage that a retarded-time calculation is not necessary, and the discrete time-dependent input data do not need to be interpolated. Additionally the algorithm is inherently parallel and easily implemented in massively parallel computers.

3 Results

The predicting capabilities of the method are investigated in the present paragraph. Calculations from the application of the method on helicopter rotors are compared against measurements. In Fig. 2 the full configuration of the BO105 helicopter model is presented together with a snap shot of the free wake created by all components except the fuselage, realised with vortex blobs. The resolutions of the grids used are 101×17 for the main rotor blade, 101×9 for the tail rotor blade the stabilisers and the endplates and 25×49 for the fuselage. The time step corresponds to a 4 degrees rotation of the main rotor. The same panelling, and time step is used in all the cases presented in this work including the cases where only the main rotor was simulated. The advance ratio of all cases presented is 0.15. The control angles are included in all flight cases presented in this work. Indicative results from the aerodynamic calculation are presented in Fig. 3. The pressure coefficient distributions, at three radial position of the main rotor blade, and at azimuth angle of 270 degrees are displayed. The simulated case is a 12 degrees climb flight at 33 m/s. The measurements were conducted within the HELINOISE project [34]. The computation as well as the experiment are conducted only the main rotor. The computations of the pressure coefficient distributions are in satisfactory agreement with measurements at all radial positions.

In Fig. 4 the microphone locations with respect to the rotor disk are illustrated. At these locations acoustic pressure signatures are recorded [34]. In Fig. 5 – Fig. 7 comparisons of the calculated with the measured acoustic pressure signals are presented, for a 12 degrees climb flight, a level flight and a 6 degrees descent flight respectively. The calculated acoustic pressure signature reproduces the general trend of the measured data. Differences between the measured and the calculated signals are expected due to the absence of aeroelastic modelling of the blades. Additionally the computed signals are less smooth than the measured due to the discrete vortex blob approximation of the wake. This is mainly observed in the level flight (Fig. 6) and the decent flight (Fig. 7) where the wake is “close” to the rotor disk. In contrast, in the climb case (Fig. 5) the computed signal is smooth, since the wake is relatively “far” from the rotor disk. An important parameter for the computation of the acoustic signal is the time resolution of the aerodynamic input. Calculations of blade vortex interactions (BVI) and the corresponding noise are strongly related to the accuracy of the approximation of the local kinematics and the dynamics of the wake, which are determined by the time resolution. In the cases presented the time resolution corresponds to a length scale of the order of the chord at the tip of the blade. Thus, the passage of a vortex above/under a blade section is not accurately represented, since it can be realised even in one time step. This result, in differences in the amplitude of the picks between the calculated and the measured noise signatures observed, especially in decent flight (Fig. 7).

In Fig. 8 calculation of the acoustic pressure signature from the simulation of the full helicopter configuration is presented. The computation includes the main rotor, the tail rotor and the fuselage, the stabilisers and the endplates of the BO105 helicopter model. The simulated case is a 12 degrees climb flight at 33 m/s. The rotational speed of the tail rotor is approximately five times the rotational speed of the main rotor. In Fig. 8 the sound pressure is plotted with respect to the main rotor revolution, with tail rotor main

blade at 105 degrees azimuth angle, when main rotor main blade is at 0 degrees azimuth angle. Comparison with measurements is not presented due to lack of experimental data. However comparison of Fig.8 with Fig. 5 clearly displays the effect of the tail rotor on the amplitude as well as the frequencies of the signal.

4 Conclusions

A numerical method for predicting the noise generated by a complete helicopter configuration has been presented and some indicative results have been discussed. The method is formulated under the assumptions of acoustic analogy, which permits the decoupling of the aerodynamics from the acoustics. A definite conclusion regarding the overall performance of the method is that the basic features of the noise generating mechanisms are reproduced. This is important since the method provides the predictions for a full configuration under reasonable cost. Certainly some aspects, such as the BVI, are not resolved in great detail, this being due to the elementary physics contained in the inviscid aerodynamic model. One way to overcome this difficulty at a minimum cost is to include a viscous-inviscid strong interaction coupling. This direction is being examined jointly by University of Rome Tre (Prof. L. Morino) and NTUA.

Particularly with respect to acoustics, the FW-H equation, which is used to estimate the acoustic pressure, turned out to be a simple and reliable approach as far as the loading and thickness terms are concerned. The quadrapole term, which is important in high flight speeds, has not been considered. It requires a different kind of aerodynamic modelling which will be able to handle weak shock waves. This is part of a work in progress that aims at imbedding into the flow region boxes in which the Euler equations are solved by a field method over a grid attached to the blade. Such boxes will be necessary in the tip regions only. In the case of a "supersonic" tip, the FW-H equation can be still used except that the surface should be chosen to cover the regions with shocks.

Another aspect, which requires further work, is the significance of the aeroelastic effects. The calculations performed so far include only the rigid body motions of the blades as provided by the tests. The aeroelastic coupling is included in GENUVP but validation has been so far performed only for wind turbine rotors [30]. Validation for helicopters is still pending basically due to the difficulties in getting detailed data.

Acknowledgements

The authors, on behalf of NTUA, thank DGXII for funding part of the work under the HELIFLOW project and the partners involved who made available technical data. In particular the authors would like to thank Dr V. Kloppel from Eurocopter Germany, Dr W. Splettstoesser from DLR, Dr R. Munt from DERA and Dr P. Renzoni from CIRA for their assistance during the course of this work. From a scientific point of view, the authors thank Prof. L. Morino for all the invaluable discussions and remarks. To a large extent this work has been inspired by his pioneering work on boundary integral methods.

References

1. F. H. Schmitz, Y. H. Yu : "Helicopter impulsive noise: Theoretical and experimental status", *Journal of Sound and Vibration* 109, (1986).
2. A. R. George : "Helicopter noise-state of the art", *American Institute of Aeronautics and Astronautics* 77-1337, (1977)
3. R. P. White : "The status of rotor noise technology", *Journal of the American Helicopter Society* 25, (1980)
4. F. Farassat : "Linear Acoustic Formulas for Calculation of Rotating Blade Noise", *AIAA Journal*, Vol.19, No. 9, (1981)
5. S. Ianniello, E. de Bernardis : "Calculation of High-Speed Noise from Helicopter Rotor Using Different Descriptions of Quadrupole Source", *AGARD Fluid Dynamics Panel Symposium on Aerodynamics and Aeroacoustics of Rotorcraft*, (1994)
6. Y. Xue, A. S. Lyrintzis : "Rotating Kirchhoff Method for Three Dimensional Transonic Blade-Vortex Interaction Hover Noise", *AIAA Journal*, Vol. 32, No 7, (1994)
7. A. Leonard : "Computing three dimensional incompressible flows with vortex filaments", *Ann. Rev. Fluid Mech.* Vol. 17, (1985)
8. L. Rosenhead : "The formation of vortices from a surface of discontinuity", *Proc. Royal Soc. Ser.A*, 134 (1931)
9. I. G. Bromilow, R. R. Clements : "Some techniques for extending the application of the discrete vortex method of flow simulation", *Aeronautical Quarterly* (1981)
10. J. P. Choquin, S. Huberson : "Particles simulation of viscous flows" *Computer and fluids* (1988)
11. A. J. Callegari, L. Ting : "Motion of a curved vortex filament with decaying vortical core and axial velocity", *SIAM J. Appl. Math.* Vol. 35 (1979)
12. A. J. Chorin : "Numerical study of slightly viscous flow", *J. Fluid Mech.* Vol. 57 (1973)
13. C. Costis, D. P. Telionis : "Unsteady vortical wakes over a prolate spheroid", *AIAA paper* 84-0419, (1984)
14. R. H. Djodjodihardjo, S. E. Widnal : "A numerical method for the calculation of nonlinear, unsteady lifting potential flow problems", *AIAA J.* Vol. 7 (1969)
15. S. M. Belotserkovskii : "Study of the unsteady aerodynamics of lifting surfaces using the computer", *Ann. Rev. Fluid Mech.*, vol.9, (1977)
16. O. A. Kandil, L. C. Chu, E. C. Yates : "Hybrid vortex method for lifting surfaces with free vortex flow" *AIAA paper* 800070, (1980)
17. B. Maskew : "Predicting aerodynamic characteristics of vortical flows on three-dimensional configurations using a surface singularity panel method", *AGARD C.P.* 208, (1980)
18. J. Katz : "Large-scale vortex lattice model for the locally separated flow over wings", *AIAA J.* Vol. 20 (1982)
19. D. Levin, J. Katz : "Vortex-lattice method for the calculation of the nonsteady separated flow over Delta wings", *J. Aircraft*, Vol. 18 (1981)
20. C. Rechbach : "Calcul numerique d'écoulements tridimensionnels instationnaires avec nappes tourbillonnaires", *Recherche Aerospaciale*, No. 5 (1977)

21. J. T. Beale, A. Majda : "Vortex Methods", Mathematics of Computation, Vol. 39, (1982)
22. P. A. Raviart : "Methodes et approximations particulaires", Lecture Notes (1989)
23. S. M. Richardson, A. R. H. Conrith : "Solution of three-dimensional incompressible flow problems", J. fluid. Mech. Vol 82, (1977)
24. L. Morino : "A general theory of unsteady compressible potential aerodynamics", NASA CR-2464, (1974)
25. J. L. Hess : "Calculation of potential flow about arbitrary three-dimensional lifting bodies", Technical Report McDonnell Douglas Corporation, MDC J5679-01, (1972)
26. D. G. Triantos, S. G. Voutsinas : "High resolution aerodynamic model with application on full Helicopter Configurations", submitted in 25th E.R.F. (1999)
27. J. E. Ffowcs Williams, D. L. Hawkings : "Sound generation by turbulence and surfaces in arbitrary motion", Phil. Trans. Royal Society, A264, (1969)
28. F. Farassat : "Theory of noise generation from moving bodies with an application to helicopter rotors", NASA T. R. R-451, (1975)
29. F. Farassat, G. P. Succi : "A review of propeller discrete frequency noise prediction methodology with emphasis on two current methods for time domain calculations", J. Sound and Vibration, 71, (1980)
30. S. G. Voutsinas, V. A. Riziotis, P. Chaviaropoulos : "Non-linear Aerodynamics and fatigue loading on wind turbines operating at extreme sites", AIAA paper 970935, (1997)
31. S. G. Voutsinas, V. A. Riziotis : "A viscous-inviscid interaction model for dynamic stall simulations on airfoils" AIAA paper 990038, (1999)
32. J. T. Beale, A. Majda : "Higher order accurate vortex methods with explicit velocity kernels", J. Computational Physics, Vol. 58, (1985)
33. R. W. Hockney, J. W. Eastwood : "Computer simulation using particles", McGRAW-HILL (1981)
34. W. R. Splettstoesser, B. Junker, K. J. Schultz, W. Wagner, W. Weitemeyer, A. Protopsaltis, D. Fertis : "The HELINOISE Aeroacoustic Rotor Test in The DNW -Test Documentation and Representative Results-", DLR Mitteilung 93-09, (1993)

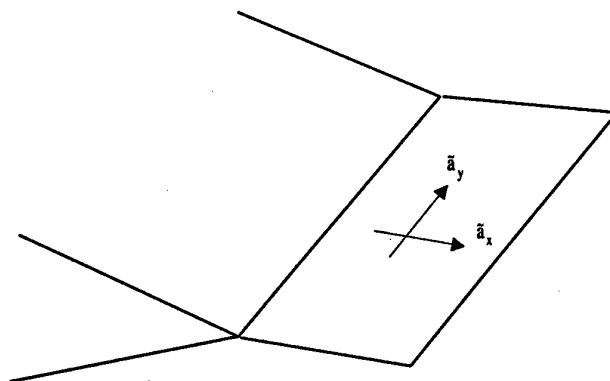


Fig. 1.: The situation at the trailing edge.

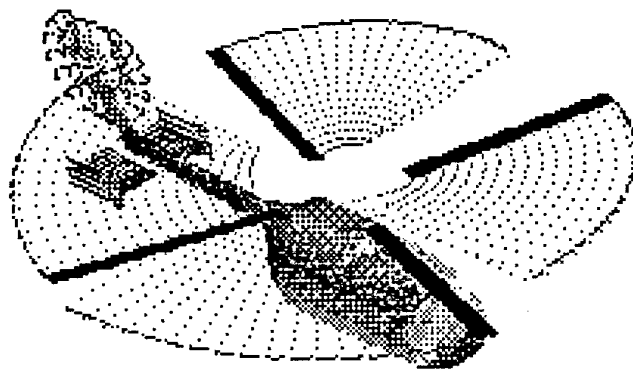


Fig. 2. : Simulation of full helicopter configuration. Free wake generated by the main rotor, the tail rotor, the endplates and the stabilizers, is realized with vortex blobs.

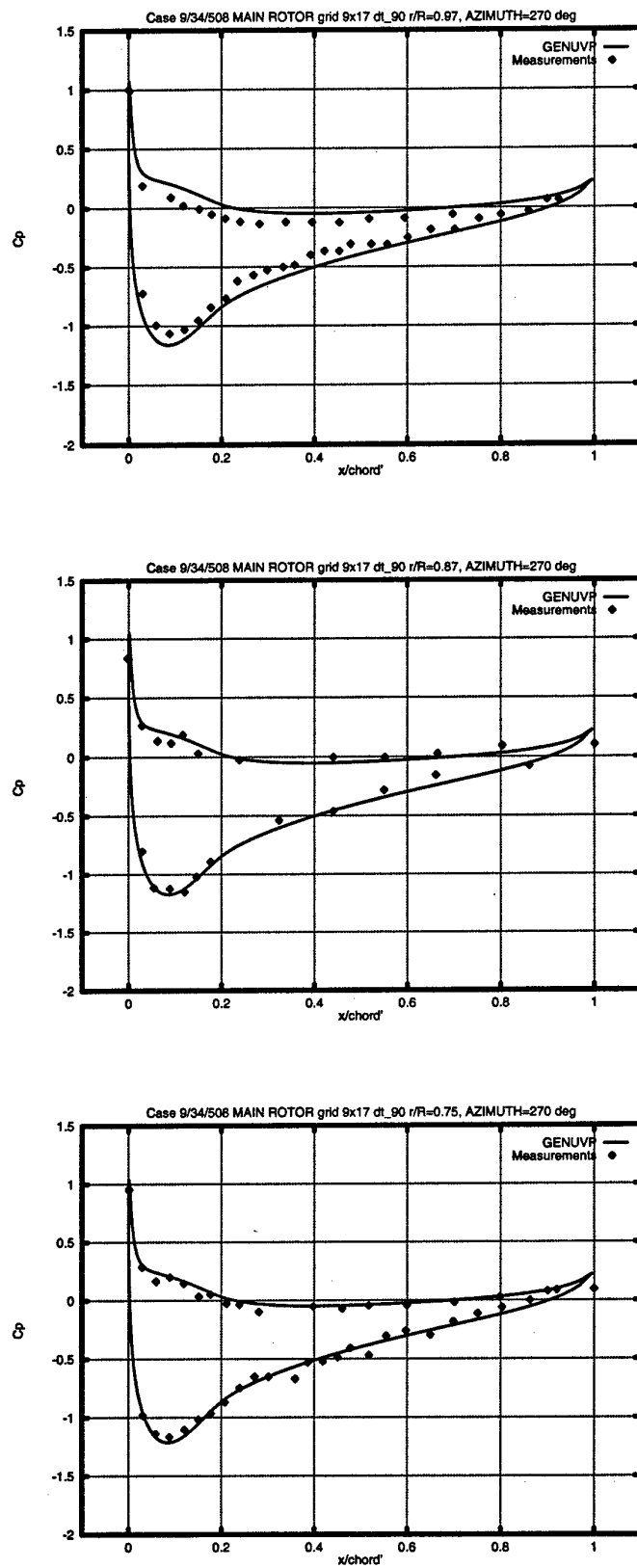


Fig. 3. : Pressure coefficient distributions at 75%, 87% and 97% of the radius of BO105 main rotor blade, at azimuth angle 270 degrees.

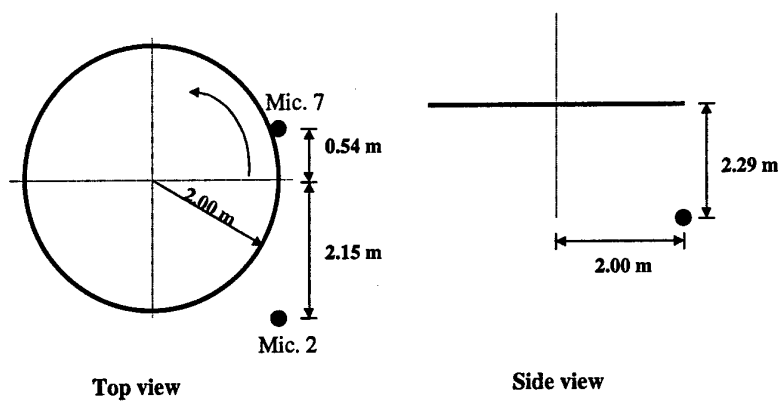


Fig. 4. : Microphones locations

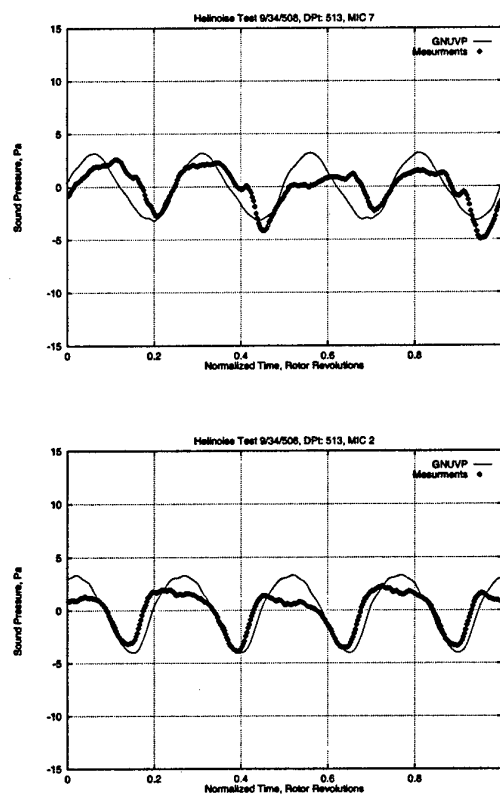


Fig. 5. : Acoustic pressure signature. Simulation of 12 degrees climb flight at 33 m/s.

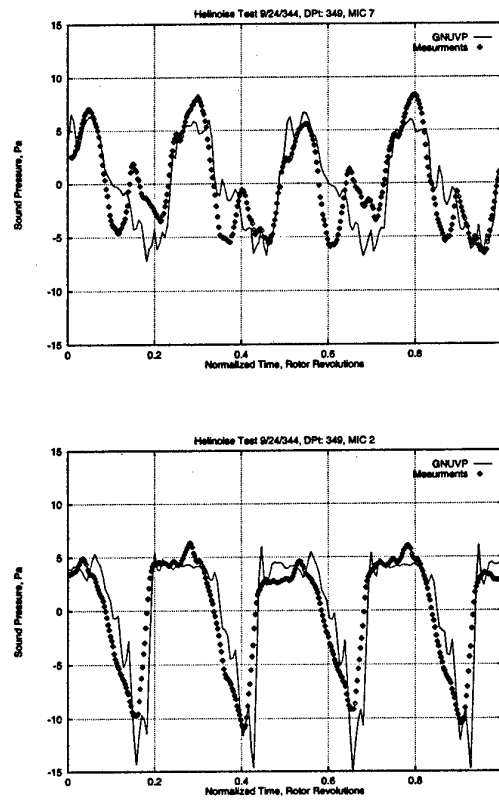


Fig. 6 : Acoustic pressure signature. Simulation of level flight at 33 m/s

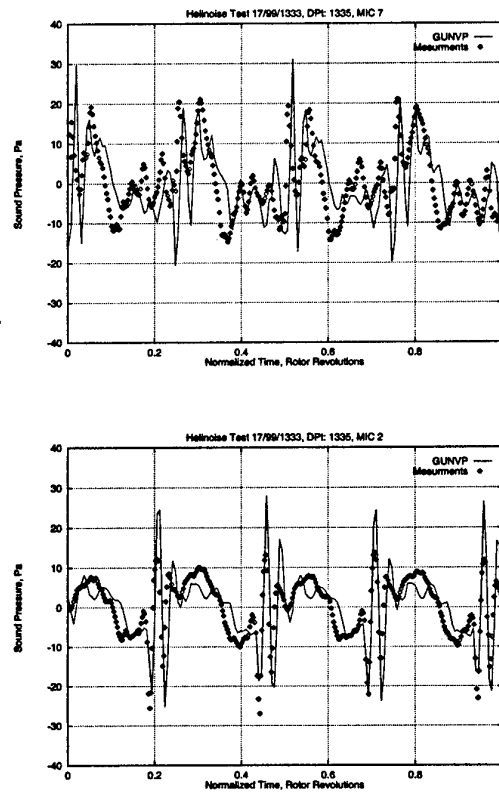


Fig. 7. : Acoustic pressure signature. Simulation of 6 degrees decent flight at 33 m/s

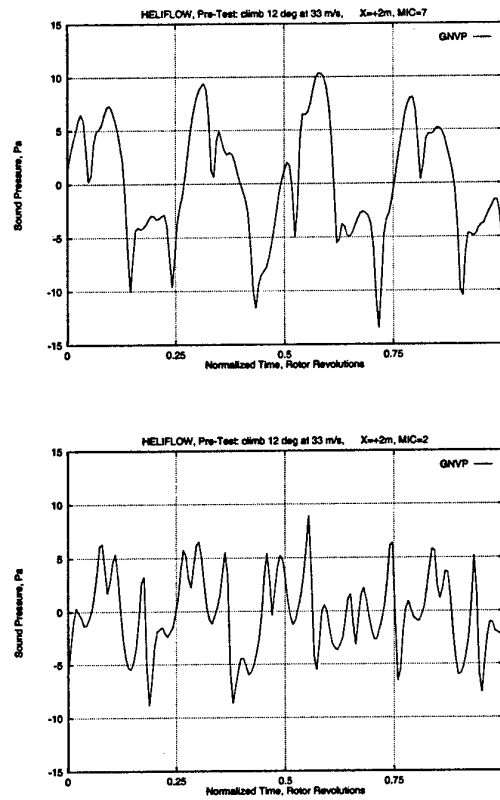


Fig.8. : Acoustic pressure signature. Simulation of 12 degrees climb flight at 33 m/s.
The simulation includes the Main Rotor, the Fuselage, the Tail Rotor, the Stabilizers, and the endplates.